AERODYNAMIC DESIGN AND ANALYSIS OF

SMALL HORIZONTAL AXIS WIND TURBINE BLADES

BY

XINZI TANG

BEng (Hons) MSc

A thesis submitted in partial fulfilment of the requirements for the degree of

DOCTOR OF PHILOSOPHY at

School of Computing, Engineering and Physical Sciences,

University of Central Lancashire, Preston, UK

September 2012

Declaration

I declare that while registered as a candidate for the research degree, I have not been a registered candidate or enrolled student for another award of the University or other academic or professional institution. I declare that no material contained in the thesis has been used in any other submission for an academic award and is solely my own work.

Signature of Candidate   Xinzi Tang

Abstract

The exploitation of small horizontal axis wind turbines provides a clean, prospective and viable option for energy supply. Although great progress has been achieved in the wind energy sector, there is still potential space to reduce the cost and improve the performance of small wind turbines. An enhanced understanding of how small wind turbines interact with the wind turns out to be essential.

This project investigates the aerodynamic design and analysis of small horizontal axis wind turbine blades via the blade element momentum (BEM) based approach and the computational fluid dynamics (CFD) based approach. From this research, it is possible to draw a series of detailed guidelines on small wind turbine blade design and analysis. The research also provides a platform for further comprehensive study using these two approaches.

A detailed review on the wind turbine aerodynamics regarding blade design and aerodynamic performance analysis using the BEM and CFD based approaches was firstly conducted. The wake induction corrections and stall corrections of the BEM method were examined through a case study of the NREL/NASA Phase VI wind turbine. A hybrid stall correction model was proposed to analyse wind turbine power performance. The proposed model shows improvement in power prediction for the validation case, compared with the existing stall correction models.

The effects of the key rotor parameters of a small wind turbine as well as the blade chord and twist angle distributions on power performance were investigated through two typical wind turbines, i.e. a fixed-pitch variable-speed (FPVS) wind turbine and a fixed-pitch fixed-speed (FPFS) wind turbine. An engineering blade design and analysis code was developed in MATLAB to accommodate aerodynamic design and analysis of the blades. The linearisation for radial profiles of blade chord and twist angle for the FPFS wind turbine blade design was discussed. Results show that, the proposed linearisation approach leads to reduced manufacturing cost and higher annual energy production (AEP), with minimal effects on the low wind speed performance.

Comparative studies of mesh and turbulence models in 2D and 3D CFD modelling were

conducted. The CFD predicted lift and drag coefficients of the airfoil S809 were compared with wind tunnel test data and the 3D CFD modelling method of the NREL/NASA Phase VI wind turbine were validated against measurements. Airfoil aerodynamic characterisation and wind turbine power performance as well as 3D flow details were studied. The detailed flow characteristics from the CFD modelling are quantitatively comparable to the measurements, such as blade surface pressure distribution and integrated forces and moments.

The verified CFD modelling methods and wind tunnel testing were employed in aerodynamic characterisation of the airfoil DU93-W-210. 3D CFD modelling was applied for power performance analysis of the BEM-designed FPVS and FPFS wind turbines. The CFD results and BEM results are generally agreeable. The flow moves in the chord-wise direction at low wind speeds and the span-wise flow occurs at high wind speeds for all the wind turbines investigated. It is confirmed that the CFD approach is able to provide a more detailed qualitative and quantitative analysis for wind turbine airfoils and rotors. With more advanced turbulence model and more powerful computing capability, it is prospective to improve the BEM method considering 3D flow effects.

Keywords: Wind Energy, Wind Turbine Aerodynamics, Small Horizontal Axis Wind Turbine (HAWT), Blade Design and Analysis, Blade Element Momentum (BEM), Computational Fluid Dynamics (CFD)

Dedicated to

My daughter Jolly

Contents

List of Tables

List of Figures

Acknowledgements

Acronyms/Abbreviations

2D	Two-Dimensional
3D	Three-Dimensional
AEP	Annual Energy Production
AMWS	Annual Mean Wind Speed
AoA	Angle of Attack
AR	Aspect Ratio
BEM	Blade Element Momentum (Theory)
CAD	Computer Aided Design
CFD	Computational Fluids Dynamics
CNC	Computer Numerical Control
CoE	Cost of Energy
DES	Detached Eddy Simulation
DNS	Direct Numerical Simulation
D-S	Du-Selig
FP	Flat Plate (Theory)
FPFS	Fixed-Pitch Fixed-Speed
FPVS	Fixed-Pitch Variable-Speed
HAWT	Horizontal Axis Wind Turbine
HSC	Hybrid Stall Correction (model)
LES	Large Eddy Simulation
MRF	Multiple Reference Frame
RANS	Reynolds-Averaged-Navier-Stokes
Re	Reynolds Number
RPM	Rotation Per Minutes
S-A	Spalart-Allmaras
SST	Shear Stress Transport
TSR	Tip Speed Ratio
V-C	Viterna-Corrigan

Symbols

ρ	Air density, in kg/m^3
α	Angle of attack, in degree
φ	Angle of relative wind, in degree
θ_r	Angle of relative wind at position r, in degree
ϕ	Angle of relative wind, in rad
$\bar{v}$	Annual mean wind speed, in m/s
a	Axial induction factor
c_r	Chord at position r, in m
c	Chord of an airfoil, in m
v_i	Cut-in wind speed, in m/s
v_c	Cut-out wind speed, in m/s
C_d	Drag coefficient
C_{Ds}	Drag coefficient at stall onset
F_D	Drag force, in N
F_t	Force in the flow direction, in N
F_T	Force perpendicular to the flow direction
α_s	Inflow angle at stall onset, in rad
l	Length of a blade element, in m
C_l	Lift coefficient
C_{Ls}	Lift coefficient at stall onset
F_L	Lift force, in N
λ_r	Local speed ratio at position r
U	Nature wind speed, in m/s
Z	Number of blades
θ_P	Pitch angle, in degree
C_P	Power coefficient
F	Prandtl tip-hub loss factor

v_r	Rated wind speed, in m/s
U_{rel}	Relative flow velocity, in m/s
Ω	Rotational speed, in rad/s
D	Rotor diameter, in m
P	Rotor Power, in W
R	Rotor radius, in m
ω	Rotor speed, in rad/s
r	Section span position, i.e. local radius, in m
λ_h	Speed ratio at hub
a'	Tangential induction factor
F_N	Thrust to a rotor, in N
λ	Tip speed ratio
T	Torque to a rotor, in Nm
φ_r	Twist angle, in degree
v	Variable wind speed, in m/s
dr	Width of a blade element, in m

CHAPTER 1   INTRODUCTION

1.1   Background

Energy is essential to human civilisation development. With progress of economics and socialisation, there is an expanding demand on renewable energy resources to secure energy supply, such as solar power, wind power, tide and wave power etc. As a clean renewable resource, wind power plays a more and more important role in modern life. According to the British Wind Energy Association (BWEA), it was estimated that wind power production met 12.2% of electricity demand in the UK around the end of 2011, and the government aims to reach a target of 20% from renewables in 2020 [1].

Power in the wind comes from the transformation of the air that is driven by the heat of the sun, which is abundant, clean and renewable. As one of the most popular renewable energy resources, wind power exploitation is growing rapidly. At the beginning of 2006, the total installation of wind turbine capacity reached 59,206 MW worldwide [2]. In June 2011, a total installation of 5,560MW was operational in the UK and it is predicted by RenewableUK that in 2012 the annual wind power capacity will increase to 1.2GW [3]. It was also released by the Global Wind Energy Council that in 2011, a total annual increase in wind power industry reached 41GW worldwide, which is corresponding to an annual growth of 21% comparing to the previous year. It has been estimated that the global capacity could reach no less than 200GW by 2014 [4]. From quantity to quality, wind turbine technology is undergoing great development. With the advancement of materials, manufacturing technology, intelligent control, and rotor aerodynamics, the rotor diameter of a 5MW wind turbine (Repower) has reached 126 meters [5].

A wind turbine converts kinetic energy into mechanical power through a rotor, and then converts the mechanical power into electric power through a generator which is linked to the rotor with and without a gearbox. Various types of wind turbines are designed to take advantage of wind power based on the principles of aerodynamics. Depending on the wind turbine rotor orientation, there are two types of wind turbines, horizontal axis

wind turbine (HAWT) and vertical axis wind turbine (VAWT). Generally speaking, according to wind turbine capacity (size), modern wind turbines can be classified as small wind turbines (below 50kW), medium size wind turbine (50kW~250kW) and large wind turbines (above 250kW). When considering installation sites, there are onshore (free standing or building mounted) and offshore wind turbines. Based on the operation scheme, wind turbines can be divided into stall-regulated (fixed-pitch) wind turbines and pitch-controlled (variable-pitch) wind turbines. According to the relative flow direction of the wind turbine rotor, horizontal-axis wind turbines are either upwind or downwind turbines. Most modern HAWTs have three blades; however there are turbines with two blades. For small wind turbines, there are also turbines with 5 or 7 blades. Three-bladed upwind HAWT is the most common topology due to higher efficiency, better balanced performance and aesthetic appreciation. Nowadays, offshore pitch controlled giant wind turbines have gained a particular emphasis in the wind power industry and research organisations. However, the fixed-pitch wind turbine remains one of the most popular topologies for small wind turbines due to the advantages of simplicity, reliability, easy to access, well-proven and low cost. Most of small wind turbines are three-bladed upwind fixed-pitch HAWTs, which are investigated in this thesis unless otherwise stated.

Small wind turbines can be utilised for both on-grid and off-grid applications, and have been deployed both in urban and rural areas. Comparing to significant power contribution of large wind turbines connected to the national electricity grid, the research and development of small wind turbines lack an incentive policy and public interest. According to the fourth annual small wind turbine systems UK market report, it is indicated that the estimated UK annual market growth in 2011 is 167% and the total installed capacity of small wind turbine systems reached 42.97MW at the end of 2011[6]. It is deemed that small wind turbines will play a more and more important role in distribution networks and therefore significantly strengthen the existing electricity grid.

Although great progress has been achieved in the wind energy sector; yet there is a long way to go in expanding wind energy supply and achieving necessary reduction in cost of energy (CoE). It was estimated that 30% to 50% cost reductions are still needed for wind energy to meet 10% of world electricity demand by the end of 2020 [7]. The

challenges in the wind energy community are to develop optimised wind turbines which have maximum annual energy production (AEP) and minimum CoE, as well as high stability and reliability.

1.2 The Role of Aerodynamics in Wind Turbine Design

A wind turbine is a complex system which consists of several components, including a rotor, a transmission system, a generator, a nacelle, a tower and other electro-mechanical subsystems. The rotor blades are the most important components. In order to transfer wind energy into mechanical power, the blade is designed as an aerodynamic geometry with nonlinear chord and twist angle distributions. The section view of a wind turbine blade is of an airfoil shape (one or more airfoils), which is expected to generate high lift and low drag forces. The shape of the blade is vital as it determines the energy captured, and the loads experienced. The study of interaction between wind flows and wind turbines is wind turbine aerodynamics which plays an important role in wind turbine design and analysis.

Wind turbine aerodynamics is originally from propeller aerodynamics. To introduce wind turbine aerodynamics in a simple way, a "tube" is introduced to describe the flow passing through a rotor in the classical disk theory as shown in Figure 1-1.
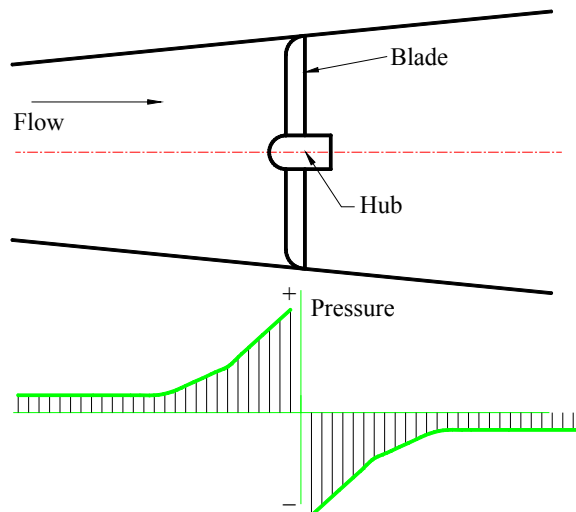
Figure 1-1 Stream tube sketch

In the disk theory, the flow is assumed equivalent across the sectional area of the tube, and the rotating rotor is regarded as a disc. When the inflow wind blows and strikes the blades, the velocity drops and the pressure increases just before the rotor plane; and

immediately after the rotor plane, an adverse pressure distribution appears. With a pressure deficit between the upwind surface and the downwind surface along the span of the blade, once the total torque is able to conquer the cogging torque and the resistant torque of the system, the turbine rotor starts to rotate. With adequate wind inflow velocity (generally higher than 3-4 m/s), the turbine accelerates and the generator begins to produce electricity. An optimal wind turbine blade design usually has a high power efficiency, which is named as power coefficient (*Cp*), and is calculated as the ratio of the rotor power output of the wind turbine to the power in the wind.

Moreover, there are many other aspects of concern in wind turbine blade design, such as maximum annual power capability, structure safety, economics, material availability and site suitability. All these factors contribute to CoE, which is the final goal of a wind turbine design. Wind turbine blade design is a multiple-objective optimisation process as many disciplines are required including aerodynamic, structure, material, and economics. The design process is often executed in a heuristic manner. Within the time limits of this PhD project, the structural, material aspects and unsteady aerodynamics are not the topics of this thesis.

A typical wind turbine design process is illustrated in Figure 1-2, where the aspects involved in the design process and their relationship are depicted. The design process is composed of three main models which are an aerodynamic model, a structure model and an economics model (cost model). These three models form the main frame of wind turbine design. Among the three models, the aerodynamic model is the most fundamental one which determines the power extracted and the loads experienced. As a result, the AEP, the CoE and the life time of wind turbine are all affected by the aerodynamic model used. In a word, the aerodynamic model has a great importance on design of wind turbine rotor blades and other components and subsystems. An accurate aerodynamic model is the first consideration in the wind turbine design process.
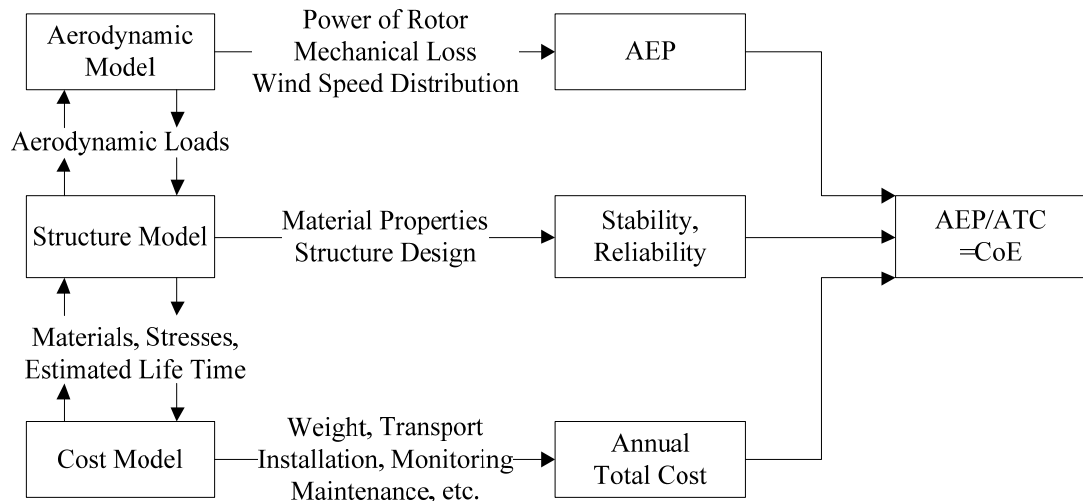
Figure 1-2 A typical wind turbine design process

1.3   Current Status of Wind Turbine Aerodynamics

From simplicity to complexity, there are mainly three ways to model wind turbine aerodynamics: Blade Element Moment (BEM) method, Lift line/surface/panel method, direct Computational Fluid Dynamics (CFD) method.

The most popular theory in wind turbine aerodynamics is the Blade Element Moment (BEM) Theory which was firstly published by Glauert in 1948. In the BEM theory, the blade is divided into several sections and each section sweeps an annular area when the rotor rotates. These annuli are separated and no interaction between each other. In other words, the stream tube is decomposed along different radius positions and each annulus has its own momentum balance. By calculating the torque and thrust forces using wind tunnel tested airfoil lift and drag coefficients for each annulus, the total power and thrust forces can be obtained by integral of an infinite number of sections/elements. This is a great development in the history of the wind turbine aerodynamics, which relates the blade geometry to power and thrust forces using lift and drag coefficients. It provides a principle to design optimal blade geometry.

Lifting line/surface/panel methods and Computational Fluid Dynamics (CFD) methods are widely applied in airfoil aerodynamic analysis. All these numerical methods are employed in near wake and far wake analysis. As defined in reference [8], near wake refers to the region from the wind turbine rotor plane to one or two rotor diameters

downstream which is directly affected by wind turbine geometry, while far wake concerns the far downstream region which is influenced by the reduced axial velocity and turbulence intensity. In other words, investigation of one wind turbine is near wake analysis, while investigation of multiple wind turbine downstream wakes, such as for wind farm development, is far wake analysis. In this project, only near wake analysis is within the scope of research as wind turbine blade design and power performance are concerned.

Table 1-1 shows a comparison of different aerodynamic models. Based on the nature of these methods, the BEM and CFD methods are the suitable methods as far as wind turbine blade geometry is concerned. Among these methods, the BEM theory is most widely used in wind turbine blade design and analysis. However, there is a debate on the limitations of the BEM method, such as lack of description for: three dimensional (3D) flows, heavy-loaded turbulent conditions, stall-delay phenomenon (presented an increase in measured power compared to expected values at high wind speeds), unsteady flows and yawed conditions [9]. Meanwhile, direct 3D CFD method has been greatly strengthened with better and better computing capacity. Although the turbulence models are still under improvement and the direct 3D CFD method is not yet reported to be integrated in the automatic blade design process, the direct 3D CFD method gives an insight of detailed flows and makes innovative blade shape design feasible [10].

Method	Near wake/ Wind turbine	Far wake	Pros and cons
Momentum	Thrust coefficient	Similarity at all times and length scales	Simplest
BEM	Actuator disk and blade elements	2D momentum theory	Efficient, ignore 3D flows
Lifting line/surface	Line/surface	Free/fixed vortices sheet	Fast Blade shape is simplified
Vortex lattice/particle	Blade elements/chords and twists	Free/fixed vortices sheet, particles	Relatively slow Wake model is needed
Panel	Surface mesh	Free/fixed vortices sheet	Fast Predicting lift and pressure drag, no skin fiction drag(viscous effects)
Generalised actuator CFD	Body force in disk/line/planar surface	Volume mesh, Euler/RANS/LES	Fast Blade shape is simplified
Direct CFD	Discretisation of actual blade surface and volume mesh	Volume mesh, Euler/RANS/LES	Very time-consuming Detailed flows

Table 1-1 Comparison of aerodynamic models

1.4 Project Aims and Objectives

1.4.1. Problem Statement

The exploitation of small horizontal axis wind turbines provides a clean, prospective and viable option for enhancement of energy supply. To reduce the risk in wind turbine development and improve the performance of the wind turbine systems, a better understanding of how these devices interacting with the environment/winds is indispensable. This can be achieved via scaled-model laboratory experiments, full-scale field testing, or through numerical modelling. It is clear that the advantages of numerical modelling are lower cost, lower risk and rapid design cycle, although it needs to be validated against measurements.

An efficient approach for modelling the wind turbine blades is the blade element momentum (BEM) method, which was developed by Glauert in 1935 [11]. It represents the blade by several annular elements in prediction of loads and power outputs, which are calculated from wind tunnel tested lift and drag coefficients. The BEM approach has been widely used for wind turbine blade design and analysis in both engineering and research communities [9;10]. However, in the wind energy industry, there is a desire for a supplementary approach which is theoretically correct in all operating conditions in the long term [12].

An alternative approach is computational fluid dynamics (CFD) method. The majority of the CFD approaches are based on finite volume method, and discretisation is applied to the control volumes. It is a discretised computational analysis method for exploring the complex flows and wakes near the wind turbine blades. CFD modelling is more appropriate especially when the wind turbine is in complex flow conditions including heavy-loaded blades, radial flows in three-dimension and deep-stall [13]. In these conditions, the behaviours of wind turbine blades cannot be simply modelled using the pre-defined lift and drag coefficients and wake models in the BEM method. Moreover, the CFD approach provides a detailed quantitative analysis including blade surface pressure distributions, blade surface shear stress, and field pressure and streamlines. However, an explicit CFD modelling is computationally expensive and has not been mature enough to become a design tool [14].

The BEM and CFD approaches are complimentary and both methods are employed in in wind turbine blade design and analysis. However, there are several problems to be solved regarding to the BEM and CFD approaches for wind turbine blade design and analysis:

(1) There are uncertainties of pre-defined lift and drag coefficients in the BEM method for describing airfoil aerodynamic characteristics of rotating wind turbine blades. The lift and drag coefficients from wind tunnel tests lead to deviation in power prediction at high wind speeds.

(2) The BEM method has been corrected at highly loaded conditions. However, there are various wake models in the BEM method in terms of the wake induction factors.

(3) The effects of rotor parameters and blade design on power performance needs clarification for different wind turbines. There is still a strong desire for guidelines of blade design using the BEM method in engineering applications.

(4) The CFD method is under development comparing to the BEM method and needs to be validated against measurements. Systematic and comparative dependency studies are needed for further improvement in CFD modelling.

1.4.2. Aims and Objectives

This project aims to provide a better understanding of both the BEM based approach and the CFD based approach for small wind turbine blade design and analysis. To accomplish this, a detailed investigation and discussion of small wind turbine blade design and power performance analysis using these two approaches through case studies were conducted.

These specific objectives of the project have been achieved:

(1) To review the BEM approach and the CFD approach.

(2) To examine the existing correction models for the BEM method. This was achieved through a case study of the NREL/NASA Phase VI wind turbine.

(3) To develop a BEM code for small wind turbine design and analysis.

(4) To explore the blade design philosophy for two different wind turbines (a fixed-pitch variable-speed wind turbine with mixed airfoils and a fixed-pitch fixed-speed wind turbine with single airfoil) and provide guidelines for blade aerodynamic design and optimisation.

(5) To establish both 2D CFD and 3D CFD modelling methods with validation against the airfoil S809 and the NREL/NASA Phase VI wind turbine measurements.

(6) To conduct both 2D CFD and 3D CFD analysis on the BEM-designed wind turbines.

1.4.3. Methodology and Work Flow

In this project, the investigation of small wind turbine blade design and analysis was divided into two parallel approaches. The approaches and work flow of this project are shown in Figure 1-3. Firstly, the BEM method with different existing correction models was examined using the NREL/NASA Phase VI wind turbine data. Secondly, BEM based approaches were employed in two kinds of wind turbine blade design: the fixed-pitch variable-speed (FPVS) wind turbine and the fixed-pitch fixed-speed (FPFS) wind turbine. Meanwhile, the published S809 airfoil wind tunnel tested data and NREL/NASA Phase VI wind turbine measurements were used to validate the 2D and 3D CFD modelling for airfoil aerodynamic characterisation and wind turbine power performance analysis. The 2D CFD approach was then applied to investigate the airfoil DU93-W-210 at relatively low Reynolds number flows and validated against the wind tunnel tests in the University of Hertfordshire. The 3D CFD approach was further employed in power prediction for the BEM-designed wind turbines. Finally, project findings and recommendations were summarised for small wind turbine blade design and analysis.
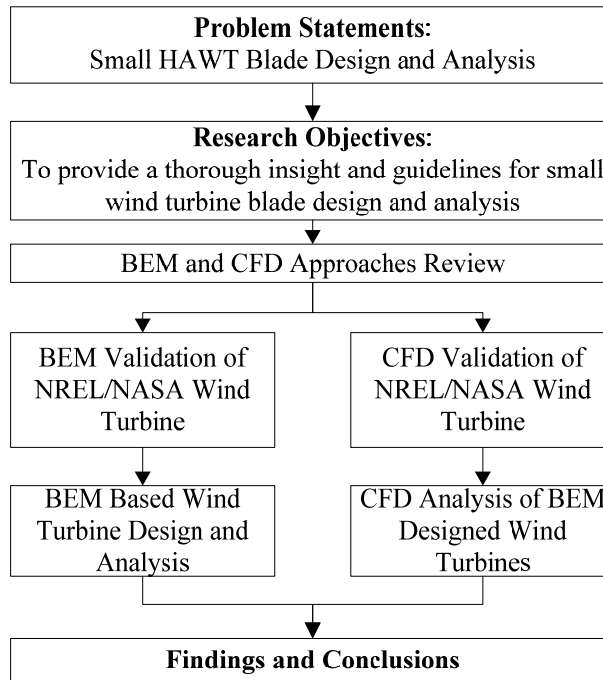
Figure 1-3 Work flow of this PhD project

1.5   Thesis Structure

In this thesis, the presentation of a detailed investigation of the BEM based method and CFD based method for small wind turbine blade design and analysis is organised into 7 chapters.

The previous sections of this chapter gave a brief outline of the BEM and CFD based approaches in small wind turbine blade design and analysis. The project aims and objectives were stated.

Chapter 2 reviews the key elements, current status and challenges of the BEM and CFD based approaches. The axial induction correction models and stall correction models for the BEM method are summarised. The mesh topology and turbulence models of the CFD method in wind turbine aerodynamics are reviewed.

Chapter 3 investigates the BEM limitations and corrections. The induction correction models and stall correction models are examined and discussed. A hybrid stall correction model is proposed and applied to the NREL/NASA Phase VI wind turbine for power prediction.

Chapter 4 explores the blade design philosophy using the BEM based method for two kinds of small wind turbines: FPVS and FPFS wind turbines. The effects of the main rotor parameters such as rotor diameter, design wind speed, design tip speed ratio as well as blade chord and twist angle distributions on power performance are investigated. A blade design approach considering tip-hub loss and drag effect by searching optimal induction factors is developed. A heuristic blade linearisation approach is presented.

Chapter 5 demonstrates the 2D CFD modelling for the airfoil S809 and the 3D CFD modelling for the NREL/NASA Phase VI wind turbine with measurement validation. The integrated torques, blade root flap moment as well as blade surface pressure distributions and streamlines are obtained and presented.

Chapter 6 employs the validated 2D CFD modelling and wind tunnel testing in the airfoil DU93-W-210 aerodynamic characterisation at relatively low Reynolds number flows. The 3D CFD modelling is applied for power performance analysis of the two BEM-designed wind turbines. The CFD calculated and the BEM calculated power curves are compared and discussed.

The final chapter summarises the research and highlights the contributions of this research work. Recommendations are given for future work in this field.

CHAPTER 2   LITERATURE REVIEW

2.1   Introduction

Since wind energy became an increasingly important and widespread green energy source in the last decades, the technology in wind energy has been greatly developed. As the most popular wind turbine aerodynamic model, the Blade Element Moment (BEM) based approach/method has been widely researched and generally reported to be acceptably efficient in wind turbine design and analysis. With the development of advanced computing technology, the Computational Fluid Dynamics (CFD) based approach/method proved to be an alternative prospective approach for wind turbine aerodynamics more recently.

This chapter reviews the BEM based approach and the CFD based approach for HAWT blade design and analysis. The key elements, current status and challenges of the BEM method are summarised in Section 2.2, and the CFD method are outlined in Section 2.3.

2.2   Blade Element Momentum (BEM) based Approach

As the classical theory of wind turbine rotor aerodynamics, the BEM method (also known as Strip theory or Glauert/Wilson method) combines the Momentum theory and Blade Element theory [9]. By dividing the wind turbine blades into annular blade elements and applying one-dimensional linear momentum conservation to the annular elements, the forces and power are calculated and integrated based on the sectional airfoil lift and drag coefficients, the chords and twist angles of the blade geometry. The airfoil aerodynamic characteristic data i.e. the lift drag and moment coefficients are often obtained from wind tunnel measurements. The definition of lift and drag coefficients, blade chord and twist angle distributions, the main equations used in this thesis and other nomenclatures of the BEM method are presented in Appendix A.

2.2.1. Key Elements of BEM Method

In the BEM based approach, there are two main elements which are decisive for the successful application: the induction factors and airfoil aerodynamic characteristics.

(1) Wake induction model. To describe the axial induced velocity and tangential induced velocity, axial and tangential induction factors are defined in the BEM method (see Appendix A for definition). The two inductions factors are critical to the calculation of total power coefficient for both on-design and off-design analysis.

(2) Lift and drag coefficients. Description of the airfoil aerodynamic characteristics at both low angle of attack and high angle of attack are inevitable in the BEM method. Different lift and drag data directly lead to different power output results.

2.2.2. Current Status and Challenges

In the following sections, the advantages and limitations of the BEM method are summarised in Section 2.2.2.1, the wake induction correction models of the BEM method are reviewed in Section 2.2.2.2, and the stall correction models are included in Section 2.2.2.3.

2.2.2.1 Advantages and Limitations

It has been accepted by many researchers that the BEM method is the most widely used and efficient approach for wind turbine blade design and analysis [15-30]. It has the following advantages:

(1) All the aerodynamic problems are described and solved in an analytical way with averaged values calculated for each element. Thus it is less time-consuming.

(2) The airfoil profile is represented by the lift, drag and moment coefficients. It is flexible in application of the airfoil aerodynamic characteristics to different wind turbine blades.

(3) The power coefficient is directly related to the chord and twist angle distributions of the blade. Therefore, the BEM method can be integrated in any codes, such as aero-elastic codes. Along with advanced search algorithms, an

automatic global optimisation is feasible.

(4) It does not need to solve the detailed flows; therefore less computational resource is needed.

(5) It is well-proven and reasonably accurate.

Therefore, it has been widely researched and employed in wind turbine blade design. Various programs and codes have been developed to calculate the optimal chord and twist angle distributions, and to assess the rotor power and aerodynamic performance. The popular design and analysis codes in the wind energy community, such as GH-Bladed [31], AeroDyn [32], WT_Pref [33] etc., are all based on the classical BEM theory. There are also many in-house codes developed and adapted to their own needs in the industry, research institutes and universities. Maalawi [34;35] presented an approach to obtain the optimal relative angle of wind given a rotor diameter and a rotor solidity. Vitale [36] developed a code to obtain the optimum blade shape for HAWT with optimum rotor power efficiency. It is well-known that the BEM method is the mostly acceptable method in wind turbine design and analysis. However, there is a debate on the limitations of the BEM method in the research community.

Although the BEM theory has been widely used for wind turbine blade design with an acceptable accuracy and efficiency in pre-stall steady flows, it is necessary to study the impact of the real 3D flow for both steady and unsteady (i.e. stall) conditions. Many researchers reported that the BEM method becomes unreliable at turbulent wake conditions and under-predicts loads and power output at stall conditions [9]. These are mainly due to the underlying assumptions: in the momentum theory, the change of the moment in the air stream is purely caused by the thrust on the disc. However in real flows, when the turbine operates at high wind speeds, the downstream expands largely and is full of turbulence and recirculation. The momentum theory is no longer able to describe this complex flow. Moreover, the blade element theory assumes that there is no flow interaction between annular blade elements. In other words, the annular tubes are not penetrable. In fact, the flows in different annular tubes tend to interact, and the interaction of the flows presents 3D dimensional flows such as span-wise flows. The two main limitations for un-yawed conditions can be described as below:

(1) Failure at turbulent wake conditions.

According to the momentum theory, the flow velocity of far downstream is $U(1-2a)$, where U is the nature upstream velocity, a is the axial induction factor. When $a \geq 0.5$,

the velocity of far downstream becomes negative, which is obviously unreasonable. The BEM model fails to describe the relationship between the thrust coefficient and the axial induction factors for heavy-loaded conditions. As shown in Figure 2-1, the measured data show large deviations from results of the momentum theory: the measured thrust coefficient is much higher than that from the momentum theory when the axial induction factor is above 0.5.
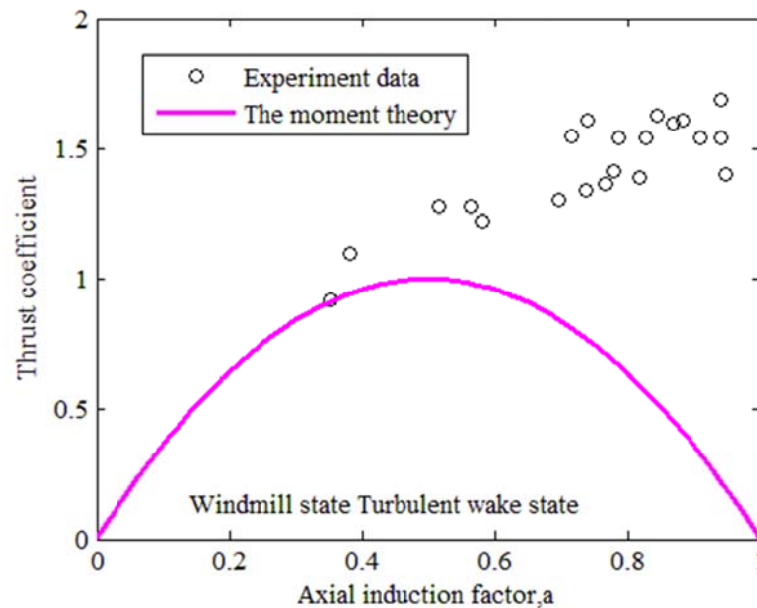
Figure 2-1 Glauert correction to thrust coefficient

(Experiment data reproduced from Marshall 2005)

(2) Under-prediction at stall conditions.

In the BEM method, the forces of the blade elements are determined by the lift and drag coefficients of the airfoil. These data are obtained from two dimensional (2D) wind tunnel testing or could be generated from computational codes, such as EPPLER[37] and XFOIL [38]. It was pointed out that methods relying on pure 2D flow characterizations may not be capable of simulating the complex 3D flows [39]. Flow details demonstrate that blade rotation has an effect on the pressure distribution on the surface of the blade, which may give rise to higher lift and lower drag as compared with the 2D aerodynamic data, and lead to 3D stall-delay in stall condition [40]. In the 3D rotating frame, the centrifugal forces contribute to span-wise flow pumping and the Coriolis forces produce a delay of chord-wise flow separation. As illustrated in Figure 2-1, the behaviour of the airfoil shows major difference at non-rotating and rotating conditions. At high angles of attack (AoA), the lift coefficients (Cl) are much higher for a rotating wing than a stationary wing as tested in wind tunnel. Thus, stationary airfoil

characteristic data from wind tunnel testing are not competent to predict power performance accurately at high angles of attack.

This phenomenon was firstly reported by Himmelskamp in 1940's for helicopter propellers. However, no increase of drag was observed by Himmelskamp [41]. Since stall angle is delayed, many researchers introduce a reduction of drag coefficient inherently [40]. More specifically, according to the measured pressure distributions, increased lift and drag coefficients were observed at the blade root section while reduced values were recorded at the blade tip [41]. As for the power produced, it was generally evidenced that the wind turbine rotor power was higher than the values calculated from stationary coefficients at high wind speeds for stall-regulated wind turbines. This is called "stall-delay" or "rotational effects" in wind turbine aerodynamics by many researchers [42,43].
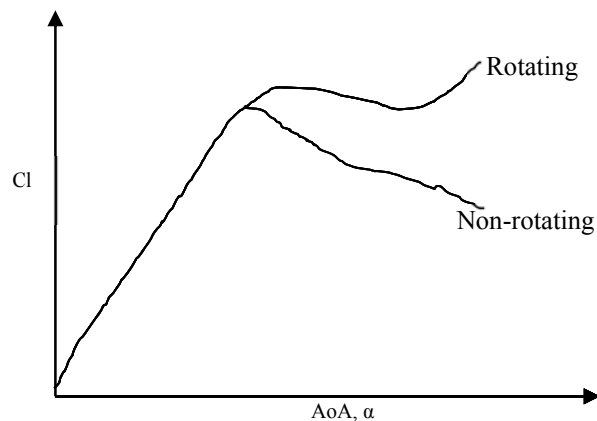
Figure 2-2 Lift coefficients of rotating and non-rotating wings

Although the BEM method is accurate and efficient for blade design and assessment at design conditions, off-design aerodynamics is still an open issue due to its unsolved limitations in describing the axial induction factor for heavy-loaded conditions (high wind speeds, low tip speed ratios), modelling the stall delay phenomenon etc. The optimal blade design is only optimal at design conditions. When wind speed changes, the turbines is not really working at its optimal designed conditions. As a result, the turbine works at both on-design and off-design conditions for a whole range of wind speeds throughout the year. Moreover, the airfoil data used in wind turbine design and analysis are often very limited. These data are originally from two dimensional (2D) wind tunnel tests. These wind tunnel experiments are very time-consuming and expensive. It is not viable to have airfoil tested at high angle of attack as heavy vibration

occurs with large uncertainties. It is also not realistic to have tested data for a wide range of Reynolds number. Moreover, the behaviours of an airfoil in 2D stationary wind tunnel test and those in three dimensional (3D) rotating blades are distinctively different. The vortex structures near a rotating wind turbine blade is much complex than the tested wing model in wind tunnels.

In summary, the challenges of the BEM theory in wind energy community are[1]: to evaluate the wake induction factors correctly and to represent the lift and drag coefficients in correct mathematical expressions. From these two points of view, various correction models are reviewed for wake induction corrections and stall corrections in the following paragraphs.

2.2.2.2 Wake Induction Correction Models

When a wind turbine is in heavy-loaded conditions, the axial induction factor calculated from the momentum theory is higher than 0.5, thus it is not valid anymore because the velocity cannot be minus for these conditions. Several empirical models have been developed to improve the momentum theory: such as Glauert model, Spera model, Buhl model, AeroDyn model, GH-Bladed model, Burton model and Vaz model, which are described below:

(1) Glauert Model
Glauert developed an empirical turbulent wake correction model according to experiment data. Meanwhile, due to pressure difference between the suction surface and the pressure surface of the blade, the flow slips around the tip and Hub sections, resulting in reduction of the lift and hence the rotor power. Considering these losses, Prandtl developed a tip-hub loss correction model. The Glauert model [9] (combined with the Prandtl tip-hub correction) is expressed as:

$$a = (1/F)\left[0.143 + \sqrt{0.0203 - 0.6427(0.889 - C_T)}\right], a > 0.4 \qquad (2.1)$$

where a is the axial induction factor, C_T is the thrust coefficient, $F = F_t \cdot F_h$ is the multiple of tip loss factor and Hub loss factor given by:

---

[1] Unsteady flow problems including dynamic stall, gust inflow, and starting, coned, pitch-controlled and yawed rotors are out of scope of this project.

$$F_t = 2ar\cos(e^{-\frac{Z(R-r)}{2R\sin\varphi}})/\pi \qquad (2.2)$$

$$F_h = 2ar\cos(e^{-\frac{Z(r-r_h)}{2r_h\sin\varphi}})/\pi \qquad (2.3)$$

The Glauert wake model along with the Prandtl tip-hub loss correction is widely used in wind turbine aerodynamic analysis.

More recently, Madsen [44] proposed a corrected BEM model in term of axial induction factor and tangential induction factor based on Actuator Disk (AD) simulation results. Considering the pressure term in the wake and wake expansion, this corrected BEM model predicts a higher thrust coefficient for the low local tip speed ratio compared to the Glauert model. While at a tip speed ratio from 6 to 8, this corrected BEM model correlates very well with the Glauert model.

(2) Spera Model

Spera [45] developed a model which describes a liner relationship between the thrust coefficient and the axial induction factor after a critical point of 0.2.

$$C_T = 4[a_c^2 + (1\text{-}2a_c)a], \quad a \geq a_c = 0.2 \qquad (2.4)$$

where a is the axial induction factor, a_c is the critical axial induction factor, C_T is the thrust coefficient.

(3) AeroDyn Model

AeroDyn [32] is a series of routines designed by NREL to predict wind turbine aerodynamic behaviours including steady wake and dynamic wake. The correction of the wake induction model used in AeroDyn is similar to the Glauert model, which is stated below:

$$a = \frac{18F - 20 - 3\sqrt{C_T(50-36F) + 12F(3F-4)}}{36F - 50}, C_T > 0.96F \qquad (2.5)$$

where a is the axial induction factor, C_T is the thrust coefficient, F is the tip-hub loss factor.

(4) Buhl Model

Buhl [46] proposed an empirical correction model taking into account of the Prandtl tip-hub loss:

$$C_T = \frac{8}{9} + (4F - \frac{40}{9})a + (\frac{50}{9} - 4F)a^2, \ a \geq 0.4 \tag{2.6}$$

where a is the axial induction factor, C_T is the thrust coefficient.

The Buhl model was compared with the Glauert model in [24]. Moreover, the Glauert model and Buhl model were further compared with the AeroDyn model in [47]. Comparing with the experiment results, the Glauert model proved to be more accurate than the other two models in calculation of rotor torque and axial thrust coefficients.

(5) GH-Bladed Model

As an international wind turbine analysis expert, "GH-Bladed" [48] applies the following empirical models in BEM for wind turbine loads and power performance prediction:

$$C_T = 0.6 + 0.61a + 0.79a^2, \ a \geq 0.3539 \tag{2.7}$$

where a is the axial induction factor, C_T is the thrust coefficient.

(6) Burton Model

Burton [49] proposed a line that is tangential to the momentum theory curve to correct the thrust coefficient:

$$C_T = C_{T1} - 4(\sqrt{C_{T1}} - 1)(1 - a), \ a \geq a_T \tag{2.8}$$

$$a_T = 1 - 0.5\sqrt{C_{T1}} \tag{2.9}$$

Here, a_T is the tangential point of the momentum theory parabolic curve and the straight line, C_{T1} is the thrust coefficients at induction factor of 1. Burton suggested a best fit value of 1.816 for C_{T1} and 0.326 for a_T. Burton also mentioned that Wilson and Lissaman chose a value of 1.6 for C_{T1} and 0.3675 for a_T.

(7) Vaz Model

Vaz [50] stated that the Glauert model fails to provide reliable results with respect to its performance at very low tip speed ratios (< 2), and a modified Glauert wake correction model was presented. This model provides the thrust expression using the axial induction factor at the rotor, a, and axial induction factor in the wake, b.

$$a = \frac{b}{2}[1 - \frac{b^2(1-a)}{4X^2(b-a)}] \tag{2.10}$$

$$C_T = 2b[1 - \frac{a}{2}(5-3a)]F, a > 1/3 \tag{2.11}$$

Here X is tip speed ratio. It is obvious that in the Vaz model, if a is equal to 1 then b is equal to 2, and the thrust coefficient is zero. This is different to other empirical models. Generally speaking, such low tip speed ratio occurs for fixed-pitch variable-speed (FPVS) wind turbine at the starting process and fixed-pitch fixed-speed (FPFS) wind speed under deep-stall at high wind speed. Due to the very low tip speed ratio in the Vaz model, it will not be further discussed in this thesis.

Figure 2-3 presents an overall picture of the above correction models along with the experimental data. The tip-hub loss factor is included with a value of 0.95. The results produced by all these models are close to the experimental results except the Sepra model. The Glauert model, the GH-Bladed model, the Burton model and the Sepra model are well tangential to the standard momentum theory without consideration of the tip-hub loss. However, they are disconnected with the momentum theory when considering the tip-hub loss factor. The AeroDyn model and the Buhl model have very similar (almost the same) forms, which are well tangential to the momentum theory including the tip-hub loss factor. When the tip-hub loss factor is considered in BEM analysis, the discontinuity may cause instability in calculation. To compare the wake induction corrections, the Glauert model, GH-Bladed model and AeroDyn model are employed in the BEM analysis presented in Chapter 3.
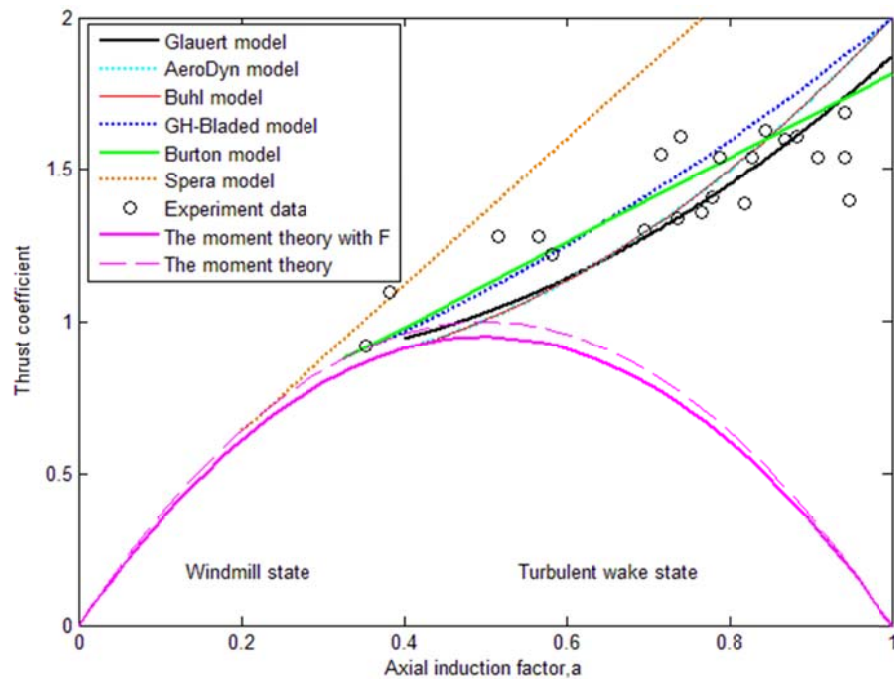
Figure 2-3 Correction models of wake induction (F=0.95)

(Experiment data reproduced from Marshall 2005)

2.2.2.3 Stall Correction Models

In the BEM method, the airfoil lift and drag coefficients are obtained from 2D wind tunnel tests at a limited range of angle of attack. However, the airfoil lift and drag coefficients at high angle of attack are needed for wind turbine rotor aerodynamic load analysis and power output prediction. Generally speaking, the lift and drag coefficients are expected to have a general mathematical model for a global range angle of attack from -180° to 180° for a whole range wind speed analysis at yawed or un-yawed conditions. At least, data of angle of attack from 0° to 90° are vital for twisted blades at normal operation conditions including idling and starting, pre-stall, stall, and deep-stall stages. Lanzafame [24] presented models for the representation of the lift and drag coefficients over on-design and off-design conditions. A global stall model for the prediction of airfoil characteristics was provided by Tangler [51]. Tangler suggested the use of the flat plat (FP) theory/model as a general guideline for airfoil coefficient extrapolation. This FP model takes the wind turbine as a flat plate, and the two main equations to predict lift and drag coefficients are given by:

$$C_L = 2\sin\alpha\cos\alpha \tag{2.12}$$

$$C_D = 2\sin^2\alpha \tag{2.13}$$

Here, α is the angle of attack. These two equations give a common principle for any kind of airfoil. However, it is too rough for specific wind turbine airfoil analysis. The lift and drag coefficients are highly airfoil and blade dependent.

To characterise "stall-delay" phenomenon observed in rotating blades, several empirical stall-delay models have been developed. Snel [52] presented an empirical correction model for lift coefficient but no drag correction was mentioned. Corrigan and Schilling [52] proposed a correction model based on the pressure gradients in the boundary layer. In this model, a shift of angle of attack was introduced to account for the stall-delay effect. Bak [53] developed a correction model based on the pressure distribution, which is a function of span-wise and chord-wise positions. The normal and tangential coefficients are then obtained from integration of the pressure difference model. Chaviaropoulos and Hansen [54] proposed a correction model for 3D rotational effects from a quasi-3D Navier-Stokes method. Breton [52] studied five stall-delay models (Snel, Bak, Corrigan and Schilling, DU-Selig, and Chaviaropoulos and Hansen) with the lifting line method and prescribed wake method, comparison analysis results demonstrate that all the above five models lead to over-prediction in power output, As shown in Figure 2-4. Breton suggested applying these models up to a certain angle of attack to improve the results.
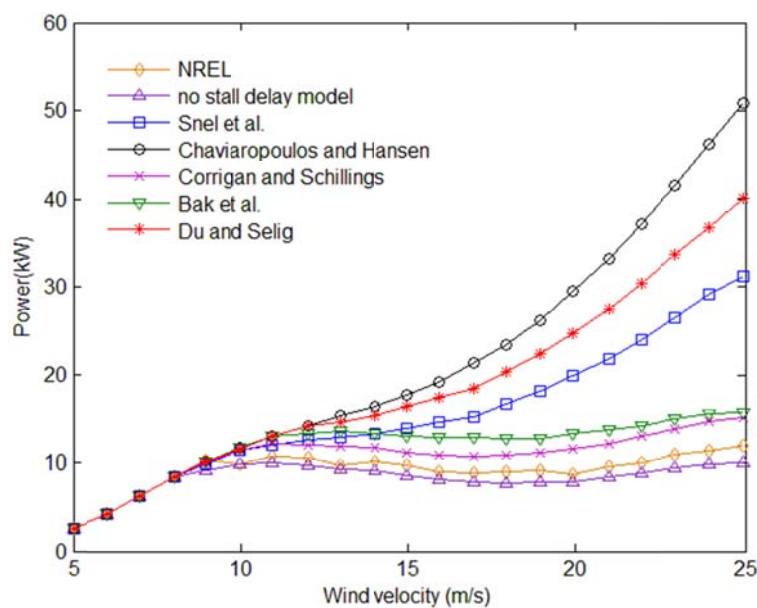
Figure 2-4 Power prediction using different stall correction models from Breton

Comparing to these stall correction models, the Viterna-Corrigan model and Du-Selig model correct the lift and drag coefficients from 2D coefficients. These two models are widely used in wind turbine engineering and research applications. The following paragraphs detail these two stall correction models:

(1) Viterna and Corrigan Model

In early 1980s, Viterna and Corrigan [51] proposed a post-stall model for fixed-pitch (stall-regulated) wind turbines, which is still widely used with further improvement nowadays. The original Viterna-Corrigan models were:

$$\begin{cases} C_{D,\max} = 2.01; AR > 50 \\ C_{D,\max} = 1.11 + 0.018AR; AR \le 50 \end{cases} \tag{2.14}$$

$$C_D = B_1 \sin^2(\alpha) + B_2 \cos(\alpha), 15° \le \alpha \le 90° \tag{2.15}$$

$$B_1 = C_{D,\max} \tag{2.16}$$

$$B_2 = (1/\cos(\alpha_s)) \cdot \left(C_{Ds} - C_{D,\max} \sin^2(\alpha_s) \right) \tag{2.17}$$

$$C_L = A_1 \sin(2\alpha) + A_2 \cos^2(\alpha)/\sin(\alpha), 15° \le \alpha \le 90° \tag{2.18}$$

$$A_1 = B_1 / 2 \tag{2.19}$$

$$A_2 = \left(C_{Ls} - C_{D,\max} \sin(\alpha_s) \cos(\alpha_s) \right) \cdot (\sin(\alpha_s)/\cos^2(\alpha_s)) \tag{2.20}$$

where,

AR is the aspect ratio between the blade length and a representative chord,

α_s is the inflow angle at stall onset (usually 15°),

C_{Ds} is the drag coefficient at stall onset,

C_{Ls} is the lift coefficient at stall onset.

From these equations, it is obvious that the Viterna-Corrigan correction is dependent on the accuracy of the selected initial separation angle and aspect ratio. It was reported that the determination of the initial separation angle and aspect ratio leads to discrepancy in power prediction [55]. As an extension to the Viterna-Corrigan correction, Tangler [51] suggested a new definition for $c_{D,\max}$ and c_D that are more dependent on the aspect ratio and the thickness to chord ratio of the airfoil, called the Viterna-Corrigan separated flow data synthesis method. In the Tangler's method, for the lift coefficients from 90° to

180° and from -180° to 0°, mirror and scale methods are used. If the airfoil is asymmetrical, the scale factor is 0.7. When the angle of attack is 180° or -180°, the lift coefficient is set to 0. At other angle of attack, the lift coefficient is obtained by linear interpolation. The drag coefficient at the whole range of angle of attack is mirrored without scale. It was also recommended that the correction data satisfy the flat plate theory from 20° to 90° by Tangler. Myers [56] suggested a guideline to generate post stall data that the Viterna-Corrigan method needs to be implemented after leading-edge separation and the c_l/c_d ratio for the initial conditions needs to agree with the flat plate theory (model) which (takes over 20 degrees).

(2) Du-Selig Model

As an extension of the Snel model, a combination of 2D wind tunnel testing results and the Du-Selig model [57] was used to produce 3D lift and drag coefficients at high angles of attack. The Du and Selig equations for lift and drag coefficients are expressed as follows:

$$\begin{cases} C_{l,3D} = C_{l,2D} + f_l(C_{l,p} - C_{l,2D}) \\ C_{d,3D} = C_{d,2D} + f_d(C_{d,p} - C_{d,2D}) \end{cases} \tag{2.21}$$

$$f_l = \frac{1}{2\pi}\left[\frac{1.6(c/r)}{0.1267}\frac{a-(c/r)^{\frac{dR}{\Lambda r}}}{b+(c/r)^{\frac{dR}{\Lambda r}}}-1\right] \tag{2.22}$$

$$f_d = \frac{1}{2\pi}\left[\frac{1.6(c/r)}{0.1267}\frac{a-(c/r)^{\frac{dR}{2\Lambda r}}}{b+(c/r)^{\frac{dR}{2\Lambda r}}}-1\right] \tag{2.23}$$

$$\Lambda = \Omega R / \sqrt{V_\infty^2 + (\Omega R)^2} \tag{2.24}$$

$$C_{l,p} = 2\pi(\alpha - \alpha_0) \tag{2.25}$$

$$C_{d,0} = C_{d,2D}, \alpha = 0. \tag{2.26}$$

where $C_{l,3D}$ is the corrected lift coefficient, $C_{d,3D}$ is the corrected drag coefficient, $C_{l,2D}$ is the 2D lift coefficient, $C_{d,2D}$ is the 2D drag coefficient, Ω is the rotor speed in rad/s, R is the rotor radius in m, a, b and d are the empirical correction factors.

In summary, these empirical wake induction correction and stall correction models contribute to the improvement of the BEM theory. However, many researches [52;58;59]

agreed that the accuracy of aerodynamic performance prediction at off-design conditions remains a big challenge. In this thesis, turbulent wake induction factor correction and stall correction are discussed with details through a case study in Chapter 3.

2.3 Computational Fluid Dynamics (CFD) based Approach

To quantify the empirical factors to support the BEM method, a better understanding of the 3D flow physics is needed [51]. The alternative approach to study the rotor aerodynamics of a wind turbine is the computational fluid dynamics (CFD) method. CFD solves the differential governing equations of the fluids in an exact and numerical way. For a fluid dynamic problem, the mathematical model is based on the continuity, momentum and energy conservation equations. These derivative equations are called Navier-Stokes equations [60;61]. Along with other variable transport equations or empirical viscosity equations, a closed form (a turbulence model) of the governing equations is established and solved time-dependently. A physical problem can be appropriately solved with advanced solution schemes and turbulences models, providing a simple but accurate description of boundary conditions and good discretisation of the interested fluid volume. The task is often executed in three steps: pre-processing, solving and post-processing. These steps can be executed separately in one or more subroutines.

To investigate the 3D flows around a wind turbine blade, the incompressible Reynolds-Averaged-Navier-Stokes (RANS) CFD method has been increasingly employed in the engineering and research community, particularly recently with the rapid development of computer capacity. It is expected that the RANS based CFD approach will be in practical use in the wind energy sector in the near future [62]. This section reviews the key elements in the RANS CFD method, the current status and difficulties in this approach for wind turbine aerodynamic analysis.

2.3.1. Key Elements of CFD Method

Due to the nonlinear behaviour of the Navier-Stokes equations, solving a whole 3D turbulent flow model of a wind turbine rotor with finest details in a time-dependent way is extremely difficult based on methods such as direct numerical simulation (DNS).

Other options like large eddy simulation (LES) and detached eddy simulation (DES) methods are also applied in wind turbine aerodynamics by some researchers [63]. However, to be computationally cost-efficient, RANS equations are most widely used to model the change of flow domain caused by turbulence around wind turbine blades. To obtain a reasonable accurate solution for wind turbine aerodynamics, three key elements are involved:

(1) A good mesh quality.

(2) An advanced turbulence model.

(3) An accurate solve scheme.

Among the above three factors, the most interactive and time-consuming process is the meshing step. For turbulence modelling, there are several existing models available as described below. The solving step is done by computer, often executed in a commercial software package (such as Fluent, CFX, etc.) or an existing code.

2.3.2. Current Status and Challenges

Regarding to wind turbine rotor performance prediction using the 3D CFD method, the current status and challenges are reviewed below. Major efforts will focus on the generation of an adequate mesh, and turbulence & transition model.

2.3.2.1 Geometry and Mesh

To model a wind turbine rotor using the CFD method, an exact 3D geometry of the wind turbine rotor is needed in a digitised format, usually in a "computer aided design" (CAD) format. A small wind turbine blade is generally twisted and tapered. The sectional airfoil of the blade is a shape often with a small rounded leading edge, and a sharp trailing edge or thin blunt trailing edge. A sufficient resolution of the boundary layer mesh is needed to solve the boundary layer around the blade surfaces. To secure an accurate solution in the boundary flow, the dimensionless cell wall distance Y PLUS should be below or at least approximated to 1. Additionally, a large-enough flow domain is needed to avoid disturbances from the domain boundary surfaces, and a fine enough time step is preferable to generate a good result. However, a good match between mesh refinement, mesh quality, domain size and time step refinement is very important to produce a quality result, i.e. accurate solution and reasonable computation cost.

Up to present, three types of mesh, i.e. unstructured mesh, structured mesh and hybrid mesh are used in wind turbine rotor aerodynamics analysis in literature [43;64-66]. To deal with the multi-components in wind turbine rotor aerodynamics modelling, multiple moving frame mesh, and dynamic overset mesh topologys are used in these scientific papers. For simplicity, single frame mesh is generally used to model one domain when no yawed flows occur and no component interactions are considered.

2.3.2.2 Turbulence and Transition

To explore the flow field near rotating wind turbine blades, there are several turbulence models presented with good results for wind turbine airfoil and rotor aerodynamics analysis: Spalart-Allmaras (S-A) model, standard k-epsilon (k-ε) model, k-omega (k-ω) model, Shear Stress Transport (SST) k-ω model, and transition SST model. The details of these models can be found in [67]. In Villalpando's research, it was reported that, the SST k-ω model has a better agreement with experimental results than other turbulence models such as the S-A model, the k-ε model and the Reynolds Stress Model (RSM) [68].

However, when stall occurs, the conclusion was drawn that the transition location is crucial for the simulation and the Menter's SST transition model was claimed to have better agreement with experiment results than other models [69-71].

In the transition SST model, the transition equations (i.e. one is for the intermittency γ and the other is for the transition momentum thickness Reynolds number $\tilde{\mathrm{Re}}_{\theta t}$) interact with the SST k-ω turbulence model. Due to two additional transport equations involved, it is apparent that the transition model is more time-consuming and more sensitive to converge than the SST k-ω model. Some research works aimed to find a middle way. Catalano[72] performed a RANS analysis using the SST k-ω model with an imposed transition location which is 10% offset downstream from the predicted point of a fully turbulence model. However, the offset is based on experience in this approach. Instead of using imposed variables to catch the transition phenomenon like turbulence models and without imposing transition location, the transition SST model was reported to have a promising accuracy in predicting transition flows [71;73-77].

Many research works have been done regarding to the transition model. The Menter's transition model was investigated on the 2D S809 airfoil and better agreements have been achieved for angle of attack from 0° to 9°, and it was indicated that the difference at high angle of attacks was more possibly caused by the 3D flow effects which 2D simulation model cannot capture [75]. A full 3D wind turbine rotor which uses the S809 airfoil were accomplished in Langtry's research, the transition model was reported to be compatible with modern CFD techniques such as unstructured grids and massively parallel execution, and the transition model was claimed to be well suited to predict wind turbine rotor aerodynamics [75]. The same conclusion was made that the Menter's transition model can predict the transition and separation more accurately, but more converging time is needed [76]. Later on, the Menter's correlations were improved and published in 2009 [73] and validated for low Reynolds number external flows [74]. In spite of computing time, the transition model is also reported to be sensitive to the inlet turbulence intensity [74;77].

In summary, the transition model can improve the results based on 2D airfoil aerodynamic data; transition modelling in 3D under stall conditions is a complex problem and remains a hot research topic at present. As demonstrated by many researchers, all RANS models lack the ability to model stall at high wind speeds [14]. Another suggested way is DES. But the DES method is much stricter and sensitive on mesh resolution and is highly computational expensive. The representative work of this approach used in wind turbine rotor aerodynamics is presented by Li in 2012 [78]. Within the limitation of time and resource in this project, it is not realistic to use the DES method. However, it is possible to provide an insight with detailed information using the 3D RANS-CFD method, i.e. pressure distribution, torque, moments and force coefficients along the span-wise direction, and therefore providing a more comprehensive understanding of the stall phenomenon.

2.4   Summary

This chapter reviewed the BEM based approach and the CFD based approach for wind turbine blade design and aerodynamic performance analysis, including its advantages, limitations, applications and current status.

BEM provides an efficient way of blade design and aerodynamic performance analysis. However, the stall correction models and the wake correction models are still being researched. The 3D CFD approach has been proposed by researchers aiming to obtain a detailed 3D flow but has not achieved the required maturity to become an engineering tool in wind turbine blade design [14]. Modelling wind turbine in a 3D frame is a great challenge [8;79].

The following Chapter 3 and Chapter 4 concern the BEM based approach for small wind turbine blade design and analysis. Chapter 5 and Chapter 6 focus on the CFD based approach.

CHAPTER 3   BEM BASED MODELLING AND VALIDATION

3.1   Introduction

This chapter investigates the existing wake induction corrections and stall corrections applied in the BEM theory. The discussion of the BEM theory and its corrections is conducted through a case study of National Renewable Experiment Laboratory (NREL) Phase VI wind turbine, which is designed for research purpose. This NREL/NASA Phase VI turbine is a 20kW wind turbine with a single airfoil, fixed pitch (stall-regulated) and fixed yaw (yaw angle is zero). Various measurements of this turbine were conducted in NASA Ames wind tunnel and results were published, while generally it is unrealistic to have all kinds of data measured from a commercial turbine. This turbine is a typical stall-regulated wind turbine and the publicly available measurement data provides a good opportunity to study wind turbine aerodynamics, thus it is selected in this research. The blade configuration of the NREL/NASA Phase VI turbine is described in Section 3.2 and discussion of the wake induction corrections is discussed in Section 3.3, and the stall corrections in Section 3.4 and Section 3.5, with a short summary in Section 3.6.

3.2   NREL/NASA Phase VI Wind Turbine

3.2.1. Wind Turbine Blade Configuration

The NREL/NASA Phase VI wind turbine is a two bladed, fixed-yaw and fixed-pitch (stall-regulated) turbine, and a single airfoil S809 was used through the whole blade span. The blade was nonlinearly twisted and almost linearly tapered [80], as shown in Figure 3-1. The detailed data of the blade is presented in Appendix E. The power measurements were conducted in the NASA-Ames wind tunnel at wind speed range from 7m/s to 25m/s. During the test, the tip pitch angle of the blades was fixed to 3°

towards feather and the yaw angle was locked at 0° [80].
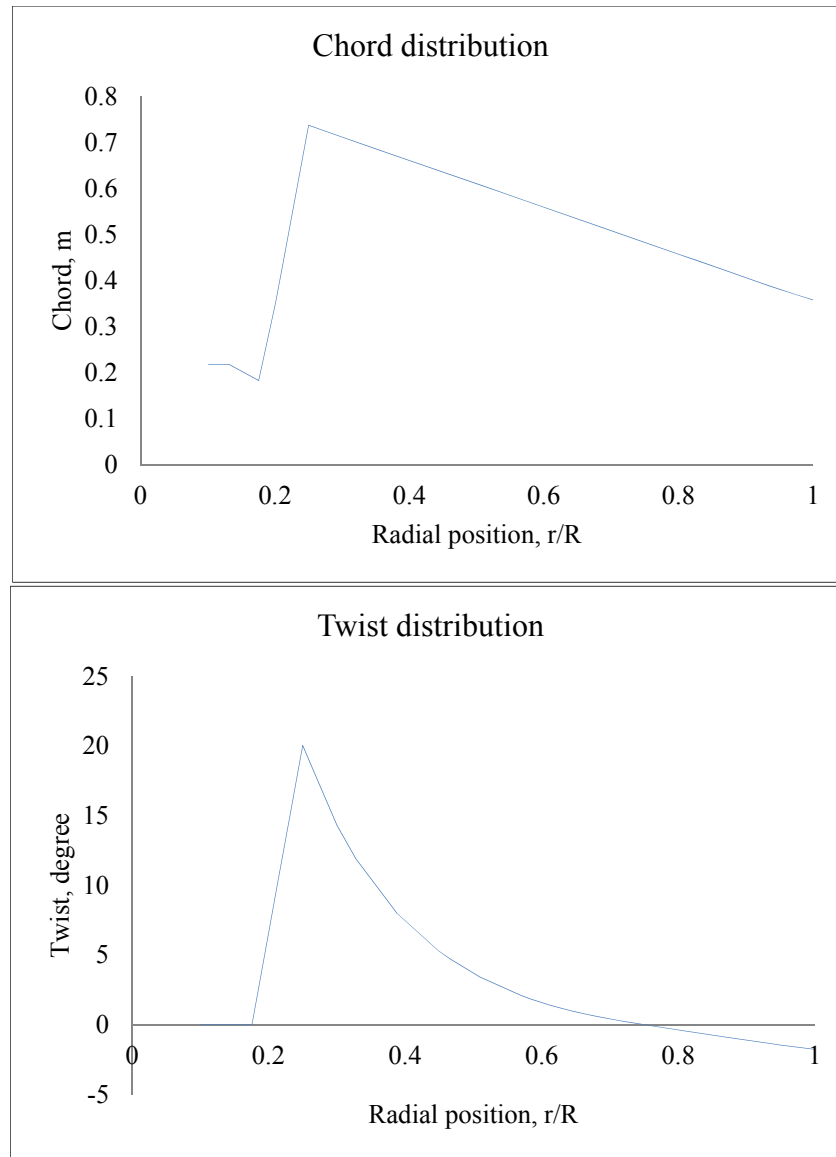
Figure 3-1 Chord and twist angle distributions of the NREL/NASA Phase VI wind turbine blade

3.2.2. Blade Airfoil Characteristics

The S809 airfoil aerodynamic coefficients were provided by NREL and measured by Delft University of Technology (TUDelft) at Reynolds number of 1×10^6 [80;81]. Other measurements from Ohio State University (OSU) at Reynolds number of 1 million and from Colorado State University at Reynolds numbers from 0.3×10^6 to 0.65×10^6 were compared with the TUDelft results by C. Lindenburg [41]. It was reported that the OSU test results were identical to the TUDelft test results except for an offset of -0.53° for

the angle of attack.

With a rotational speed of 72RPM and wind speed of 15m/s, the Phase VI turbine works at Reynolds number of 1,000,000 with a reference chord at the blade middle span location, as shown in Table 3-1:

Radius (m)	r/R	Chord(m)	Relative wind speed at 10m/s	Re at 10m/s	Relative wind speed at 15m/s	Re at 15m/s	Relative wind speed at 20m/s	Re at 20m/s
1.1335	0.23	0.544	13.15	490,003	17.26	643,076	21.75	810,166
2.257	0.45	0.636	19.74	859,582	22.68	987,902	26.26	1,143,612
3.172	0.63	0.543	25.92	963,845	28.23	1,049,668	31.18	1,159,195
4.023	0.80	0.457	31.94	999,442	33.84	1,058,909	36.33	1,136,949
5.029	1.00	0.358	39.21	961,286	40.78	999,593	42.87	1,050,879

Table 3-1 Reynolds numbers for the NREL/NASA Phase VI wind turbine blade

It is well-known that Reynolds number has impacts on aerodynamic coefficients of airfoils. The effect of Reynolds number is not included here considering the relatively narrow range of Reynolds number. The aerodynamic coefficients from the TUDelft wind tunnel test at Reynolds number of 1,000,000 [80] are used.

The TUDelft data and OSU data are plotted in Figure 3-2. The lift and drag coefficients from these two different wind tunnel tests are almost identical at low angles of attack. At high angles of attack, the lift coefficient curves are very close while some discrepancies occur for the drag coefficients at angles of attack from 10.2° to 18.19°. The OSU drag coefficients are smaller than those from the TUDelft, and there is a drop at angle of attack 10.2° in the OSU drag coefficient curve, therefore, the TUDelft data have been used in this research.
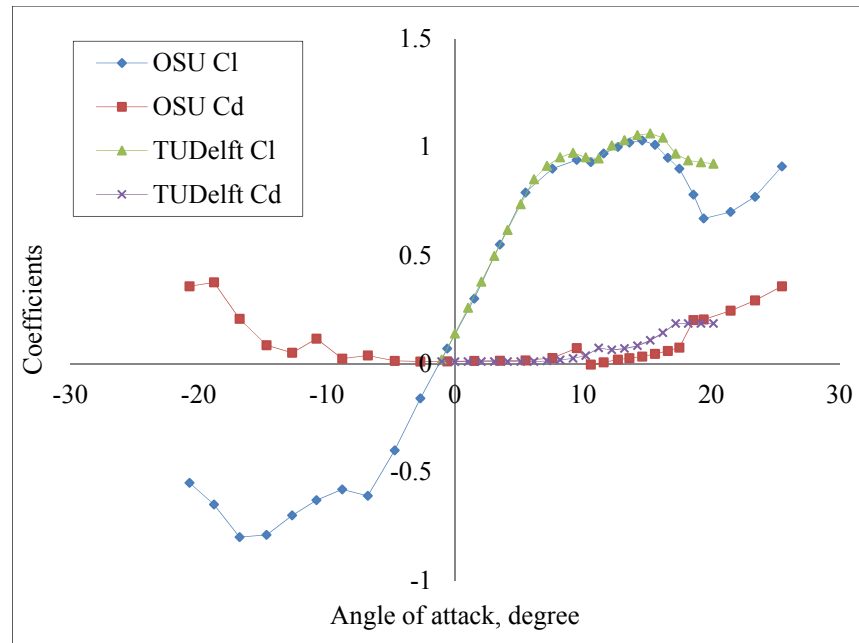
Figure 3-2 Wind tunnel measured lift and drag coefficents of S809 at Reynolds number of 1×10^6

3.3 Wake Induction Correction Models

To describe the wake induced velocity in the BEM theory, the wake induction factor is often calculated from the parabolic relationship between the thrust coefficient and wake induction factor. However, as addressed in Chapter 2, the standard momentum equation in the BEM theory is not valid for higher induction factors (a>0.5). Several empirical models have been developed to represent the relationship between the thrust coefficient and wake induction factor. As shown in Figure 2-3, considering the tip-hub loss factor, the Glauert model, GH-Bladed model, Burton model and Spera model have discontinuity problems with the momentum theory, while AeroDyn model and Buhl model are well tangential to the momentum theory including the tip-hub loss factor. The AeroDyn model is the same as the Buhl model (Actually the Buhl model is used in AeroDyn). The most typical three models, i.e. the Glauert model, GH-Bladed model and AeroDyn model are selected and discussed here.

To predict power output for the NREL/NASA Phase VI wind turbine, 2D wind tunnel tested aerodynamic coefficients (further discussion is addressed in section 3.4) are used to corporate with these three models. Based on these models, a MATLAB code is

developed to predict the power curve and power coefficient Cp. To determine the airfoil aerodynamic coefficients, linear interpolation is used for iteration in the MATLAB code, which is used as a sub-routine for wind turbine design and analysis. The MATLAB program routine will be presented in Chapter 4. The power coefficient and power output from different models are compared in Figure 3-3 and Figure 3-4. Note that, at this point no stall correction model is used. The lift and drag coefficients from TUDelft wind tunnel test are used for low angles of attack and those coefficients at high angles of attack are derived from the standard flat plate theory. Also, the agreement between the measured data and numerical results in Figure 3-3 appears better than the agreement in Figure 3-4. This is purely because the discrepancies of the power coefficient at high wind speeds are scaled down from the power output by the cube of wind speed.
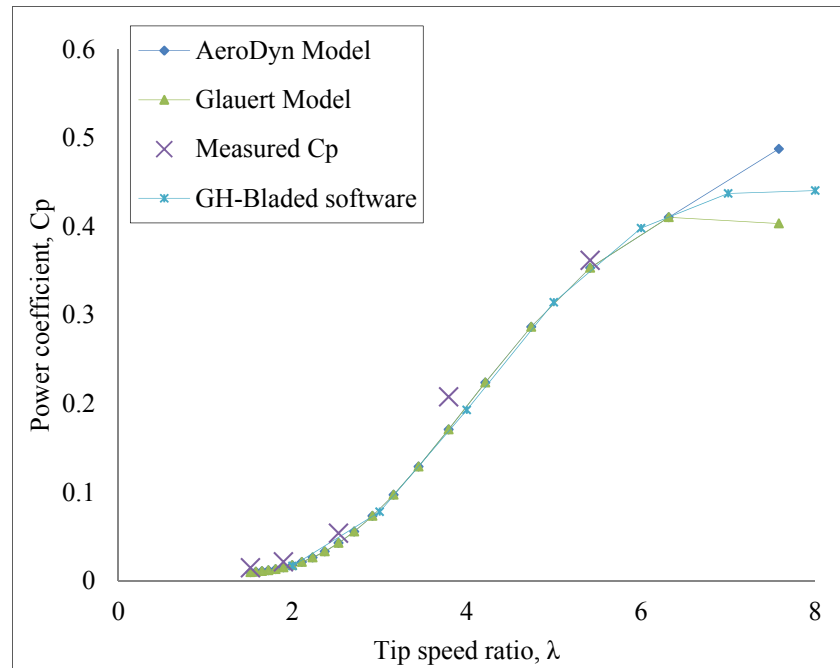
Figure 3-3 Cp curves predicted with different wake induction correction models
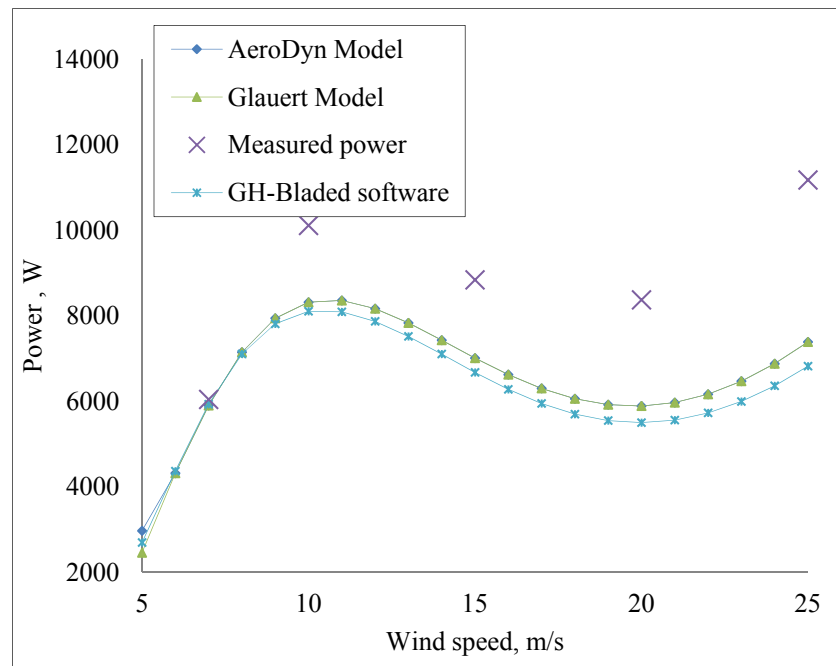
Figure 3-4 Power curves predicted with different wake induction correction models

As shown in Figure 3-3, for power coefficient prediction at wind speed from 7m/s to 25m/s, all the three models demonstrate good agreements with the measurement. For the Phase VI wind turbine, all the airfoil lift and drag coefficients used are purely wind tunnel test results from TUDelft, and no stall correction model is used. The blade tip speed ratio locates from 1.58 (for wind speed of 25m/s) to 7.58 (for wind speed of 5m/s) with rotor speed of 72RPM and rotor radius of 5.029m. Noted here, higher blade tip speed ratios (higher than 8) are not within the operation range in this case. All the three models show very similar behaviours except when the blade tip speed ratio is higher than 6. The AeroDyn model predicts highest power coefficient and the Glauert model predicts lowest power coefficient at high tip speed ratio conditions (TSR>6). At high wind speeds (low speed ratios), the AeroDyn model and Glauert model produce high power output compared with the GH-Bladed model. Moreover, the discontinuity[2] of the thrust coefficients in the Glauert and GH-Bladed models does not show apparent calculation deficiency in this case.

For the Phase VI wind turbine, Figure 3-4 indicates that all the power output from the

---

[2] Please refer to Figure 2-3

three empirical wake induction correction models are under-predicted at wind speed higher than 9m/s. It is mainly because all these calculations are based on the purely 2D aerodynamic coefficients. In the following sections, the empirical GH-Bladed wake induction correction model is used for stall correction discussion.

3.4   Stall Correction Models

Considering stall-delay effect, several correction models have been reviewed in Chapter 2. In this section, the most popular stall-delay correction models, including the Viterna-Corrigan (V-C) model and Du-Selig (D-S) model are discussed. Moreover, airfoil aerodynamic coefficients derived from the NREL/NASA rotating blade surface pressure measurements are also used to compare with these models. A hybrid stall correction model is proposed in Section 3.4.4.

3.4.1. BEM method with 2D Coefficients

Prior to applying any stall-delay correction model, the predictions obtained from the BEM method with 2D lift and drag coefficients are compared with the measured data. The measured power curve was obtained from torque measurements [80] with a constant rotor speed of 72RPM. Here, no stall-delay corrections are applied to the 2D BEM prediction. The aerodynamic coefficients are purely from TUDelft wind tunnel tests, which are tabled in Appendix C. The wake induction correction model used is GH-Bladed model for all the predictions in this section. For high angles of attack, the 2D aerodynamic coefficients of the airfoil are calculated from the flat plate theory (described in Chapter 2). The S809 airfoil aerodynamic data for the whole range of angle of attack is shown in Figure 3-5. The power curves from the NREL/NASA Phase VI turbine measurements and the BEM calculations using the TUDelft test data are plotted in Figure 3-6.
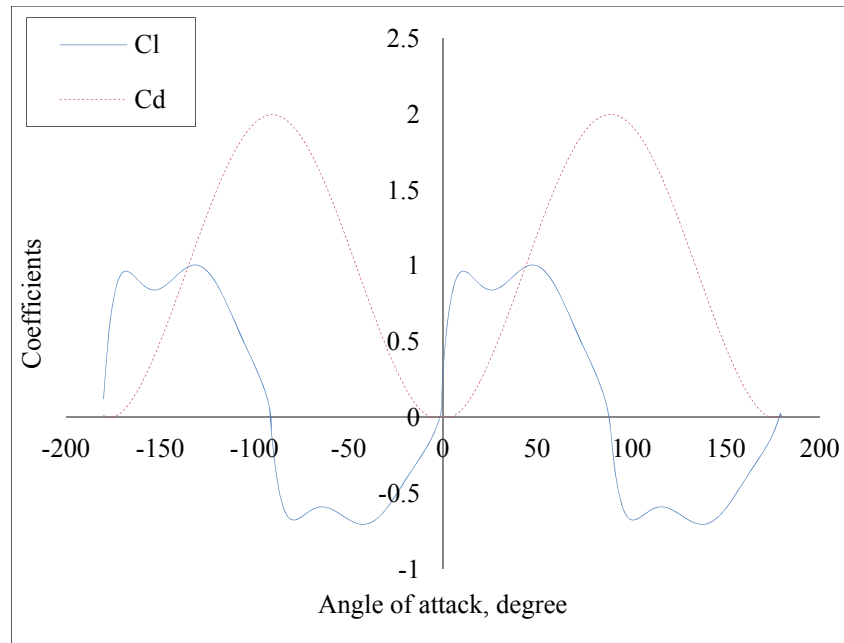
Figure 3-5 2D Global lift and drag coefficients of S809 at Reynolds number of 1×10^{6}
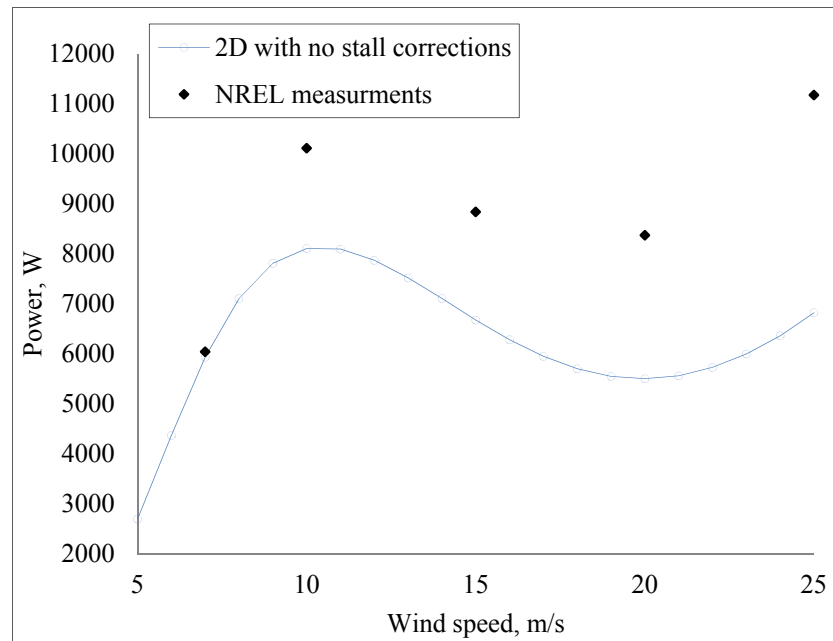
Figure 3-6 Power curve predicted with 2D BEM method and measurements

As shown in Figure 3-6, the 2D BEM method results are identical to the NREL measured data up to wind speed 7m/s. At high wind speeds, the GH-Bladed model under-predicts power outputs. At these high wind speeds, it is obvious that the turbine operates under stall conditions.

According to Equation (3.1) [9], the angles of attack are calculated for wind speeds from 7m/s to 25m/s along the blade span using the 2D lift and drag coefficients in Figure 3-5.

$$\alpha = \tan^{-1}\left[\frac{U(1-a)}{\omega r(1+a')}\right] - \beta \tag{3.1}$$

where α is the angle of attack, U is the nature wind speed, β is the twist/pitch angle in rad, r is the local radius in m, ω is the rotor speed in rad/s, a and a' are the axial and angular induction factors respectively.

The calculation tolerances of the axial and tangential induction factors are set to 10^{-3}. Figure 3-7 presents the angle of attack distributions at different wind speeds along the whole blade span, which are calculated from Equation (3.1).
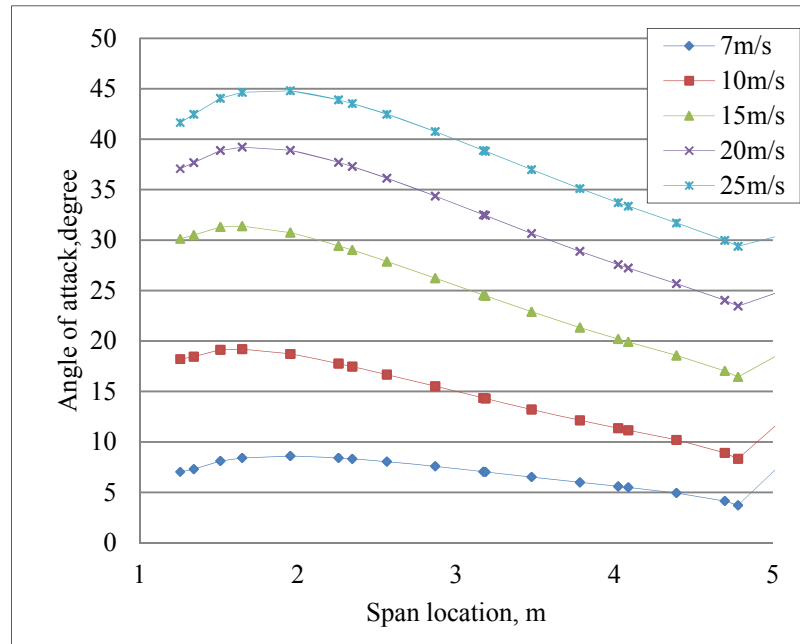
Figure 3-7 Angle of attack distributions along the blade span at different wind speeds

Figure 3-7 shows that, at low wind speed of 7m/s, most of the sections along the blade span have low angle of attack except at the blade root section, which means most of the blade sections experiences attached flows according to the airfoil wind tunnel test data. The angle of attack is higher at higher wind speed. When the wind speed is above 10 m/s, stall occurs at almost half of the blade span locations according to the 2D stall angle (the angle of attack at which stall starts, i.e. 15° for S809) from wind tunnel test data. When the wind speed is higher than 15m/s, the whole blade span is in full stall.

Therefore, it can be concluded that before stall occurs, the power prediction using the BEM method with 2D aerodynamic coefficients coincides very well with the measured power output; however, the BEM method fails at high wind speeds where stall exists. It is therefore critical to include the stall-delay corrections in the BEM method so as to improve the power prediction accuracy at high wind speeds.

3.4.2. BEM Method with Viterna-Corrigan Model

This section presents the application of the Viterna-Corrigan (V-C) method[3] for the Phase VI wind turbine with S809 airfoil. The TUDelft wind tunnel tested lift and drag coefficients are used to extrapolate the coefficients. The input aspect ratio ($AR = radius/chord$) is selected as 14 according to the tip chord of 0.358m and radius of 5.029m for the Phase VI turbine blade. The initial stall angle is a difficult parameter to cope with. Three initial stall angles of 9.21°, 15.23° and 20° have been tried, however, none of these initial stall angles produces satisfactory results of the power prediction based on the BEM method. The reason is that the lift to drag ratios at these two angles of attack do not follow the flat plate theory ($Cl/Cd = \tan\alpha$), and serious drop occurs in the calculated lift and drag coefficient curves at these initial stall angles where the V-C correction starts. To cope with this "drop", it is necessary to reduce the gap between the 2D tested aerodynamic coefficients and the V-C corrections at the angle of attack where the V-C correction starts and keep the corresponding lift to drag ratio been guided by the flat plate theory. Without an accurate initial input of initial stall angle of attack and corresponding lift and drag coefficients, the V-C method shows no improvement in power prediction compared with the BEM method using the 2D wind tunnel tested coefficients as presented in Section 3.4.1.

The research work of Tangler [51] also stated that the results from the Viterna-Corrigan method are dependent on the initial input values of the stall angle and the input aspect ratio, and it was also suggested that the applied method should follow the flat plate theory. Tangler suggested using the averaged 3D lift and drag coefficients (derived from the surface pressure measurements of the NREL/NASA Phase VI wind turbine rotating blades at five span locations) to bridge up this gap. The TUDelft measured 2D lift and

---

[3] Please refer to equations from (2-14) to (2-20).

drag coefficients and the averaged lift and drag coefficients (reproduced from Tangler's research) are plotted in Figure 3-8. It can be seen that the averaged 3D lift coefficient is much higher than the 2D lift coefficient for angles of attack from 9.21° to 20°. Above 20°, the V-C model is applied. In Tangler's work, the initial stall angle of attack in the V-C method was 20°, the corresponding lift coefficient was 1.24 and drag coefficient was 0.44. The aspect ratio was set to be 14 as calculated at the blade tip position. The power prediction using these coefficients is shown in Figure 3-9. For the angles of attack from 0° to 9.21°, from 9.21° to 20° and larger than 20°, the 2D coefficients, the 3D averaged coefficients and the coefficients extrapolated using the V-C method are applied respectively. The power prediction with the combined coefficients show improved results compared with those from the BEM method using the 2D wind tunnel tested coefficients, as shown in Section 3.4.1.
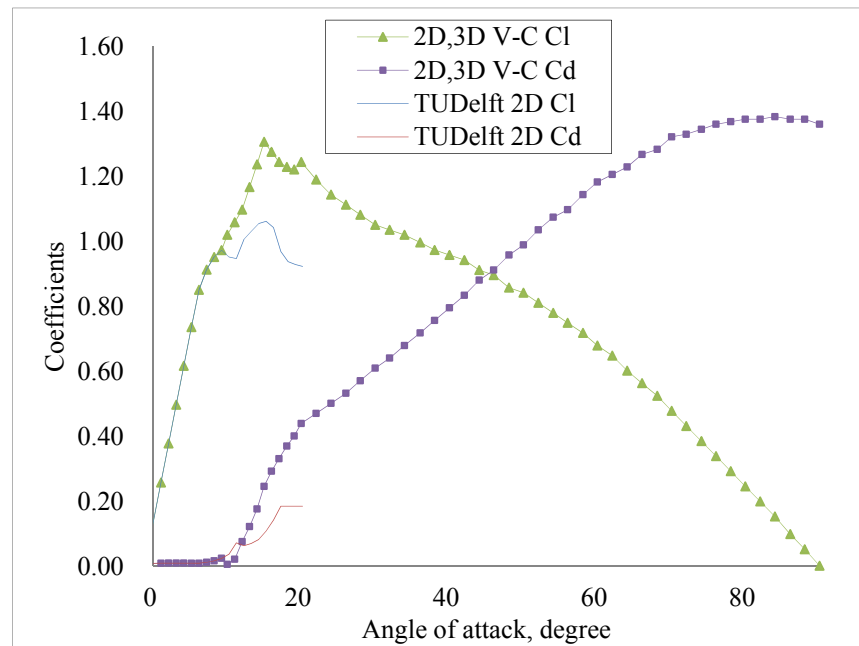
Figure 3-8 3D averaged lift and drag coefficients and 2D coefficients
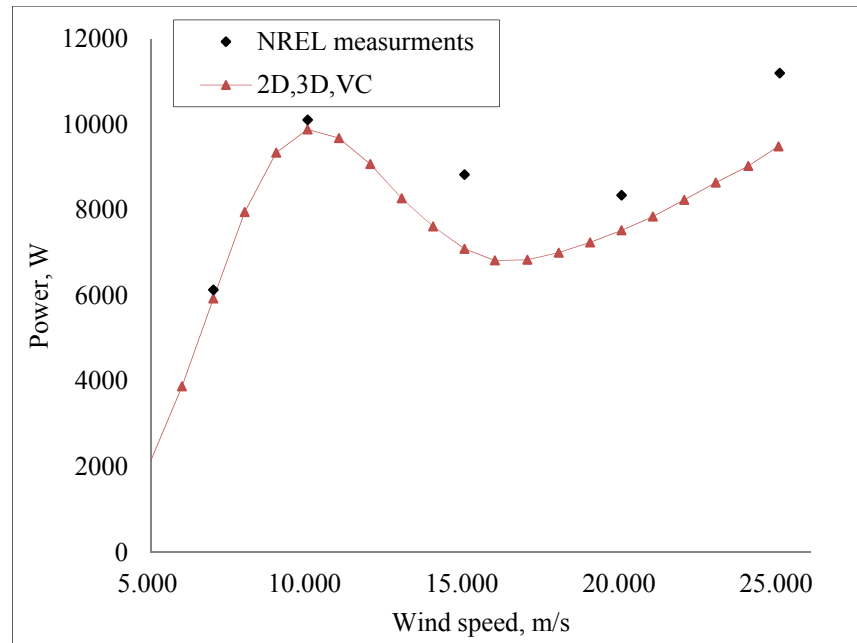
Figure 3-9 Power curve predicted with the V-C model and measurements

3.4.3. BEM Method with Du-Selig Model

This section presents the application of the Du-Selig (D-S) model[4] for the Phase VI wind turbine with the S809 airfoil. The TUDelft wind tunnel tested lift and drag coefficients are used at low angles of attack. The TUDelft wind tunnel tested 2D lift and drag coefficients, and the calculated lift and drag coefficients using the Du-Selig model are plotted in Figure 3-10. The input of the radius position (r/R) in the D-S model is set to 0.3 and the input of wind speed is set to 15m/s, which corresponds to a Reynolds number of 1×10^6. The empirical factors, including a, b and d correction factors are set to 1 in equations from (2-21) to (2-26). It can be seen that, the D-S derived lift coefficients are much higher than the 2D wind tunnel tested coefficients, and the drag coefficients are almost the same at low angles of attack. In the D-S equations from (2-21) to (2-26), the local radius position (r/R) and wind speed are the necessary input parameters. Therefore, four series of airfoil data which are derived with an input of wind speed of 15m/s. The calculated lift and drag coefficients are used for all inner blade span sections (r/R<0.8). The blade outer span sections are not considered due to weak influence of stall as claimed by researchers [41;43]. The data used for the blade outer span sections

---

[4] Please refer to equations from (2-21) to (2-26).

(where stall is weak) are 2D lift and drag coefficients.
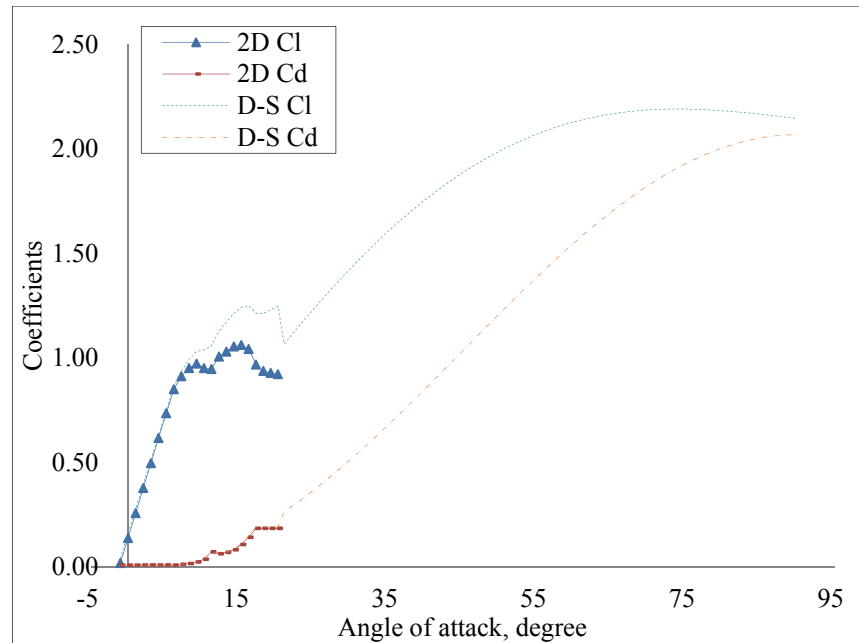
Figure 3-10 Lift and drag coefficients derived from the D-S model and 2D coefficients

Figure 3-11 presents the predicted power using the Du-Selig model and the measured power. When the wind speed is below 10m/s, the predicted power coincides well with the measured power. However, at high wind speeds, the prediction is much higher than the measurement. Similar results were also reported by Breton [52]. The over-predicted power is mainly caused by the over-corrected lift coefficients at high angles of attack from 20° to 90°, which are compared with lift coefficients extrapolated by the flat plate theory, as shown in Figure 3-10. Moreover, the drag coefficients produced by the D-S model are almost the same with those from wind tunnel tests. This could be another reason for the over-prediction. Additionally, the successful implementation of Du-Selig model at very high angles of attack also depends on the determination of the empirical factors, i.e. a, b and d correction factors in equations from (2-21) to (2-26), as described in Chapter 2. Another work showed that the D-S model is applicable to wind speed from 5m/s to 10m/s [82]. However, the power prediction at high wind speeds was not presented.
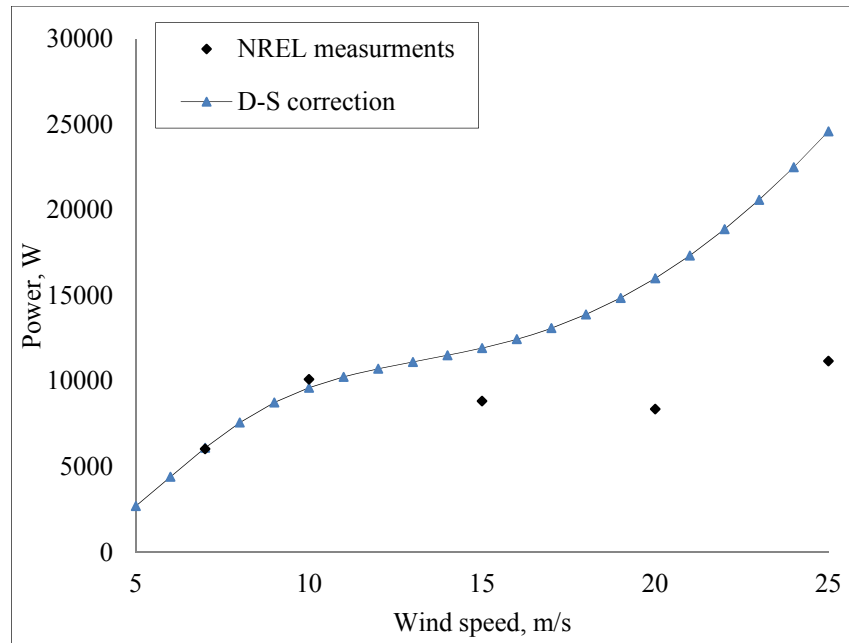
Figure 3-11 Power curve predicted with the D-S model and measurements

Based on the above analysis, it is concluded that:

Neither the initial angle of attack 15° or 20° can provide an accurate power prediction for the NREL/NASA Phase VI wind turbine using the V-C model. Tangler used the averaged coefficients at angles of attack 16° and 20° as the initial input parameters, and presented a good power prediction [55]. Moreover, the averaged lift and drag coefficients (from the blade surface pressure measurements) show better accuracy in power prediction than the wind tunnel tested lift and drag coefficients, which is the same conclusion as mentioned in Reference [51]. The initial input angle of attack and corresponding lift and drag coefficients are determinative to the accuracy of the V-C model.

For the NREL/NASA Phase VI wind turbine, the D-S model predicts very well below 10m/s; however, it over-predicts at high wind speeds. Similar calculation results were made in Reference [52;55].

3.4.4. BEM Method with Hybrid Stall Correction Model

The above corrections depict the 3D flows well to some extent, however, power prediction using these corrections show limited accuracy at high wind speeds. More recently, Lanzafame [83] presented four mathematical equations to describe lift and

drag coefficients based on experimental data. Lanzafame's results of power prediction showed excellent coincidence with experimental data except for moderate wind speeds. In this section, a Hybrid Stall Correction (HSC) model was developed for power prediction. In this HSC model, for the angles of attack from 0° to 6.16°, the TUDelft wind tunnel tested lift and drag coefficients are used. For the angles of attack from 6.16° to 20°, the 3D coefficients derived from the NREL/NASA wind tunnel pressure measurements are used. When the angle of attack is above 20°, the coefficients are derived from the following equations:

$$C_l = 2 \cdot C_{l\max} \cdot \sin\alpha \cdot \cos\alpha, \quad 20° < \alpha \le 30° \tag{3.2}$$

$$C_d = C_{d,\max} \cdot \sin^2\alpha, \quad 20° < \alpha \le 30° \tag{3.3}$$

$$C_l = 2 \cdot \sin\alpha \cdot \cos\alpha, \quad 30° < \alpha \le 90° \tag{3.4}$$

$$C_d = 2 \cdot \sin^2\alpha, \quad 30° < \alpha \le 90° \tag{3.5}$$

Here, $C_{l,\max} = C_{l,\alpha=45°}$ and $C_{d,\max} = C_{d,\alpha=90°}$. The only parameter needs to be determined is the lift coefficient at angle of attack of 45°.

Figure 3-12 shows the lift and drag coefficients obtained from the HSC model with the lift coefficient equals to 1.3 at the angle of attack of 45°, and the coefficients based on the TUDelft tests and the standard flat plate model.
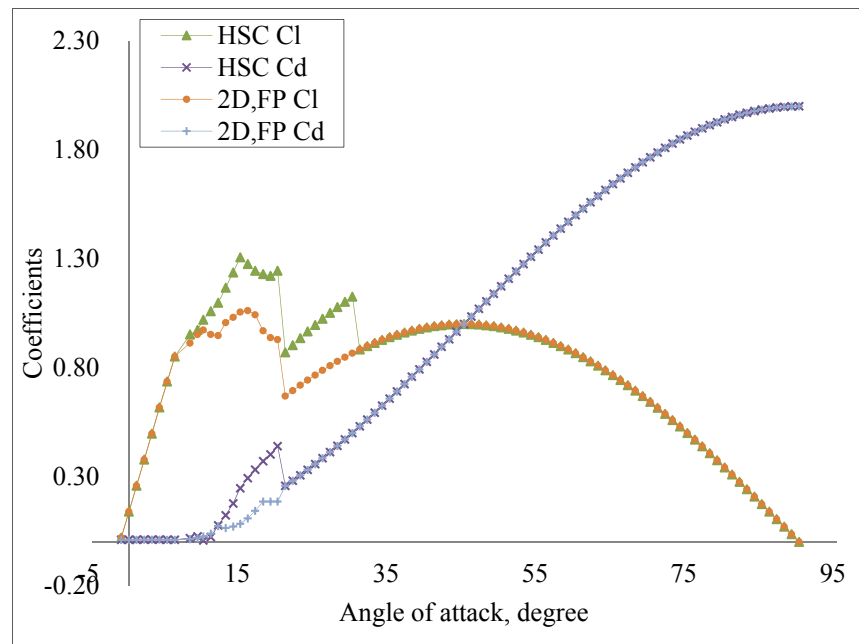
Figure 3-12 lift and drag coefficients of the hybrid stall correction model

Figure 3-13 plots the power curves predicted using lift coefficient of 1.2, 1.3 and 1.4 respectively at angle of attack of 45°, which are compared with those from the 2D measurements and the flat plate model. The power predictions at high wind speeds are greatly improved using the lift coefficients of 1.2 and 1.3 comparing with the standard flat plate model. With the lift coefficient of 1.3, excellent agreements have been achieved between the predicted power outputs and measurements with only exception for the wind speed of 20m/s. With the lift coefficient of 1.2, the power prediction at wind speed of 20m/s is closer to the measurements than using the lift coefficient of 1.3. However, using the lift coefficient of 1.3 shows better prediction overall.
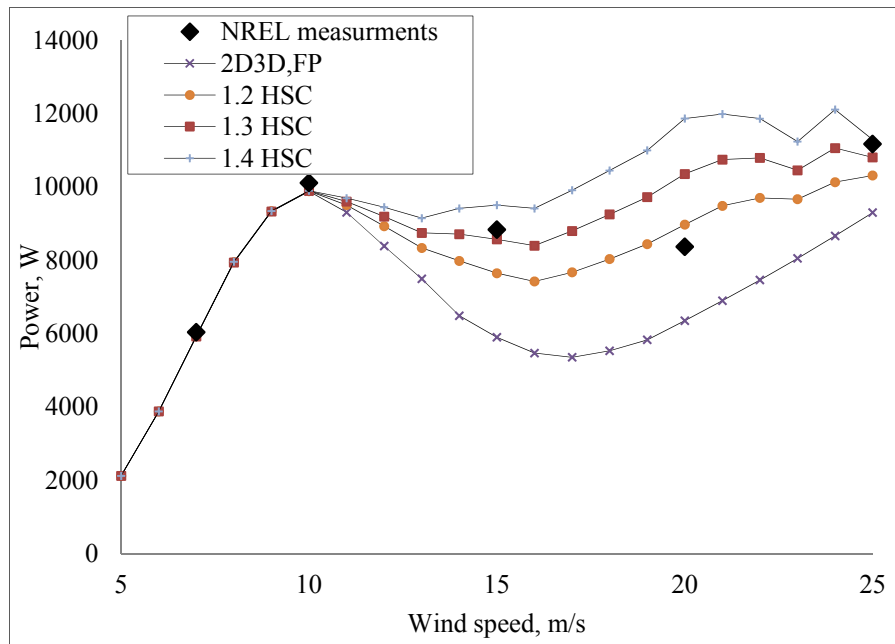
Figure 3-13 Power curves predicted with the hybrid stall correction model and measurements

3.5 Summary

In this chapter, the BEM method and its correction models were discussed. The limitations of the BEM method were further investigated through the power performance analysis of the NREL/NASA Phase VI wind turbine.

Regarding to the wake induction correction, the Glauert model, GH-Bladed model and AeroDyn model have very similar results for the NREL/NASA Phase VI wind turbine case. Considering stall-delay correction, the coefficients combined from the 2D wind tunnel tested lift and drag coefficients, the 3D coefficients (derived from rotating blade surface pressure measurements) and the coefficients derived from the V-C model (guided by the flat plate theory) provide an improved power prediction. Meanwhile, the 2D BEM method under-predicts and the D-S model over-predicts power outputs at high wind speeds. The accuracy of these correction models are highly turbine dependent and wind speed dependent. Based on the above analysis, a hybrid stall correction model was proposed and the results show better power prediction compared with the previous discussed models. Wind turbine power prediction at stall conditions is a tough task. Further validation of these models with more wind turbine measurements is needed.

The accuracy of the stall correction models at high wind speeds is highly determined by the input parameters which are turbine dependent and wind speed dependent It is therefore not easy to have a uniform mathematical expression to cover all the pre-stall, post-stall and deep-stall regions for different wind turbines.

Chapter 4 presents the rotor blade aerodynamic design and analysis for the fixed-pitch variable-speed (FPVS) and fixed-pitch variable-speed (FPFS) wind turbines.

CHAPTER 4   BEM BASED WIND TURBINE BLADE DESIGN AND ANALYSIS

4.1   Introduction

In the development of a wind turbine system, the blade is a determinative component for the whole system. The efficiency of the wind turbine blade largely determines the power performance of the wind turbine. Wind turbine blade design is a heuristic process, which cannot be finished in one single step. Iterations are needed for most cases. For the design optimisation of a wind turbine blade, an aerodynamic criterion, such as maximum power coefficient, maximum annual energy production (AEP) or minimum cost of energy (CoE) is often considered as the objective. Until an optimal blade is obtained according to the criterion, the blade aerodynamic design task is finished. In the design process, the BEM method is often used to assess the blade aerodynamic performance.

The heuristic process of blade design has been automatically accelerated by involving advanced computing algorithms. Benini [16] introduced a multi-objective evolutionary algorithm to maximize AEP and minimize CoE. Hampsey [84] used a weighted sums method for multi-objective optimisation. Méndez [85] used an genetic algorithm to obtain the optimal chord and twist angle distribution. Liu [86] selected an extended compact genetic algorithm to speed up the optimisation process. These methods are all based on the BEM theory and the blade chord and twist angle distributions were pre-defined by Bezier function. These methods show advanced computing efficiency and reduced work load and rapid process of blade design. However, the optimal blade chord and twist angle distributions of these methods rely on the initial input of the rotor parameters, airfoil aerodynamic characteristic data and the aerodynamic model. Other design methods are directly derived from BEM equations [87]. Maalawi [34] presented an approach to obtain the optimal relative angle so as to derive the chord and twist angle

distributions with given rotor diameter and a rotor solidity. Rather than developing an advanced algorithm, a thorough understanding of the blade design philosophy is highly needed to fit diverse features of various wind turbines.

To investigate the design philosophy, this chapter will address the blade aerodynamic design and analysis through two cases which are the most typical topologies for small wind turbines: one is the fixed-pitch variable-speed (FPVS) wind turbine, which is described in Section 4.2, and the other is the fixed-pitch fixed-speed (FPFS) wind turbine, which is described in Sections 4.3. The key rotor parameters and design methods are discussed through these two case studies. In the mixed airfoil FPVS wind turbine case, the blade design of maximum power coefficient (Cp) is also discussed with maximum AEP consideration. The second case is designed for a FPFS wind turbine with the airfoil S809. A comparative study of rotor parameters is presented. A blade design approach of searching optimal induction factors with consideration of the tip-hub loss and drag effects is developed in the FPFS case. The linearisation of the radial profile of the blade chord and twist angle is also discussed for this single airfoil FPFS wind turbine case. A heuristic approach of blade linearisation is presented. A chapter summary is described in Section 4.4.

4.2   FPVS Wind Turbine Blade Design with Mixed Airfoils

This section shows the BEM based blade design through a case study of a mixed airfoil 10kW FPVS wind turbine. The fundamental specification and parameters of the wind turbine are defined in Table 4-1.

Basic parameters	Unit	Value
Wind turbine generator nominal power	W	10000
Design wind speed and rated wind speed	m/s	8.5
Assumed rotor aerodynamic power coefficient at rated wind speed		0.43
Assumed total power coefficient		0.3385
Number of blades		3
Design tip speed ratio		8
Tip speed at design (rated) wind speed	m/s	68
Air density	kg/m^3	1.225
Radius of the rotor	m	5
Wind turbine rotor (generator) rated speed	RPM	130
Airfoils		DU93-W-210-40%
		DU93-W-210-30%
		DU93-W-210-25%
		DU93-W-210
		DU93-W-210-18%

Table 4-1 10kW FPVS wind turbine fundamental specifications and parameters

4.2.1. Rotor Parameters

The FPVS wind turbine operates at variable-speed to maintain a constant design tip speed ratio of 8 (constant power coefficient) below rated wind speed (at which rated power is reached). Above the rated wind speed, the rotor produces constant power by control. The main blade design parameters of this FPVS wind turbine including the airfoil type, rotor diameter, design tip speed ratio, design wind speed and design angle of attack are discussed below.

4.2.1.1 Airfoil Type

There are many different airfoils including the general aviation airfoil NACA series, which have been widely employed in wind turbine applications. With the rapid growth of wind power industry, dedicated airfoils have been developed over the last two decades. For example, the S series airfoils, which were designed by National Renewable Energy Laboratory (NREL) in the USA, are popular in stall-regulated wind turbine blades due to their gentle stall behaviours [81;88]; the FFA W series airfoils originate

from Sweden and Risø series from Denmark, which were designed for lower Reynolds number wind turbine blades [89-92]; and the DU series airfoils, which were designed in the Netherlands, are popular in middle and high Reynolds wind turbine blades [93]. Considering its high lift performance, the DUW-93-210 airfoil [94] is selected[5] for this case study. The DUW-93-210 airfoil has a maximum thickness ratio of 21% at the position of 35% of the chord, as shown in Figure 4-1.
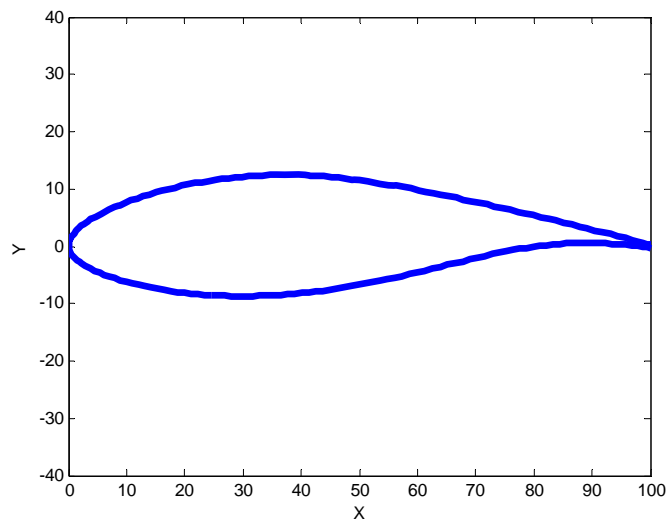
Figure 4-1 DU93-W-210 airfoil shape

In order to accommodate manufacture and structure design requirements, the baseline airfoil DU93-W-210 is modified into different thickness airfoils to fit different locations along the blade span. The original maximum thickness to chord ratio 21% is adjusted to 40%, 30%, 25%, and 18% respectively, the position where the maximum thickness locates is not changed. The baseline airfoil DU93-W-210 locates from sections between 35% and 90% of the blade span length. The 40% thickness airfoil is positioned at the blade root section, the 18% thickness airfoil is positioned at the blade tip section, and the 30% and 25% thickness ones are employed in the transition sections, as shown in Table 4-2.

---

[5] Choosing/designing the best airfoil for the wind turbine blade is a very challenging task and out of the scope of the thesis. The focus of this thesis is not on the optimal airfoil selection or design. Apparently there will be difference when a different airfoil is selected for the wind turbine blade design in terms of power and load performance.
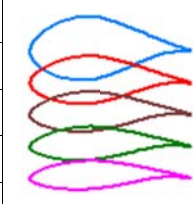
Airfoil Shapes	Thickness ratio	Airfoil Shapes	Stations
DU93-W-210-40%	40%		0.05R
DU93-W-210-30%	30%		0.1R
DU93-W-210_25%	25%		0.15R-0.3R
DU93-W-210	21%		0.35R-0.9R
DU93-W-210-18%	18%		0.95R-1R

Table 4-2 Blade airfoil configuration

4.2.1.2 Design Wind Speed and Rated Wind Speed

The rated wind speed is the wind speed at which the wind turbine reaches its rated power. The design wind speed is defined as the wind speed at which the wind turbine operates its maximum power coefficient (Cp). For variable-speed wind turbines, the wind turbine is designed to operate at its maximum Cp from cut-in wind speed to its rated wind speed. Therefore, the design wind speed is defined the same as the rated wind speed for FPVS wind turbines. Given an annual mean wind speed (AMWS), the relationship between annual energy production (AEP) and rated wind speed is further discussed in Section 4.2.4. For this 10kW FPVS wind turbine case, with a 130RPM permanent magnet synchronous generator, the rated wind speed and the design wind speed is determined as the same wind speed of 8.5m/s.

4.2.1.3 Rotor Diameter

The wind turbine rotor radius is estimated from the following equation [9]:

$$P = C_{total} \frac{1}{2} \rho V_r^3 \pi R^2 \tag{4.1}$$

where,

P is the generator nominal power, in watt,

C_{total} is the total efficiency including the aerodynamic power coefficient and the mechanical and electrical efficiency of the wind turbine system,

R is the rotor radius, in meter,

$\rho = 1.225 \, \text{Kg/m}^3$ is the air destiny,

V_r is the rated wind speed, in m/s, which is also the design wind speed for this 10kW FPVS wind turbine.

Giving a rated wind speed of 8.5m/s and a general total power coefficient of 33.8%, the

rotor radius is determined to be 5m for this 10kW FPVS wind turbine.

4.2.1.4 Design Tip Speed Ratio

The design tip speed ratio (TSR) is defined as $\lambda = \omega R / U$. A higher tip speed ratio means a higher rotor speed which is an advantage considering the efficiency of the generator. And high tip speed ratio also means smaller gearbox. Also, with higher rotor speed, smaller chord length is preferable to maintain higher power coefficient and lower thrust. The smaller chord length also means less material for the blade manufacture. However, very high tip speed ratio entails some disadvantages like audible and non-audible noise generation and erosion at the leading edge. For electric generation, a tip speed ratio of 4-10 is normally recommended [9]. For an initial selection of tip speed ratio, the empirical relation between power coefficient and tip speed ratio is considered. Wilson [9] calculated the maximum power coefficients of wind turbine rotors with a finite number of blades and an empirical relationship was developed. Çetin [95] presented a similar procedure to assess optimum tip speed ratio for different airfoils with different blade numbers. According to Çetin, the power coefficient is a function of TSR, blade number and maximum lift/drag ratio [95]:

$$C_p = C_{p\,Schmitz} \cdot (1 - \frac{\lambda}{C_l/C_d}) \cdot (1 - \frac{1.84}{Z \cdot \lambda}) \qquad (4.2)$$

Here,

$C_{p\,Schmitz}$ is the Schmitz power coefficient, which is 0.5926,

Z is the blade number, which is 3,

C_l / C_d is the maximum lift to drag ratio.

A MATLAB was developed to assess optimum tip speed ratio according to the above equation. The variation of power coefficient with tip speed ratio is presented in Figure 4-2.
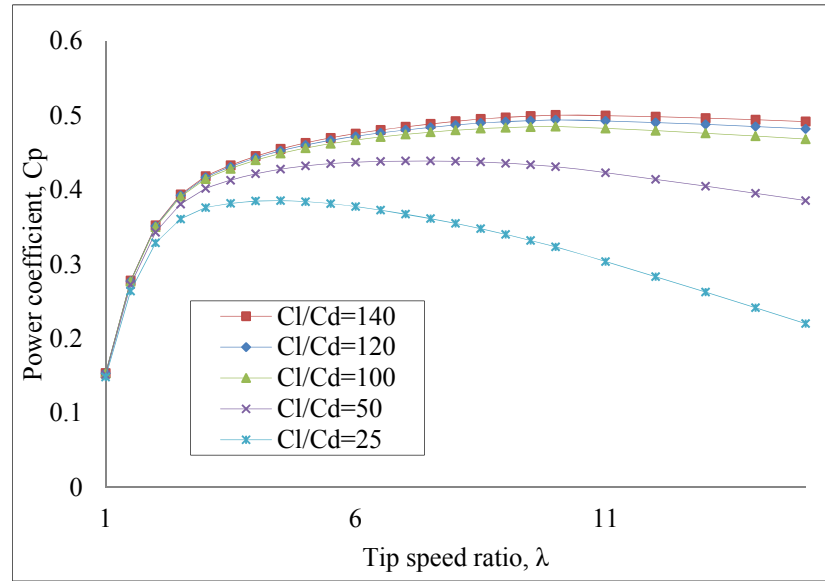
Figure 4-2 Power coefficient versus tip speed ratio

According to equation (4.2), the power coefficient increases with tip speed ratio (up to TSR of 8), as shown in Table 4-3. In this case, at Reynolds number of 500,000 (refer to Table 4-4), the maximum C_l / C_d is for DU93-W-210 is 101.41 at angle of attack of 8° (calculated by XFOIL). The maximum Cp locates around TSR of 8. In this FPVS wind turbine case, the TSR is set to 8, the blade tip speed is guaranteed not higher than 68m/s at rated wind speed (design wind speed).

TSR	Cp
3	0.457499
4	0.481944
5	0.494274
6	0.500546
7	0.503356
8	0.504003
9	0.503207
10	0.501402

Table 4-3 Theoretical power coefficient for DU93-W-210 at Reynolds number of 5×10^5

4.2.1.5 Design Angle of Attack

As for the design angle of attack, generally, a high lift (which contributes most to positive torque) and a low drag (which contributes most to thrust and cause negative torque) are preferable for maximum power coefficient design of wind turbine blades, thus the design angle of attack is often selected at the critical angle of attack where the

lift to drag ratio (c_l / c_d) is maximum. For this blade design case, the design angle of attack is set at the critical angle of attack 8°.

4.2.1.6 Airfoil Characteristics

For wind turbine blade design and analysis, it is essential to have the aerodynamic data of the selected airfoil at the corresponding flow conditions, i.e. Reynolds (Re) numbers. The Reynolds number is defined as [9]:

$$\mathrm{Re} = \frac{U_{rel}c}{\upsilon}$$
(4.3)

where:

U_{rel} is the relative wind speed (m/s),

c is chord length (m),

υ is kinematic viscosity of air (v = 14.8×10^{-6}) (m²/s),

For a radius of 5m and TSR of 8, the Reynolds number distributions of a typical 10kW wind turbine blade are tabled as following:

Reynolds number	0.1r/R	0.3r/R	0.5r/R	0.7r/R	1r/R
	Ref Chord 0.5m	Ref Chord 0.3m	Ref Chord 0.2m	Ref Chord 0.15m	Ref Chord 0.1m
V=5m/s	1.35e5	2.43e5	2.7e5	2.83e5	2.7e5
V=8.5m/s	2.3e5	4.135e5	4.59e5	4.82e5	4.59e5

Table 4-4 Re and Mach numbers of a typical 10kW wind turbine blade

As shown in Table 4-4, the Reynolds number is from 135,000 to 459,000 at the wind speeds from 5m/s to 8.5m/s[6]. Due to the variation of the Reynolds number at different wind speeds and different blade span sections, the power coefficient is different at different wind speed with the same tip speed ratio. And the power output is slightly lower at lower wind speeds (below 8.5 m/s) than prediction using one Reynolds number calculated from the wind speed of 8.5 m/s at the blade tip section. For the maximum Cp design, the blade can only be optimal at one wind speed corresponding to one Reynolds number. The effects of Reynolds number in blade design regarding to maximum AEP design was discussed in Reference [96]. The results demonstrate that the maximum Cp design is not necessary the maximum AEP design; however, when the design wind speed is the same as the rated wind speed, only a negligible small amount AEP

---

[6] For FPVS wind turbine, we assume constant rated power output is achieved through generator torque and speed control above design wind speed.

improvement occurs when the variation of Reynolds number (due to change of wind speed) are considered in blade design. Therefore, the Reynolds number corresponding to the design wind speed (rated wind speed of 8.5m/s) at the blade tip section, i.e. 500,000 is selected for blade chords and twists calculation.

Moreover, from Table 4-4, it is seen that at wind speed 8.5m/s, the Reynolds number for the main part (0.3r/R to 1R) of the 5m blade varies from 4.13×10^5 to 4.82×10^5. The Reynolds number effect on power output prediction for this small blade (with 5m radius) would be very small and negligible. And for the DU93 airfoil series, no wind tunnel test results of the airfoil at Reynolds numbers below 1×10^6 are available within the author's knowledge. For an initial design, the aerodynamic data were calculated using XFOIL code at Reynolds number of 5×10^5. To calculate the aerodynamic date of the airfoil, the XFOIL code was integrated in MATLAB code as shown in Figure 4-3.
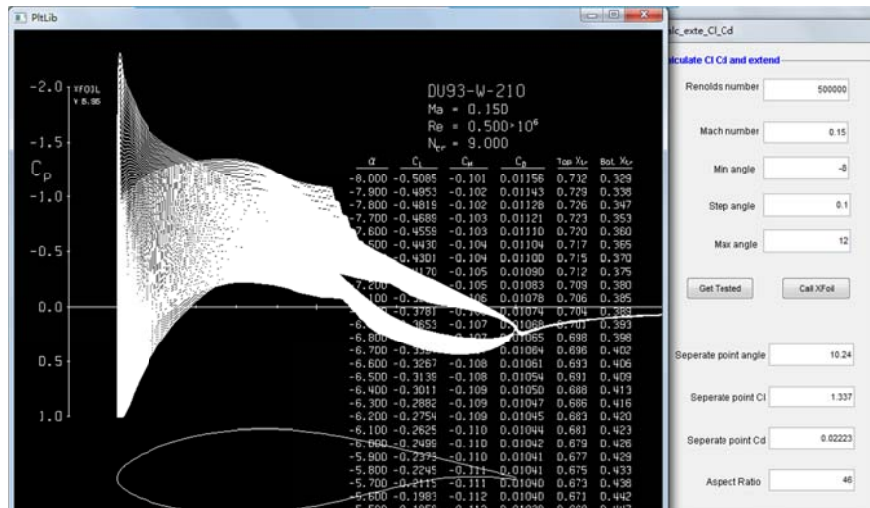
Figure 4-3 Integrated XFOIL user interface

Figure 4-3 shows the MATLAB code interface integrated with XFOIL code for lift and drag coefficient calculation. Providing basic parameters, i.e. the airfoil coordinate data, the Reynolds number and Mach number, the calculation range and step of angle of attack, the corresponding lift and drag coefficients are obtained. This is especially useful when no wind tunnel tested airfoil aerodynamic data are available. This sub-routine along with the blade design code works as an engineering tool for blade design and assessment.

In order to validate XFOIL calculation, the calculated lift and drag coefficients at Re of

10^6 are compared with published TUDelft wind tunnel testing results[7], as shown in Figure 4-4. Good agreement occurs only at low angles of attack and slightly over-prediction exists at moderate angles of attack. This indicates that the XFOIL data is relatively reliable at low angles of attacks at the Reynolds number of 1×10^6, i.e. in the pre-stall region. Since the design angle of attack is selected at the critical angle of attack where the maximum lift to drag ratio locates, the wind turbine is working in the pre-stall condition at the design tip speed ratio of 8. It is therefore acceptable to use XFOIL calculated data in the initial blade design when no wind tunnel tested coefficients are available, even though slightly over-prediction exists[8]. The lift to drag ratios of the DU93 airfoil series are plotted in Figure 4-5.
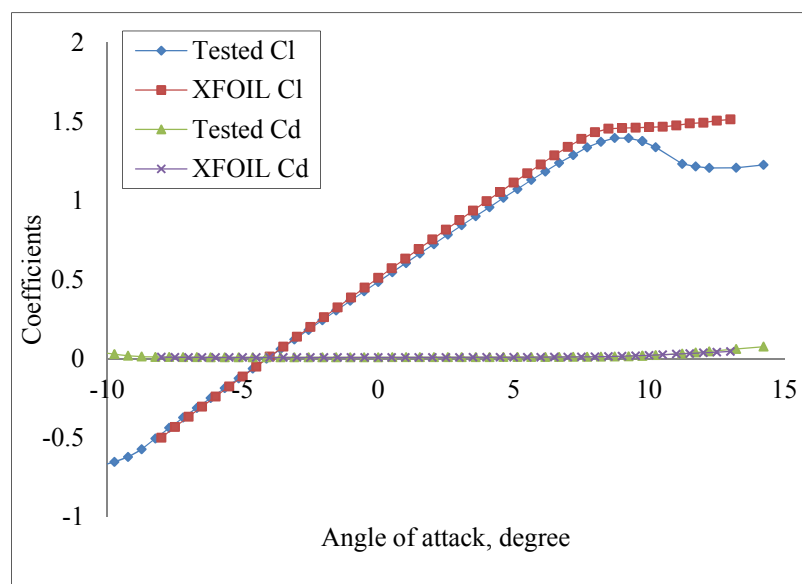
Figure 4-4 Comparison of XFOIL and wind tunnel test results of DU93-W-210 at Reynolds number of 1×10^6

Figure 4-5 depicts the lift to drag ratios, which are calculated using XFOIL, of the DU93 airfoil series, as listed in Table 4-2. Please note, the critical angles of attack of the airfoils, where the lift to drag ratios drop, vary with the thicknesses of the airfoils.

---

[7] Wind tunnel test data retrieved from TUDelft by Christoph Rudolph, who was a visiting student at UCLan from Germany from personal emails.

[8] The coefficients calculated using XFOIL at Reynolds number of 5×10^5 are very close to the coefficients at Reynolds number of 1×10^6. This may cause an over-prediction in the power prediction. Wind tunnel tests at Reynolds numbers from 2×10^5 to 5×10^5 for the airfoil DU93-W-210 will be detailed later in Chapter 6.
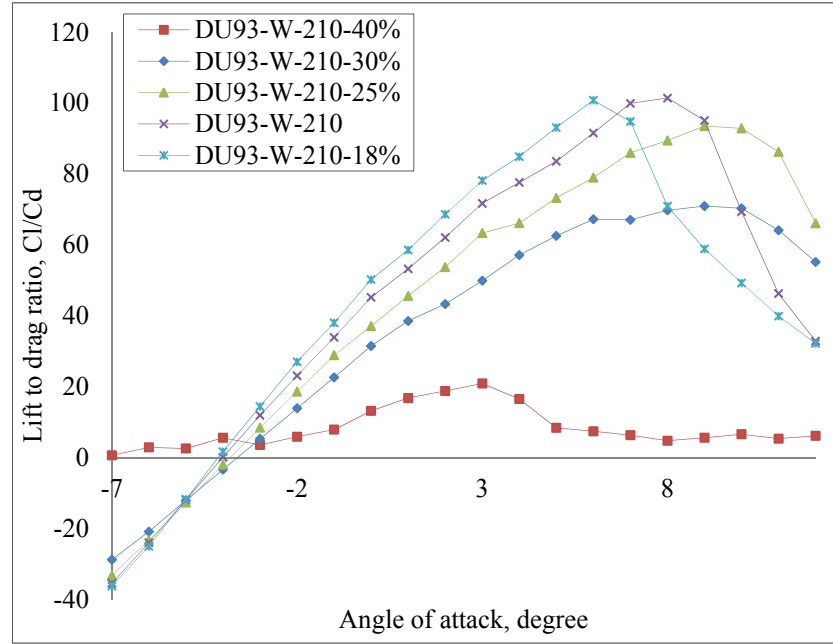
Figure 4-5 Lift to drag ratios of DU93 series airfoils calculated by XFOIL at Reynolds number of 5×10^5

4.2.2. Blade Chord and Twist Angle Distributions

In the standard BEM method, if the *Cp* of each section along the blade span is at its maximum, the maximum power coefficient of the whole blade is achieved. Referring to equations of the standard BEM method (see Appendix B), the sectional power coefficient is expressed as:

$$F \sin^2 \phi (\cos \phi - \lambda_r \sin \phi)(\sin \phi + \lambda_r \cos \phi) \lambda_r^2 \left[1 - (C_d / C_l) \cot \phi \right] \rightarrow Max \qquad (4.4)$$

where,

F is the tip-hub loss factor,

ϕ is the relative angle of attack in rad,

λ_r is the local tip speed ratio,

C_d / C_l is the drag to lift ratio.

Ignoring the tip-hub loss and drag effect, i.e. F is equal to 1 and C_d / C_l is equal to zero, with the partial derivative of the main part being zero, the optimum twist angle is obtained. In the standard BEM method, the following equations are often used to calculate the optimal blade chords and twist angles [9]:

$$\phi_r = (2/3)\tan^{-1}(1/\lambda_r) \qquad\qquad (4.5)$$

$$C_r = \frac{8\pi r}{ZC_l}(1-\cos\phi_r) \qquad\qquad (4.6)$$

where,

r is local radius in m,

ϕ_r is the local relative angle of attack in rad,

λ_r is the local tip speed ratio,

C_r is the local chord in m,

C_l is the lift coefficient at the critical angle of attack.

Using these two equations, the chords and twist angles for this mixed-airfoil blade are obtained. Due to different critical angle of attack for these DU93 airfoils, the initial chord and twist angle distributions show discontinuous variations along the blade span, and irregular chord length and twist angle appear in the transition area between the sections along the span. This discontinuous variation may cause negative effects on both aerodynamic and structure dynamics performance. The aerodynamic flow over these blade sections is even complex and may yield secondary loads and stress concentration. Furthermore, the discontinuous feature could be rather poor when manufactured. Therefore, the chords and twist angles of the main sections (0.35R-0.9R) were maintained, and the rest was smoothed to match the main sections, as shown in Figure 4-6. Tabled data of the blade chords and twist angles are presented in Appendix F. The airfoils and the CAD model of the smoothed blade are presented in Figure 4-7. The airfoils are centred at the position of 25% chord from the leading edge. It is noted that, the smoothed chord at the 0.1 r/R position is smaller than the 0.2 r/R position. From structure point of view, this feature allows a tender transition from airfoil to blade root cylinder for a real blade. For a practical blade design, the chord and twist angle at 0.1 r/R position can also be derived using a linear transition between the airfoil at 0.2 r/R position and the cylinder at the root position.
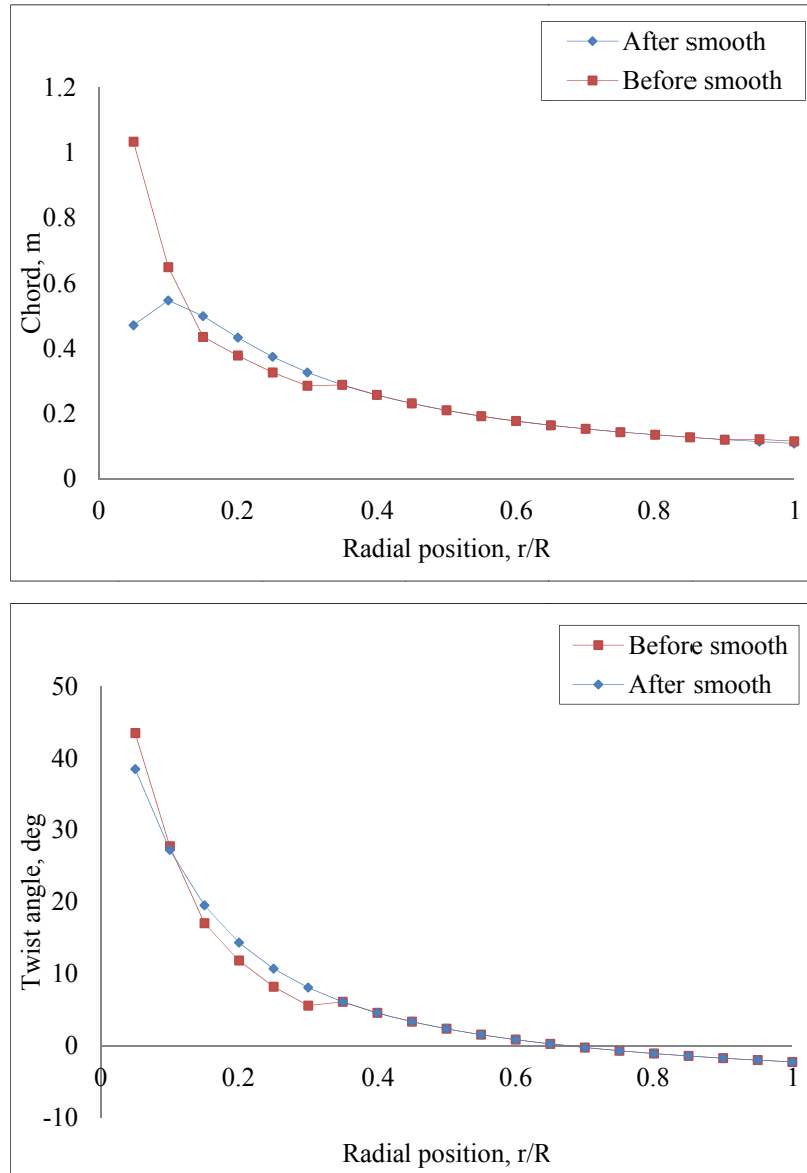
Figure 4-6 Blade chord and twist angle distributions before and after smoothing
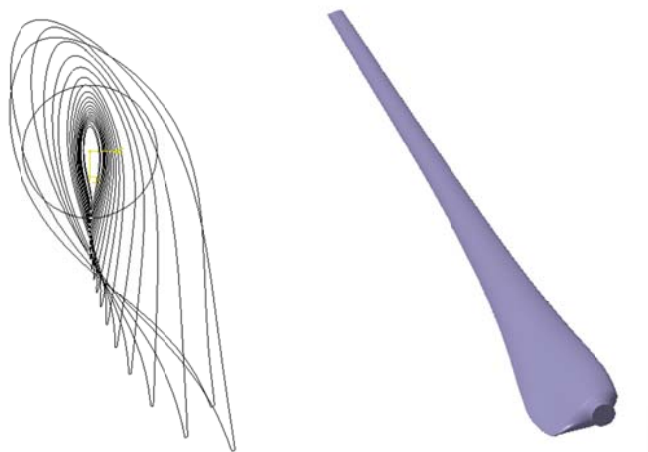
Figure 4-7 Section airfoils and blade CAD model of the FPVS wind turbine

4.2.3. Power Curve

The BEM predicted power coefficient of this FPVS wind turbine is 0.48 at TSR of 8 (BEM equations for power prediction are presented in Appendix B). For this FPVS wind turbine, the wind turbine operates at variable-speed to maintain a constant design tip speed ratio of 8 before the rated power is reached. It is assumed that the power output above the rated wind speed is constant (as shown in in Figure 4-8). In realities, the power fluctuates about the rated power with control and the generator can tolerate about 20% overloading.
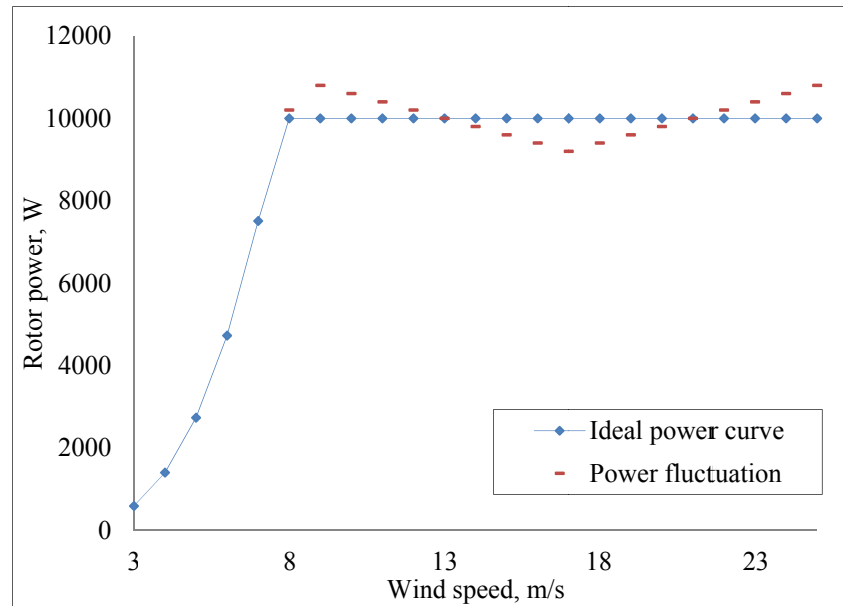
Figure 4-8 Power curve of the 10kW FPVS wind turbine

4.2.4. Maximum AEP Consideration

For a FPVS wind turbine, the AEP (or annual power output) is calculated according to the following equation:

$$\text{AEP} = 8760 \cdot \frac{1}{2} \rho A \eta C_{p,o} \int_{cut\ in}^{rated} v^3 f_{Rayleigh}(v)\, dv + 8760 \cdot P \int_{cut\ in}^{cut\ out} f_{Rayleigh}(v)\, dv \qquad (4.7)$$

where,

A is the wind turbine rotor area (m^2),

η is efficiency including mechanical and electrical efficiency of the wind turbine system,

$C_{p,o}$ is the maximum power coefficient of the blade,

61

$f_{Rayleigh}(v)$ is the Rayleigh wind speed distribution, which is defined as:

$$f_{Rayleigh}(v) = \frac{\pi}{2}\frac{v}{\overline{v}^2}\exp\left(-\frac{\pi}{4}\frac{v^2}{\overline{v}^2}\right) \tag{4.8}$$

Here, $\overline{v}$ is the annual mean wind speed (AMWS), in m/s.

Since the $C_{p,o}$ is constant below rated wind speed for a FPVS wind turbine and the power is constant above rated wind speed, the maximum AEP design is much related to the rated wind speed. Based on Equation (4.7), assuming $C_{p,o}$ is 0.4, η is 0.82, and AMWS is 6m/s, as shown in Figure 4-9, for a 10kW wind turbine, with a mean wind speed higher than 3 m/s, the AEP is higher with a lower factor k, which is defined as $k = v_{rated}/\overline{v}$. This indicates that lower rated wind speed leads to higher AEP for FPVS wind turbines. But it is necessary to point out that a lower rated wind speed means a larger rotor, which causes an increase in cost. This finding was also published in the author's paper [97].
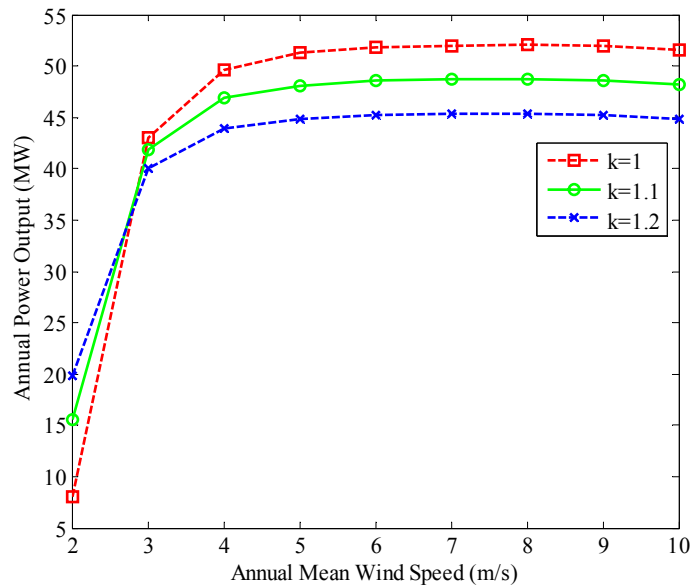
Figure 4-9 Annual power output versus AMWS of a 10kW FPVS wind turbine

4.3   FPFS Wind Turbine Blade Design with Single Airfoil

This section presents the blade design of a 12kW FPFS (stall-regulated) wind turbine with a single airfoil S809. Since the airfoil S809 has gentle stall performance and its aerodynamic data are available in literature [80, 81], in this section, the S809 airfoil is used for all the sections along the span. The fundamental specification and parameters are defined in Table 4-5. A comparative study of these rotor parameters is addressed in

Section 4.3.1. Using two BEM based methods with and without the tip-hub loss, and drag effect for blade design is presented in Section 4.3.2, and blade linearisation for maximum AEP design is discussed in Section 4.3.2 and Section 4.3.4.

Parameters	Unit	Value
Wind turbine generator nominal power	W	12000
Design wind speed	m/s	8.4
Rated wind speed	m/s	9.5
Assumed total power efficiency at rated wind speed		0.36
Number of blades		3
Design tip speed ratio		7
Tip speed at rated power	m/s	58.8
Air density	kg/m^3	1.225
Radius of the rotor	m	4.5
Wind turbine rotor speed	RPM	124.8
Airfoil		S809

Table 4-5 12kW FPFS wind turbine fundamental specifications and parameters

4.3.1. Rotor Parameters

For a FPFS wind turbine, the rotor speed is constant from cut-in wind speed to cut-out wind speed. The power coefficient of the rotor varies with the wind speed. The power curve is much more complex than a variable-speed wind turbine, and the power curve is purely dependent on its aerodynamic design of the blades. The rotor parameters are critical to a FPFS wind turbine blade design.

4.3.1.1 Rotor Diameter

As discussed in Section 4.2.1, assuming a total power efficiency of 0.36 with a rotor radius of 4.5m, the wind turbine generator rated power 12kW is reached at wind speed of 9.5m/s.

4.3.1.2 Airfoil Characteristics

At the design wind speed, the FPFS wind turbine operates at its maximum power coefficient. While at other wind speeds (off-design conditions), the power performance remains difficult to predict [9]. At low wind speeds, the turbine is designed to work at small angles of attack with no flow separation, while at high wind speeds the turbine is

working at stall conditions with large angle of attack. As discussed in the previous chapters, to model stall-delay, many researchers increase the lift coefficients by using empirical correction models to consider the rotational effects of the blade. These empirical correction models well depict the 3D flow; however, power prediction using these empirical correction models shows discrepancy compared with measurements. Moreover, these turbine-dependent empirical correction models need to be further validated with more measured wind turbine cases. Therefore, in this section, the lift and drag coefficients derived from TUDelft wind tunnel tests are both used for this 12kW FPFS wind turbine blade design and evaluation. The initially estimated Reynolds number is 1×10^6.

4.3.1.3 Design Angle of Attack

The design angle of attack is selected at the critical angle of attack, i.e. 6.16° for S809 at Reynolds number of 1×10^6.

4.3.1.4 Design Tip Speed Ratio

The design tip speed ratio (TSR) for a FPFS wind turbine is determined according to the radius and design wind speed, which is discussed below.

4.3.1.5 Design Wind Speed and Rated Wind speed

As defined in Section 4.2.1, the design wind speed is the wind speed at which the maximum power coefficient occurs, while the rated wind speed is the wind speed at which the rated power is reached. For small wind turbines, the design wind speed is often selected as 1.4 times of AMWS according to the IEC61400-2 standard [98]. The rated wind speed is designed at a higher wind speed. The reason is simple: if the rated power is reached at low wind speed, then it is likely that the power at high wind speed is much higher than the rated power. This is very dangerous to the generator as it may burnout. In order to investigate the relationship between the design wind speed and the AEP for FPFS wind turbine, a comparative study is shown below. Two aspects are discussed: to change the blade shape (i.e. to design a blade for an existing generator) and to change the generator (i.e. to define a generator speed for the blade design).

With a fixed rotor radius of 4.5m and a fixed rotor speed 124.8RPM (to change the

blade shape and no change to generator), three design wind speeds are compared: 8m/s, 8.4m/s and 9m/s, which are corresponding to tip speed ratio of 7.35, 7 and 6.53 respectively. Figure 4-10 shows the power curve of different design wind speeds and a fixed tip speed. To guarantee the maximum power limit of the FPFS wind turbine generator (considering 120% times generator nominal power and other system efficiency of 0.9, i.e. 16kW), the tip speed ratio is set to be 7 (corresponding to design wind speed of 8.4m/s).
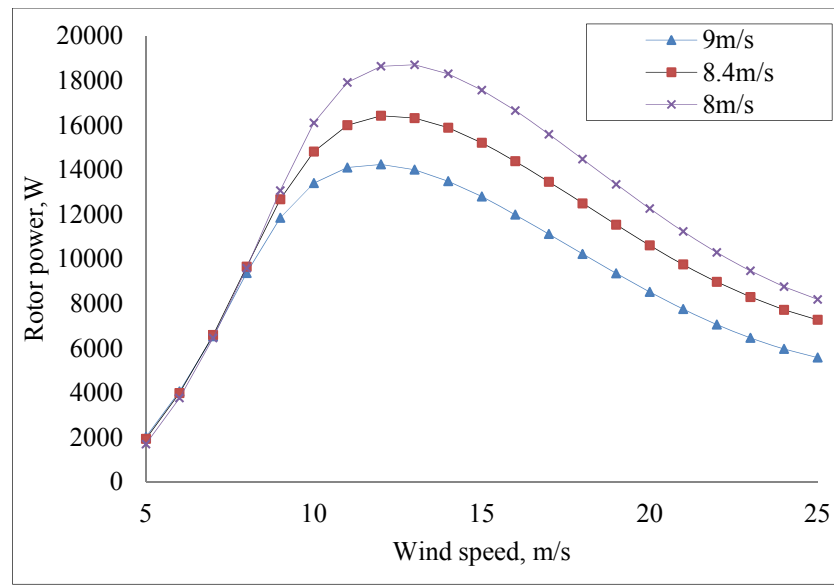
Figure 4-10 Power curves of different design wind speeds with fixed tip speed

With a fixed rotor radius of 4.5m and a fixed tip speed ratio of 7(to change the generator speed and not to change the blade shape), three design wind speeds are compared: 8m/s, 8.4m/s and 9m/s, which are corresponding to rotor speed of 118.8RPM, 124.8RPM and 133.7RPM respectively. Figure 4-11 presents the power curves of different design wind speed with fixed tip speed ratio. With a lower RPM, the power curve is flatter but less rotor power is generated at high wind speeds. With a higher RPM, the power curve is sharper and much higher power is produced by the rotor at high wind speeds.
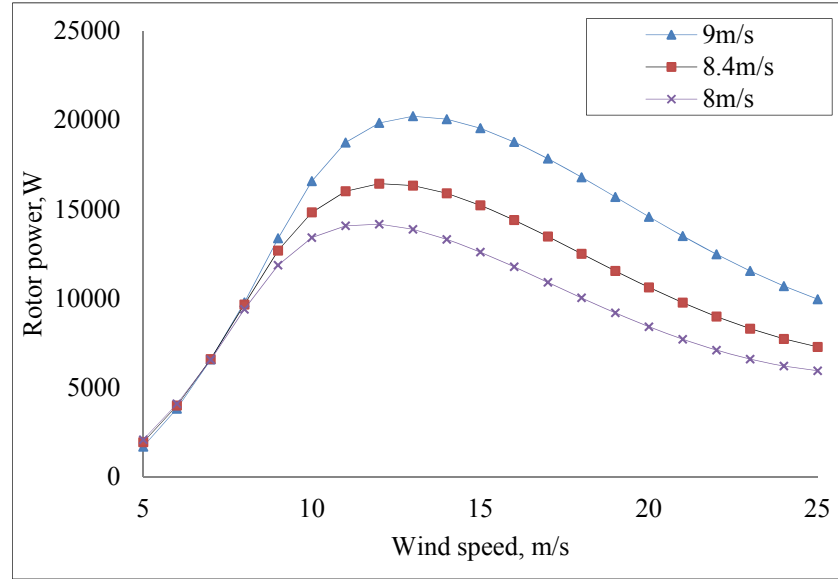
Figure 4-11 Power curves of different design wind speeds with fixed TSR

The AEP for the FPFS wind turbine is calculated in MATLAB according to the following equation:

$$\text{AEP} = 8760 \cdot \eta \int_{\text{cut in}}^{\text{cut out}} \text{P}(v) f_{\text{Rayleigh}}(v)\, dv \qquad (4.9)$$

where,

η is mechanical and electrical efficiency, which is a constant of 0.8;

$P(v)$ is the rotor power curve;

$f_{\text{Rayleigh}}(v)$ is the annual wind speed Rayleigh distribution as defined in (4.8).

Note the AMWS is 6m/s here.

Figure 4-12 presents AEP versus different design wind speed. AEP increases with design wind speed for the FPFS wind turbine. However, the higher AEP is mainly due to the higher power output at high wind speeds as described above. Considering the maximum power limits of the wind turbine generator, the design wind speed is selected at 8.4m/s with an annual mean wind speed (AMWS) of 6m/s.
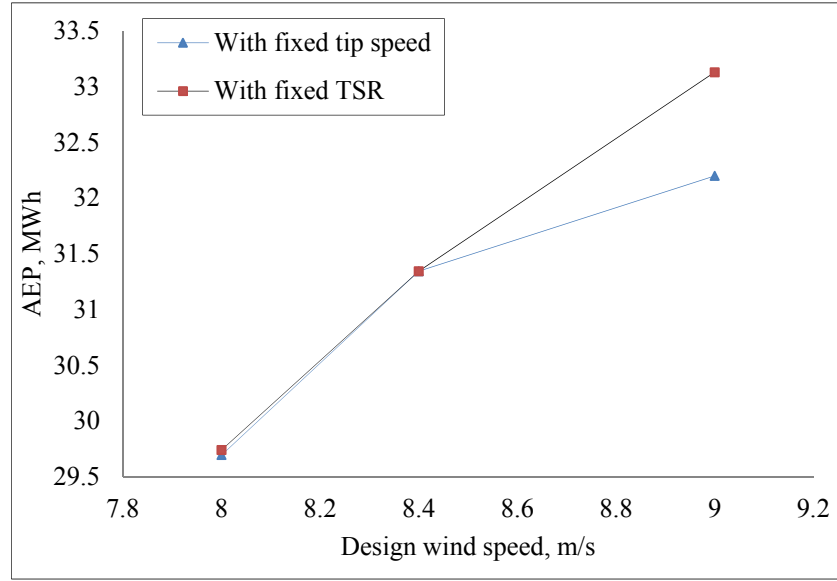
Figure 4-12 AEP versus design wind speed

4.3.2. Blade Chord and Twist Angle Distributions

4.3.2.1 Blade Design with F and Drag Effect

To obtain the blade chord and twist angle distributions, the tip-hub loss factor (F) and drag effect are ignored in the standard BEM blade design equations, i.e. equations (4.5) and (4.6), and these are only included in power performance analysis. This is acceptable since the drag is very small for many airfoils, especially for large wind turbine blade airfoil at high Reynolds numbers. However, the effect of the tip-hub loss factor on blade chord and twist angle distributions at blade tip and hub sections is considerable. This section presents a unique approach by searching for the optimal induction factors to include the tip-hub loss and drag effect in blade design. The comparison of with and without F and drag effect is discussed below.

The mathematical model [9] for wind turbine rotor aerodynamic performance analysis used here is described as:

$$a = \begin{cases} 1/[1+\dfrac{4F\sin^2\varphi}{\sigma\left(C_l\cos\varphi+C_d\sin\varphi\right)}], a<0.4 \\ (1/F)\left[0.143+\sqrt{0.0203-0.6427(0.889-C_T)}\,\right], a\geq 0.4 \end{cases} \tag{4.10}$$

$$a' = 1/[\dfrac{4F\sin\varphi\cos\varphi}{\sigma\left(C_l\sin\varphi-C_d\cos\varphi\right)}-1] \tag{4.11}$$

$$C_T = \sigma(1-a)^2 \left(C_l \cos\varphi + C_d \sin\varphi \right) / F \sin^2\varphi \qquad (4.12)$$

$$F = \left[2ar\cos(e^{-\frac{Z(R-r)}{2R\sin\varphi}}) / \pi \right] * \left[2ar\cos(e^{-\frac{Z(r-r_h)}{2r_h\sin\varphi}}) / \pi \right] \qquad (4.13)$$

$$C_p = \frac{8}{N\lambda} \sum_{i=1}^{N} F \sin^2\varphi_r (\cos\varphi_r - \lambda_r \sin\varphi_r)(\sin\varphi_r + \lambda_r \cos\varphi_r)(1-(\frac{C_d}{C_l})\cot\varphi_r)\lambda_r^2 \qquad (4.14)$$

Where, Z is the number of blades, σ is local solidity which is defined as $\sigma = ZC/2\pi r$, C_T is the thrust coefficient, C_p is the power coefficient, F is the tip-hub loss factor, C_l C_d are the lift and drag coefficient respectively, R is the rotor radius, the subscript r indicates local properties, the subscript h indicates hub properties, φ is the relative angle of wind.

4.3.2.2 MATLAB Routine

To include the tip-hub loss and the drag effect in the optimal blade design equations, a new strategy is introduced here. Given a design tip speed ratio, an optimal blade is optimal at each section to have a maximum power coefficient. Thus, the induction factors are optimal at these sections. According to this principle, if the optimal induction factors are solved to give a maximum Cp in power prediction equations including the tip-hub loss and drag effect, then the optimal blade sectional chord and twist angle can be calculated from these equations [9]:

$$\varphi_{r,op} = \tan^{-1}\left[\frac{U(1-a_{op})}{\omega r(1+a'_{op})} \right] = \tan^{-1}\left[\frac{1-a_{op}}{(1+a'_{op})\lambda_{op}} \right] \qquad (4.15)$$

$$\theta_{r,op} = \varphi_{r,op} - \alpha_{op} \qquad (4.16)$$

$$C_{r,op} = \frac{8\pi a_{op} Fr(1-a_{,op}F)\sin^2\varphi_{r,op}}{N(1-a_{op})^2(C_l\cos\varphi_{r,op}+C_d\sin\varphi_{r,op})} \qquad (4.17)$$

Where, the subscript op represents the optimal value.

Then the problem of searching for an optimal blade is converted to searching for the sectional optimal induction factors. Since induction factors are within the range from 0 to 1, it is able to search optimal values towards maximum Cp using MATLAB. The Nonlinear Constrained Minimization Function i.e. FMINCON is employed to search the optimal induction factors. The axial induction factor and tangential induction factor are the two variables. The objective function is a minus power coefficient including tip-hub

loss factor F. The equations (4.13), (4.15) and (4.19) are used as a nonlinear constraint.

$$Obj: Function = -C_p = -(8/\lambda^2)\int_0^\lambda a'(1-a)\lambda_r^3 Fd\lambda_r \tag{4.18}$$

$$NonLConstr: a'(a'+1)\lambda_r^2 = a(1-a)F \tag{4.19}$$

The blade design flow chart is shown in Figure 4-13. The fundamental rotor parameters were input by the user, and then the two optimal induction factors were calculated for each section by using nonlinear constrained minimization function. Based on the optimal induction factors, the optimal chord and twist angle can be determined for each section according to the equations (4.16-18).
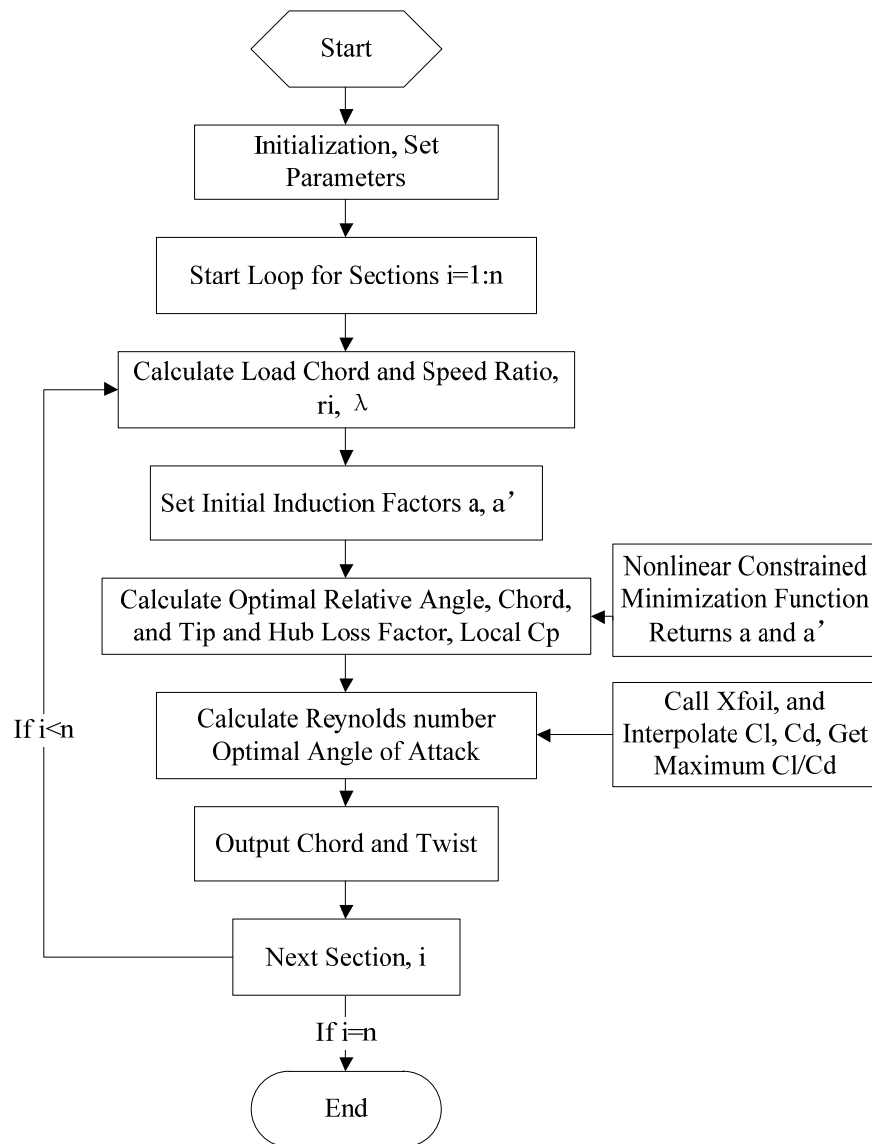
Figure 4-13 Blade optimal design flow chart

Figure 4-14 shows the user interface of blade design code developed by the author,

including rotor parameter inputs, blade chord and twist angle calculation, airfoil data calculation, power curve and power coefficient calculation and AEP calculation.
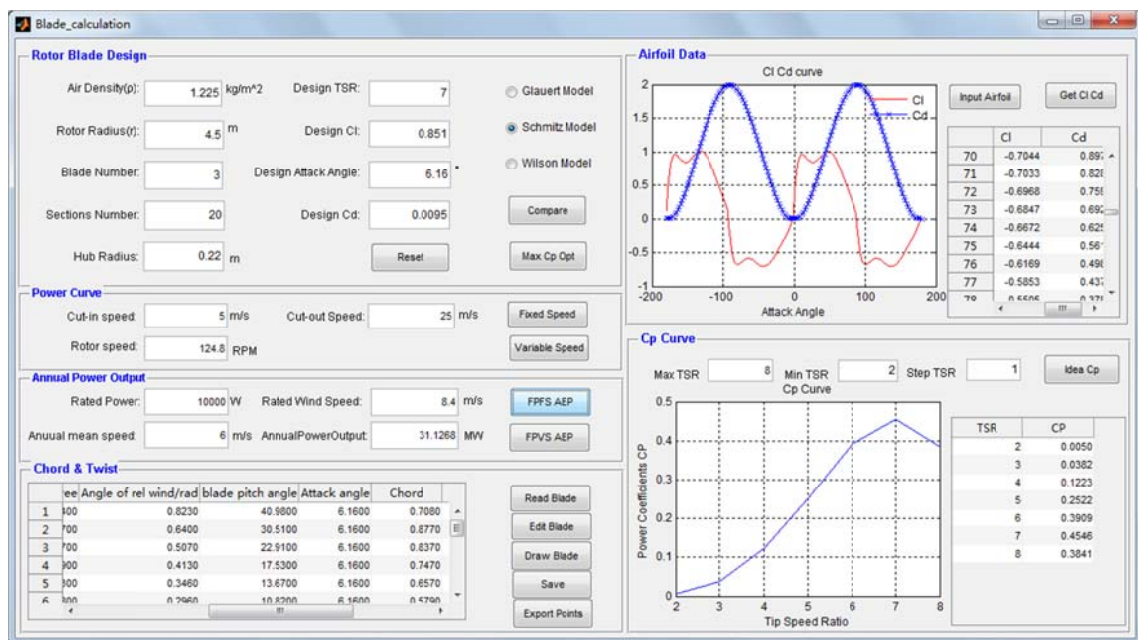
Figure 4-14 Blade design and analysis code user interface

4.3.2.3 Results and Discussion

(1) Chord and Twist Angle Distributions

The optimal blade chord and twist angle distributions with and without the tip-hub loss and the drag effects are presented in Figure 4-15. Results show that the drag has negligible influence on blade design, while the tip-hub loss factor (F) has apparent effects on both the chord and twist angle at the root and tip positions. Differences of chord and twist angle distribution occur at the 0.05R hub position and 0.95R and 1R tip positions when F and drag were included. The chord reduced to zero from location 0.95R to 1R when F and drag were considered. However, the chord and twist angle distributions of main part of the blade (from 0.15R to 0.9R) with F and drag are almost the same as those without F and drag. These results led to the conclusion that the drag has very small effect on blade chord and twist angles and the tip-hub loss bring visible effect on both blade chord and twist angles at the hub and tip sections. The blade CAD model without F and drag is presented in Figure 4-16[9].

---

[9] It is noted that using the exact aerodynamic shape at root region may increase manufacturing difficulty, and it is usually represented by linear transition from airfoil section to cylinder root in industry. However, there are also examples in wind turbine industry, such the ENERCON E-70 wind turbine which has large root chords and twist angles. (More information can be found on websites www. enercon.de.)
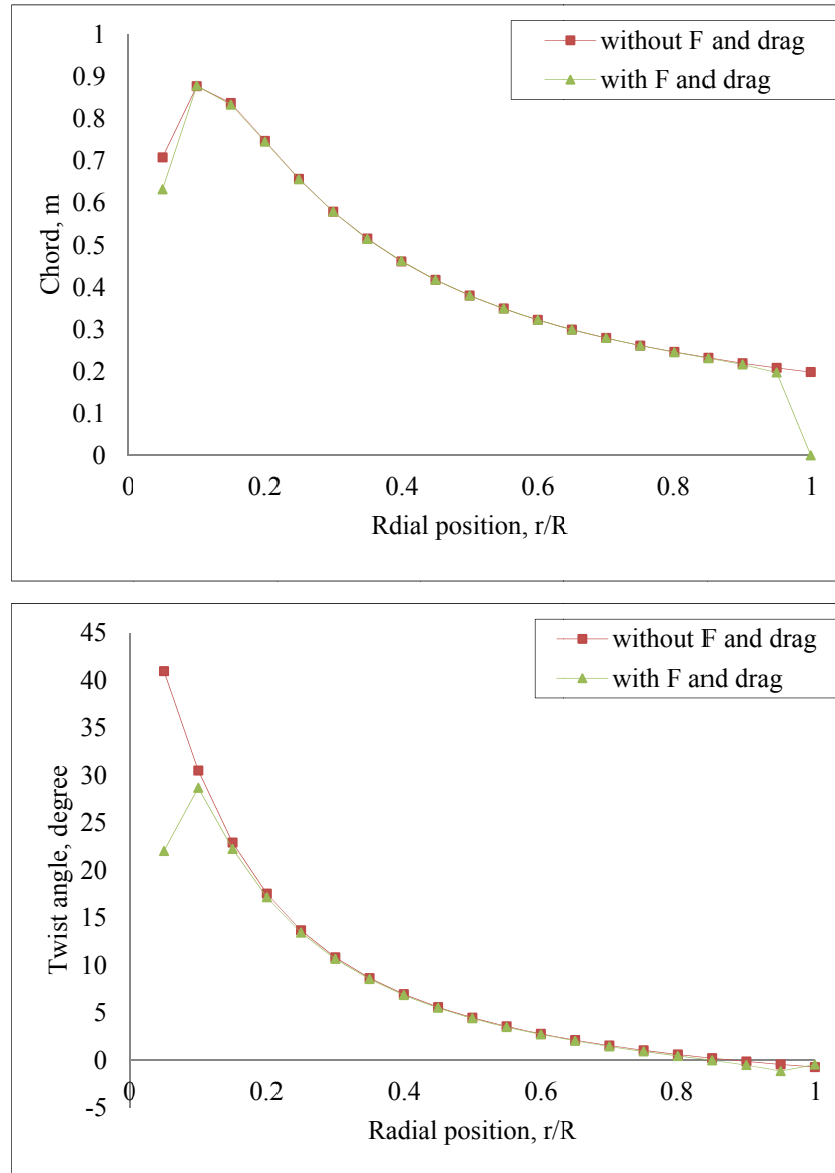
Figure 4-15 Blade chord and twist angle distributions with and without tip-hub loss and

drag
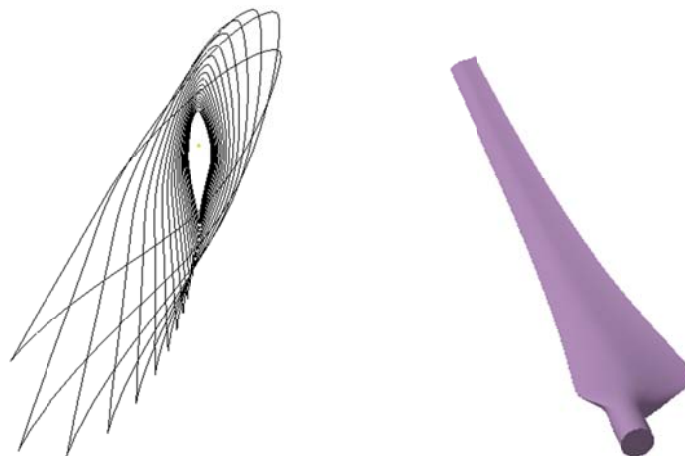
Figure 4-16 Section airfoils and blade CAD model of the FPFS wind turbine

(2) Axial Induction Factor and Angular Induction Factor

Figure 4-17 and Figure 4-18 show the local optimum axial and angular induction factors calculated in MATLAB. Without F and drag in the blade design, the optimum axial induction factor is almost constant along the blade span with an approximate value of 0.33. Considering F and drag in the blade design, the optimum axial induction factor deviates from 0.33 at the hub and tip regions. And larger angular induction factor occurs at the hub region for the blade design with F and drag. This reveals that for maximum power coefficient design with F and drag consideration, the optimum axial induction factor does not necessarily remain constant at the theoretical value of 0.33.
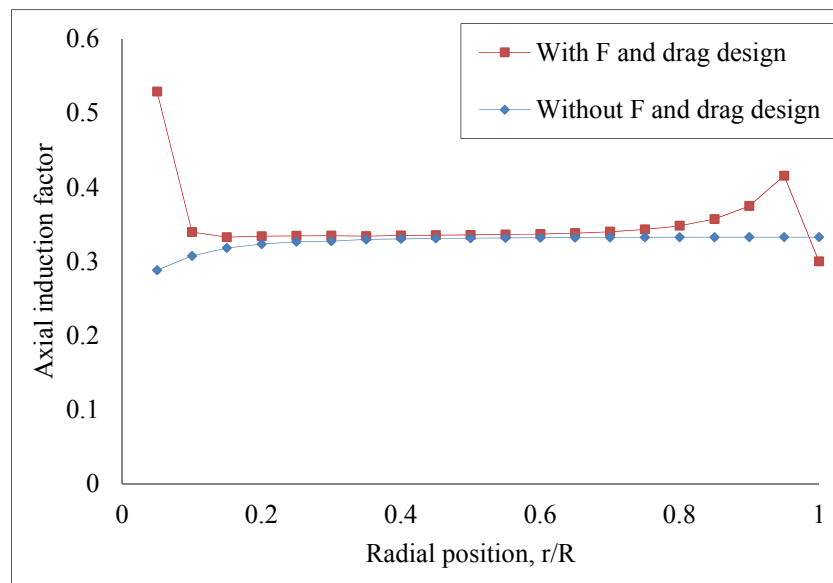
Figure 4-17 Local axial induction factor
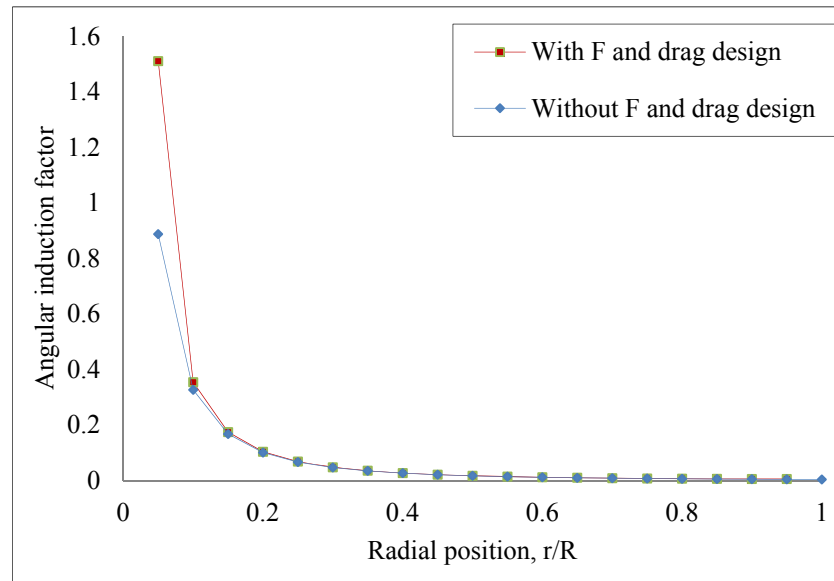
Figure 4-18 Local angular induction factor

4.3.3. Power Curve

The rotor power coefficients and power curves of the blade design with and without *F* and drag are presented in Figure 4-19 and Figure 4-20. The two designs show very similar performance while the one with wider chord and larger twist angle at tip position presented slightly higher power output at high wind speeds. This is mainly due to the small drag (Cd at design angle of attack is 0.0095) and small hub radius (hub radius of 0.22m) in this case. Although the blade design method with *F* and drag did not bring big difference in this case, the approach is meaningful for blade root and tip region design.

It is worthwhile to mention that, for a stall-regulated fixed-pitch fixed-speed wind turbine, the power curve shows a drop above rated wind speed. This is because the power output cannot be controlled due to fixed speed.
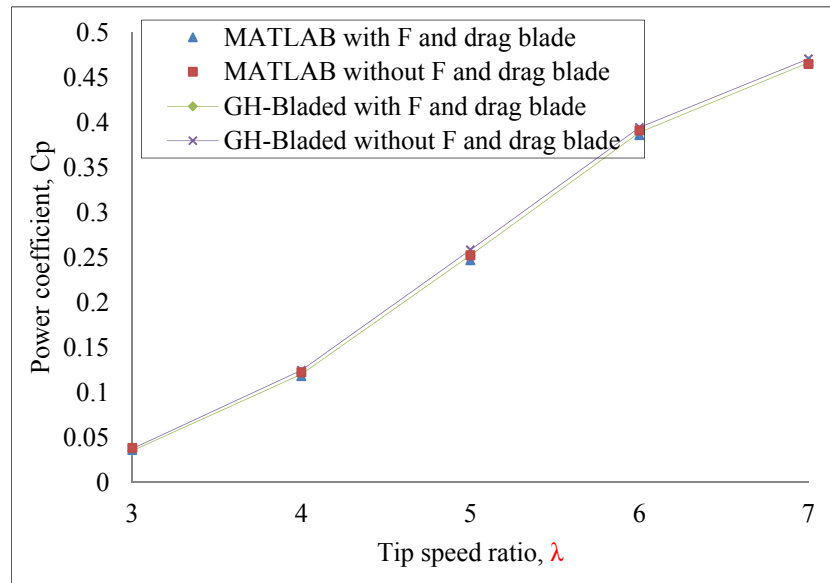
Figure 4-19 Rotor power coefficient comparison with 2D coefficients
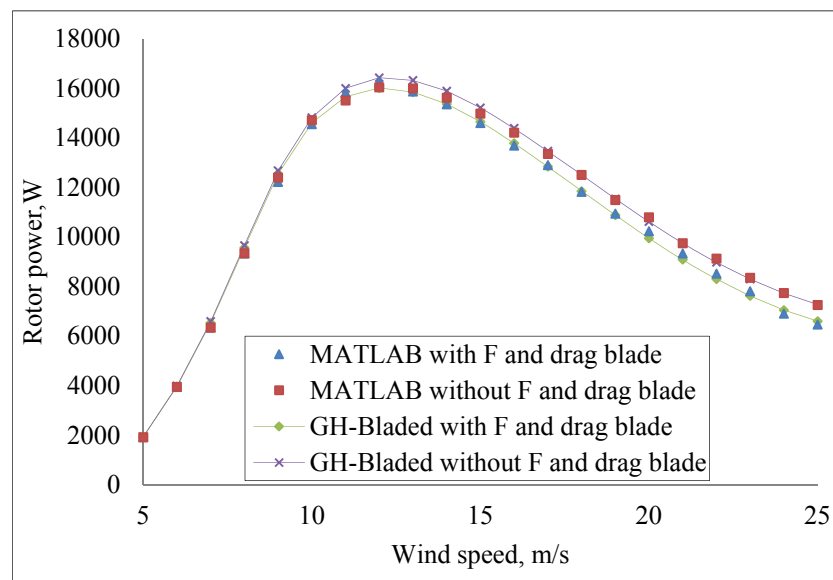
Figure 4-20 Rotor power curve comparison with 2D coefficients

4.3.4. Blade Linearisation Case Study

The theoretically optimal blade (that maximises power coefficient as described above) has large chord and twist angle at the root part. This feature is efficient but will increase complexity to manufacture thus is costly [9, 49]. For ease of manufacture, wind turbine blades can be linearised. Moreover, for small wind turbines, linearisation should be carefully considered to avoid poor starting problems. When the twist angle distribution is linearised, the twist angles at the inner sections are often smaller than the original

twist angles. At low wind speeds (starting), the attack angles are increased since the twist angles are reduced. For example, the wind turbine is standstill before starting; the attack angle may be increased from 50° to 70° at inner sections. Dual purpose design should be considered when the turbine rotor is started by itself. Wood presented a small wind turbine design taking minimum starting time and maximum Cp as dual purpose considerations [99]. Due to lack of airfoil coefficients at extremely low Reynolds number and high angle of attacks, research on wind turbine starting is a very tough task. As an alternative option, most cases induction generator wind turbine takes generator as a motor to make a self-starting. Considering self-starting, the wind turbine starting problem is not considered here.

In wind turbine industry, blade linearisation has been a general practice to minimise the manufacturing cost. There are different ways for the chord and twist angle linearisation. Maalawi [34] suggested that the linearised chord line should be the tangent line to the theoretical distribution at 0.75R span position while the twist angle distribution should be an exponential distribution. Tony Burton [49] drew a straight line through the points of theoretical chord distribution at span position of 0.7R and 0.9R to linearize the chord. Manwell [9] gave a general linear form of chord and twist angle linearisation by using two constants in chord approximation expression and one constant in twist angle approximation expression. Azad [100] linearised the blade chord and twist angle distributions between span position of 0.5R and 0.9R. These studies demonstrate different ways to linearize the blade chord distribution; however an insight of the linearisation is still needed to justify and guidance is highly expected. Three questions have to be answered: (1) to apply linearisation on both chord and twist angle distribution or only chord distribution; (2) what positions should be remained; (3) how does the linearisation affect power curve at low wind speeds and high wind speeds. To answer these questions, the following paragraphs investigate the blade linearisation based on the optimal blade discussed above (original baseline blade)[10].

The local power coefficient varies along the span of the blade. Figure 4-21 plots the power coefficient distribution along the original blade span calculated in MATLAB. The *Cp* appears a linear increase with span position except the blade tip positions from 0.9R to 1R. The blade outer span elements (from 0.5R to 1R) contribute more *Cp* than the

---

[10] The blade designed without F and drag was used as the baseline blade for linearisation.

inner span elements (from 0.05R to 0.5R). The elements at positions close to the blade root contribute less *Cp* than those at the middle and close to the blade tip. As it was stated by Seki [101] that 80% energy production comes from the sections at 30% to 95% position of radius, these outer sections should be carefully designed according to the theoretical chord and twist angle distributions. This *Cp* distribution provides an initial guideline for linearisation. Meanwhile, to avoid lager amount of material, it is reasonable to remain the outer parts of the blade rather than inner parts (large chords occur at inner positions).
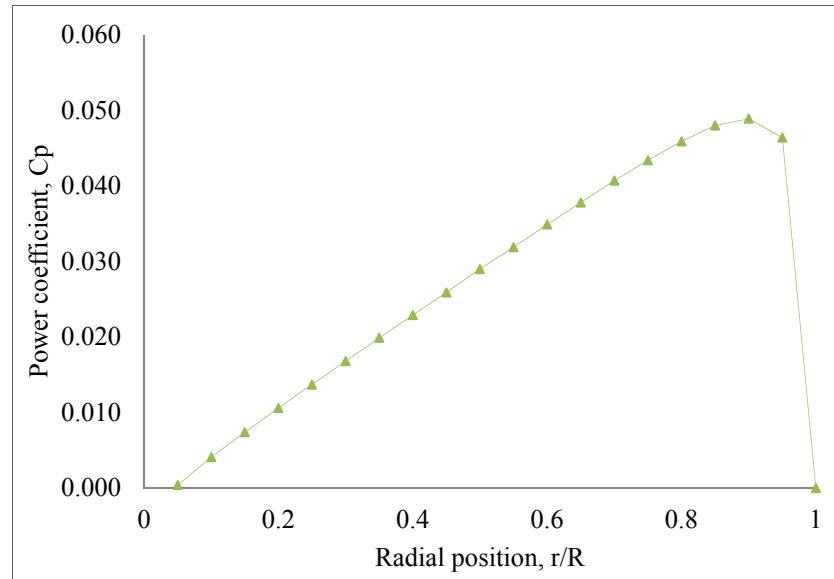
Figure 4-21 Power coefficient distribution along the original baseline blade span

Based on the original chord and twist angle distributions presented in the above Section 4.3.3, three linearised blade cases are discussed as listed in Table 4-6:

Cases	Chord	Twist
Case A	Linearised at r/R of 0.7 and 0.9	Original
Case B	Linearised at r/R of 0.7 and 0.9	linearised at r/R of 0.7 and 0.9
Case C	Linearised at r/R of 0.5 and 0.9	Linearised at r/R of 0.5 and 0.9

Table 4-6 Blade linearisation case definition

Figure 4-22 presents the chord and twist angle distributions of the linearised blades and the original theoretical blade. Twenty blade elements are used for the calculation. The linear expressions based on positions of 0.7R and 0.9R are:

$$c = -0.3 \cdot r + 0.489 \tag{4.20}$$

$$\theta = -8.4 \cdot r + 7.41 \tag{4.21}$$

The linear expressions based on positions of 0.5R and 0.9R are:

$$c = -0.4025 \cdot r + 0.58125 \qquad (4.22)$$

$$\theta = -11.5 \cdot r + 10.245 \qquad (4.23)$$
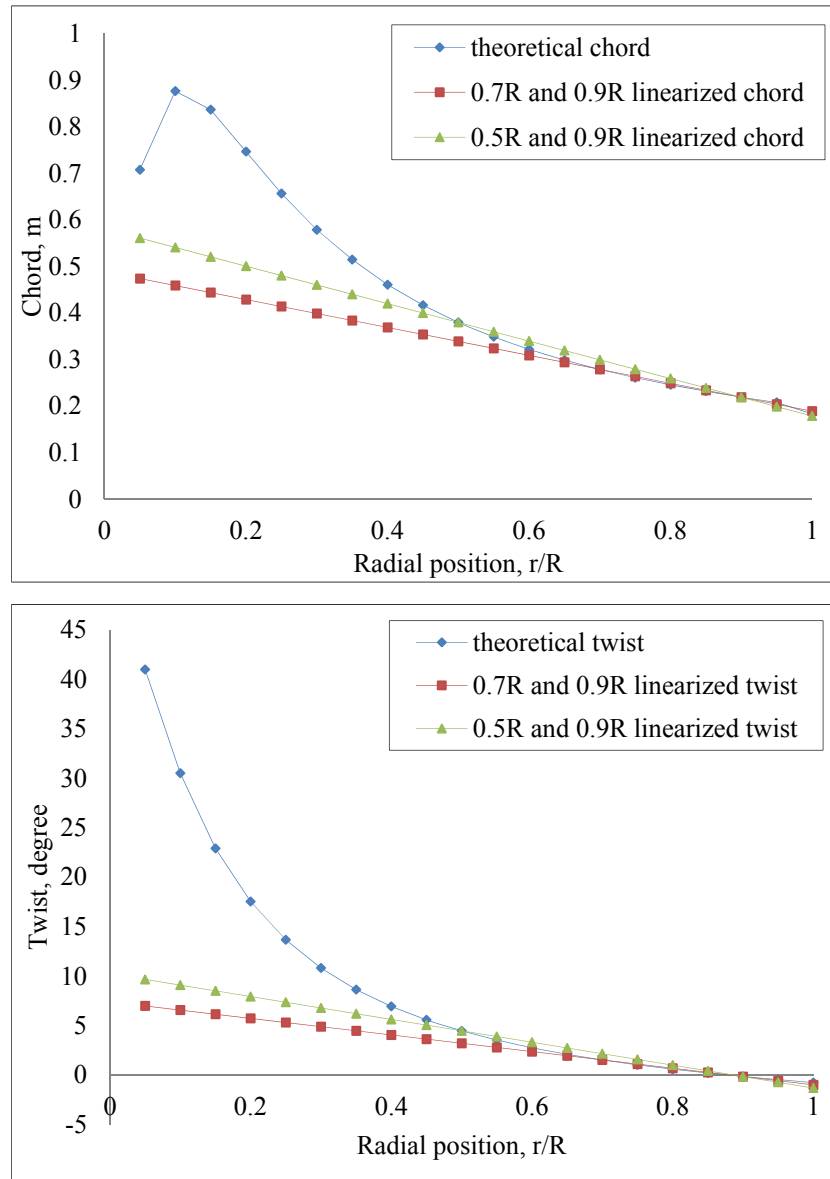
Figure 4-22 Chord and twist angle distributions of the linearised blades and the original theoretical blade

Figure 4-23 plots the power coefficient curves of the modified blades and the original theoretically optimal blade. Linearisation both chord and twist angle at positions of 0.7R and 0.9R has slightly smaller max Cp than linearisation at positions of 0.5R and 0.9R (Case C is better than Case B). Only linearisation of chord proves to be the best solution regarding to maximum Cp (The max Cp of Case A is higher than those of other two cases) and less material (smaller chord). Both linearisation of chord and twist

presents smaller max *Cp* than only linearisation of chord (Case A is better than Case C). The twist angle proves to be more important to maximize *Cp*.

Figure 4-24 presents the power curves of linearised blades and original blade. Given an annual wind speed of 6m/s, the AEP is calculated according to equation (4.9) in MATLAB. The cut-in wind speed is 5m/s and the cut-out wind speed is 25m/s. The material is represented by summary of the chord values of twenty sections. The AEP and summary of the chord values of these three linearised cases and the original blade are plotted in Figure 4-25 and Table 4-7. Considering less material and higher AEP, Case A provides the best approach for blade linearisation.
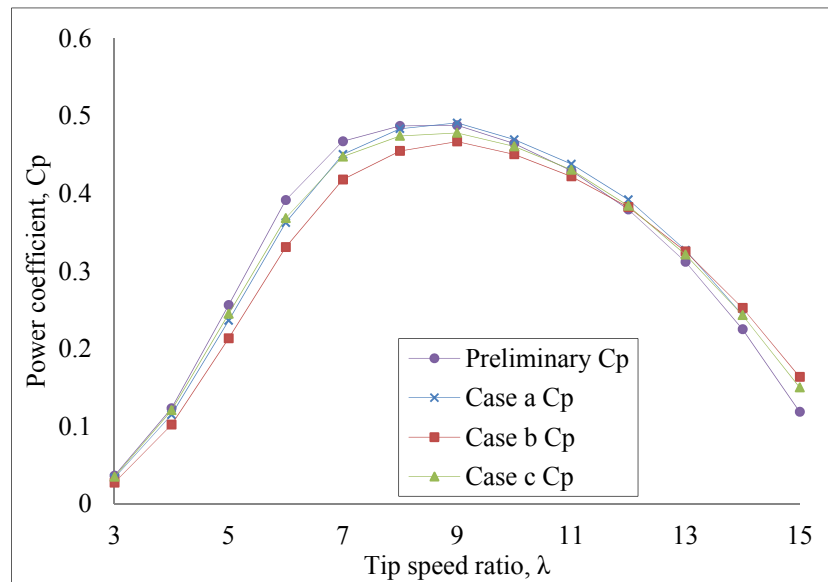
Figure 4-23 Power coefficient curves of the modified and theoretical optimal blades
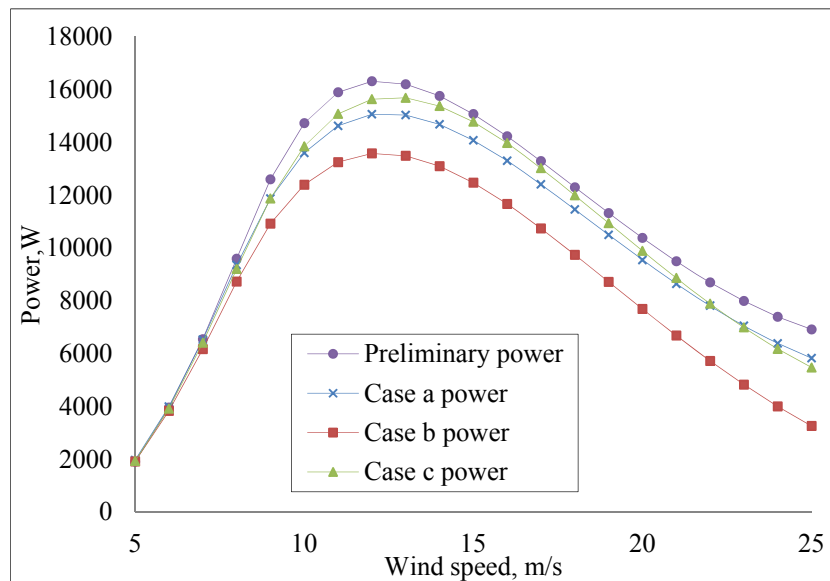
Figure 4-24 Power curves of the modified and theoretical optimal blades
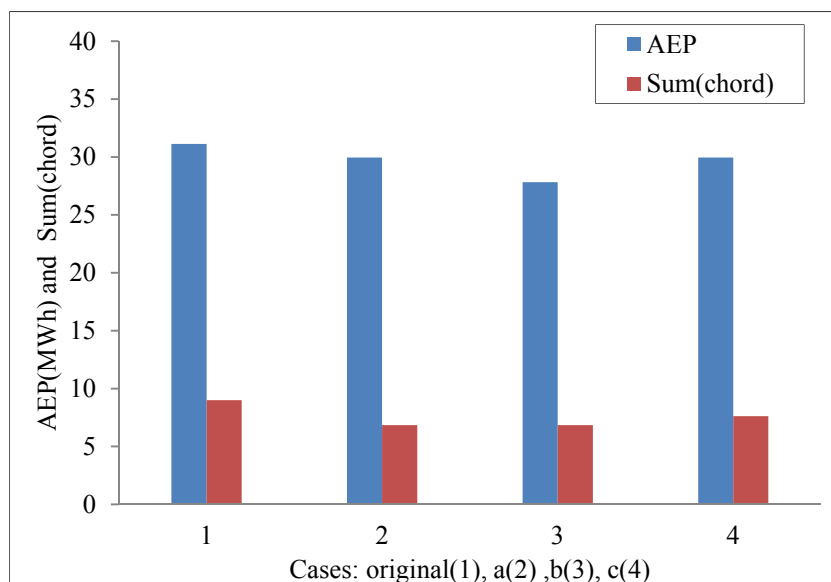
Figure 4-25 AEP and material of linearisation cases

	AEP(MWh)	Chord Sum(m)
Preliminary	31.127	8.994
Case A	29.957	6.848
Case B	27.821	6.848
Case C	29.955	7.618

Table 4-7 AEP and chord sum of linearisation cases

4.3.5. A Heuristic Approach for Maximum AEP Blade Linearisation

The above studies demonstrate different ways to linearize the chord and twist angle distributions. The original chord and twist angle distributions are based on a particular design wind speed and design TSR. Since the TSR varies with wind speed for a FPFS wind speed, the originally optimized chord and twist angle distributions may not necessarily provide the best power performance for the wind turbine at a particular site, i.e. for a particular wind speed Rayleigh distribution. Therefore, adjusting the chord and twist angle distributions may offer an opportunity to optimise the wind turbine blade design so as to achieve a further optimised power performance, apart from low manufacturing cost. This section demonstrates a heuristic approach for the blade design optimization through linearisation of both the chord and twist angle distributions, the calculated results show an increase in AEP with linearised blade chord and twist angle distributions. The base wind turbine used for this study is the 12kW FPFS wind turbine with the S809 airfoil.

4.3.5.1 Methodology

The chord and twist angle of the preliminary blade design are nonlinear distributions, as shown in Figure 4-15. The value of the chord and twist angle decreases gradually from the blade root to the blade tip. In this section, the method[11] of linearisation of the chord and twist angle distributions is fixing the chord and twist angle at the blade tip and changing the value at the blade root, which results in sets of linearised chord and twist angle distributions (in the form of a matrix). The optimal linearised chord and twist angle distributions are determined based on the criterion of maximum annual energy production (AEP) for a wind speed Rayleigh distribution with an annual mean wind speed (AMWS) of 6m/s. To fix the chord and twist angle at the blade tip and change the value at the blade root to linearize chord and twist angle distributions, the following equations are used:

$$c_{i,n} = c_{t,0} + (0.7c_{r,0} - c_{t,0})\frac{(n-1)}{N}\frac{r_i}{R}, \quad n = 1, 2, ..., N+1 \qquad (4.24)$$

---

[11] There are other ways to do so, this section aims to demonstrate the optimization strategy, and is not intended to try all the other different ways.

$$\theta_{i,n} = \theta_{t,0} + (\theta_{r,0} - \theta_{t,0})\frac{(n-1)}{N}\frac{r_i}{R}, \quad n = 1, 2, ..., N+1 \tag{4.25}$$

where

n is the n th linearised chord line,

$c_{i,n}$ is the chord at the i th blade element of the nth linearised chord line,

$\theta_{i,n}$ is the twist angle at the i th blade element of the nth linearised twist line.

Note here, $c_{t,0}$ and $c_{r,0}$ are the chords at blade tip and root of the preliminary blade respectively, $\theta_{t,0}$ and $\theta_{r,0}$ are the twist angles at the blade tip and root of the preliminary blade respectively, N is the number of division.

4.3.5.2 Results and Discussion

(1) Linearised Chord and Twist Angle Distributions

Assuming the number of division $N = 18$ for equation (4.24) and $N = 30$ for equation (4.25), 589 combinations with 19 choices of chord distribution lines and 31 choices of twist angle distribution lines are shown in Figure 4-26 and Figure 4-27. For each linearisation case, in order to reduce calculation time, only 10 blade elements instead of 20 (as used in the above section) are used to calculate the power performance. The calculated power output is slightly lower than using 20 elements but it does not affect the comparison study.
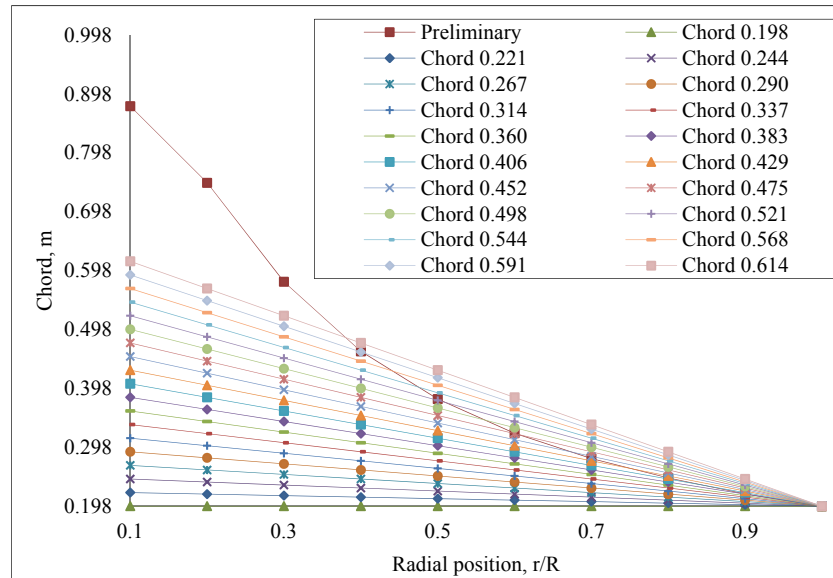
Figure 4-26 Choices of chord linearised distribution lines
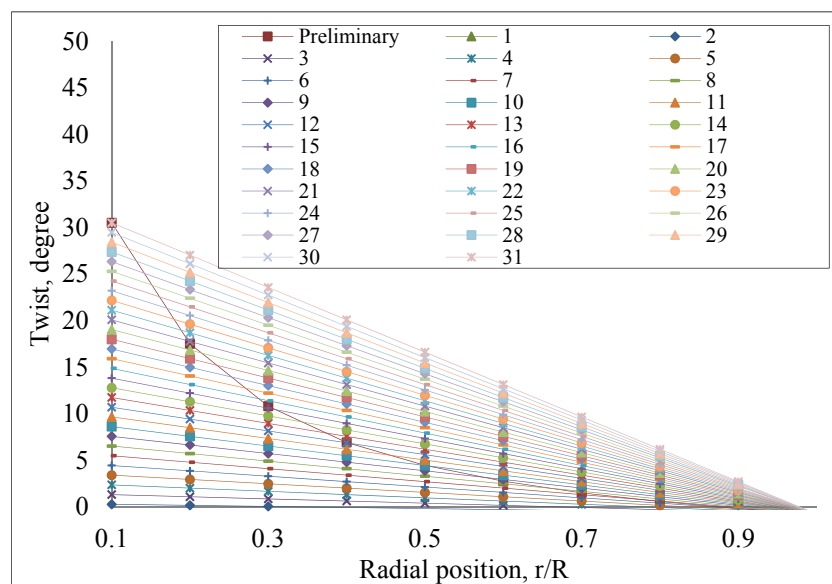
Figure 4-27 Choices of twist angle linearised distribution lines

Figure 4-28 illustrates the AEP of the 589 combinations of the wind turbine blade design for an AMWS of 6m/s, which are calculated according to Equation (4.9). It is shown that the relationship between the AEP and the blade root twist angle appears similar to a parabolic curve. Overall, the AEP is maximized when the blade root twist angle is about 14.8º. When the blade root chord is larger than 0.406m (approximately 60% of the maximum chord of the preliminary blade), the AEP of the linearised blade is higher than that of the preliminary blade (35.65MWh). Moreover, the AEP increases with the blade root chord for all linearised twist angle distribution. However, due to the overloading constraint of the generator, the blade root chord can only be limited to assure that the power output of the generator is not exceeding the maximum power of overloading. Figure 4-29 illustrates the estimated material of the preliminary blade and the linearised blades, which is represented by the sum of the chords. The linearised blades have smaller chord and twist angle than the preliminary blade, which indicates reduced materials and manufacturing cost.
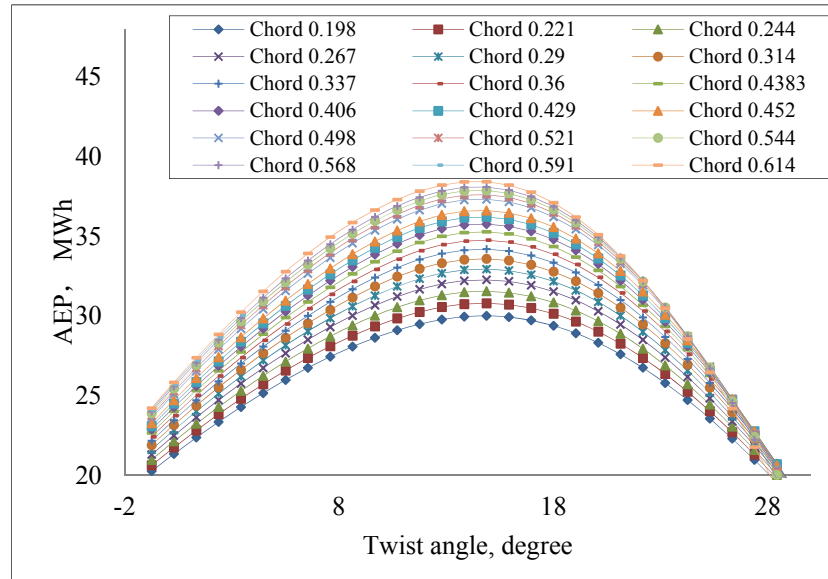
Figure 4-28 AEP of the 589 design solutions for AMWS of 6m/s
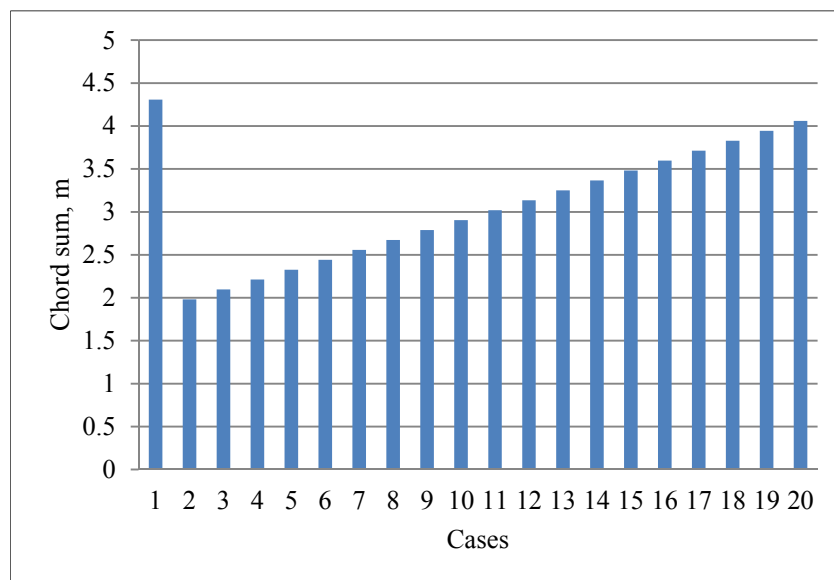
Figure 4-29 Comparison of the sum of the chords: the preliminary case (No.1) and 19 linearised chord cases (No.2 to No.20)

In this case, the baseline wind turbine is a 12kW wind turbine, the maximum overloading of the generator is assumed to be 120% (i.e.14.4kW). With a system efficiency of 0.8, the maximum rotor power should be limited to 18kW, which should be considered as a constraint for the blade design optimization. The chord and twist angle distributions of the optimal blade and these of the preliminary blade are depicted in Figure 4-30 and Figure 4-31. The blade root chord is 0.475m and the root twist angle is 12.8°.
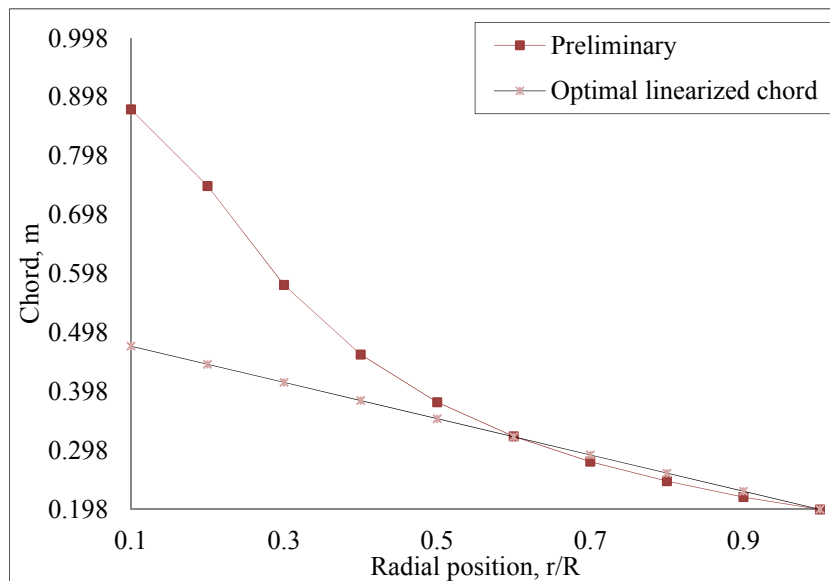
Figure 4-30 Chord distributions of the optimal blade and preliminary blade
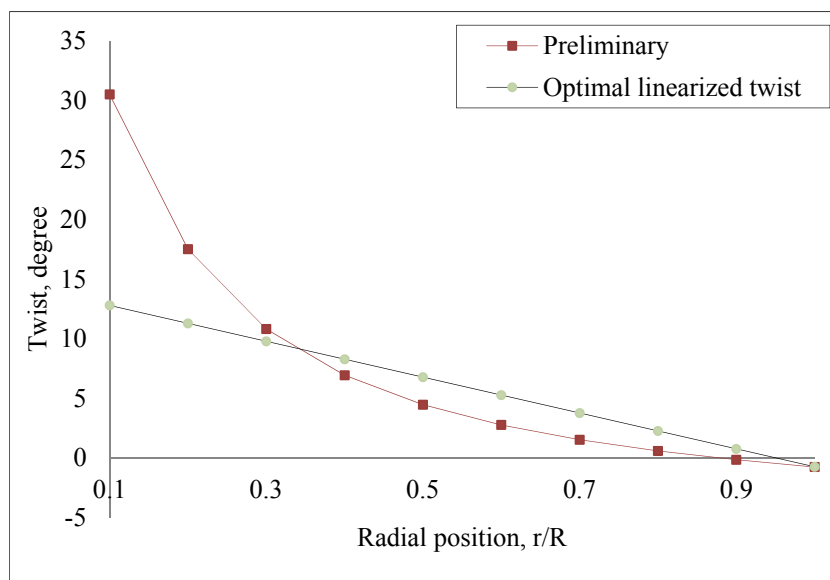
Figure 4-31 Twist angle distributions of the optimal blade and preliminary blade

(2) Power Curve, Power Coefficient and AEP

Figure 4-32 compares the calculated power coefficients of both the preliminary blade and the optimal linearised blade. The optimal linearised blade has a wide "flat top" power coefficient curve, which is desirable for the wind turbine. And the optimal blade shows a higher power coefficient compared with the preliminary blade at all tip speed ratios.
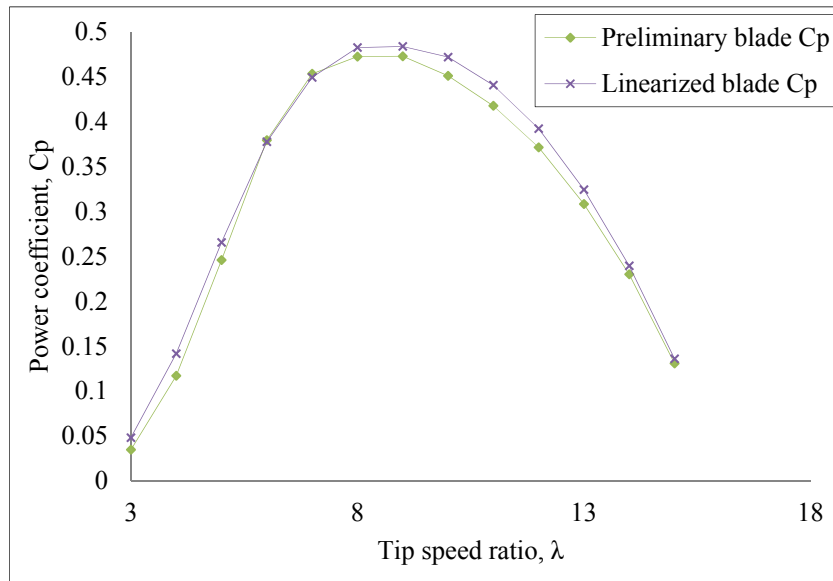
Figure 4-32 Power coefficient of the optimal blade and the preliminary blade

The calculated power curves of the wind turbine rotors with preliminary blades and the optimal linearised blades are shown in Figure 4-33. The outcome demonstrates that the power output of the optimal linearised blade is higher than that of the preliminary blade. It also shows that the top rotor power is 17.6kW, which happens at wind speed 14m/s and is within the 120% overloading limit.
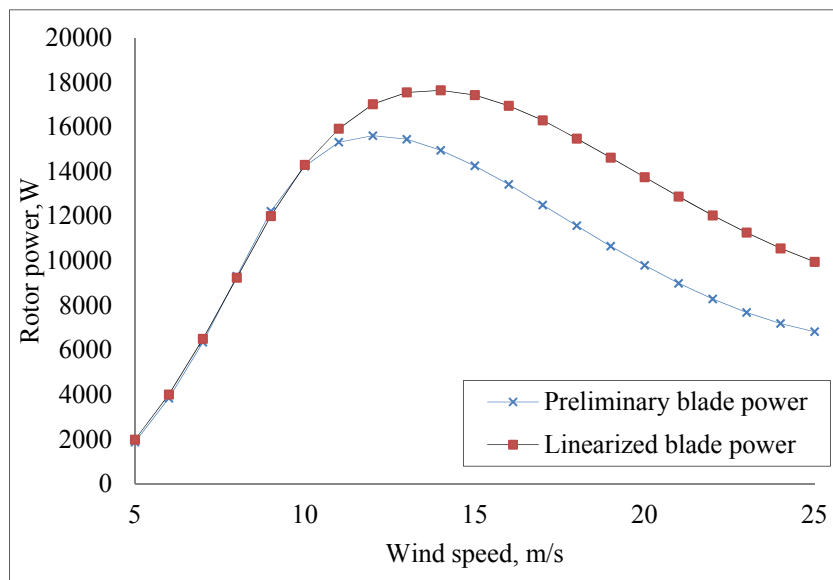
Figure 4-33 Rotor power output of the optimal blade and the preliminary blade

The calculated AEP of the wind turbine with the optimal (linearised) blade and preliminary blade is shown in Table 4-8. The results demonstrate that there is a significant increase of the AEP of the optimal blade design for the whole range of

annual mean wind speed from 5.0m/s to 8.0m/s.

AMWS (m/s)	AEP (MWh)_Preliminary blade	AEP (MWh)_Linearised blade	Increase rate
5	18.3174	18.6596	1.87%
6	30.1214	30.8609	2.46%
7	41.6814	43.247	3.76%
8	51.8679	54.6957	5.45%

Table 4-8 AEP of the linearised blade and preliminary blade

In summary, this section presents a heuristic approach for the blade design optimization through linearisation of both the chord and twist angle distributions for fixed-pitch fixed-speed small wind turbines by case study of a 12kW FPFS wind turbine with S809 airfoil. Linearisation of the chord and twist angle distributions with fixed values at the blade tip from a preliminary blade design offers a promising optimisation strategy for FPFS wind turbine blade design with improved power performance, and reduced both materials and manufacturing cost. With consideration of the constraints of the maximum rotor power, an optimal blade design is achieved through linearisation of the chord and twist angle distributions with fixed values at the blade tip. The optimal design achieves an AEP increase 2.46% for AMWS of 6m/s than the preliminary design with a reduced materials and manufacturing cost. This method can be used for any practice of fixed-pitch fixed-speed wind turbine blade design. It could also be utilised for wind turbine blade refurbishment based on an existing baseline wind turbine, which uses the existing gearbox and generator with fixed rotor speed.

4.4 Summary

This chapter investigated the BEM blade design philosophy through two most typical wind turbines: a fixed-pitch variable-speed (FPVS) wind turbine and a fixed-pitch fixed-speed (FPFS) wind turbine. The effects of the key rotor parameters on power curve and AEP were thoroughly studied. These parameters are determinative to wind turbine performance.

The tip-hub loss and drag effect were compared with the standard BEM method and presented through the blade design case study for a 12kW FPFS wind turbine. A unique approach of searching optimal induction factors was developed in MATLAB code to obtain the optimal blade chord and twist angle distributions. Results show that the

tip-hub loss factor F and drag have apparent effects on blade hub and tip region. With F and drag considerations, smaller blade chord and twist occur for hub and tip regions. The drag, tip and root loss effects are included in BEM design codes in the form of power performance analysis/assessment. The blade chord and twist angle distributions are derived from the equations ignoring drag, tip and hub loss in the standard BEM methods. In this section, those effects can be included in the initial calculation of blade chord and twist angle distributions. This research is of particular importance for blade tip and hub design and improvement.

Linearisation strategies of blade chord and twist angle distributions were firstly investigated through case studies. The un-linearised twist angle strategy (only chord is linearised) show higher power production compared with the linearised twist strategy (both twist and chord are linearised). This is an informative conclusion when other aspects are considered in linearisation. Considering less materials and relatively higher AEP, it is preferable to linearize the chord according to the points at outer span positions. Considering small twist range thus less manufacturing cost, the blade twist distribution is also linearised. A heuristic approach of blade design optimization through linearisation of both the chord and twist angle distributions for FPFS small wind turbines was developed. This approach can be used in any practical wind turbine linearisation and refurbishment.

To further investigate wind turbine airfoil characteristics and power performance, the CFD based approach is discussed in the Chapter 5.

CHAPTER 5   CFD BASED MODELLING AND VALIDATION

5.1   Introduction

The computational fluid dynamics (CFD) approach has been used to model and analyse the aerodynamic behaviour of wind turbines, the detailed flow field characteristics around a rotating wind turbine rotor/blade as well as the power performance can be obtained by the CFD approach [8;62;65;72;73;75;102-111].With the increasing computing capacity, the CFD approach is becoming a practical tool to model and simulate wind turbine aerodynamic performance in three dimensional spaces and instantaneous time domain [78].

In this chapter, 2D CFD and 3D CFD simulations are conducted for the S809 airfoil and NREL/NASA Phase VI wind turbine. The S809 airfoil is a well-tested airfoil in high quality wind tunnels and the airfoil aerodynamic data are available in literature. The 2D airfoil modelling was performed to study the turbulence models and mesh topologies, and the work is presented in Section 5.2. The Phase VI wind turbine was tested in the NASA Ames 80×120 feet wind tunnel under different operational conditions, and detailed measured data were published. This provides a great opportunity to study the wind turbine aerodynamics from 2D to 3D. Based on the 2D airfoil CFD modelling in Section 5.2, the 3D CFD modelling of the Phase VI turbine is presented in Section 5.3, where the 3D CFD approach is validated against the published measured data.

5.2   Two-Dimensional CFD Modelling and Validation

As discussed in Chapter 2, the main concerns of solving CFD problems using the existing Reynolds Averaged Navier-Stokes (RANS) codes are turbulence models and mesh topologys. The 2D airfoil modelling is used to study the sensitivities of turbulence models and mesh topologys. The Large Eddy Simulation (LES) codes and Detached Eddy Simulation (DES) codes are out of scope in this research due to limited time and

available resources. The airfoil S809 is analysed and compared with the documented wind tunnel test data [80]. The Reynolds number is one million, the same chord and wind speed in the wind tunnel test are used in the CFD model and simulation, which are 0.6m and 25m/s respectively. The turbulence models and mesh topologies are discussed in the following section.

5.2.1. 2D CFD Method

5.2.1.1 Turbulence and Transition Models

The RANS CFD approach has been widely used in airfoil flow field simulations. Many turbulence models have been developed to model the flow field around airfoil, such as: Spalart-Allmaras (S-A) model, standard k-epsilon (k-ε) model, k-omega (k-ω) model, and Shear Stress Transport (SST) k-ω model. Using the S-A turbulence model and a two dimensional (2D) mesh, five different Reynolds numbers from 1.25×10^5 to 9.05×10^5 were investigated for S1223 airfoil, and it was found that the maximum lift to drag ratio and the stall angle decrease with a reduction of the Reynolds number[112]. Wolfe [108] developed a 2D CFD model to calculate the flow field and aerodynamic coefficients of S809 airfoil and concluded that the standard k-ε turbulence model was not appropriate to model the flow separation on the suction surface of the airfoil. Guerri [113] compared the SST k-ω model and the Renormalization Group (RNG) k-ε model, their results confirmed that the SST k-ω model can provide satisfactory solutions for turbulent flows. Villalpando [68] reported that the SST k-ω model has a better agreement with experimental results than other turbulence models such as the S-A model, the k-ε model and the Reynolds Stress Model (RSM). Freudenreich [69] studied both by experiments and CFD modelling using the standard k-ω and SST k-ω models for DU97-W-300, and concluded that the Menter's SST transition model [73;75] could improve the agreement with experiments. Catalano [72] suggested to use the SST k-ω model with an imposed transition location which was 10% offset downstream from the predicted point of a fully turbulent model. Bertagnolio [92] compared the fully turbulent model, fixed transition position model and simplified transition model in terms of 2D or 3D simulations, Reynolds-Averaged Navier–Stokes (RANS) and Detached Eddy Simulation (DES). In his research, the SST k-ω model and the transition model showed good agreements in the linear region for S809. The conclusion can be drawn from the above literature

review that the transition position is crucial for accurate 2D CFD modelling under stall conditions.

More recently, to simulate the laminar to turbulence transition flow, a correlation based SST γ-Reθt transition model was developed by Menter [70]. And later a new local correlation-based transition model (LCTM) which was improved for natural and separation induced transition was presented [71]. Instead of using non-local variables to catch the transition phenomenon like turbulence models and without imposing transition location, the newly developed correlation based transition model was reported to have a promising accuracy in predicting transition flows. The Menter's transition model was investigated on the 2D S809 airfoil and better agreements have been achieved for angles of attack from 0° to 9°, and it was indicated that the difference at high angles of attack was likely to be caused by 3D flow effects, which 2D simulation cannot capture [75]. The same conclusion was made that the Menter's transition model can predict the transition flow and flow separation more accurately, but longer convergence time is needed [76]. Later on the Menter's correlations were further improved [73] and validated for low Reynolds number external flows [74], and it was reported that the transition SST model proved to be a more accurate model for the cases studied.

From the above analysis, it can be concluded that to model transition and turbulent flows of an airfoil, the most appropriate models are the SST k-ω model and the transition model. In this section, the SST k-ω model and the transition model are employed for S809 airfoil 2D CFD modelling and the results are compared and analysed. The boundary of the flow domain is defined large enough (15 times chord upstream and 20 times chord downstream from the airfoil) to avoid tunnel wall effects. The experimental data have been corrected including the tunnel effects; therefore, it is not needed to include the tunnel in the airfoil simulations. The flow domain inlet is defined as free stream velocity inlet and outlet is set as pressure outlet. The inlet turbulence intensity is set to the level of 0.02% as in the experiments. All the cases are solved in FLUENT. The convergence criterions for the absolute residuals of equation variables (i.e. continuity, x- and y-velocity, k, ω) are set below 10^{-5}.

5.2.1.2 Mesh topology and Mesh Size

The mesh quality and element/domain size of the 2D CFD model do affect the

computation accuracy and convergence time. A good mesh should be parallel with the streamlines of the flow and the domain size should be large enough to avoid boundary effects. There are many mesh topologies for airfoil CFD modelling. The "O" mesh which is selected to provide a circular field surrounding an airfoil as shown in Figure 5-1, is often used with a far-field pressure boundary condition and ideal gas. The most popular mesh topology is the "C" mesh which is designed to have a C-type topology around the airfoil as shown in Figure 5-2. Considering the viscosity effects, the normal air (not ideal gas) is considered for wind turbine aerodynamics. The mesh used here is the C-topology structured mesh. The airfoil is positioned at the centre of the domain having a distance of 15 times the chord upstream and 20 times the chord downstream as shown in Figure 5-2. The mesh was created in ICEM CFD. The nodes were placed closer near the leading edge of the airfoil. The boundary layer mesh was created around the airfoil where the dimensionless wall unit Y PLUS was controlled to less than 1.
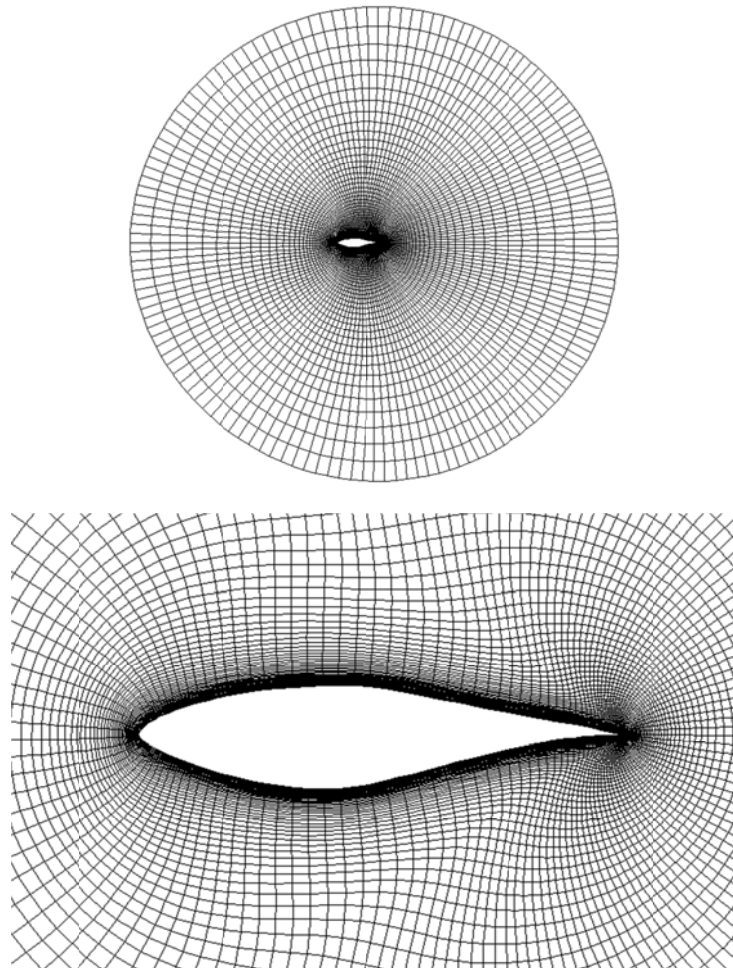
Figure 5-1 O-topology mesh for airfoil S809

Considering the type of the mesh element, quadric-element structured meshes are more predominant than tri-element unstructured mesh in terms of efficiency in data

interpolation, which leads to lower computational cost and better accuracy. For the mesh size, a balance is required between the desired calculation tolerance and the accepted computing time. In [68], a total number of more than 80,000 cells was reported to be adequate to guarantee results from a 2D airfoil simulation with a 2D domain of 12 times the chord distance upstream in the flow field and 20 times the chord downstream for all the turbulence models including the RNG k-ε model, the SST k-ω model, the S-A model and the RSM model. For the transition SST model, the total cells of 98,790 were also tested to yield satisfactory results with 20 times the chord distance for the 2D domain [74].

In order to study the mesh dependency, the number of nodes normal to the airfoil surface, n, the number of nodes parallel to the airfoil profile, t, and the number of nodes behind the airfoil, m, were increased step by step until there was no apparent difference in results, as discussed below.
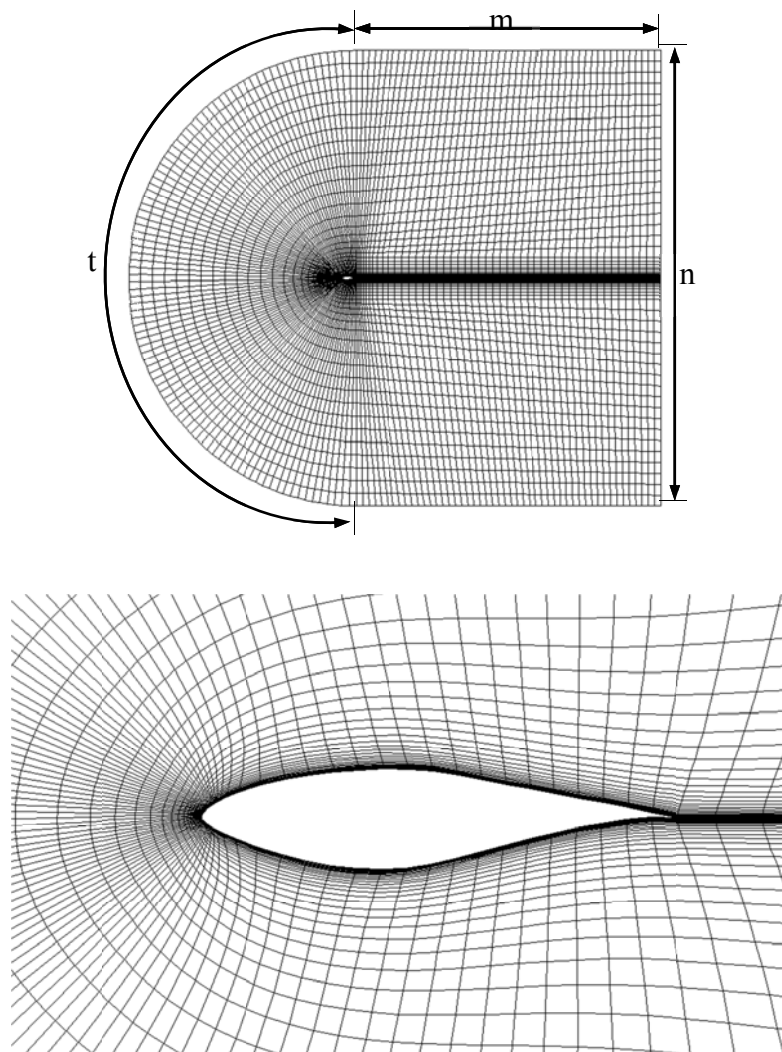
Figure 5-2 C-topology mesh for airfoil S809

5.2.2. Results and Discussion

5.2.2.1 Sensitivity of Mesh Size

The sensitivity of mesh size was studied by applying different node numbers for the normal direction and tangential direction around the S809 airfoil. All the cases were solved by the SST k-ω model. The convergence criterion for residuals is set to 1×10^{-5} for all the cases. The air density is 1.225kg/m^3 and the viscosity of the air is 1.7894×10^{-5} kg/m·s. The calculated lift and drag coefficients were obtained for different mesh sizes at the angle of attack of 2.05°[12], as shown in Table 5-1.

case	nodes	Cl	Cd	Y PLUS max	cells
M1	t=100,n=140,m=50	0.42047	0.01569	0.035	13260
M2	t=140,n=196,m=50	0.41403	0.01537	0.045	22560
M3	t=200,n=280,m=50	0.37865	0.01419	0.046	40710
M4	t=300,n=280,m=80	0.3603	0.01348	0.047	63821
M5	t=280,n=392,m=100	0.36403	0.0136	0.0475	92150
M6	t=400,n=560,m=100	0.3781	0.0137	0.055	165410

Table 5-1 Lift and drag coefficients for different mesh size

Without looking at the experimental data, the lift coefficient converges to a value of 0.378 and the drag coefficient converges to a value of 0.0137 in case M6 by refining the mesh. With further mesh refinement, there is no apparent improvement in predicted lift and drag coefficients. It is noted that the errors of lift coefficient in M4 and M5 are larger than that in M3; this is mainly due to the mismatch of the three numbers (t, n, and m) in M4 and M5.

The averaged computing time of one iteration step for these mesh methods is plotted in Figure 5-3. It is a general trend that the computing time is longer when the mesh is finer. Considering a balance between the fidelity and time, the case M3 mesh was selected for the rest of the cases in this chapter.

---

[12] The mesh sensitivity analysis was firstly done based on AoA of 2.05, and then an adequate mesh was selected and used for the whole range of AoA. It is believed that it is not necessary to repeat the sensitivity analysis for each AoA.
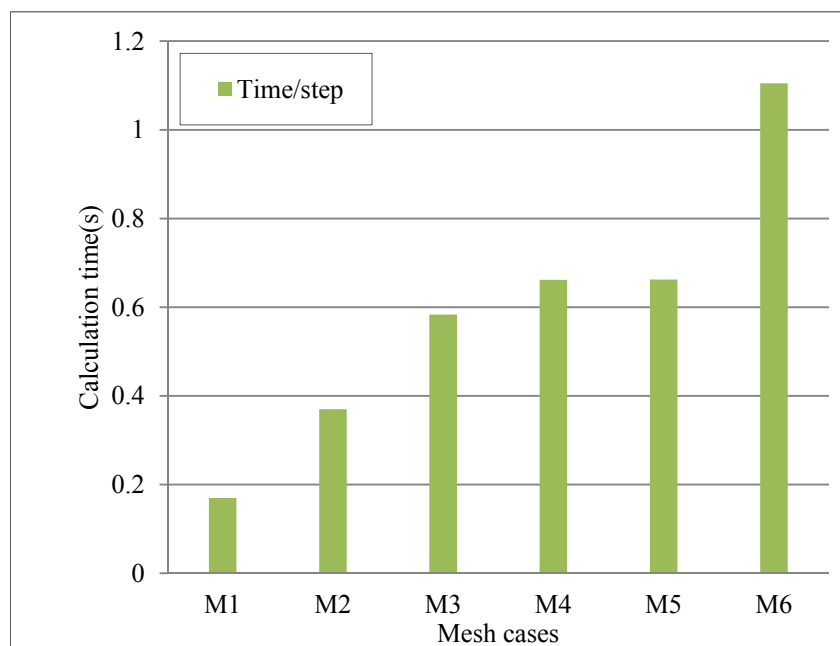
Figure 5-3 Calculation time comparison of different mesh sizes

5.2.2.2 Transition Model and SST k-ω Model

The transition model and SST k-ω model are compared using the case M3 mesh size described in the previous sub-section, and validated with the TUDelft wind tunnel test results. The residual convergence criterion for the cases using the SST k-ω model was set to 10^{-5}. For the SST k-ω model, all the calculations were found to converge with no variation in lift and drag coefficients below the angle of attack (AoA) of 10.2° after 30000 iterations. Above the AoA of 10.2°, an apparent periodic variation appears in the calculated residuals and predicted lift and drag coefficients, and averaged values are used after 40000 iterations. For transition cases, the convergence criterion were set to 10^{-7} and 80000 iterations were performed to obtain the lift and drag coefficients.

Plots shown in Figure 5-4 and Figure 5-5 compare the calculated results from CFD and measured lift and drag coefficients of S809 airfoil using the transition model and SST k-ω model. Comparing to wind tunnel measurements, the calculated results demonstrate an overall good agreement using these two models.

As shown in Figure 5-4, at low AoA, the SST k-ω model under-predicts the lift

coefficients after the critical AoA of 6.16°[13] while the transition model slightly over-predicts the lift coefficients. At high AoA, the SST k-ω model shows better stability than the transition model. The transition model predicts higher lift coefficients before 12.23° AoA and lower lift coefficients after 12.23° AoA compared with the measurements.

Figure 5-5 shows an enlarged view of the drag coefficients. At low angles of attack, the transition model presents excellent agreement with the measurements. The SST k-ω model slightly over-predicts the drag coefficients before the maximum lift coefficient at 9.21° AoA (according to the measurements). After 9.21° AoA, both the transition model and the SST k-ω model show similar results of the drag coefficients, which were all under-predicted compared with the test data. In conclusion, the transition model demonstrates better accuracy than the SST k-ω model in drag coefficient prediction but more time consuming.
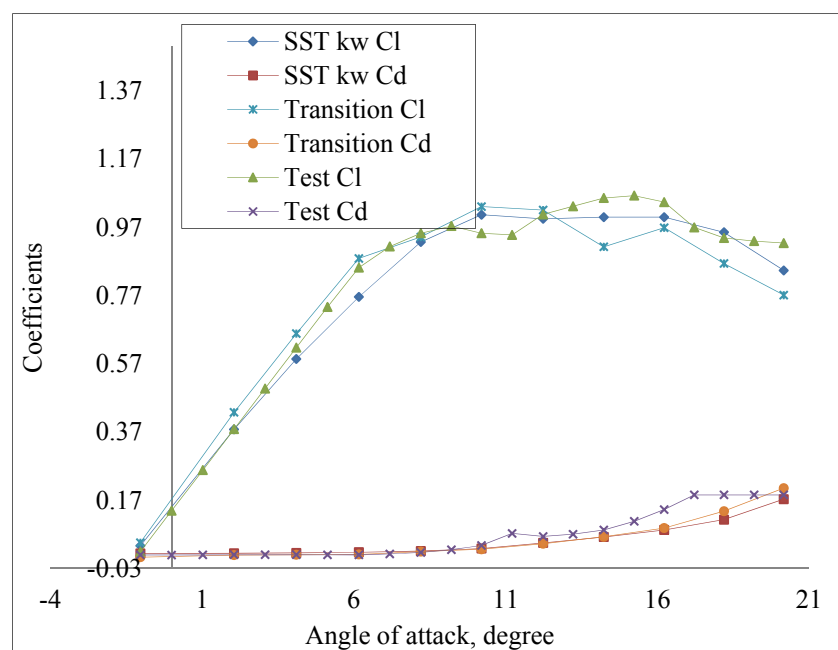
Figure 5-4 Lift and drag coefficient comparison between CFD predictions and measurements

---

[13] The maximum lift to drag ratio occurs at angle of attack 6.16° according to measurements.
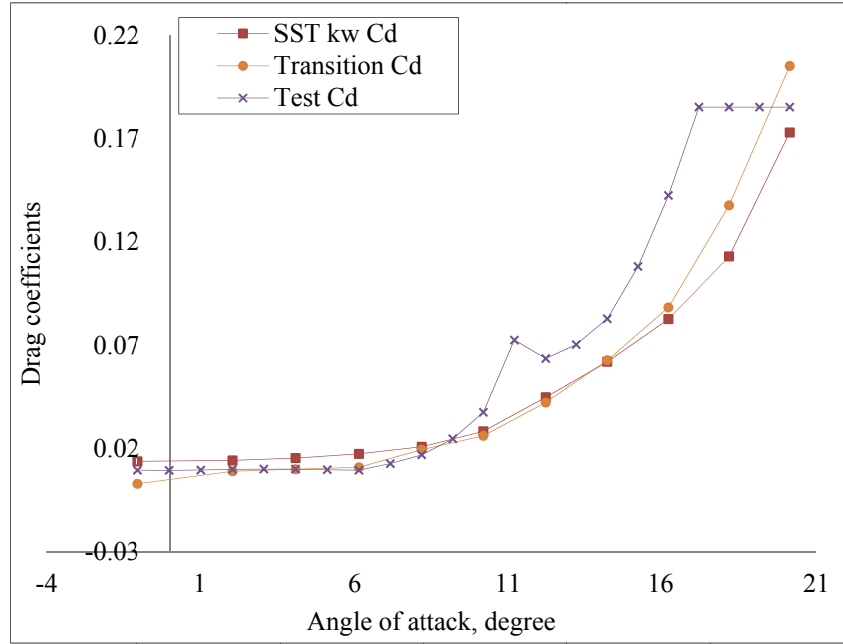
Figure 5-5 Drag coefficient comparison between CFD predictions and measurements

Figure 5-6 plots the pressure coefficient distributions of the airfoil surface predicted by the transition model and the SST k-ω model at the AoA of 4.10°. The transition model presents slightly larger pressure deficit between the pressure side and the suction side of the airfoil, which leads to higher lift coefficient prediction. Figure 5-7 shows the flow pressure field and streamlines at the AoA of 4.10° by using the two models. Very similar flow field and streamlines are observed.
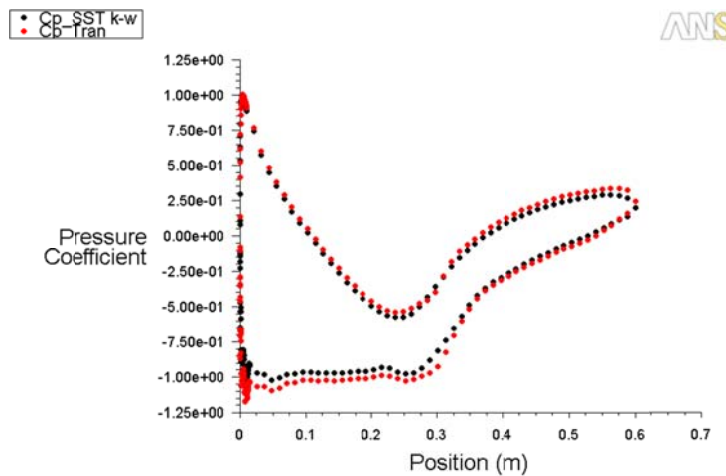
Figure 5-6 Pressure coefficient distributions predicted with the transition model and the SST k-ω model at the AoA of 4.10˚
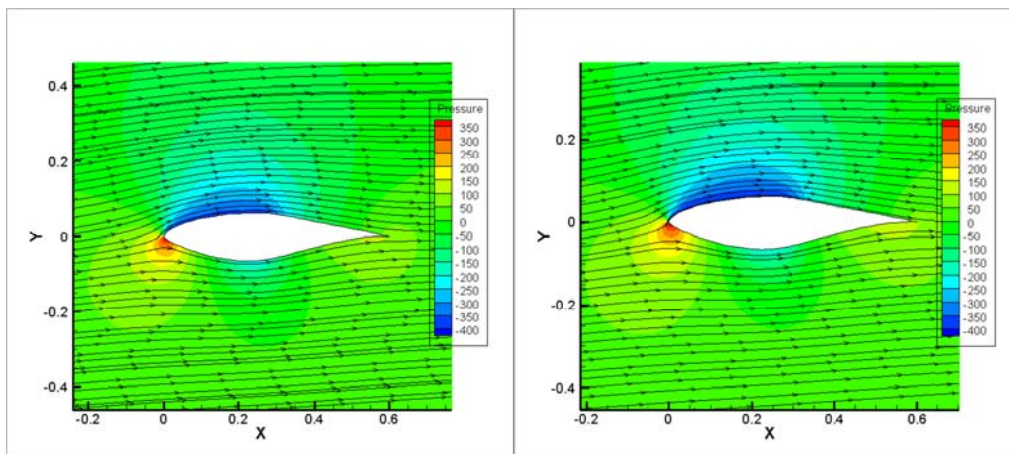
Figure 5-7 Streamlines around airfoil predicted by the SST k-ω model and the transition model at the AoA of 4.10°

Figure 5-8 and Figure 5-9 present the pressure coefficient distributions and streamlines predicted by the transition model and the SST k-ω model at the AoA of 18.19°. A smaller pressure deficit prediction occurs with the transition model, which leads to lower lift prediction comparing to the SST k-ω model. As shown in Figure 5-9, the flow separation is stronger when predicted by the transition model instead of the SST k-ω model. The stronger flow separation leads to lower lift and higher drag for the case using the transition model.
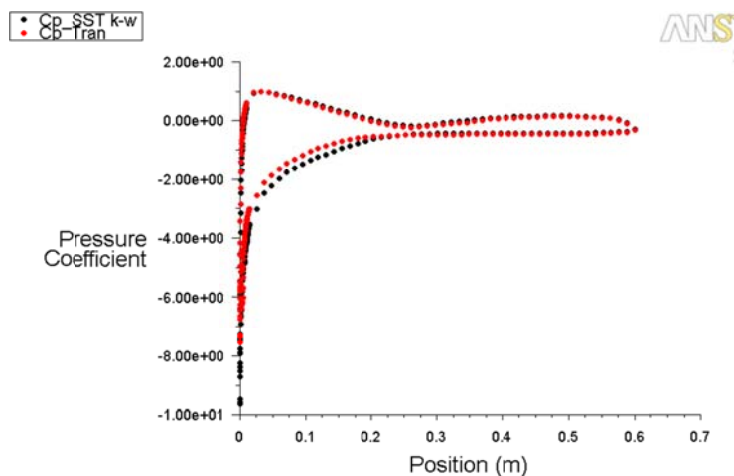
Figure 5-8 Pressure coefficient distributions predicted by the transition model and the SST k-ω model at the AoA of 18.19°
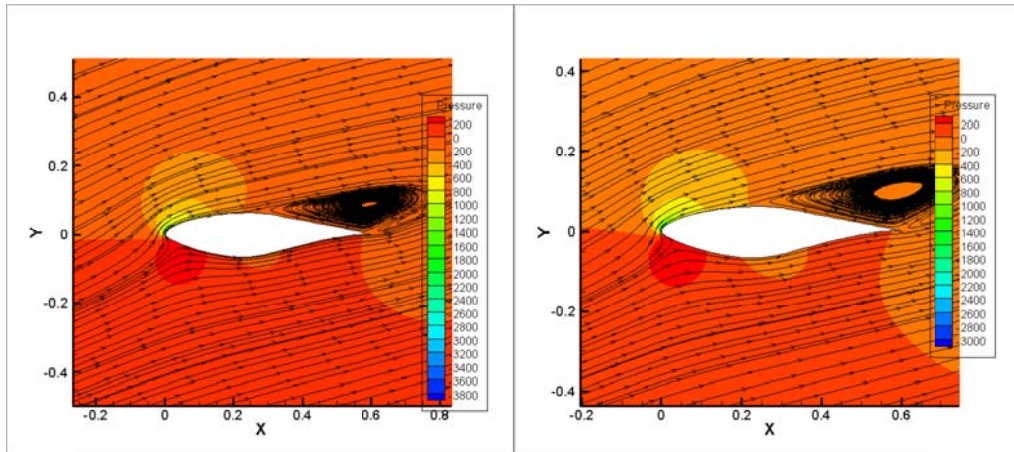
Figure 5-9 Streamlines around airfoil predicted by the SST k-ω model and the transition model at the AoA of 18.19°

5.2.2.3 Aspect Ratio Effects

To consider the effects of the aspect ratio (AR=chord length/blade span length) on the lift and drag coefficients, a quasi-3D modelling of S809 airfoil with an aspect ratio of 8 was compared with its 2D modelling. The mesh of the quasi-3D domain is extruded from the 2D mesh by 20 layers with 0.04mm per layer. Velocity-inlet and pressure-outlet boundary conditions are applied. The mesh of the flow domain is shown in Figure 5-10. The convergence criterion was set to 10^{-7}. All the calculations were considered to be converged after 30000 iterations with no variation in both lift and drag coefficients. If the tolerance was achieved, the calculations stopped no matter whether 30000 iterations were finished; if the tolerance was not achieved then the calculation stopped until 30000 iterations were finished. The transition model was employed to calculate the lift and drag coefficients, which were compared with the outcomes from the 2D modelling, as shown in Figure 5-11. The quasi-3D prediction and 2D prediction present very similar results for both the lift and drag coefficients.
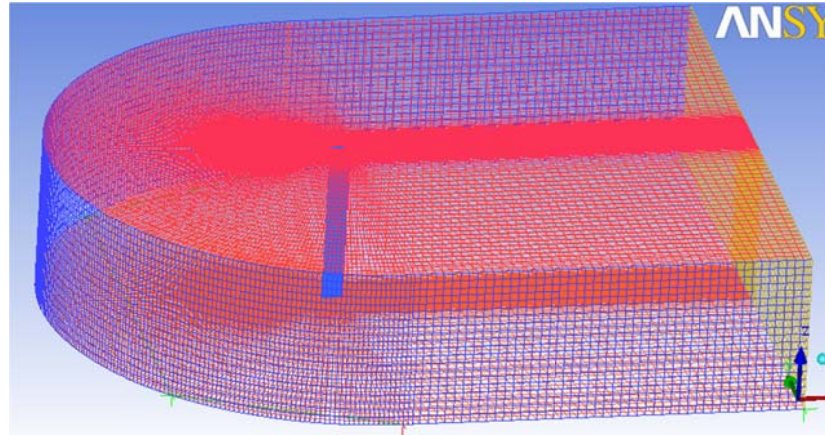
Figure 5-10 Flow domain of Quasi-3D S809 with an AR of 8
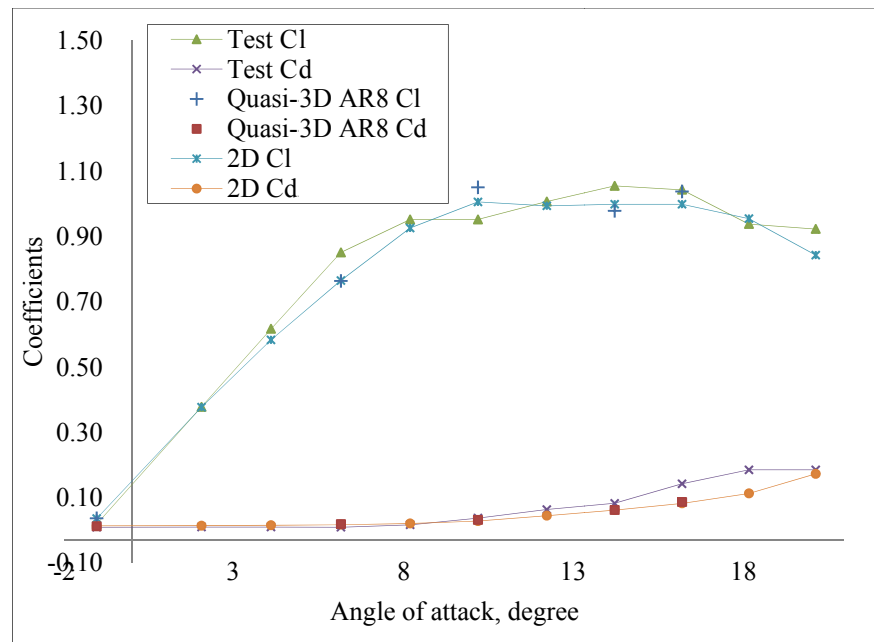
(a)
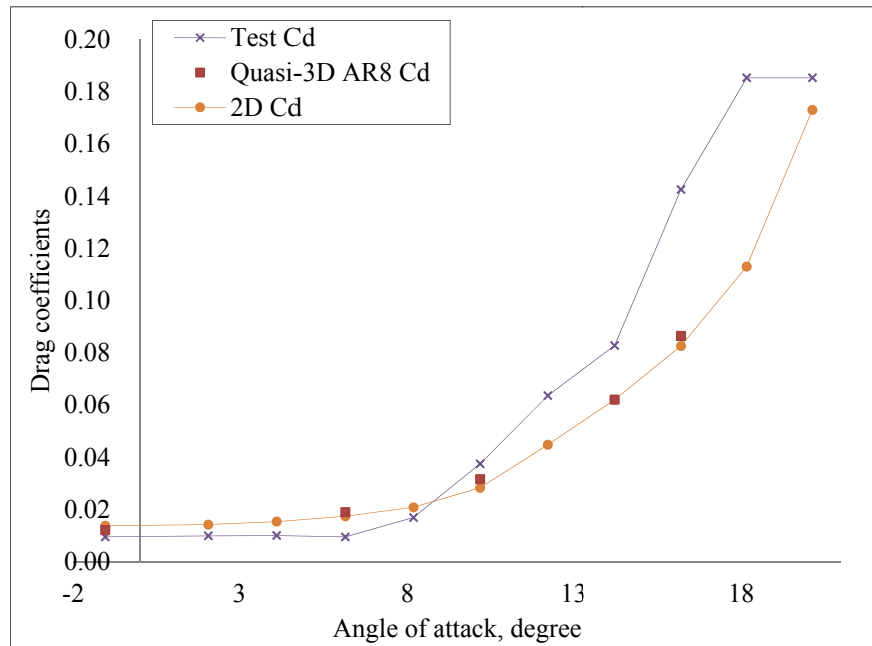
(b)

Figure 5-11 Lift and drag coefficients of 2D and Quasi-3D modelling of S809

(a) Lift and drag coefficients; (b) Enlarged drag coefficients

Figure 5-12 plots the pressure field and streamlines obtained from the 2D and Quasi-3D CFD modelling at the AoA of 16.22°. The pressure field and streamlines show no big difference by using the 2D and quasi-3D approaches. Figure 5-13 presents the pressure coefficient distribution along the chord obtained from the 2D and Quasi-3D CFD modelling at AoA of 16.22°. Again, almost the same pressure coefficient distributions are observed. Therefore it can be concluded that, the 2D approach has the equal level of accuracy compared with the quasi-3D approach. Considering the computing time, the 2D approach is more efficient.
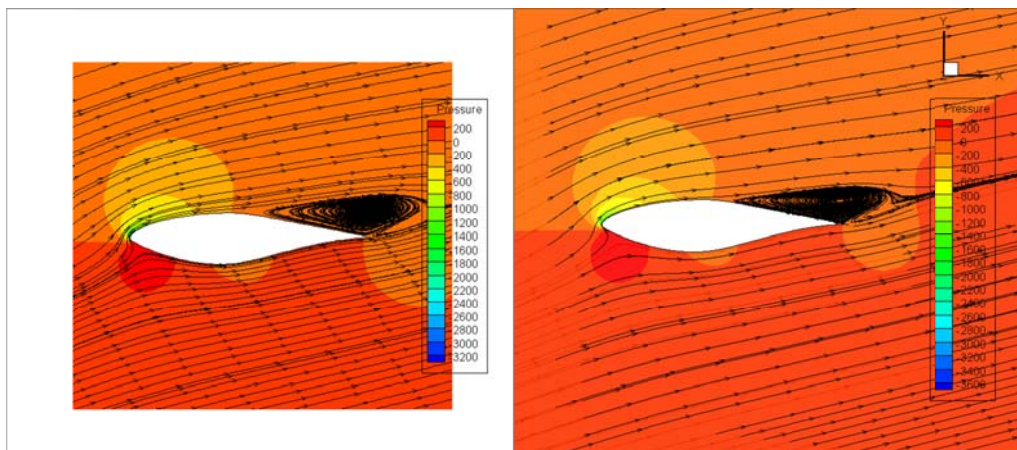
(a) 2D model   (b) Quasi-3D model

Figure 5-12 Pressure fields and streamlines of 2D and Quasi-3D modelling of S809
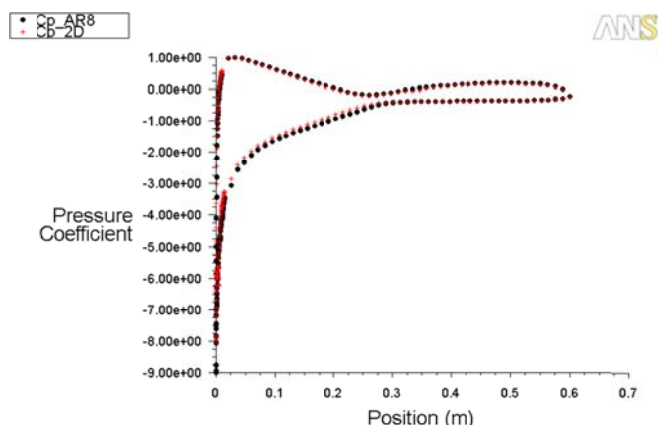
Figure 5-13 Pressure coefficient distributions of 2D and Quasi-3D modelling of S809

5.3 Three-Dimensional CFD Modelling and Validation

It is well-known that the NREL/NASA Phase VI wind turbine has been tested in Ames wind tunnel and released with measurements. This turbine has been simulated by many researchers using the RANS approach [43;66;109-111;114]. These research works provide comparatively good prediction and qualitative analysis for attached flow and moderate stall flows. However, it is admitted in the wind energy community that 3D RANS CFD simulation is still a great challenge regarding to turbulence and flow separation modelling [8;14;62]. The discussion of 3D RANS CFD simulation remains a hot issue at present. In this section, a comparative study of 3D RANS CFD modelling for the NREL/NASA Phase VI wind turbine is presented. The effects of mesh topologys, turbulence models, and time step of transient calculation are discussed.

5.3.1. 3D CFD Method

5.3.1.1 The NREL/NASA Phase VI Wind Turbine Blade

The NREL/NASA Phase VI wind turbine blade described in Chapter 4 is a twisted and tapered blade with a length of 5.029m. The recreated blade geometry is shown in Figure 5-14. The blade chord and twist distributions are exactly the same as the one in the NREL/NASA wind tunnel tests. The hub and tip region of the real blade is approximated as no data is available. This is not expected to introduce apparent

difference to the simulation results, as the effect of exact representation of the blade root and tip geometry was indicated to be secondary to the effects of the aspect ratio and blade pitch under working conditions [115].
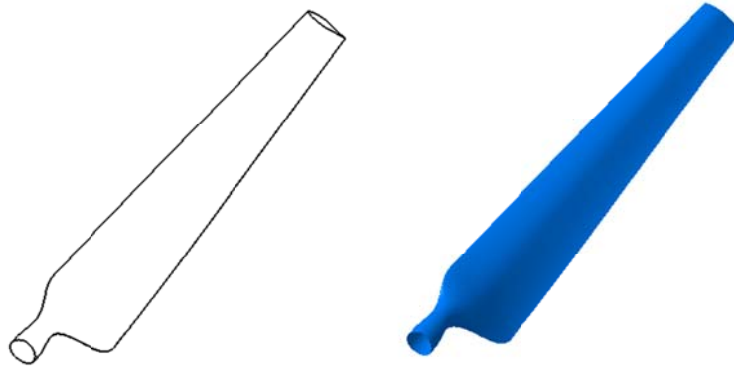
Figure 5-14 Blade geometry of NREL/NASA Phase VI wind turbine

Figure 5-15 shows the whole flow domain which combines two sub-domains, i.e. the outer domain and the inner domain. These boundary conditions are applied as shown in Figure 5-15: velocity inlet, pressure outlet, far wall, periodic and interface. The blade surface is regarded as non-slipping wall. The whole domain is 25m in length upstream before the rotor and 75m downstream behind the rotor to allow fully wake development, which means the inner domain is at the ¼ position (axial wise) of the outer domain. According to the momentum theory, the velocity of the stream decreases after the turbine; applying the mass conservation to the stream tube, the cross section downstream is considered to expand. The domain radius is 25m rotor radius at the inlet and 40m rotor radius at the outlet for the blade tip pitch angle of 1.225°. These parameters are considered to be similar to the Ames wind tunnel test section (36.6×24.4 m). The radius of the inner domain is 5.3m (slightly larger than the rotor radius), and the thickness is 1.6m. The multiple reference frames (MFR) method and sliding mesh (moving mesh) method are used to model the rotating wind turbine rotor, i.e. the outer domain is defined as stationary while the inner domain is defined to be rotating with the rotor blades. The two domains interact through mesh interfaces.
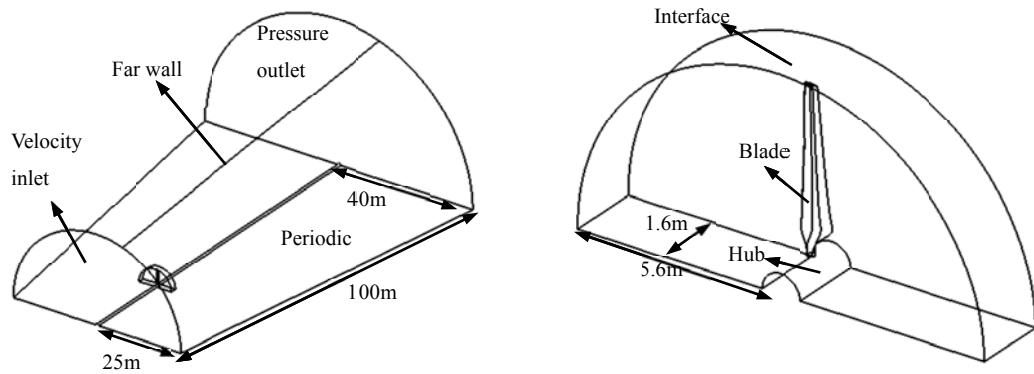
Figure 5-15 Mesh domain for the blade tip pitch angle of 1.225°

The meshes were produced in ICEM CFD. Periodic boundary was defined to solve a half domain only. All the cases were solved by transient pressure based solver in FLUENT. The air density for all computing cases was defined as 1.225kg/m^3 except where otherwise stated[14]. Since only the upwind configuration was considered, the interference between the rotor and the tower was thus approximately ignored. The inflow was regarded as unique for the whole rotor area ignoring vertical wind shear effects. As the tower effect and the wind shear effect are not particularly studied in this research, these simplifications are generally acceptable and were also applied in other research work [43]. All the cases were undertaken as transient computations and the initial condition is the steady solution.

In the following sections, after discussing the mesh dependency, the power predictions and details of the flow field are compared and discussed with different mesh topologies, turbulence models and time steps for the wind turbine rotor 3D CFD simulation.

5.3.1.2 Mesh Dependency Study

As shown in Figure 5-16, an unstructured mesh (USM) scheme is used around the sharp trailing edge blade. Tetrahedral mesh is applied in the inner domain and hexahedral mesh is used in the outer domain. Different mesh sizes are applied. In the USM1, a coarser mesh layer is around the blade, while a finer mesh layer is located in the USM2. The mesh size arrangements are listed in Table 5-2.

As shown in Table 5-2, the differences between the 2 mesh were the mesh/grid cell size and the cell numbers. The domain size remains the same. 180 steps equal to 2.16

---

[14] The air density varies from 1.246kg/m^3 to 1.22kg/m^3 in Ames wind tunnel tests.

revolutions for the NREL Phase VI wind turbine. 2.16 revolutions were performed for each operating condition. The monitored torque value remains constant thus the computed solutions are considered to be converged.
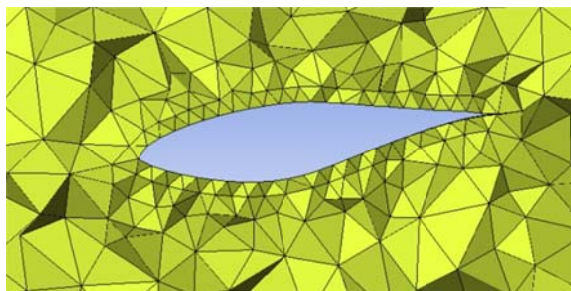
(a) USM1
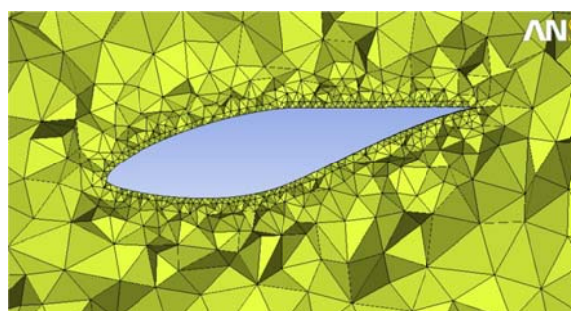
(b) USM2

Figure 5-16 Unstructured mesh dependency study: USM1 and USM2

	blade surface cell size (mm)	Hub surface cell size (mm)	Sub domain cell size (mm)	rotational domain cell size (mm)	static domain cell size (mm)	Total cell numbers
USM1	30	80	80	200	4000	968,581
USM2	20	80	80	100	2000	3,627,101

Table 5-2 Different mesh sizes for the NREL/NASA Phase VI wind turbine blade

In all these cases, the multiple reference frame (MRF) moving mesh method was used, and the mesh nodes of the inner domain and outer domain were made consistent at the interfaces. The SST k-ω model was used for all the calculations and the calculation was performed in transient mode with 40 iterations per step. The time step was set to 0.01 seconds per step and 180 steps (1.8 seconds) were simulated. All the calculations were found to converge with the residuals under 10^{-5}. The calculation results are plotted in Figure 5-17.
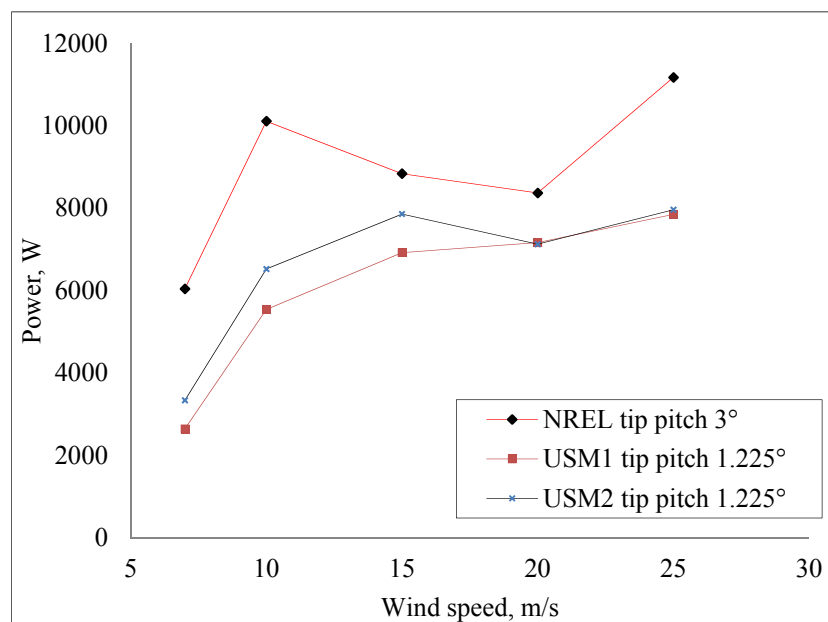
Figure 5-17 Power curves of different mesh sizes: USM1 and USM 2

As shown in Figure 5-17, the calculated torques thus power outputs are improved with a finer mesh. Within the limits of the computing capacity, the mesh has not been further refined. Although more curves can be added, the results of the coarse mesh (USM1) cases and the refined mesh (USM2) cases indicate that a better prediction can be achieved with a finer mesh especially for the wind speeds under 20m/s. While above 20m/s, the blade is fully stalled and the two cases have surprisingly similar results. This reason may be that the mesh is not fine enough for the very large flow separation. With the unstructured mesh USM2, the calculated minimum Y PLUS (i.e. the dimensionless wall distance) of the first layer near blade surface is 8 at low wind speeds and 10 at high wind speeds. Generally speaking, to catch the flow characteristics near the blade, the Y PLUS of the first layer near blade surface should be less than 1. In order to get more confident results, a study on even finer boundary layer mesh study was conducted as described later.

5.3.1.3 Turbulence Model Comparison

Although the turbulence models have been initially studied in 2D cases, it is necessary to validate it in 3D models. Calculations were conducted for the case with blade tip pitch angle of 1.225°. Note here, the blade tip pitch angle was 3° in the measurements (no measurements for blade tip pitch angle of 1.225° are available); however it does not

affect qualitative comparison of the turbulence models (More results for the case with tip pitch angle of 3° are presented in Section 5.3.2). The standard k-ε model, plus enhanced wall treatment, and the SST k-ω model were compared based on mesh USM2. All the calculations were converged based on the residual criterion of 10^{-5}. Table 5-3 lists the calculated torques, and the torque curves are plotted in Figure 5-18. With this USM2 mesh resolution, the k-ε standard and enhanced models produce very similar results for wind speeds under 15m/s.

	Torque (Nm)				
	at 7m/s	at 10m/s	at 15m/s	at 20m/s	at 25m/s
USM2: k-ε standard	443	894	1075	1034	1177
USM2: k-ε enhanced	400	882	1055	1040	1191
USM2: SST k-ω	442	865	1042	945	1056
USM2: Transition	423	867	1061	1032	1092
Measured	801	1341	1172	1110	1482

Table 5-3 Comparison of different turbulence models
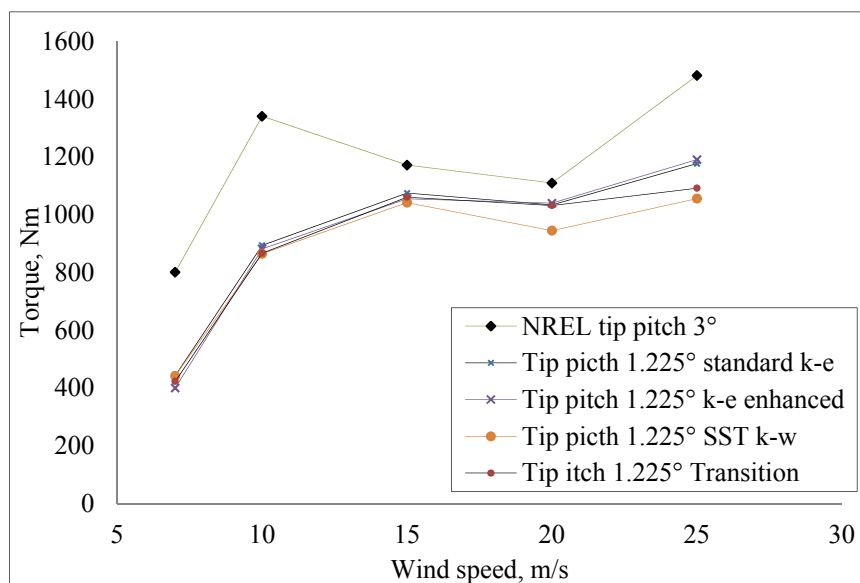
Figure 5-18 Rotor torque curves of different turbulence models

5.3.1.4 Time Step Dependency Study

Since turbulence flows present an unsteady problem, it is more appropriate to simulate in a transient mode. Thus, the real time per step and over all time steps may have an impact on the accuracy of the results. The time per step should be smaller enough to capture the transient behaviour. The smaller the time per step and the larger the step

number should be used, the better the results should be expected. However, a more powerful computer and computing time are required at the same time. Three series of time per step were used for the NREL/NASA Phase VI wind turbine blade with tip pitch angle of 3° and wind speed of 7m/s. The total cells were 1.4millions for a half calculation domain. The SST k- ω model and the MRF method were used. All calculations were found to converge with a residual convergence criterion of 10^{-5}. The calculated results are listed in Table 5-4.

Tip pitch 3°,7m/s	Time step	Torque (Nm)
Case A	0.01s/step, 180 steps	590
CaseB	0.001s/step,840 steps	688
Case C	0.0001s/step,1670 steps	664
Measured		801

Table 5-4 Comparison of time steps

As shown in Table 5-4, the case B (0.001s per step) has a higher calculated torque comparing to that of the case A (0.01s per step). However, the case C (0.0001s per step) showed a slightly lower torque. This may be affected due to only 1670 steps calculated. By running on a work station of Intel Xeon CPU E5520 2.27GHz with 4 parallel processors, it required 22hours for the 0.001s/step with 840 steps and 7 hours for the 0.0001s/step with 1670 steps. The torque may be improved by a longer time calculation for the 0.0001s/step case. However, the 0.0001s/step case takes a much longer calculation period if the total calculation time is equal to 2-3 working revolutions with rotor speed of 72RPM (0.833 second/revolution). With one case calculated in 2000 steps at 7m/s, the monitored torque showed no big difference, the setting of 0.001s/step and 840 steps therefore was selected as a better choice regarding the balance between accuracy and computing time.

5.3.1.5 Boundary Layer Mesh Improvement

A big challenge of wind turbine turbulence modelling is to solve boundary flows around the rotating blades. To capture the boundary flow, the first layer height of the mesh close to the blade surfaces needs to be fine enough. The free form of the blade with sharp airfoil shapes, twisted sectional pitch angles and tapered chords, and a wide range of dimension scales greatly increase the difficulty in mesh generation: The computing domain is 100m long, the blade chord is 0.358m, and the height of the first mesh layer

is expected to be at the level of 0.01mm, according to the Y PLUS criterion (http://geolab.larc.nasa.gov/apps/YPlus). The S809 airfoil has a sharp trailing edge which is obviously not for the real blade and unnecessarily complicates the mesh construction. The sharp trailing edge of S809 is therefore replaced by a blunt trailing edge which is chamfered with 0.5% chord thickness. This modification is more realistic and was also used and stated in [116]. To have an adequate mesh resolution for the boundary layer, three approaches have been tried as described below.

(1) Y PLUS Adaption

The Y PLUS adaption is an adaptive method according to the current Y PLUS values. The mesh is reproduced at the defined areas when the current Y PLUS is higher or lower than the demanded values. The 1.4million cell mesh is adapted to have an improved Y PLUS. All calculations are conducted using SST k- ω model in 0.001s per time step and 840 steps in total. The residual converge criterion is 10^{-5}. The corresponding rotor torque and first layer height are listed in Table 5-5. The torque curves are plotted in Figure 5-19. With Y PLUS adaption, the calculation results have been improved for all the cases.

Tip pitch 3° cases	Torque (Nm) before adaption, minimum cell distance 2mm	Error	Torque (Nm) after adaption, minimum cell distance 1mm	Error	Measured torque (Nm)
7m/s	688	-14%	706	-12%	801
10m/s	870	-35%	902	-33%	1341
15m/s	818	-30%	880	-25%	1172
20m/s	992	-24%	890	-20%	1110
25m/s	840	-33%	1046	-29%	1482

Table 5-5 Y PLUS adaption
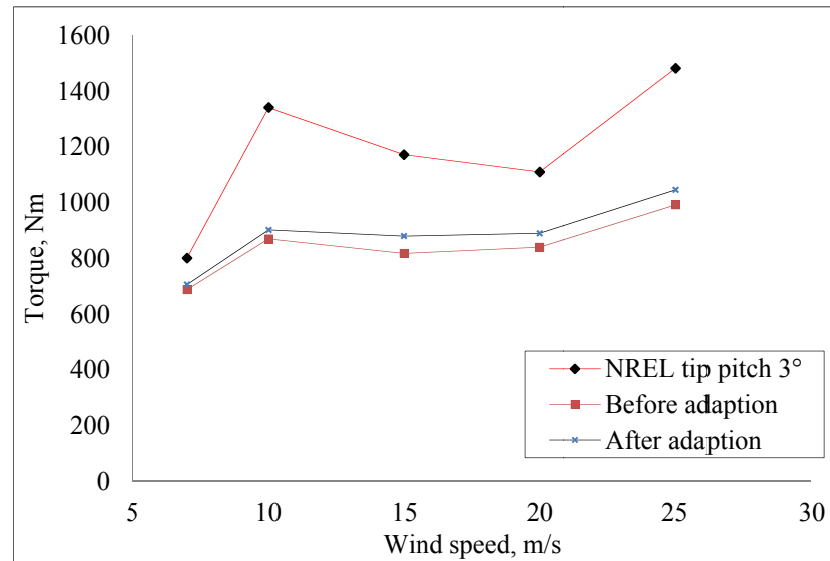
Figure 5-19 Torque comparison before and after Y PLUS adaption

(2) Tetrahedral Cells plus Prisms Cells

To capture the boundary flow, a hybrid mesh of tetrahedral cells and prism cells is used in the inner domain and a hexahedral mesh is employed in the outer flow domain for the tip pitch of 1.225°. The tetrahedral mesh with the prism boundary layer mesh is shown in Figure 5-20. With different first layer heights, two mesh cases were compared. The calculations were executed with the SST k-ω model with 0.01s per time step and 840 steps in total. The residual convergence criterion was set to 10^{-5}. The calculated results for different heights are list in Table 5-6.
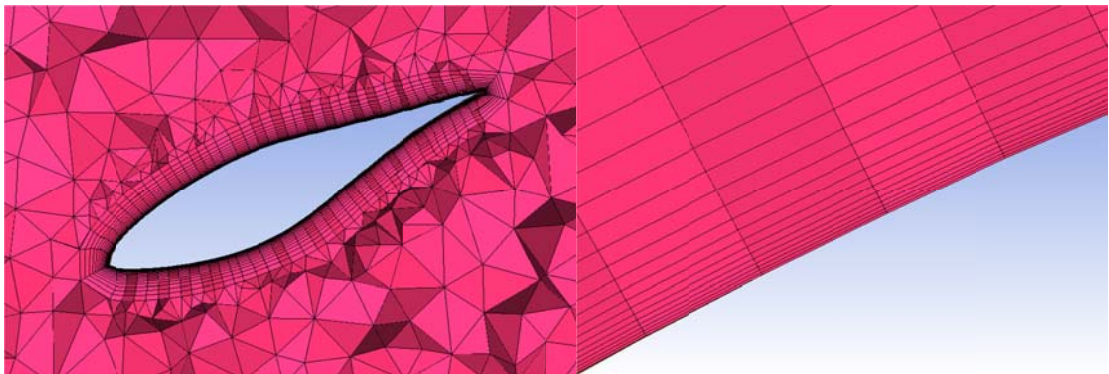
Figure 5-20 Tetrahedral plus prism boundary layer mesh

Mesh	The first layer height (mm), ratio, layers, mesh quality in ICEM	Blade surface Y PLUS	Torque at 7m/s(Nm)	Torque at 10m/s(Nm)
Hybrid Case A	1×1.2 ×3, Q_{min}=0.0125	3-133	358	717
Hybrid Case B	0.1×1.2 ×20, Q_{min}=0.038	0.16-78	390	718
Original tetrahedral	Approximately 10, Q_{min}=0.126	10-400	443	865

Table 5-6 Torques calculated with tetrahedral mesh and prism boundary layer mesh

As shown in Table 5-6, Case B improved the predicted torque at wind speed 7m/s comparing to Case A; however, similar results are obtained at 10m/s. Both of these hybrid cases produce lower torque comparing with the original tetrahedral mesh case. The mesh numbers of case A and case B are 4 million and 5 million respectively, while the number of the original case is 3.6 million. Moreover, a total of 5million cells in Case B caused a much longer calculation time (11hours for Case A against 20 hours for Case B for 7m/s calculation with 4 processors). When trying to refine the first boundary layer under 0.001mm height, the mesh orthogonal quality went below 0.002. The mesh quality was dramatically reduced by adding prism layer in to the tetrahedral mesh, which produces larger discrepancies in power prediction.

(3) Hexahedral Mesh

An overall hexahedral mesh generated in ICEM is employed for the NREL/NASA Phase VI wind turbine. The entire domain is meshed with hexahedral cells, and the turbine blade surface is meshed using quad cells as shown in Figure 5-21. The number of total nodes around the airfoil is 108 and the number of nodes along the span is 65. The minimum height of the blade surface boundary layer is 0.2mm (corresponding to minimum Y PLUS of 1.2). The total number of mesh cells is 2,370,136 for the half domain. The minimum mesh quality is 0.176 and minimum orthogonal quality is 0.135. Periodic conditions are applied.
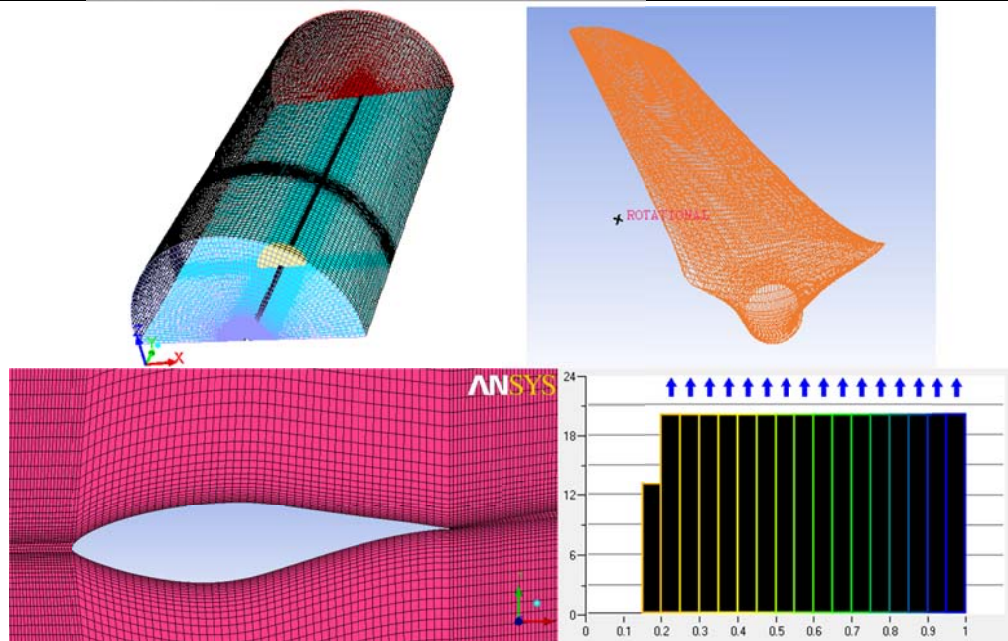
Figure 5-21 Hexahedral mesh for the NREL/NASA Phase VI wind turbine blade

After 2000 iterations with 0.001s per step, the calculation converged at 10^{-5}. Each calculation case took about 50 hours running on an 8-processors computer of Intel® Xeon® E5520 @2.27GHz. The calculated torques are 560Nm, 560Nm and 596Nm for 7m/s, 10m/s and 15m/s respectively. Comparing to the previous tetrahedral mesh with the Y PLUS adaption approach, the rotor torque was under-predicted. The under-prediction is mainly due to inadequate mesh nodes around airfoil surface. However, due to a long calculation time and limited computer resource, the number of hexahedral mesh cells has not been further increased.

5.3.2. Results and Discussion

5.3.2.1 The Calculation Setup

The following results were obtained with the SST k-w model and the hybrid mesh. The mesh strategy was based on tetrahedral elements with Y PLUS adaption for the inner (rotational) domain and hexahedral mesh for the outer (stationary) domain. A total number of 2 million cells were generated in ICEM and the minimum first layer height was set to 0.9mm. Periodic condition was applied to the half calculation domain. The calculation conditions are listed in Table 5-7. All calculations were converged with the residuals below 10^{-5}. A total of 1000 steps with 0.0001s per step were simulated for all the cases since no big difference showed in a case with 2000 steps at 7m/s. The

monitored torque curve showed constant for further steps. The calculation for one wind speed took about 20 hours using an 8-processor machine of Intel® Xeon® E5520 @2.27GHz.

Wind speed (m/s)	Air density (kg m^{-3})	Viscosity (kg m^{-1} s^{-1})	Turbulence intensity	Rotor speed (RPM)
7	1.246	1.769	1%	71.9
10	1.246	1.769	1%	72.1
15	1.224	1.784	0.5%	72.1
20	1.221	1.786	0.5%	72.0
25	1.220	1.785	0.5%	72.1

Table 5-7 Calculation conditions of the NREL/NASA Phase VI wind turbine

The following sections present the calculated forces, power coefficient and flow visualisation of the RANS 3D CFD calculations. Firstly, the calculated low-speed shaft toques and root flap moments from wind speeds 5m/s to 25m/s are compared with the results from Ames wind tunnel measurements, the BEM method with wind tunnel tested lift and drag coefficients and the 3D CFD results of Sørensen [43]. Since all measurements except the pressure distributions from wind tunnel tests are averaged values, the standard deviations (STDEV) are also shown in torques and moments to indicate variation over one revolution [43]. Secondly, the pressure distributions are compared with measured distributions. Finally, the pressure filed and streamlines are presented.

5.3.2.2 Torques, Root Flap Moments and Power Coefficient

Figure 5-22 plots the calculated torques and root flap moments of the NREL/NASA Phase VI wind turbine with the tip pitch of 3° at the wind speeds from 5m/s to 25m/s, comparing to the UAE Ames wind tunnel measurements and the results of Sørensen [43]. Though quantitative difference exists between the CFD calculated torques and measurement torques, the overall shape is generally well predicted. Very good agreements occur between the CFD calculated results and the results of Sørensen except for 10m/s. At higher wind speeds when stall happens, excellent coincidence exist between the CFD calculated results the results of Sørensen. Comparing to the measurements, the torque is well predicted at 7m/s with slight under-prediction, while at higher wind speeds above 10m/s under stall conditions, the CFD calculations

under-predict the torques. At wind speeds of 15m/s, 20m/s and 25m/s, the CFD calculations under-predict the torques by almost the same amount compared with the measured torques.
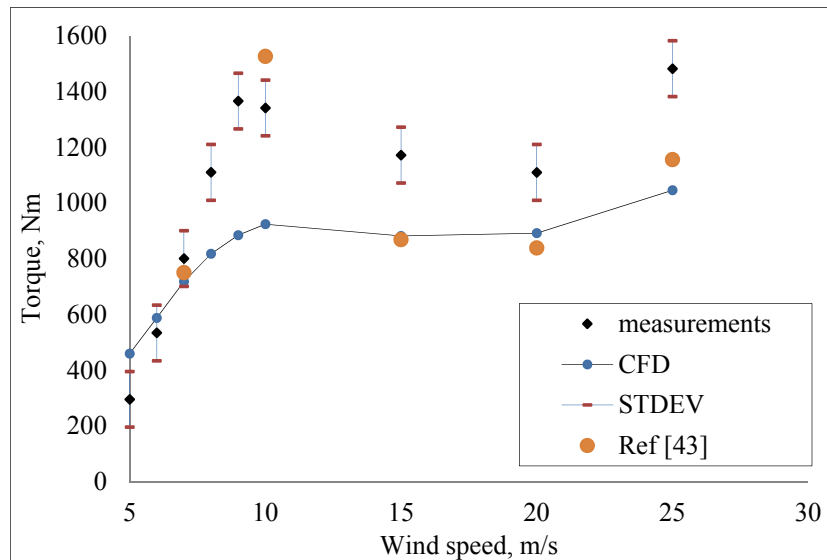
Figure 5-22 Comparison of torques of CFD, BEM and measurements

Figure 5-23 illustrates the comparison of the CFD calculated and measured blade root flap moments, along with the results from Sørensen's work. Very good qualitative agreements are achieved. The overall trend of root flap moments is well predicted. Moreover, for high wind speeds of 15m/s, 20m/s and 25m/s, the CFD calculated results are within the standard deviations of the measurements.
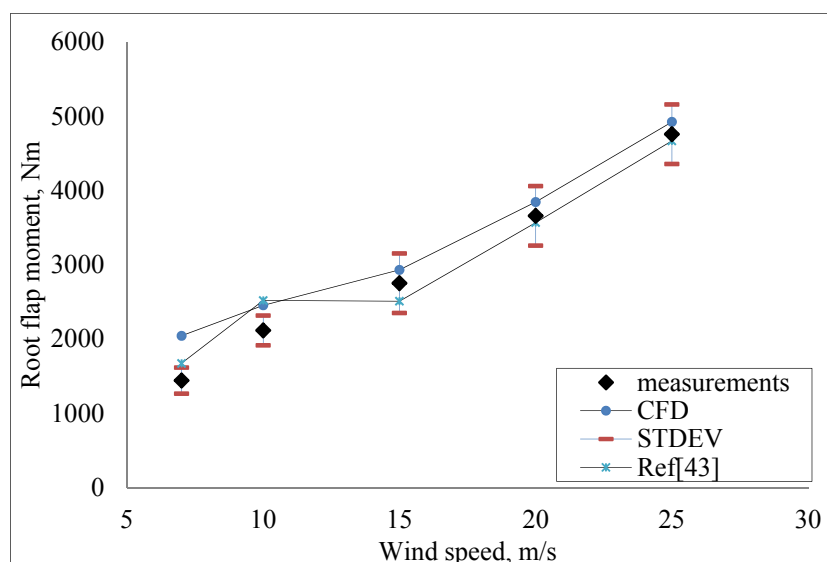
Figure 5-23 Comparison of root flap moments of CFD, BEM and measurements

Figure 5-24 presents the power coefficients versus wind speeds from CFD calculations, measurements, and BEM calculations with 2D wind tunnel lift and drag coefficients.

The power coefficients versus tip speed ratios are demonstrated in Figure 5-25. An overall good agreement is achieved. The CFD calculations and BEM calculations are seen to coincide for the high wind speeds of 15m/s, 20m/s and 25m/s, with both under-predicting the power compared with the measurements.
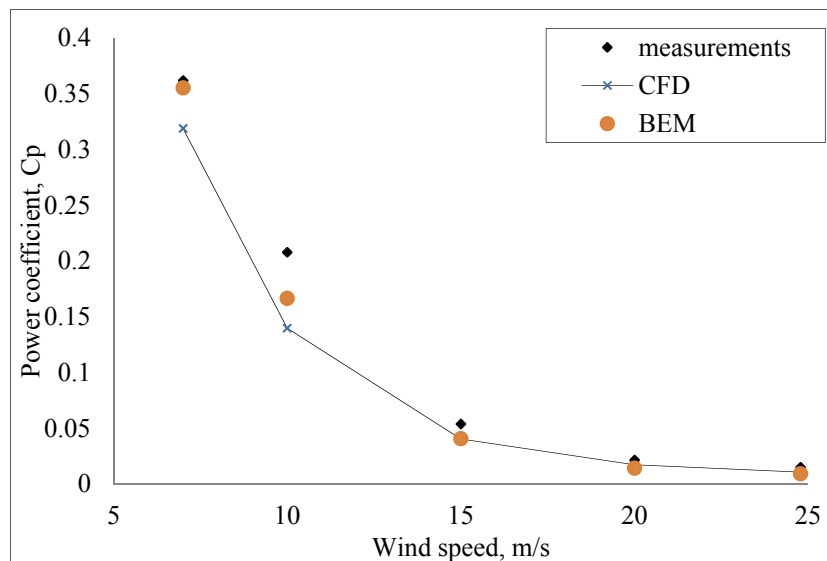
Figure 5-24 Power coefficient versus wind speed
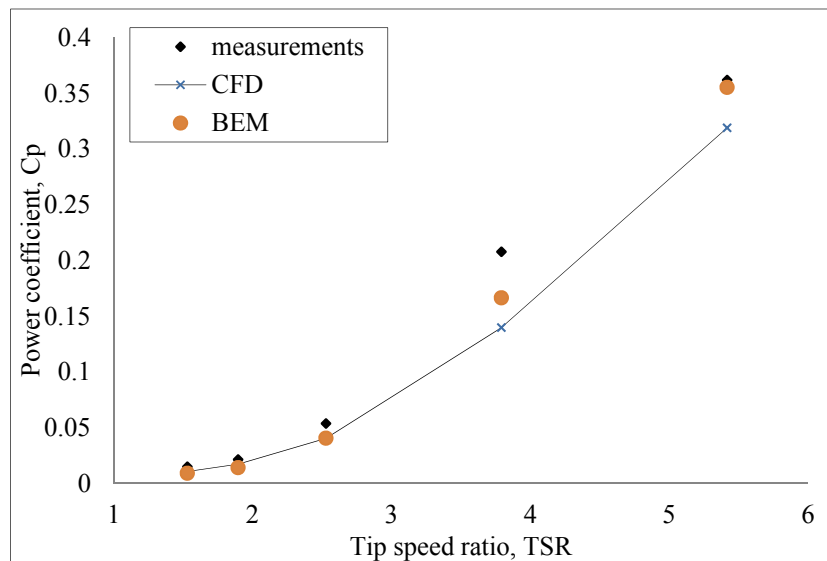
Figure 5-25 Power coefficient versus tip speed ratio

5.3.2.3 Pressure Distributions

From Figure 5-26 to Figure 5-30, the CFD calculated and measured pressure coefficient distributions of the NREL/NASA Phase VI wind turbine are compared at wind speeds from 7m/s to 25m/s. The pressure coefficient is defined as:

$$C_p = \frac{P - P_\infty}{0.5\rho[(V_\infty)^2 + (\omega r)^2]} \qquad (5.1)$$

where,

P_∞ is pressure at far field,

ρ is air density, which is 1.225 kg/m^3 here,

V_∞ is flow velocity of far way stream, which is equal to the inlet wind speed,

r is radius position of each section,

ω is rotor angular velocity, which is equal to 7.54 rad/s.

As shown in Figure 5-26, very good agreements are presented for all the five span sections at wind speed of 7m/s. This is in accordance with the good torque prediction at wind speed of 7m/s as previously discussed. While referring to Figure 5-31, the section streamlines and static pressure contours indicate that the flow is almost attached at wind speed of 7m/s for all the sections.

Figure 5-27 plots the pressure distribution at five span locations at wind speed of 10m/s. Very good agreements are obtained except for the 47% radius location. The discrepancy at 47% radius location is mainly due to the flow separation. As shown in Figure 5-33 the flow separation at the middle location of the chord is observed at 47% at wind speed of 10m/s. On the suction side of the blade, sharp suction peak is predicted at the leading edge (no flow separation at the leading edge), while flow separation occurs at leading edge according to the measurements.

As shown in Figure 5-28, at wind speed of 15m/s, the predicted pressure distributions from CFD have very similar shapes with slight differences comparing to the measured values. These differences are located on the suction surface (back to the incoming flow) of the blade where flow separation takes place, while the pressure of the pressure surface side (face to the incoming flow) is well predicted. This flow separation at 15m/s is also clearly illustrated in Figure 5-31.

Figure 5-29 and Figure 5-30 show the pressure distribution at 20m/s and 25m/s. Good approximations of the pressure distribution are presented. The differences between the predicted pressure distributions and those from those from the measurements are observed at the suction side surface for these two highest wind speeds. These differences at deep-stall conditions were also reported in Sørensen's work [43].
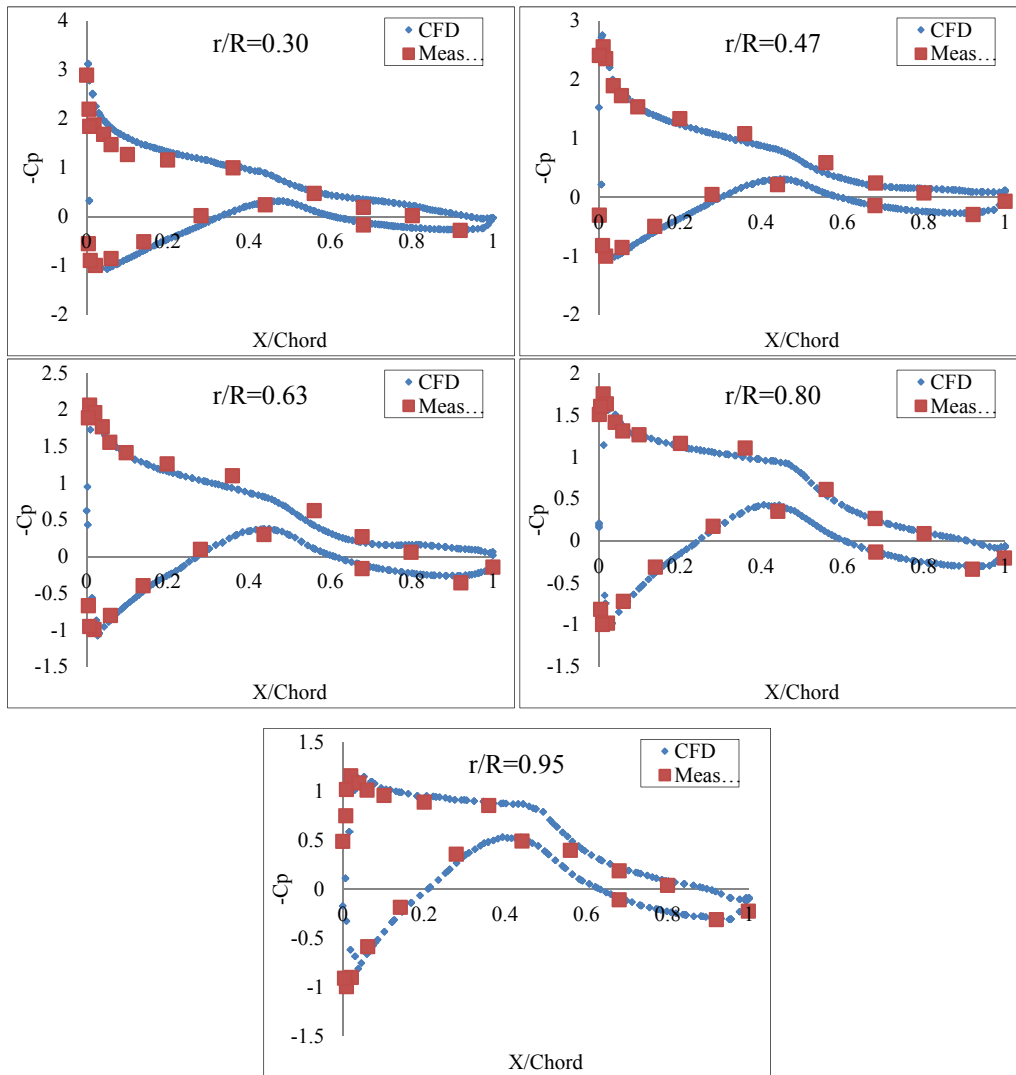
Figure 5-26 Pressure distributions of CFD predictions and measurements at 7m/s
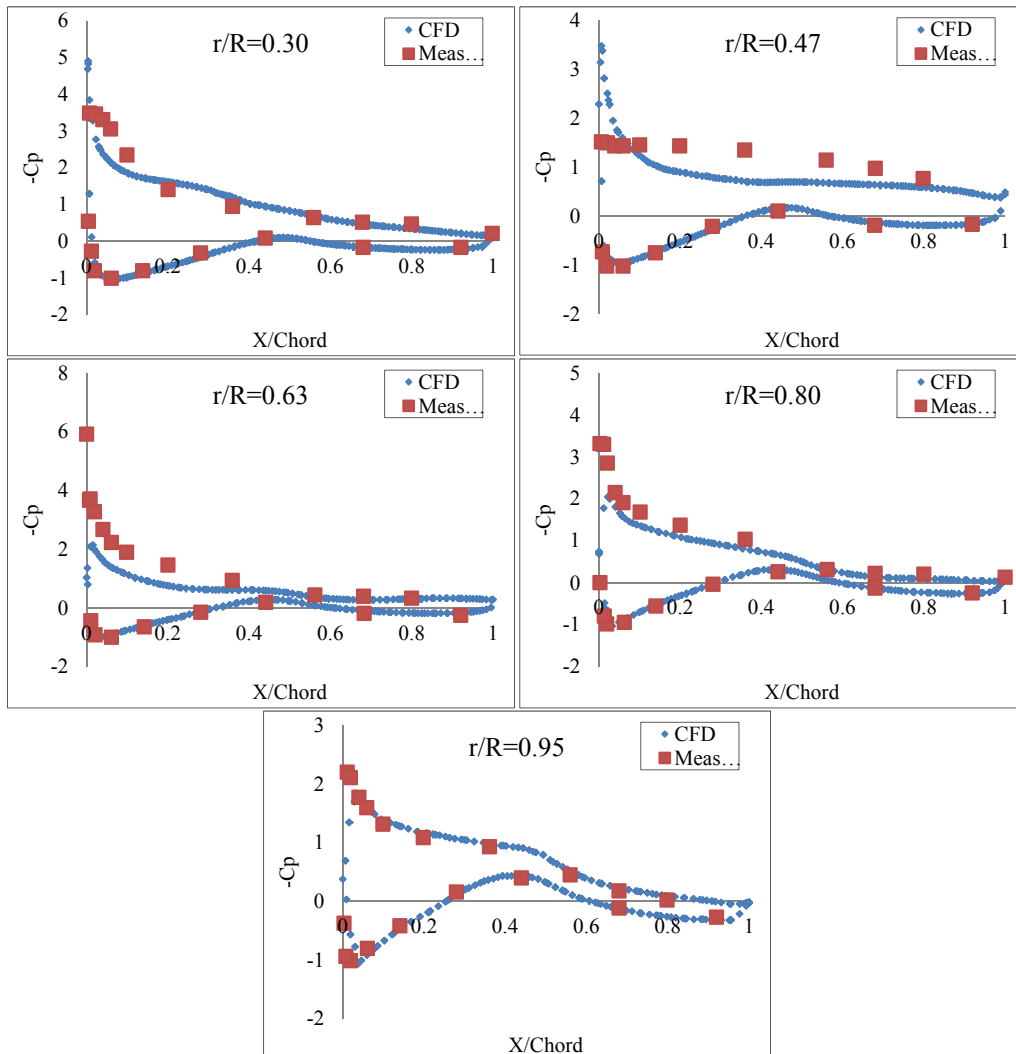
Figure 5-27 Pressure distributions of CFD predictions and measurements at 10m/s
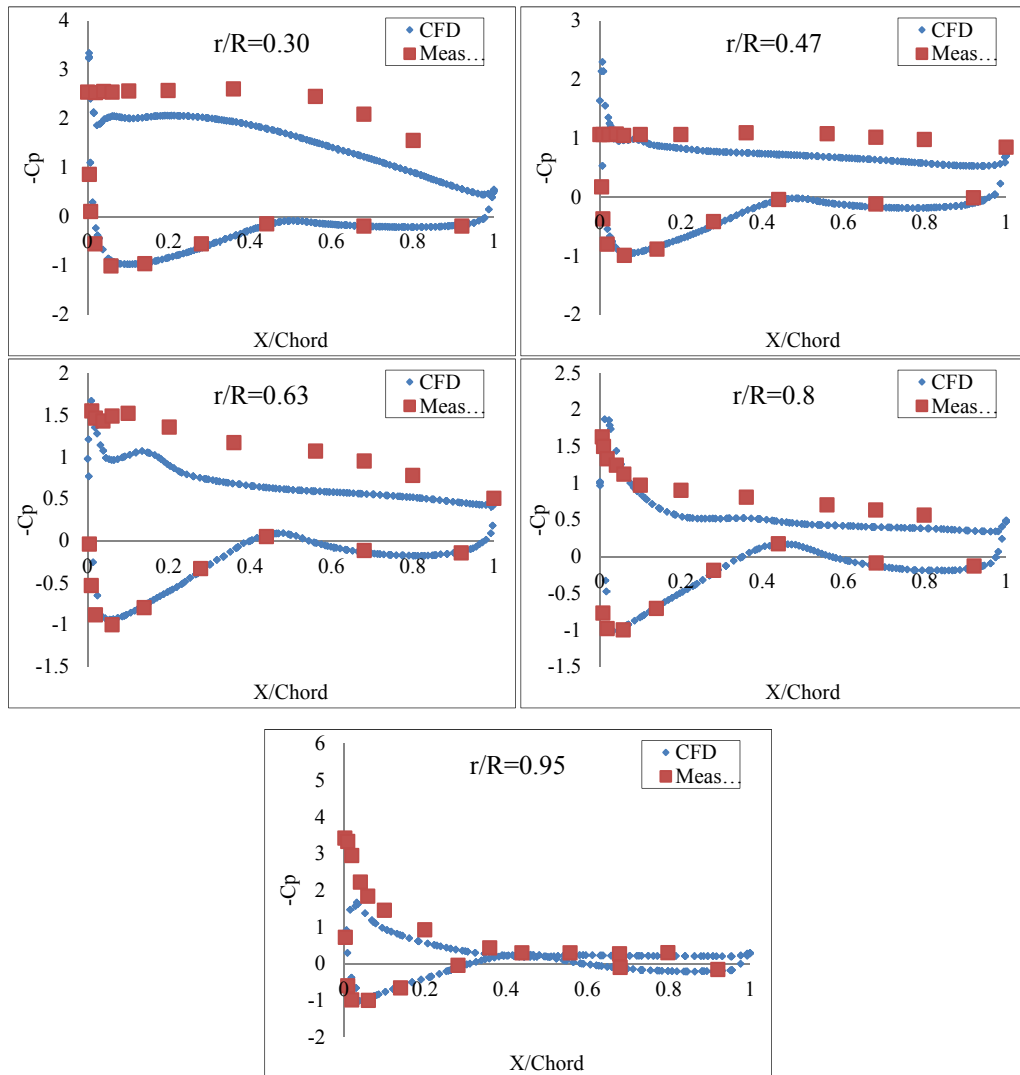
Figure 5-28 Pressure distributions of CFD predictions and measurements at 15m/s
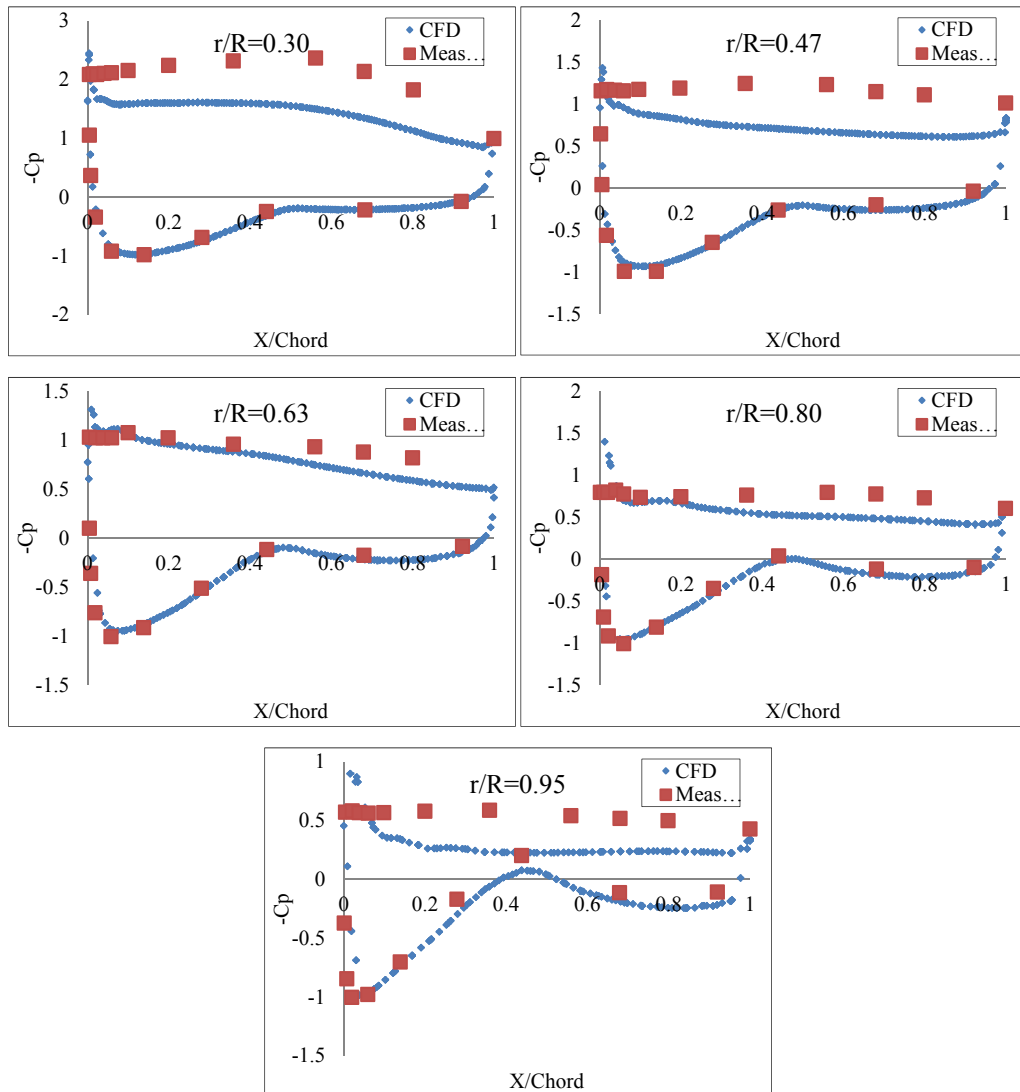
Figure 5-29 Pressure distributions of CFD predictions and measurements at 20m/s
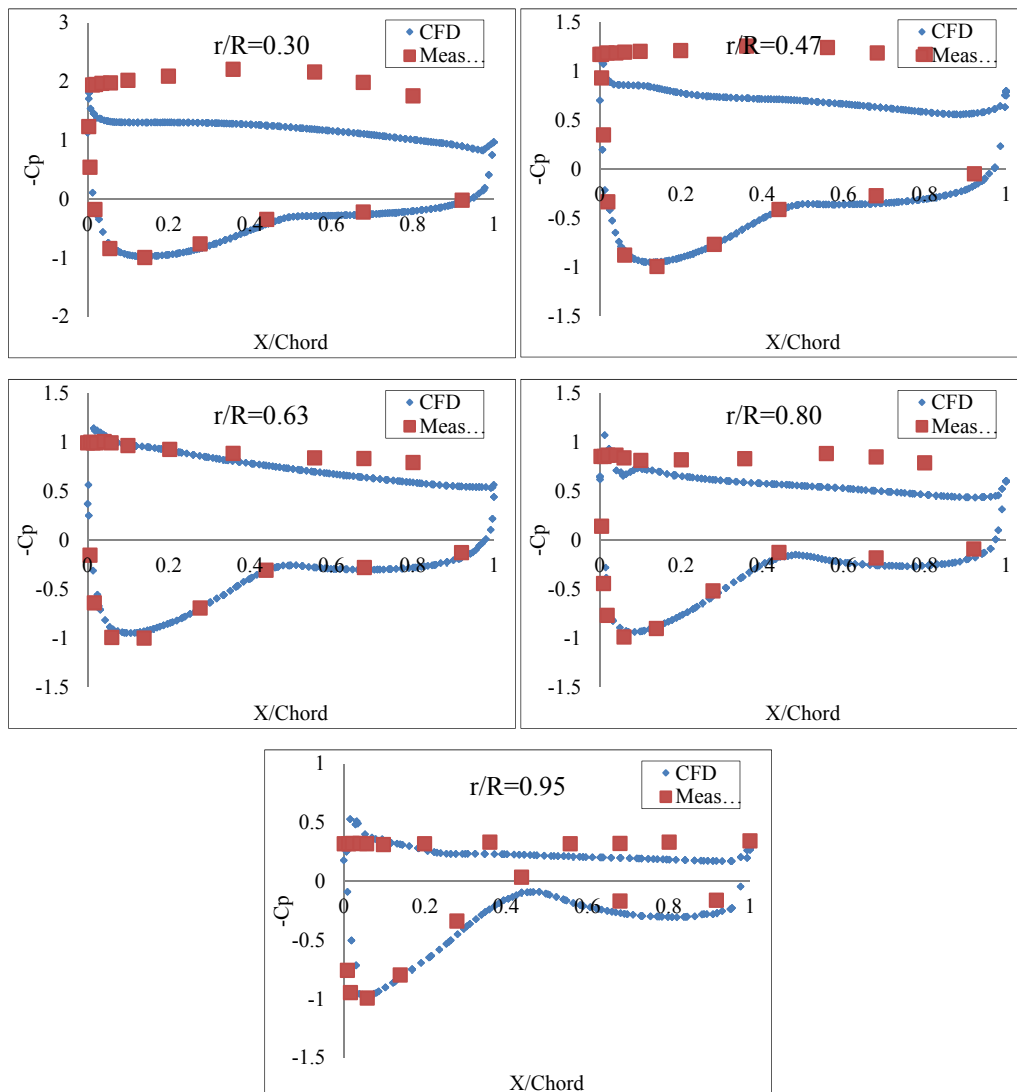
Figure 5-30 Pressure distributions of CFD predictions and measurements at 25m/s

5.3.2.4 Blade Surface Limiting Streamlines and Pressure Contour

Figure 5-31 shows the blade surface limiting streamlines and pressure contours for both pressure side and suction side of the blade at wind speed from 7m/s to 25m/s. These streamlines have the same trends as the streamlines reported in scientific literatures[41;43]. At wind speed of 7m/s, the direction of the flow near blade suction surface is almost parallel to the chord-wise direction, which means most of the blade is covered by attached flows. At wind speed of 10m/s, span-wise flow occurs at more than half-span locations of the blade. At wind speed of 15m/s, the blade is almost dominated by full span-wise flow except for small chord-wise flow appears at the tip locations. For wind speeds from 15m/s to 25m/s, the whole blade is fully covered by span-wise flow,

which means deep-stall occurs and strong flow separation happens.

Pressure side   Suction side

V=7m/s

Pressure side   Suction side

V=10m/s

Pressure side   Suction side

V=15m/s

Pressure side   Suction side

V=20m/s

Pressure side   Suction side

V=25m/s
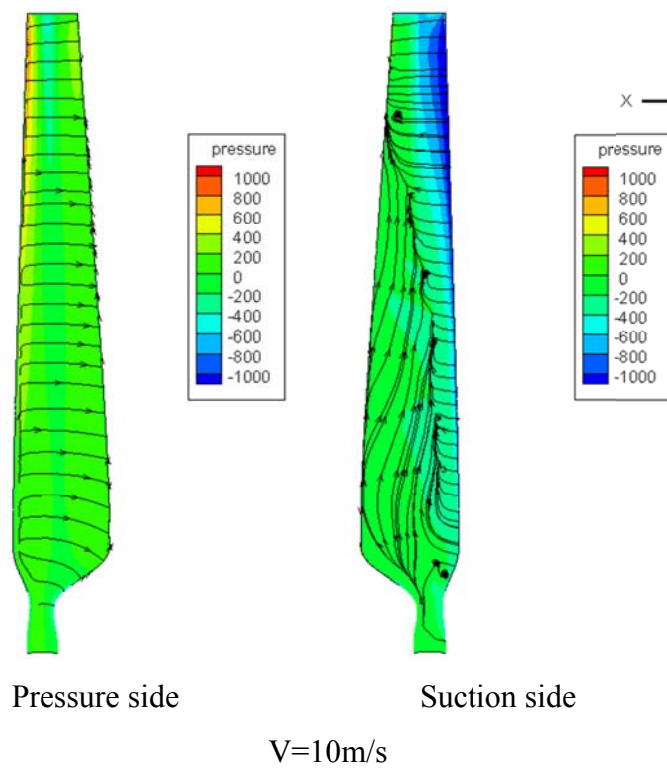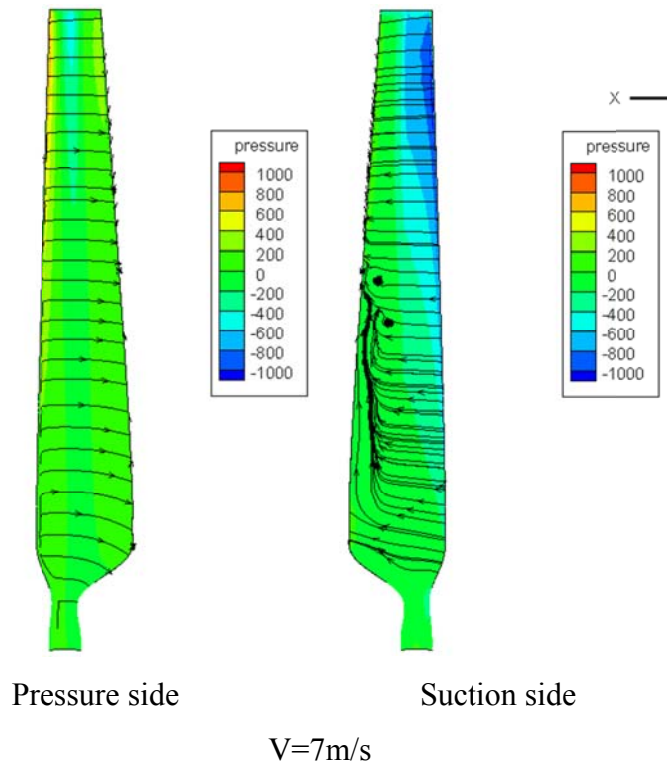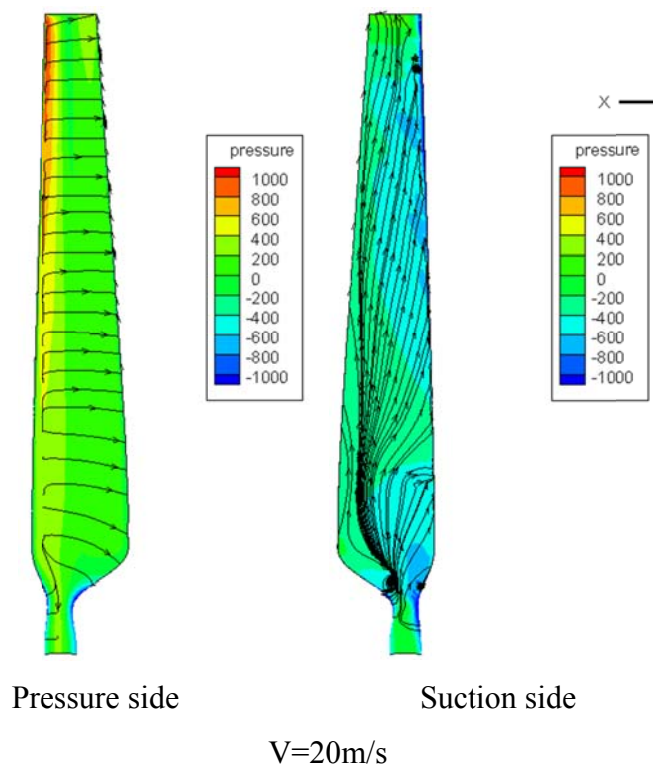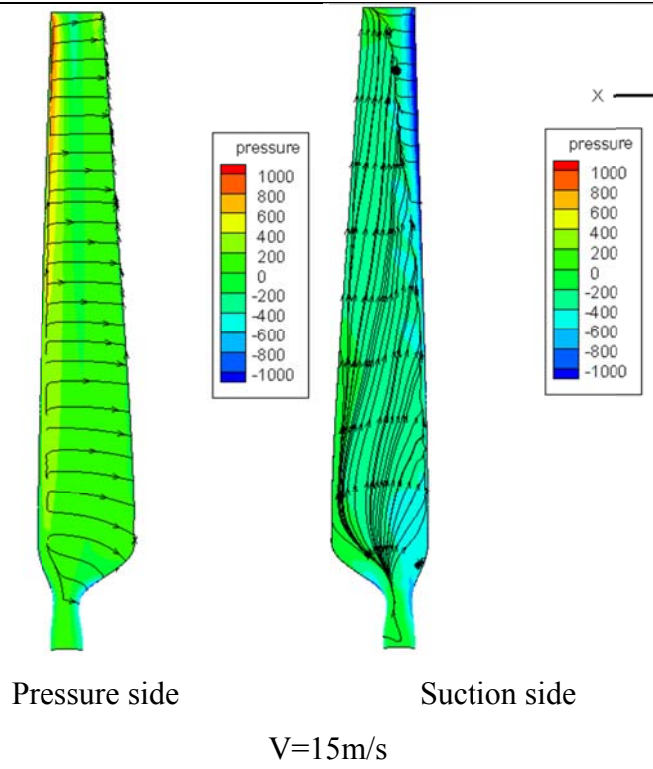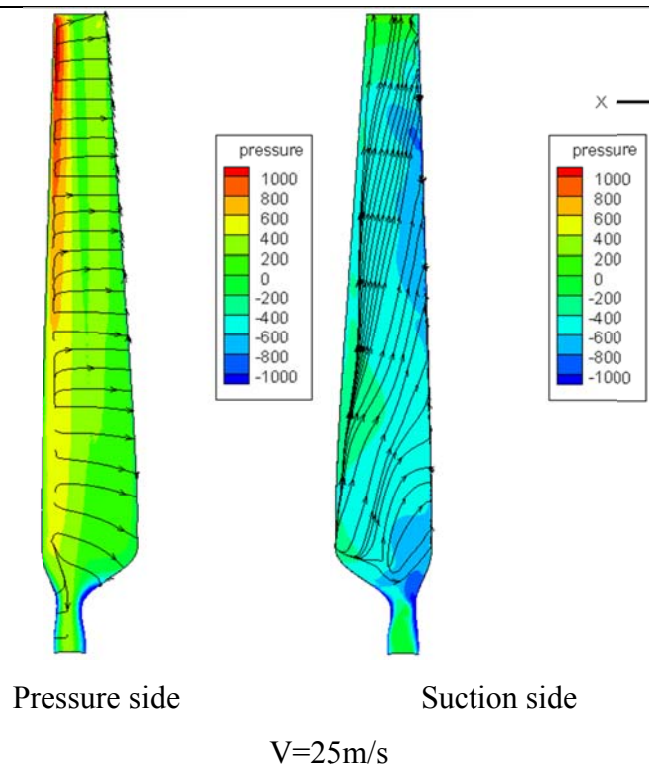
Figure 5-31 Surface limiting streamlines and pressure

5.3.2.5 Section Streamlines and Pressure Contour

The section streamlines and pressure contours at wind speeds from 7m/s to 25m/s are plotted from Figure 5-32 to Figure 5-36. Overall, the stall is stronger with a higher wind speed and the flow separation is stronger for inner locations than outer locations.

To compare different sections at a one wind speed: at wind speed of 7m/s, most of the blade span locations are covered by attached flows except for very weak flow separation at 47% radius and 63% radius. At wind speed of 10m/s, more than half of the blade span locations are dominated by separated flows. The flow separation of inner span locations is stronger than that of the outer locations. Above wind speed of 15m/s, the whole span of the blade is observed with flow separation, and the flow separation point moves towards leading edge from outer locations to inner locations. These observations lead to the conclusion that the stall (flow separation) is stronger at the span sections 47% and 63% than other sections, and the stall is relatively weak at tip sections. The weak stall at 30% radius is mainly due to stronger rotational effects which delay stall. It is reasonable that the 47% radius section and 63% radius section are also affected by rotational effects, and the inner location has stronger rotational effects than the outer locations as indicated by other researchers [41;43;82].

To compare different wind speeds at one section: as shown in Figure 5-32, at span location of 30% radius, the flow is fully attached at wind speed of 7m/s and starts to separate from the trailing edge of the airfoil at 10m/s. The flow is fully separated from the airfoil leading edge above wind speed of 15m/s. As shown in Figure 5-33and Figure 5-34, at span location of 47% and 63% radius, a very weak flow separation at the trailing edge is observed at wind speed of 7m/s and a fully flow separation occurs above wind speed of 15m/s, while the flow separates at approximately middle location of the chord at wind speed of 10m/s. As shown in Figure 5-35 and Figure 5-36, at span location of 80% and 95% radius, the flow is fully attached at wind speed of 7m/s, while at wind speed of 10m/s, the flow is slightly separated at the trailing edge at 80%. At wind speed of 15m/s, the 80% radius and 90% radius locations are presented with separated flows. Above wind speed of 15m/s, the flow is separated at all the sections. These observations lead to the conclusion that the stall is enhanced with a higher wind speed.

As shown from Figure 5-32 to Figure 5-36, the visualisations of the pressure fields for all five span locations at wind speeds from 7m/s to 25m/s demonstrate that: stronger pressure suction (on the suction side) and larger pressure deficit (between the pressure side and suction side of the blade) occurs at a higher wind speed. The pressure suction and pressure deficit are more pronounced for inner sections compared with outer sections for all the wind speeds. This verifies the above analysis that the stall is stronger at inner sections especially at 47% and 63% sections and the stall enhances with an increase of wind speed.

More CFD data visualisation is presented in Appendix H.
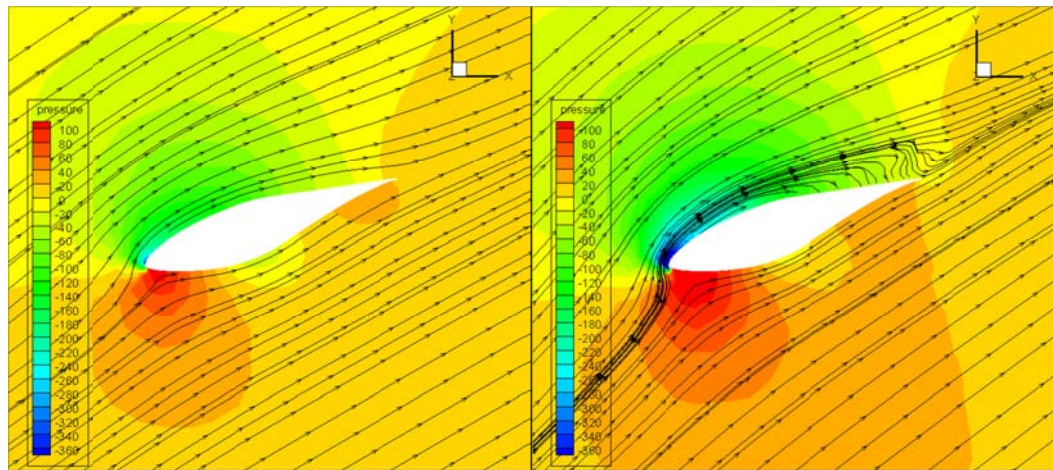
V=7m/s   V=10m/s
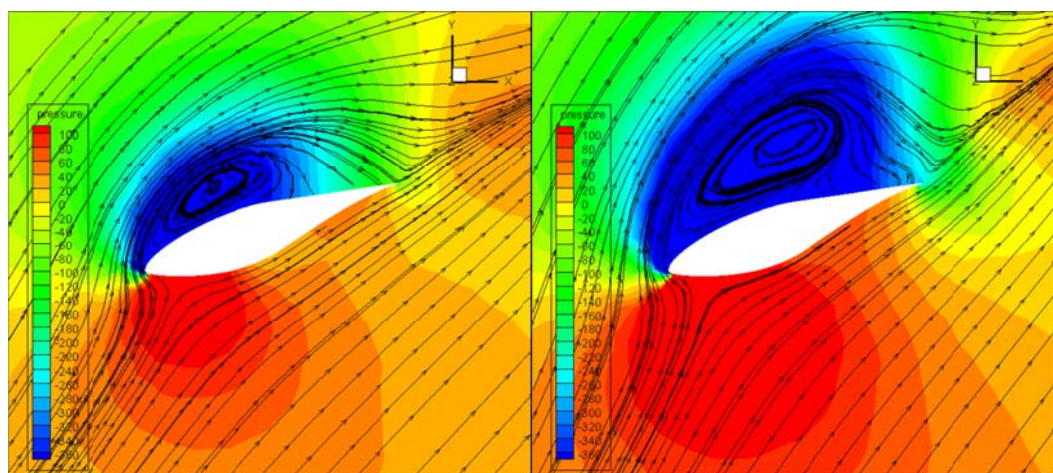
V=15m/s   V=20m/s
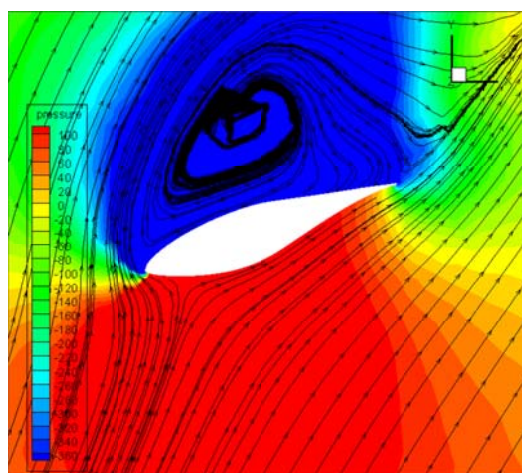
V=25m/s

Figure 5-32 Section streamlines at span location of 30%R
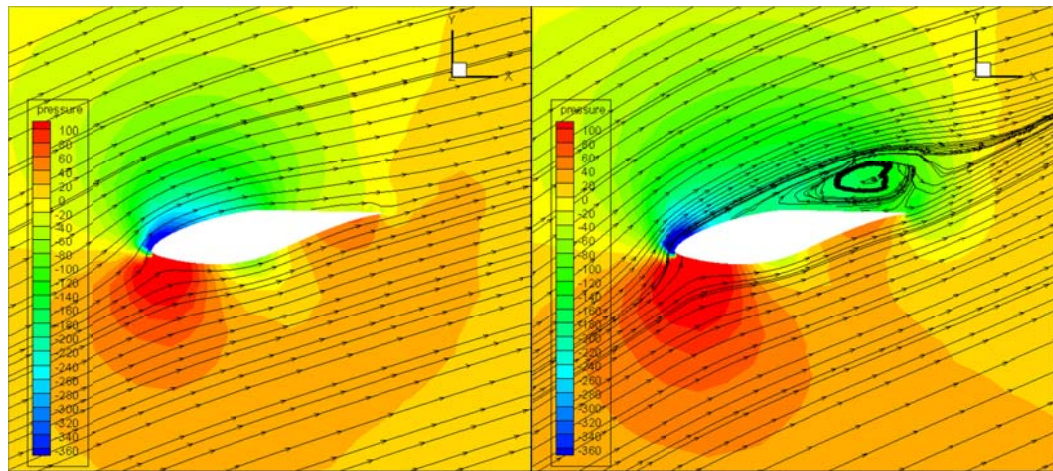
V=7m/s   V=10m/s
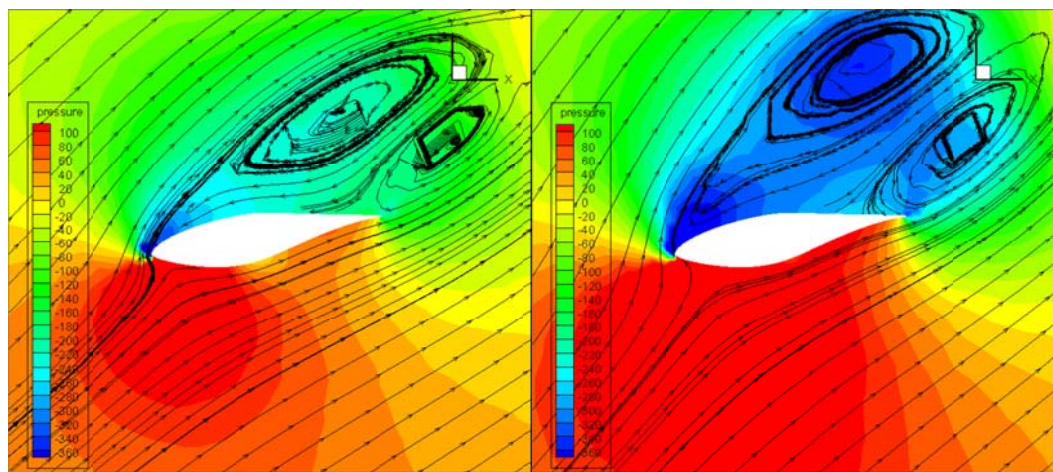
V=15m/s   V=20m/s
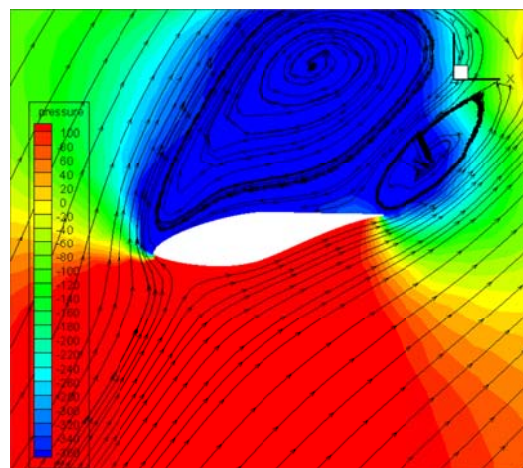
V=25m/s

Figure 5-33 Section streamlines at span location of 47%R

V=7m/s   V=10m/s

V=15m/s   V=20m/s

V=25m/s
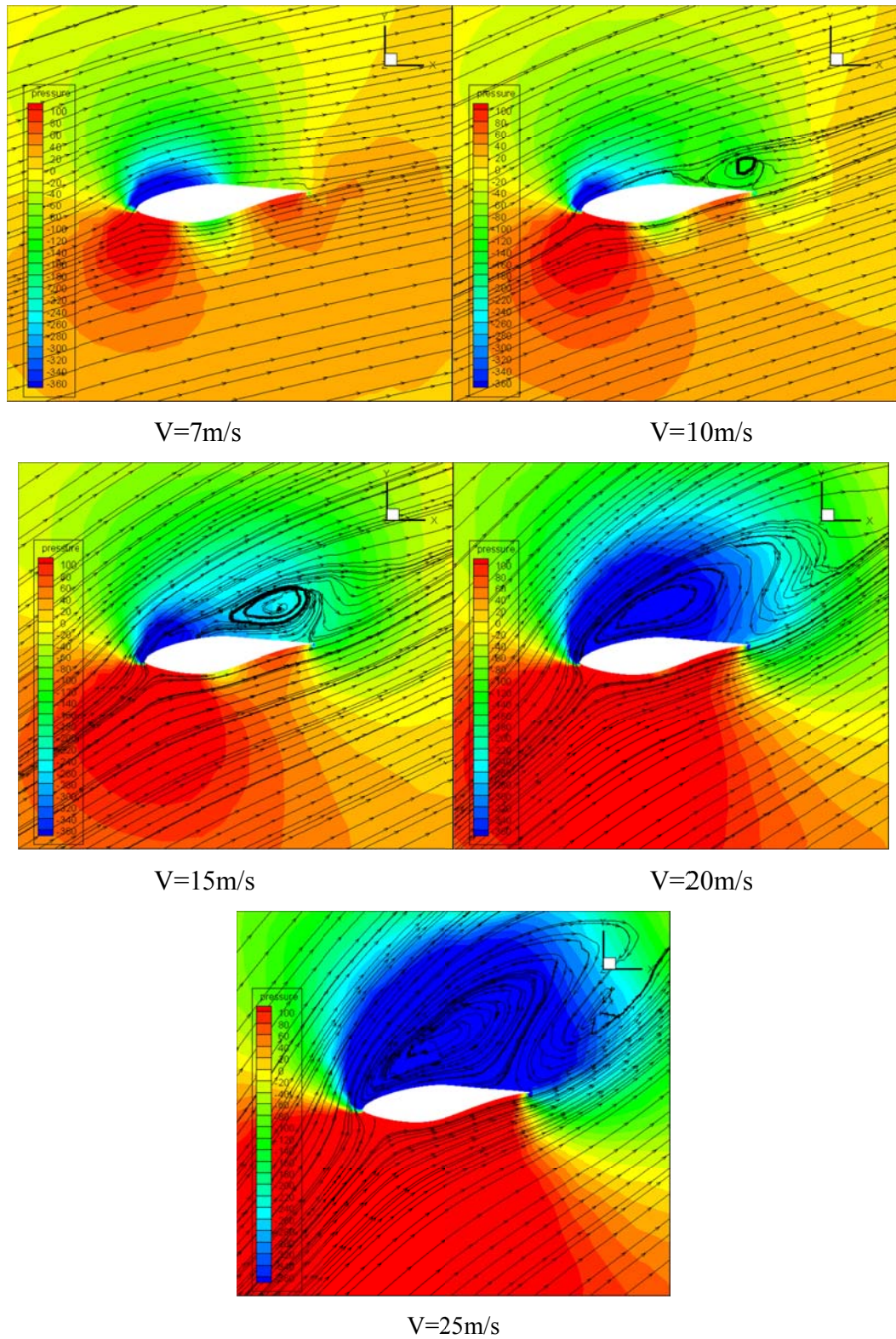
Figure 5-34 Section streamlines at span location of 63%R

V=7m/s   V=10m/s

V=15m/s   V=20m/s

V=25m/s
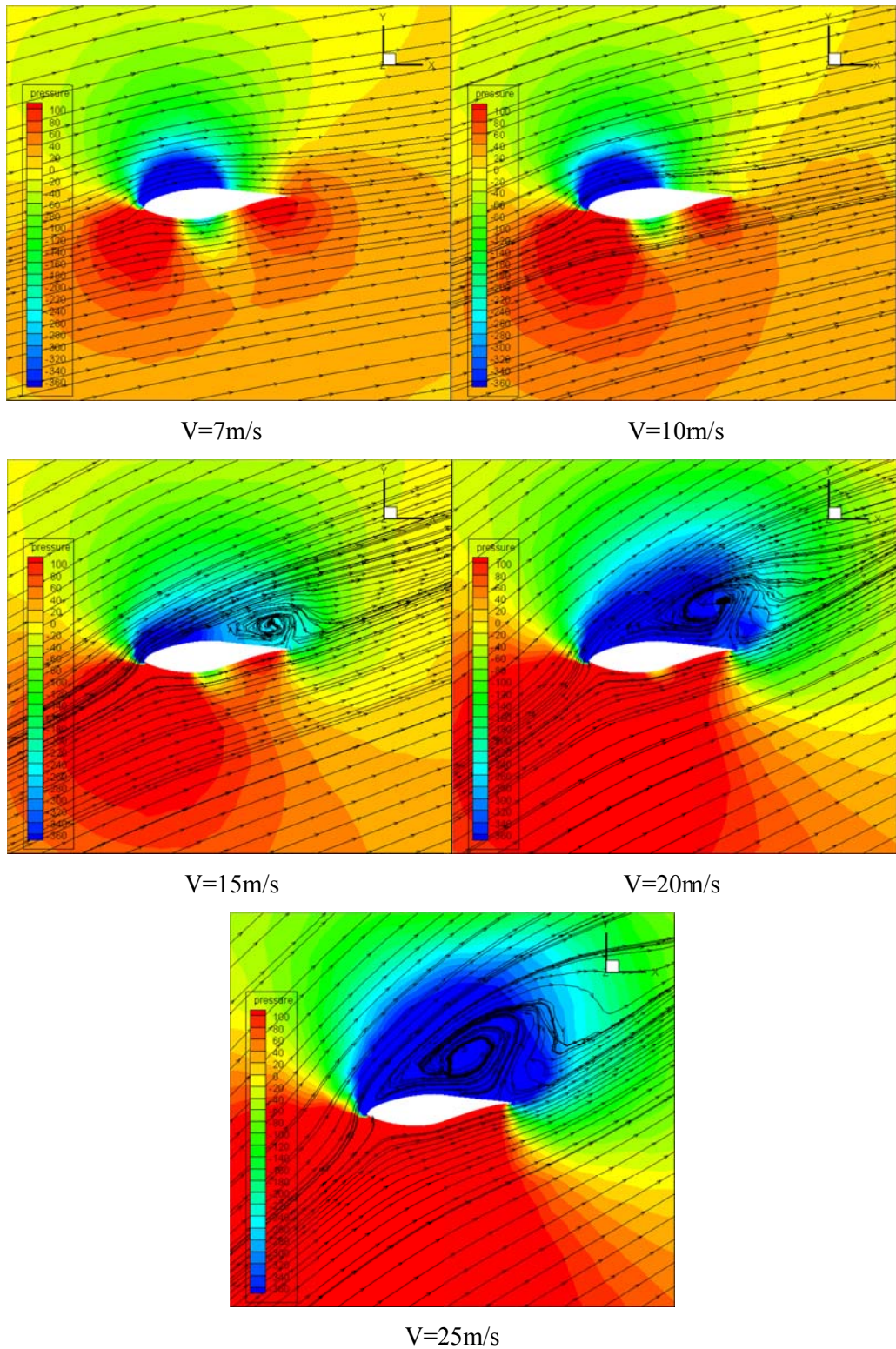
Figure 5-35 Section streamlines at span location of 80%R

V=7m/s   V=10m/s

V=15m/s   V=20m/s

V=25m/s
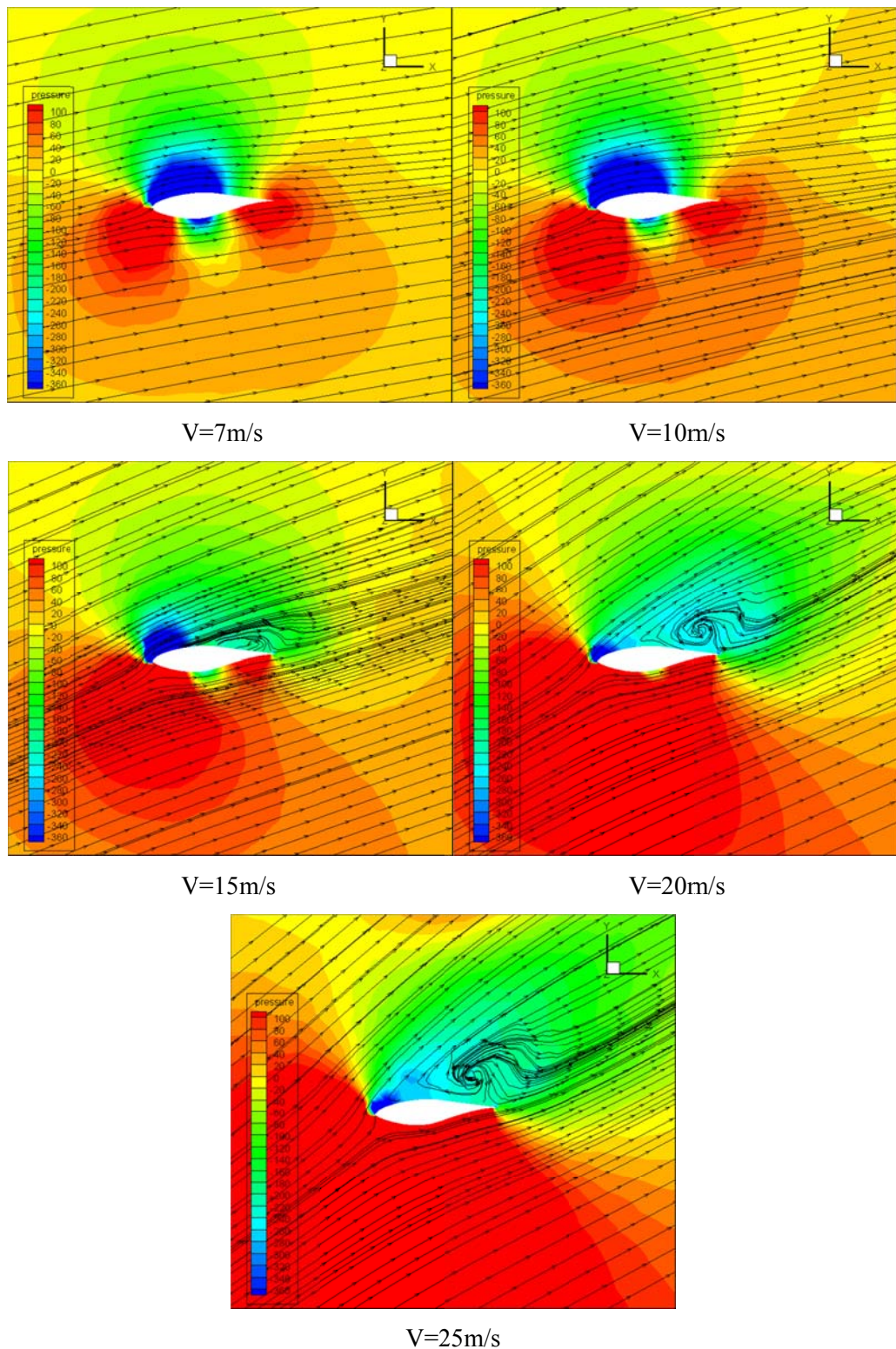
Figure 5-36 Section streamlines at span location of 90%R

5.4   Summary

This chapter investigated the 2D CFD modelling and 3D CFD modelling through validation study of the S809 airfoil and NREL/NASA Phase VI wind turbine

measurements.

In the 2D CFD modelling, a study on mesh dependency and turbulence dependency was conducted. Results show that the mesh node numbers around the airfoil affect the accuracy of the prediction for a rough mesh resolution. For a high mesh resolution, the accuracy is improved but more computing time is needed. Comparing with measured results, the SST transition model shows better agreement in drag coefficient prediction than the fully turbulent SST k-ω model. The quasi-3D CFD modelling produces very similar results in lift and drag coefficients prediction but needs more computing time compared with 2D CFD modelling.

In 3D CFD modelling, a series of computations were conducted and validated with measured torques and pressure distributions. Results show good qualitative and quantitative agreements with the measurements and other research work in scientific papers. The purposes of validation and deep insight view of detailed flows for stall phenomenon have been fully achieved.

The comparative study of mesh dependency and turbulence models is instructive for any kind of wind turbine CFD modelling. These modelling methods are employed in analysis of BEM-designed wind turbines in Chapter 6.

CHAPTER 6   CFD ANALYSIS OF BEM-DESIGNED WIND TURBINES

6.1   Introduction

Since no aerodynamic data of airfoil DU93-W-210 at low Reynolds numbers (below 5×10^5) is available in literature, the aerodynamic performance of the airfoil DU93-W-210 is experimentally and numerically studied. Based on the CFD modelling methods in Chapter 5, the characteristics of DU93-W-210 airfoil are analysed and investigated through wind tunnel tests and 2D CFD modelling in Section 6.2. The 3D CFD calculated results for the two BEM-designed FPVS and FPFS wind turbines are discussed and compared with the BEM calculated results in Section 6.3 and Section 6.4. A short summary is made in Section 6.5.

6.2   Wind Tunnel Test and 2D CFD Modelling

6.2.1. Wind Tunnel Experiment Setup

The wind tunnel tests of the airfoil DU93-W-210 were performed in a subsonic low turbulence closed return wind tunnel in the Aerodynamics Laboratory at University of Hertfordshire (UH). The wind tunnel is 1.145m×0.845m in test cross-section area with a maximum wind speed of 25m/s and equipped with a six-balance system for measuring lift, drag and pitching moments. To achieve the desired Reynolds numbers and ensure an appropriate blade aspect ratio, the airfoil section model was designed to be 0.3m in chord and 0.8m in span length. According to the definition of Reynolds number (i.e. $Re = UC/v$, where U is the free stream velocity, C is the chord length, v is the kinematic viscosity which is 14.8×10^{-6}m²/s for the air, and the air density is 1.2kg/m3 at the temperature of 20°C in the wind tunnel tests, a relative low Reynolds number from 2×10^5 to 5×10^5 can be achieved. Having a constant chord and with no twist along the span, the testing model was made from Sikablock M650 by Computer Numerical Control (CNC) machining to keep a good consistency in the whole length span. The

upper and lower surfaces were sanded with p1000-grit sand paper to have an approximately roughness equal to 0.018mm. The smoothed and clean airfoil section model is shown in Figure 6-1.

Figure 6-1 The DU93-W-210 airfoil section model

The airfoil section model was mounted horizontally spanning across the width of the test section of the wind tunnel, as shown in Figure 6-2. The wind velocities were set at 10m/s, 15m/s and 25m/s to achieve different low Reynolds numbers from 2×10^5 to 5×10^5 respectively. The testing rig was controlled by a computer control system and the angles of attack of the airfoil were changed from -5° to 23° with an increment of 1°. Very high angles of attack (higher than 23°) were not tested due to severe flow separation and vibration occurred during the tests.

Figure 6-2 Wind tunnel test facility and mounting scheme

6.2.2. Data Correction

The tested raw data were calibrated with boundary corrections which are specified as blockage correction, buoyancy correction and streamline curvature correction [117;118].

Blockage correction includes solid blockage correction and wake blockage correction. Solid blockage refers to the flow velocity increase due to the effective area decrease while a testing model is settled down in the test section of the wind tunnel. The correction of solid blockage is expressed as equation (6.1). Wake blockage refers to an increased drag force due to the decrease of velocity in the wake of the airfoil and increase of velocity out of the wake, which is corrected in equation (6.2). Buoyancy is the phenomenon of a decrease in static pressure due to the boundary layer growth at the test section walls, which leads to an additional drag force. With a constant area of the test section, this kind of effect is negligible. The boundary-layer growth of the tunnel walls was considered in velocity correction by Selig. According to Selig [118], the main effect of the buoyancy (circulation effect) can be considered in the velocity correction in equations (6.3) and (6.4) with a factor of K_{vel}. Streamline curvature is used to describe the phenomenon of the flow which is squeezed by the physical constrains of the test section, thus the airfoil effective camber is increased which leads to an increase in lift force, moment and angle of attack. The corrections of lift force, moment and angle of attack are addressed in equations (6.5), (6.7) and (6.8).

$$\varepsilon_{sb} = \frac{0.74V_m}{A^{3/2}} \tag{6.1}$$

$$\varepsilon_{wb} = (\frac{c}{2h})C_{du} \tag{6.2}$$

$$V_c = V_u K_{vel}(1 + \varepsilon_{sb} + \varepsilon_{wb}) \tag{6.3}$$

$$K_{vel} = 1.015755 - 0.0002391V_u + 0.00001712\sqrt{V_u} + \frac{0.1296}{\sqrt{V_u}} \tag{6.4}$$

$$C_l = C_{lu}(1 - \sigma - 2\varepsilon_b) \tag{6.5}$$

$$C_d = C_{du}(1 - 3\varepsilon_{sb} - 2\varepsilon_{wb}) \tag{6.6}$$

$$C_m = C_{mu}(1 - 2\varepsilon_b) + \frac{1}{4}\sigma C_{lu} \tag{6.7}$$

$$\alpha = \alpha_u + \frac{57.3\sigma}{2\pi}(C_{lu} + 4C_{m,c/4u}) \tag{6.8}$$

$$\sigma = \frac{\pi^2}{48}(\frac{c}{h})^2 \qquad (6.9)$$

where,

V_m is the volume of the airfoil section model,

c is the chord of the airfoil section model,

h is the inner height of the wind tunnel test section,

A is the area of the wind tunnel test section.

Note here, subscript c denotes corrected value and u uncorrected value, ε_b is the total blockage correction including the solid blockage correction ε_{sb} and the wake blockage correction ε_{wb}.

The corrected lift and drag coefficients at wind speeds from 10m/s to 25m/s are plotted in Figure 6-3 and Figure 6-4. Detailed Data are tabled in Appendix D. The lift and drag coefficients show the same trends at these three wind speeds. The lift coefficients were observed to be very similar at linear region (low angles of attack). The drag coefficients decrease slightly with the increase of wind speeds for all tested angles of attack.
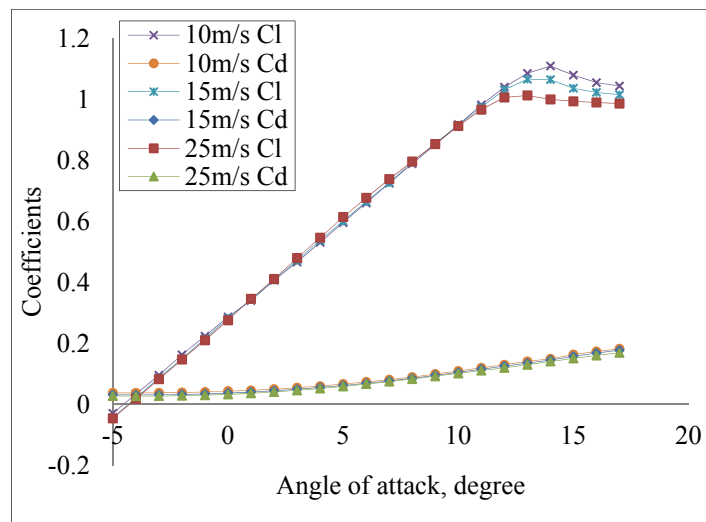
Figure 6-3 Lift and drag coefficients at different wind speeds from UH wind tunnel tests
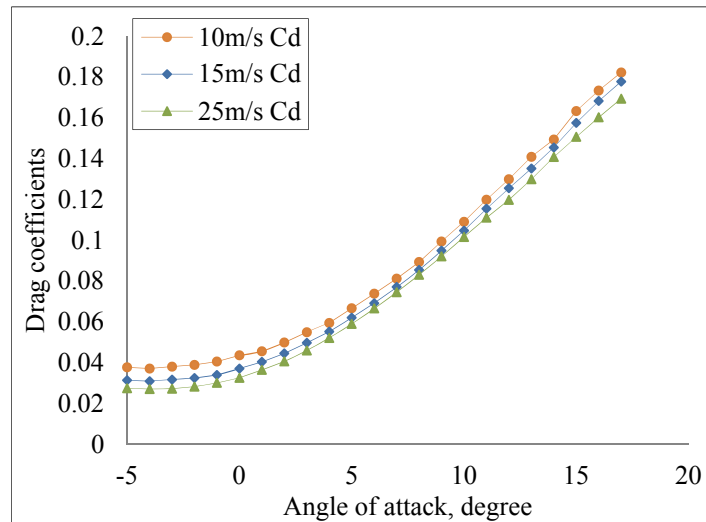
Figure 6-4 Drag coefficients at different wind speeds from UH wind tunnel tests

As shown in Figure 6-3 and Figure 6-4, the lift coefficient increases linearly with the angle of attack before stall for all the three Reynolds numbers. The drag coefficient increases gradually as the angle of attack increases. The lift coefficients coincide well with each other for these Reynolds numbers at low angles of attack, and the same finding as other researchers reported is that with the higher Reynolds number, the higher lift and the lower drag were observed. Although the lift slope changed slightly for these three low Reynolds numbers, it was found that the stall occurs earlier at a higher Reynolds number. The stall angle moves from 14° to 12° with the Reynolds number changing from 2×10^5 to 5×10^5, while the stall angle of the same airfoil is around 10° at 1×10^6 [93].

6.2.3. 2D CFD Modelling of DU93-W-210 Airfoil

6.2.3.1 2D CFD Method

The flow domain is "C" type which is 15 times the chord length in radius in front of the airfoil (upstream) and 21 times the chord length behind the airfoil (downstream). The same chord length of the tested airfoil section model is used in CFD, i.e. 300mm. The hexahedral mesh block strategy in ICEM CFD is defined in Figure 6-5. 160 nodes (a=160) are distributed around the airfoil and 180 nodes (n=180) are located normal to the airfoil edges with a growth ratio of 1.2. 140 nodes (t=140) are located behind the airfoil with a growth ratio of 1.2 and 80 nodes (m=80) are set at the trailing edge. These

nodes lead to a total mesh number of 103,909 cells for the whole flow domain.
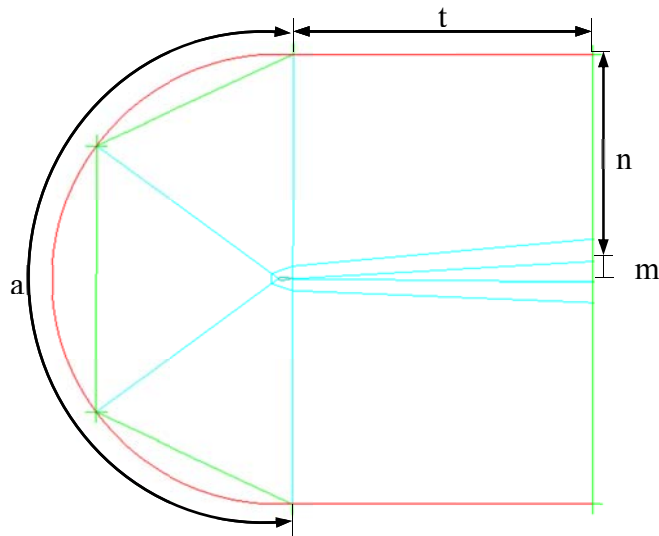
Figure 6-5 Mesh block strategy in ICEM

An overall view of the mesh domain and a large view of the mesh near the airfoil are shown in Figure 6-6. Velocity inlet and pressure outlet boundary conditions are applied, and the airfoil is defined as no-slip wall. A second order upwind, Gauss-node based spatial discretization scheme is used for all the cases. A series of simulations are conducted for angles of attack from -5° to 25°.
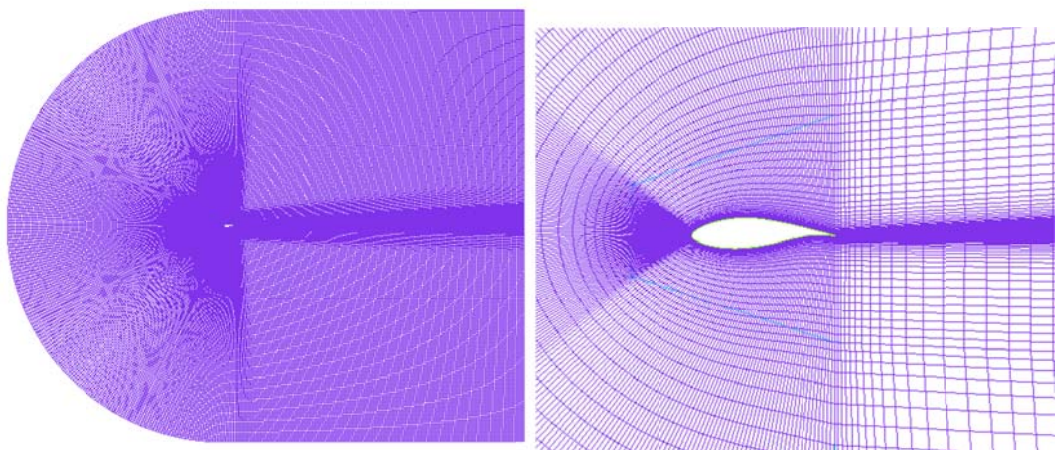
Figure 6-6 Mesh around airfoil and domain size

6.2.3.2 Results and Discussion

The CFD calculated lift and drag coefficients at Reynolds number of 2×10^5 (corresponding to 10m/s) are compared with test results in Figure 6-7 and Figure 6-8.

Good agreements between the calculated results and wind tunnel test results were achieved at low angles of attack using both the SST k-ω model and the transition SST model. At high angles of attack where stall occurs, a better agreement with the test was shown by using the transition SST model. At deep-stall angles, the transition calculation is getting very unsteady and it takes longer time to converge. Although good agreements are demonstrated using these two models, apparent discrepancy occurs between the tested values and calculated values of the drag coefficient. This may be caused by the lack of correction of 3D flows in the wind tunnel tests. The flow pattern is not real 2D but 3D due to the absence of end boards. The wind tunnel tests can be further improved by adding end boards to avoid end flows. The turbulence intensity was not measured in the wind tunnel tests, which adds another uncertainty for the gradually increasing pattern in the plot of the drag coefficients, as shown in Figure 6-8.
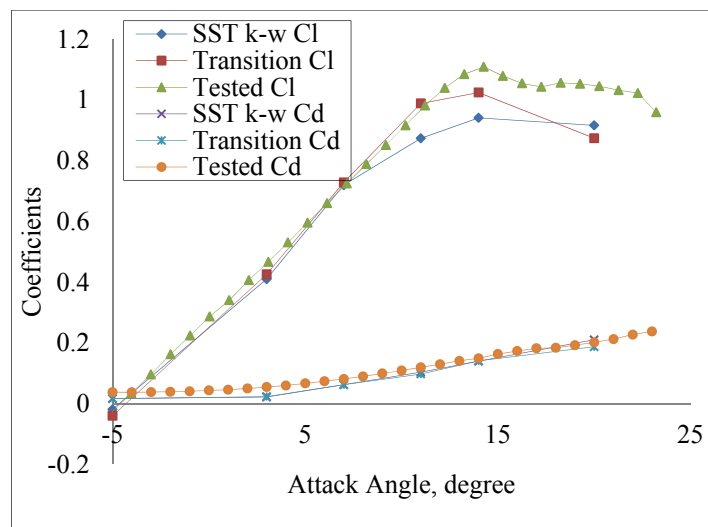
Figure 6-7 Lift and drag coefficient comparison at Reynolds number of 2×10^5
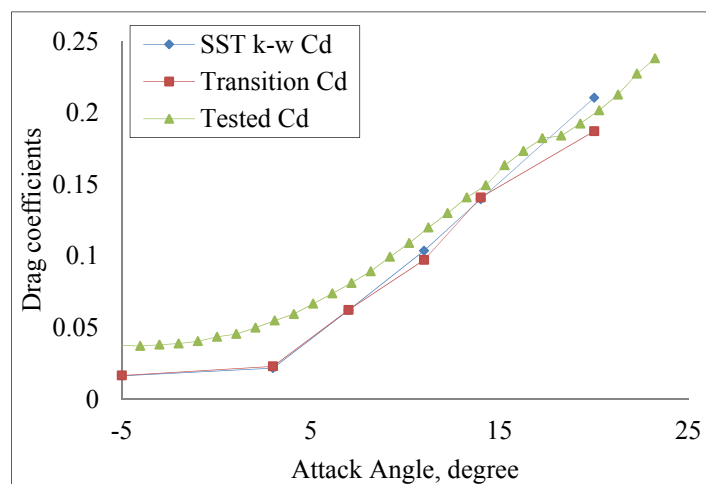
Figure 6-8 Drag coefficient comparison at Reynolds number of 2×10^5

The calculated and tested lift, drag and moment coefficients at different Reynolds

numbers from 2×10^5 to 3×10^5 are presented from Figure 6-9 to Figure 6-11. An overall agreement has been achieved between the calculated and tested coefficients. All these CFD results were calculated using the SST k-ω model. Comparing to the measurements, the SST k-ω model under-predicts the lift and drag coefficients at high angles of attack. it is likely that the stall is early-predicted by the SST k-ω model. It is noted that the measured drag coefficients are much higher than the calculated results for all Reynolds numbers. There are possible reasons for this: the flow pattern in wind tunnel tests was not actually two-dimensional due to the gap between the ends of airfoil section model and the wind tunnel side walls. The flow tends to escape from the two ends of the airfoil section model, which is a complex three-dimensional flow. These complex flows at the ends of the airfoil section model affected the drag measurements.
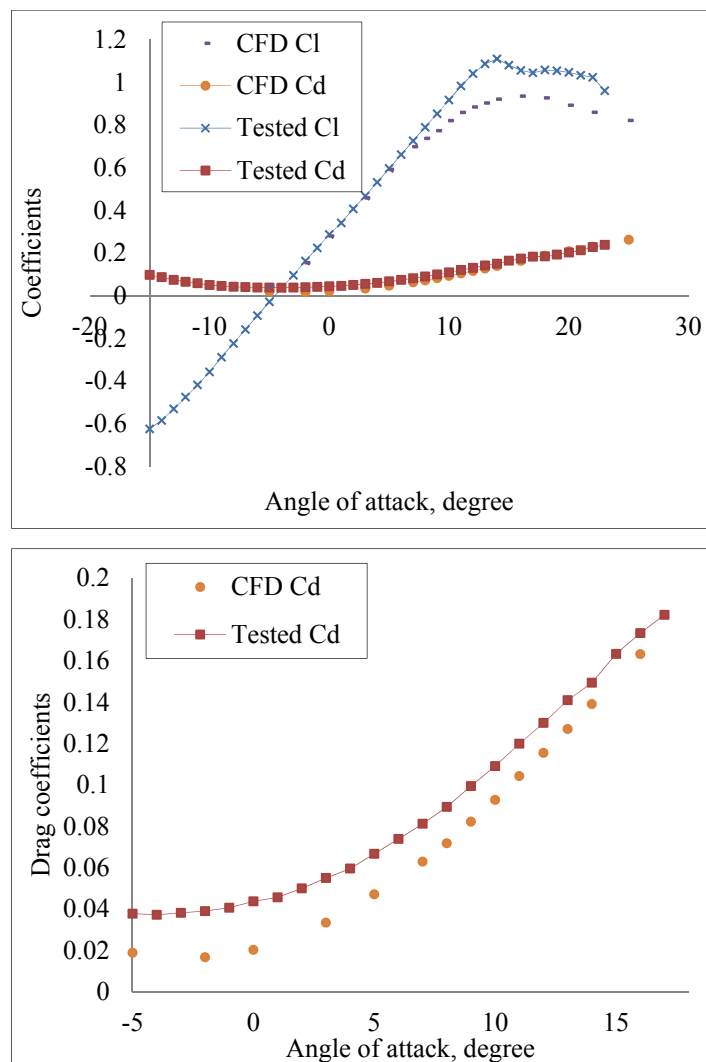
Figure 6-9 Lift and drag coefficients at Reynolds number of 2×10^5
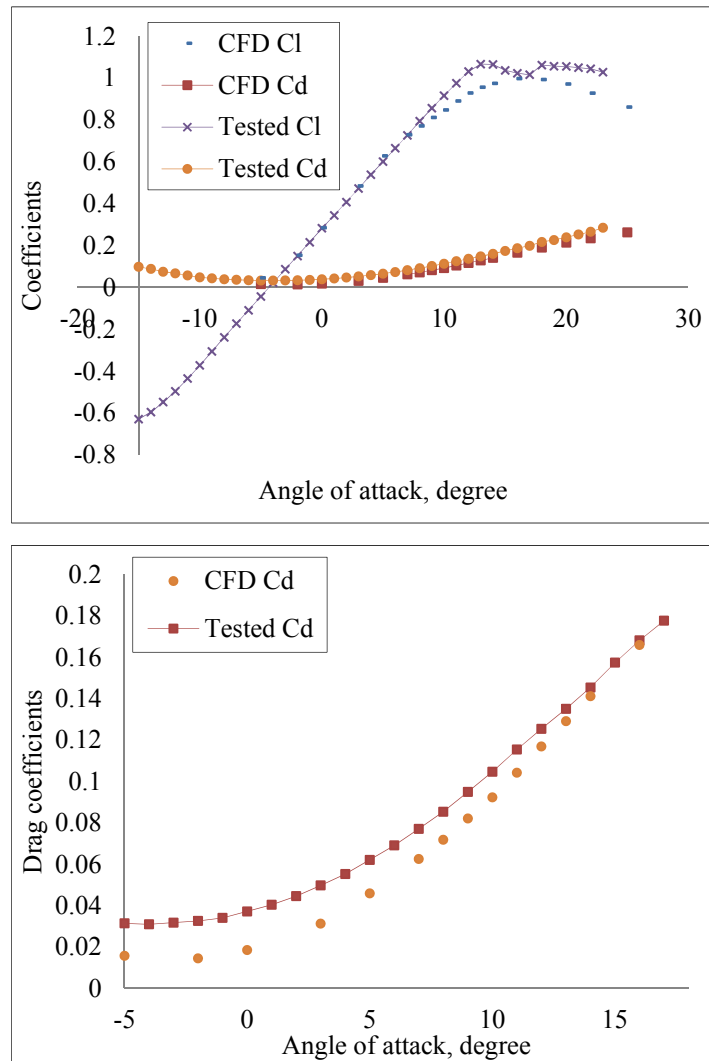
Figure 6-10 Lift and drag coefficients at Reynolds number of 3×10^5
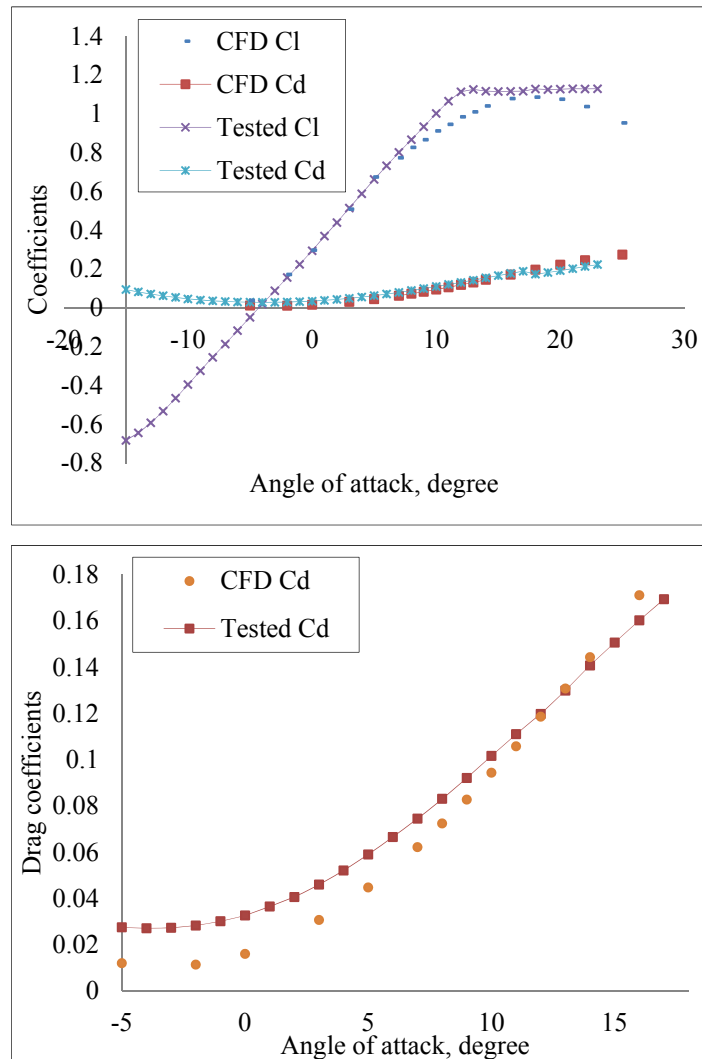
Figure 6-11 Lift and drag coefficients at Reynolds number of 5×10^5

6.3 3D CFD Analysis of FPVS Wind Turbine Rotor

6.3.1. 3D CFD Method

This section addresses the methodology employed in 3D CFD modelling of the BEM-designed 10kW FPVS wind turbine. The blade geometry with mixed airfoils (see Section 4.2) is shown in Figure 6-12. The designed wind turbine rotor is 5m in radius and the blade is 4.775m long. The three blades of the rotor are symmetry and only one blade is needed in the CFD modelling. Figure 6-13 presents the mesh domain size and boundary conditions. The mesh domain is a one-third sector shape and divided into two sub domains: inner (rotational) domain and outer (stationary) domain. As shown in

Figure 6-13, the radius of the velocity inlet boundary is 25m and the radius of the pressure outlet boundary is 40m. The velocity inlet boundary is 25m in front of the rotor plane and the pressure outlet boundary is 75m behind the rotor plane. The inner rotational domain is 5.6m in radius and 1.6m in length. These two domains are defined in a multiple reference frame, and interfaces are set at the coincided faces between the rotational domain and the stationary domain. Periodic boundary conditions are used at the sector planes to reduce calculation time. The wind turbine blade is regarded as a rotating wall with no slip.
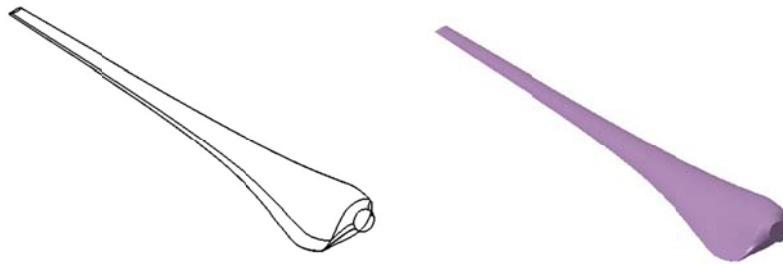
Figure 6-12 Blade geometry of the FPVS mixed airfoil wind turbine
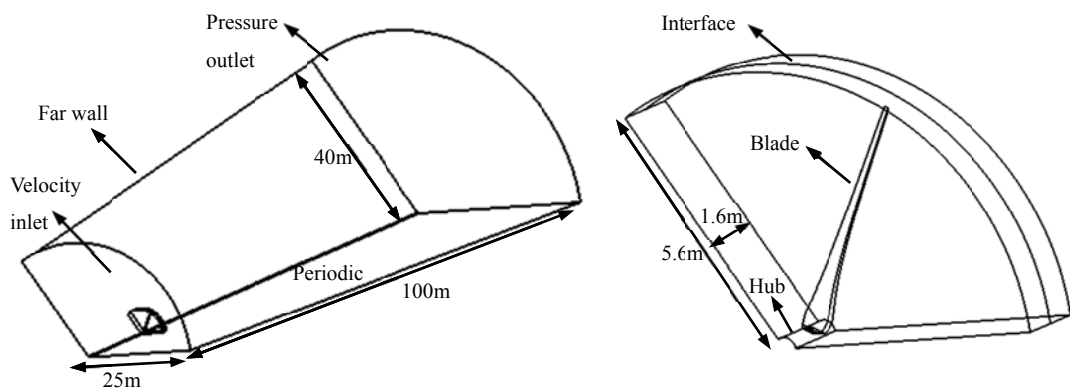
Figure 6-13 Mesh domain of the FPVS mixed airfoil wind turbine

The inner domain is meshed with tetrahedral cells and the outer domain with hexahedral cells. The minimum height of the first layer mesh near blade surface is 0.9mm. The inner mesh domain is meshed with 3,038,599 cells and the outer domain with 1,130,732 cells, which result in a total number of 4,169,331 cells. All the cases were calculated in transient mode with the SST k-ω model and converged with the residuals below10^{-5}. A total of 1000 steps were simulated with time step of 0.0005s. In this case, 1000 steps are equal to 0.5 seconds. The rotor speed is 130rpm, thus 0.5s are equal to 1.08 revolutions. The simulations were run as transient simulations which were time-dependent.
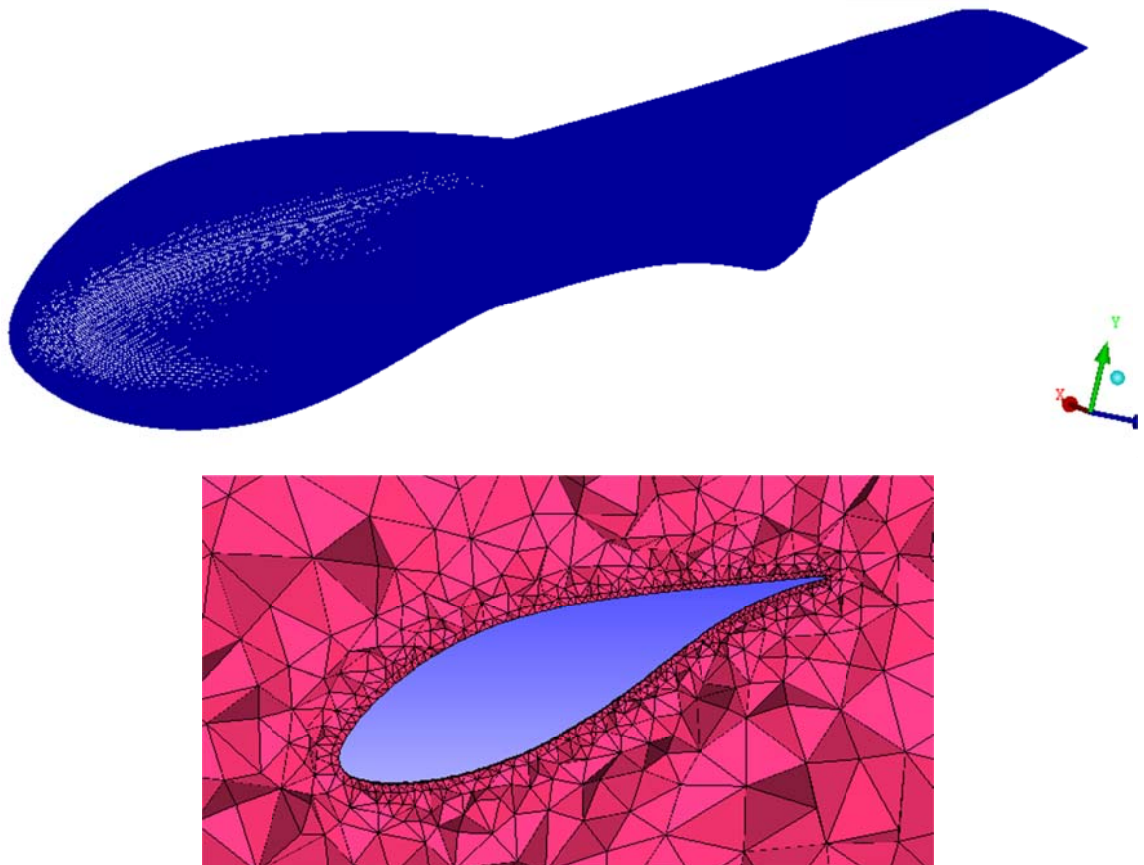
Figure 6-14 Blade surface mesh and section view of the mesh

6.3.2. Results and Discussion

6.3.2.1 Power Prediction

A series of 3D CFD calculations were conducted by fixing the tip speed ratio under wind speed of 8.5m/s. The rotor speed variation is shown in Table 6-1. The air density in the CFD calculation is 1.225kg/m^3, the air viscosity is 17.89kg/m^{-1}s^{-1}, (The air density in wind tunnel tests is 1.2 kg/m^3, this should not bring big difference to the results), and the turbulence intensity is 1%.

Wind speed (m/s)	Tip speed ratio	Rotor speed (rad/s)
5	8	8
6	8	9.6
7	8	12.5
8	8	12.8
8.5	8	13.6

Table 6-1 Calculation conditions of the FPVS wind turbine

Three series of results from the BEM methods were obtained regarding to the

coefficients from the UH wind tunnel tests, XFOIL and 2D CFD modelling in Section 6.2. Coefficients at high angles of attack are extrapolated from the standard flat plate theory as described in Chapter 3 and linear interpolation is applied in the BEM methods.

A comparison of the power curves from the BEM methods and the CFD method is showed in Figure 6-15. The 3D CFD calculated power curve has the same trends as those from the BEM methods with different coefficients except for slight under-prediction at wind speed of 8.5m/s. The BEM method with XFOIL coefficients predicts a higher power output compared with the other results. This is mainly due to the over-prediction in lift coefficients as stated in Section 4.2.1. The BEM methods with the 2D CFD coefficients and UH tested coefficients produce very similar results. The same trends of these results are mainly because this wind turbine operates at a fixed design tip speed ratio where no flow separation exists. The 3D CFD over-predicts the power output compared with the BEM method using 2D CFD coefficients and UH tested coefficients, and under-predicts the power output compared with the BEM method using the coefficients calculated from XFOIL.
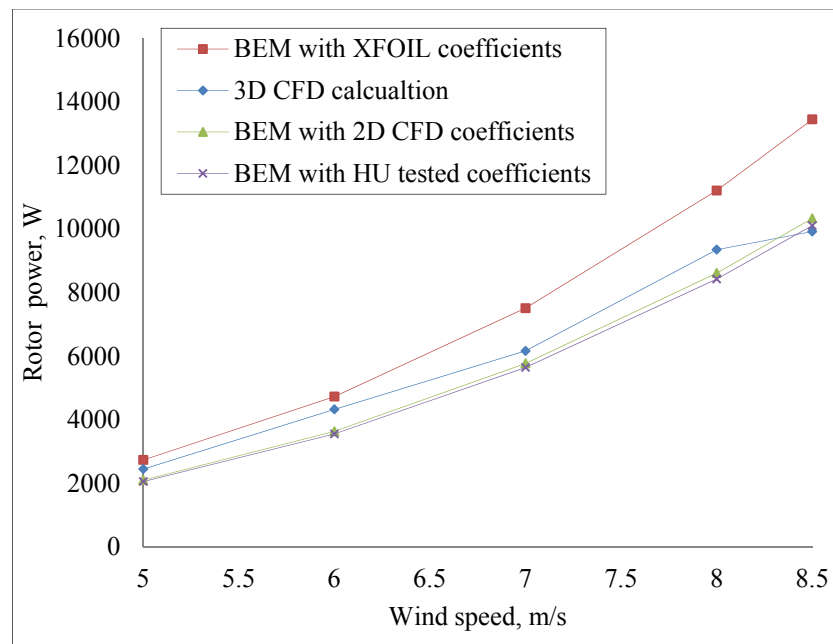
Figure 6-15 Power curves of 3D CFD and BEM results with fixed tip speed ratio of 8

In order to have a further deep insight of the flow separation of this mixed airfoil blade, more CFD calculations were conducted for the blade at a fixed rotor speed of 130RPM. Figure 6-16 plots the power curves predicted using the 3D CFD method and the BEM method at a fix rotor speed of 130RPM. A good agreement has been achieved between 3D CFD and BEM with 2D CFD coefficients at wind speeds of 7m/s and 8.4m/s.

Discrepancies exist at wind speeds of 10m/s and 12m/s where flow separations take place. This can be referred to Figure 6-18 which shows the streamlines and pressure contours at four span locations of 1m, 2m, 3m, and 4m. It gives also the same conclusion as above that the 3D CFD over-predicts the power output compared with the BEM method using 2D CFD coefficients and UH tested coefficients.
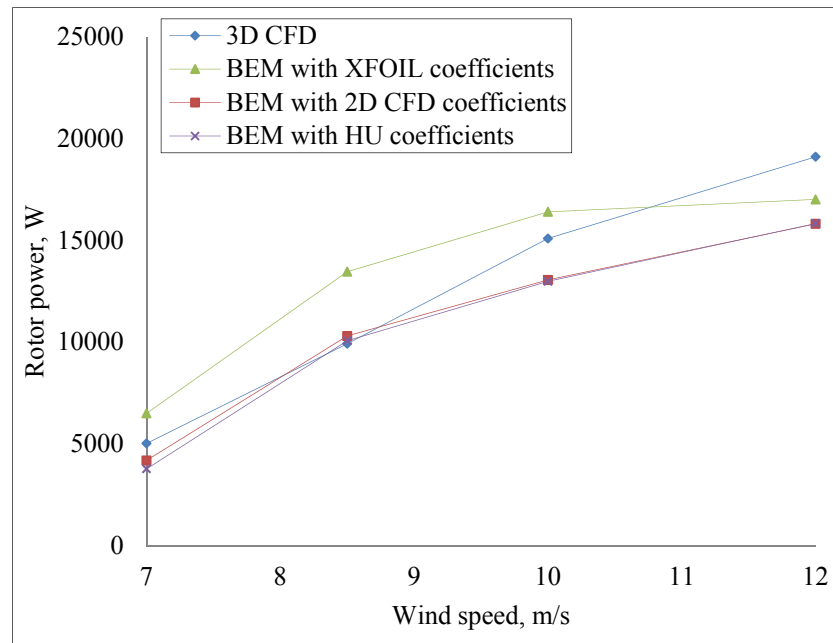
Figure 6-16 Power curves of 3D CFD and BEM with fixed rotor speed of 130RPM

6.3.2.2 Blade Surface Limiting Streamlines

Figure 6-17 shows the blade surface streamlines of the pressure side and suction side at wind speeds of 7m/s, 8.5m/s and 12m/s with a fixed rotor speed of 130RPM. At wind speeds of 7m/s and 8.5m/s, no flow separation is visible. The flow direction is parallel to the chord-wise direction as a single airfoil blade. At wind speed of 12m/s, apparent span-wise flows occur at the suction side of the blade.

Pressure side at 7m/s and 130RPM

Suction side at 7m/s and 130RPM

Pressure side at 8.5m/s and 130RPM

Suction side at 8.5m/s and 130RPM

Pressure side at 12m/s and 130RPM

Suction side at 12m/s and 130RPM
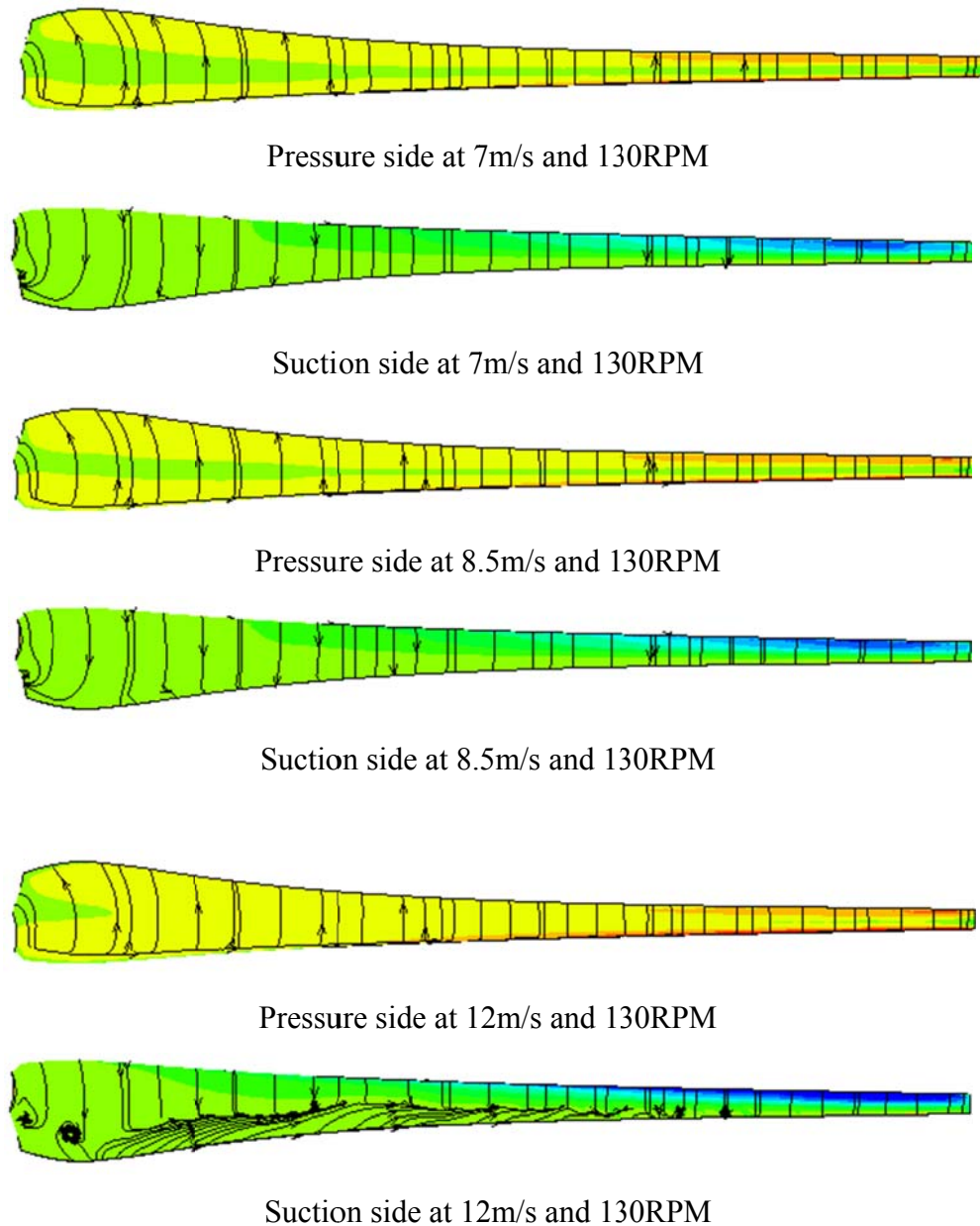
Figure 6-17 Blade surface limiting streamlines

6.3.2.3 Section Streamlines and Pressure Contour

Figure 6-18 presents the streamlines and pressure contours of four sections (0.2R, i.e. 1m, 0.4R, i.e. 2m, 0.6R, i.e. 3m and 0.8R, i.e. 4m) at wind speeds of 8.5m/s and 12m/s with a fixed rotor speed of 130RPM. At wind speed of 8.5m/s, the flow is fully attached along the blade. At high wind speed of 12m/s, weak flow separation exists at location of 0.2R, moderate flow separation occurs at location of 0.4R and 0.6R, and no flow separation is observed at location of 0.8R.
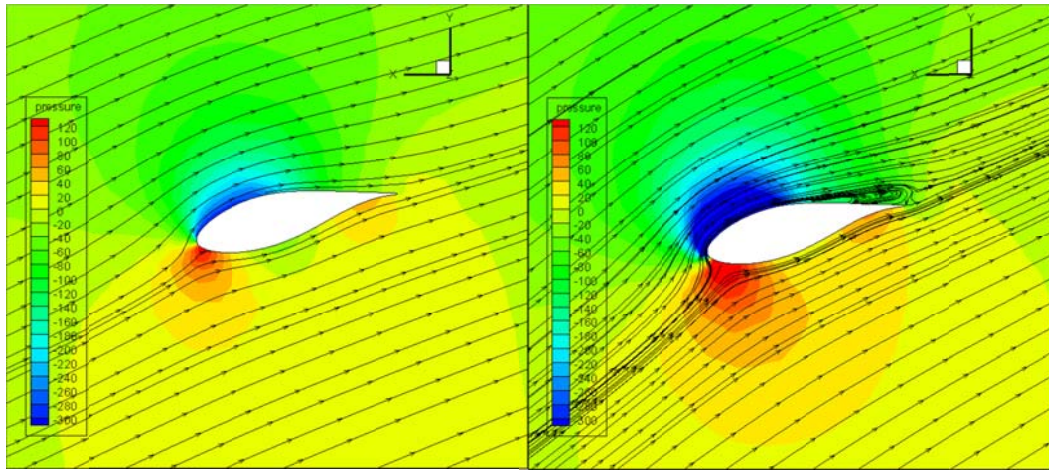
V=8.5m/s   V=12m/s

Span location=0.2R
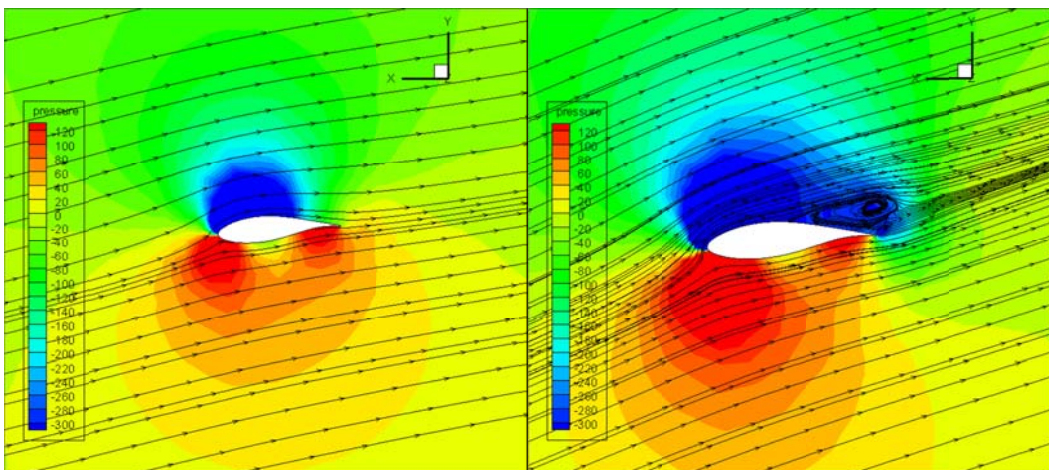
V=8.5m/s   V=12m/s

Span location=0.4R

V=8.5m/s   V=12m/s
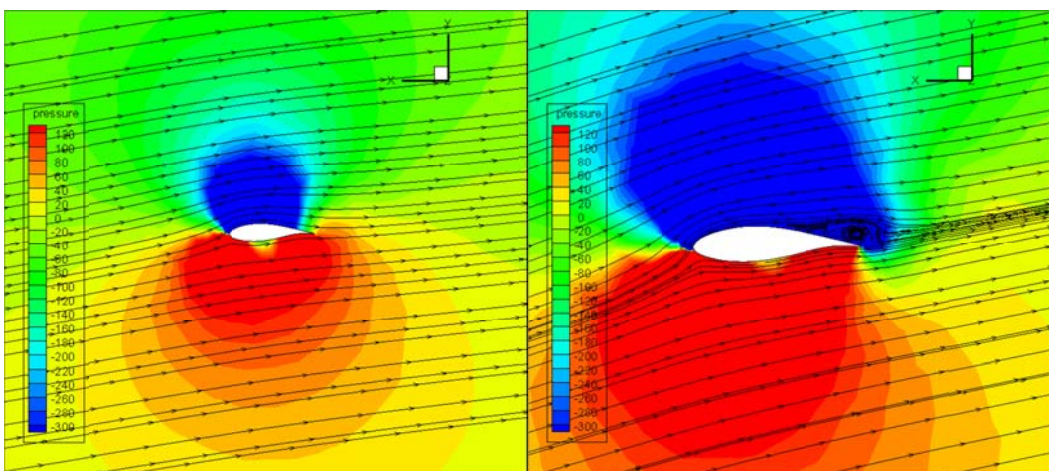
Span location=0.6R

V=8.5m/s   V=12m/s

Span location=0.8R
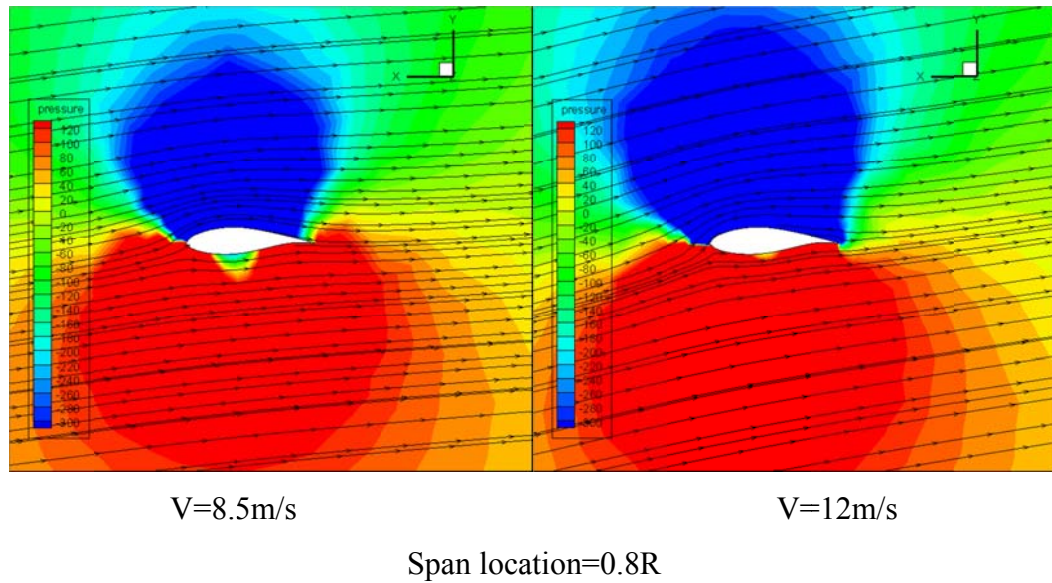
Figure 6-18 Section streamlines and pressure contour at wind speeds of 8.5m/s and
12m/s

6.4   3D CFD Analysis of FPFS Wind Turbine Rotor

6.4.1. 3D CFD Method

The same method described in Section 6.3.1 is employed for the 3D CFD of FPFS wind
turbine blades with airfoil S809. The blade geometry is shown in Figure 6-19. The mesh
domain size and boundary conditions are presented in Figure 6-20 and the blade mesh is
depicted in Figure 6-21. A total number of 4 million mesh cells are produced by ICEM,
and the minimum height of the first layer near the blade surface is 0.48mm. The time
step is 0.0005s, and a total of 1000 steps which is equal to 0.5s are simulated. After
about 48 hours of iteration, the calculated rotor torque converged at residual of 10^{-5}.
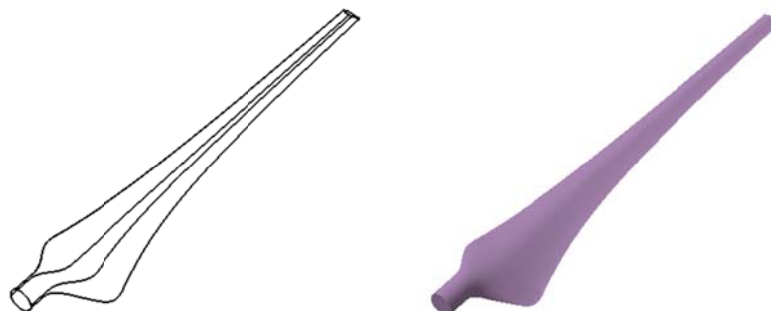
Figure 6-19 Blade geometry of the FPFS wind turbine
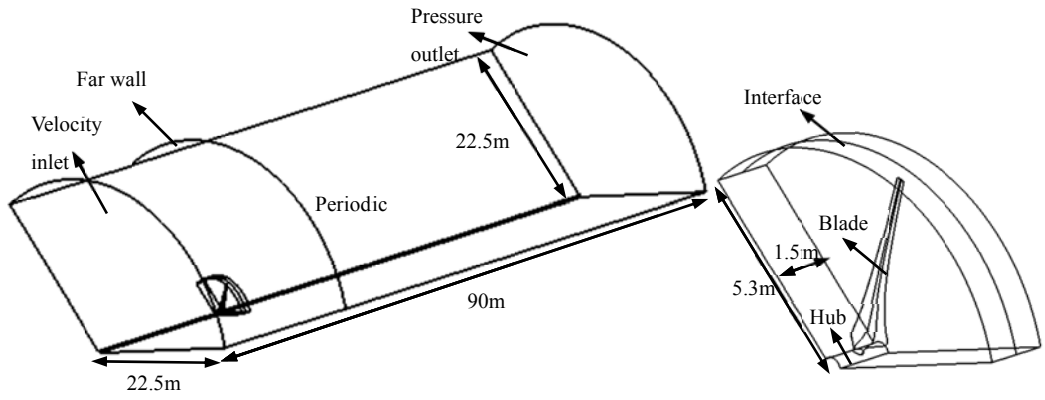
Figure 6-20 Mesh domain of the FPFS airfoil wind turbine
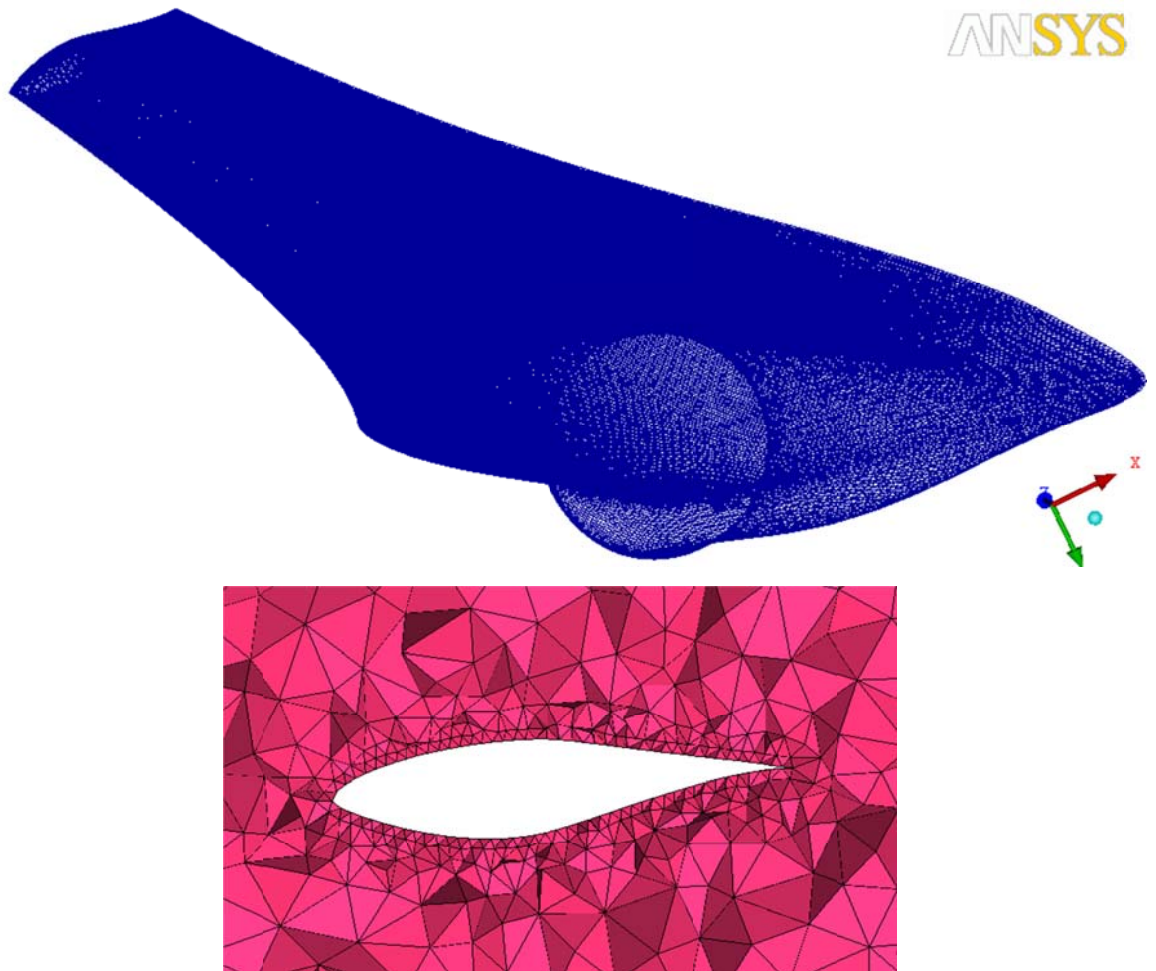
Figure 6-21 Blade surface mesh and section view of the mesh

6.4.2. Results and Discussion

6.4.2.1 Power Prediction

Figure 6-22 presents the power curve calculated from the 3D CFD method and the BEM method using the TUDelft wind tunnel coefficients from 0° to 20° and extrapolated coefficients from the standard flat plate theory and the modified flat plate theory from 20° to 90°. In the standard flat plate method, equations (2.12) and (2.13) are used to extrapolate the coefficients at high angles of attack. In the modified flat plate method, equations from (3.2) to (3.5) are employed to derive the coefficients, and the lift coefficient at angle of attack of 45° is 1.3.

As shown in Figure 6-22, good agreements between the 3D CFD results and the BEM results at wind speeds of 7m/s, 8.4m/s and 10m/s. At wind speed 12m/s, the 3D CFD over-predicts the power output compared with the BEM method. Comparing to the BEM methods, the 3D CFD overall slightly over-predicts at low wind speeds while under-predicts at high wind speeds. Referring to Figure 6-23, the flow is fully attached at 8.4m/s along the blade, while flow separates near the trailing edge for some inner parts of the blade span locations at 10m/s. Moreover, most of the blade span locations are covered by separated flows at wind speed of 12m/s. It cannot be quantified the uncertainties in the calculated power from both the 3D CFD and the BEM methods at higher wind speeds are due to complex flow patterns. However, these methods provide reasonably good agreements in power prediction.
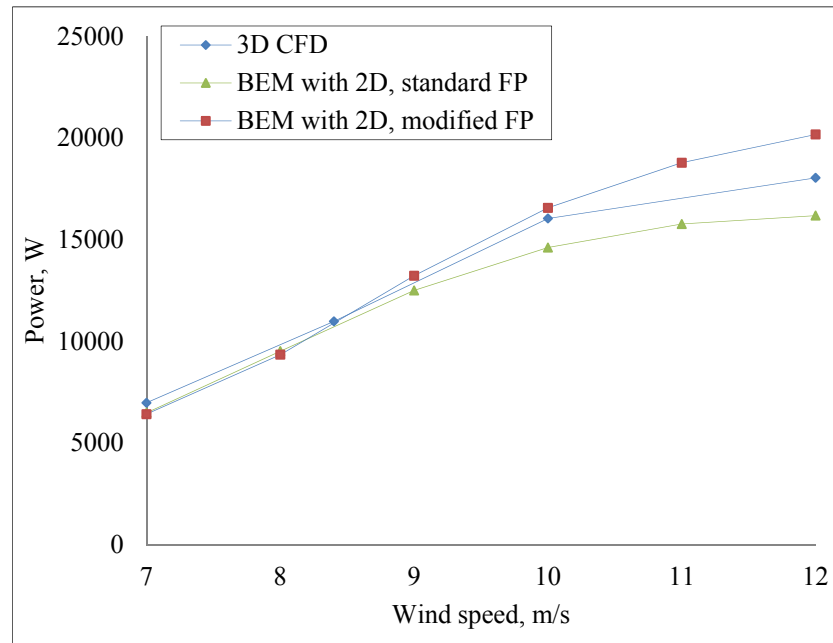
Figure 6-22 Comparison of 3D CFD and BEM results of the FPFS wind turbine

6.4.2.2 Blade Surface Limiting Streamlines

Figure 6-23 plots the blade surface streamlines of the FPFS wind turbine at different wind speeds with a fixed rotor speed of 124.8RPM. At wind speed of 8.4m/s, most of the blade surface is covered with chord-wise flows. At wind speed of 10m/s, small amount of span-wise flows near the trailing edge are observed at some inner parts of the blade span locations. At wind speed of 12m/s, apparent flow separation occurs at more than half span locations of the blade.
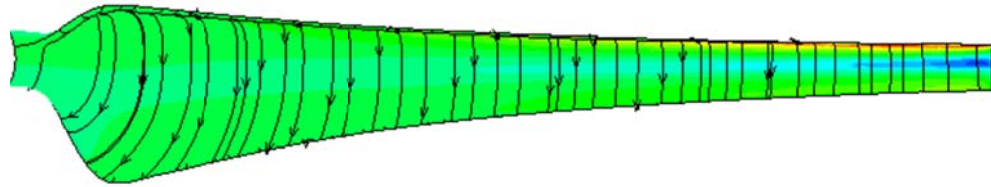
Pressure side at 8.4m/s and 124.8RPM
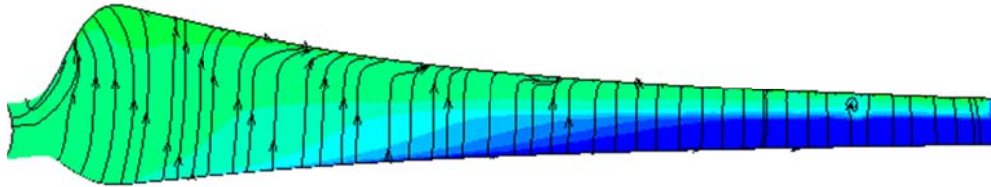
Suction side at 8.4m/s and 124.8RPM
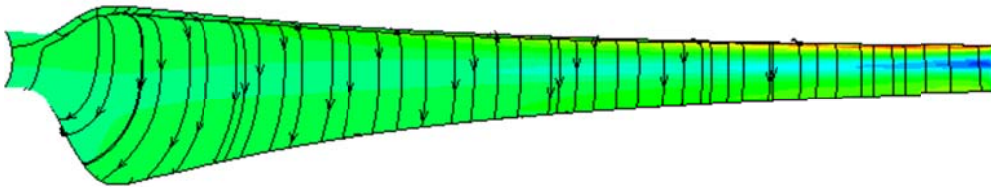
Pressure side at 10m/s and 124.8RPM
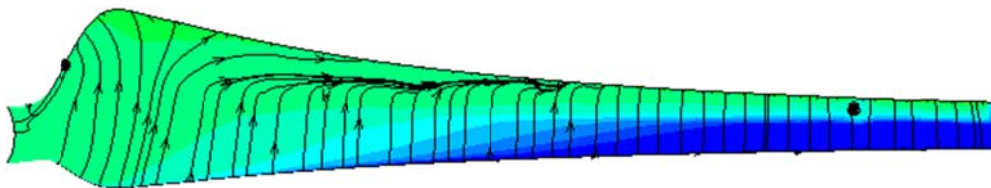
Suction side at 10m/s and 124.8RPM
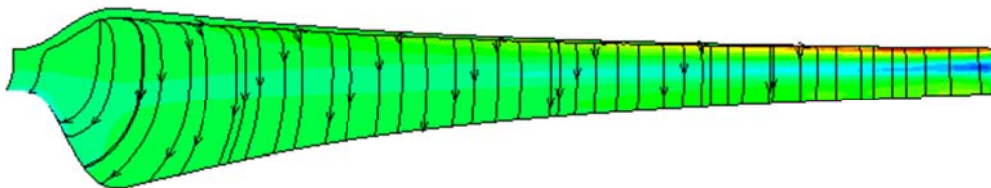
Pressure side at 12m/s and 124.8RPM
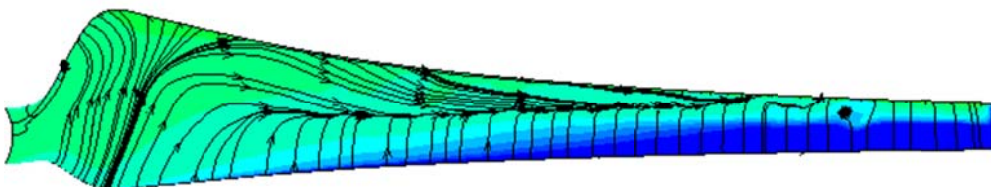
Suction side at 12m/s and 124.8RPM

Figure 6-23 Blade surface limiting streamlines at wind speeds of 8.4m/s, 10m/s and

12m/s

6.5 Summary

This chapter presented the 2D CFD analysis and wind tunnel tests of the DU93-W-210 airfoil at relatively low Reynolds numbers from 2×10^5 to 5×10^5, and the 3D CFD analysis of the two BEM-designed wind turbines as described in Chapter 4.

The wind tunnel tests were conducted at three wind speeds of 10m/s, 15m/s and 25m/s in the Aerodynamics Laboratory at the University of Hertfordshire. The lift, drag and moment coefficients of the airfoil DU93-W-210 were measured at this range of Reynolds numbers without any published data available. All the measured coefficients show the same trend at the three Reynolds numbers. The lift coefficients increase with the Reynolds number and the drag coefficients decrease with the Reynolds number, which indicates a higher lift to drag ratio is expected at a higher Reynolds number. The stall angle moves from 14° to 12° with Reynolds number changing from 2×10^5 to 5×10^5, while the stall angle of the same airfoil is around 10° at Reynolds number of 1×10^6 [93]. The wind tunnel test results and the 2D CFD results show reasonable agreements. It is noted that the measured drag coefficients are higher than the calculated drag coefficients. The discrepancies in drag coefficients are mainly due to the complex flows, which are caused by the gap between the ends of the airfoil section model and the wind tunnel side walls.

In the 3D CFD modelling of the FPVS wind turbine rotor, a series of calculations were carried out by fixing the tip speed ratio under wind speed of 8.5m/s. The power performance of the rotor is well predicted compared with the BEM methods. In order to have a further deep insight of the flow details, more calculations were done with a fixed rotor speed. The 3D CFD predicted blade surface streamlines reveal that before stall the flow direction is parallel to the chord-wise direction and the span-wise flow exists at high wind speeds.

For the FPFS wind turbine rotor, 3D CFD calculations were performed at four wind speeds before and after stall. The calculated results were then compared with the BEM results. Good agreements occur at 7m/s, 8.4m/s and 10m/s. The 3D CFD predicts a slightly higher power output at high wind speeds compared with the BEM method using the coefficients from the TUDelft wind tunnel test and the standard flat plate method.

Further the 3D CFD predicts lower power output compared to the BEM method with coefficients extrapolated from the modified flat plate method.

From the above analysis, it is concluded that the CFD approach is able to provide a more detailed qualitative and quantitative aerodynamic analysis for wind turbine blades and airfoils. With more advance turbulence models and more powerful computing capability, it is prospective to improve the BEM method regarding to 3D flow effects.

In the next chapter, the thesis summary is presented. Project major findings and contributions are highlighted, and recommendations for future work are addressed.

CHAPTER 7   CONCLUSIONS AND FUTURE WORK

This thesis presents the research that has applied BEM and CFD based approaches in small wind turbine blade design and analysis. The research works are summarised in Section 7.1, the major project findings and contributions are highlighted in Section 7.2, and future works in this field are recommended in Section 7.3.

7.1   Thesis Summary

This section provides an outline of the research works as presented in the previous chapters.

The BEM method with wake induction correction models and stall correction models were examined through power performance analysis of the NREL/NASA Phase VI wind turbine. For wake induction correction, the Glauert model, the GH-Bladed model and the AeroDyn model demonstrate very similar results for the studied case. Without stall correction, the BEM method with purely 2D coefficients under-predicts power output from moderate wind speed to high wind speed. With V-C stall correction model, the combined coefficients provide improved power prediction. With D-S stall correction model, the BEM gets good results at low wind speeds and over-predicts power outputs at high wind speeds. A hybrid stall correction model was proposed and it shows better power prediction compared with the previous discussed models. It is therefore concluded that the accuracy of stall correction models are highly wind turbine dependent and operation condition dependent. Further validation of these models with more wind turbine measurements is needed.

The BEM blade design philosophy was investigated through two most typical small wind turbines: fixed-pitch variable-speed (FPVS) wind turbine and fixed-pitch fixed-speed (FPFS) wind turbine. The effects of the key rotor parameters on power curve and AEP were thoroughly studied. These parameters as well as the blade chord

154

and twist angle distributions are determinative to wind turbine performance. A blade design approach of searching optimal induction factors was developed in MATLAB code to obtain the optimal blade chord and twist angle distributions. The tip-hub loss and drag effect were included in the blade design of a 12kW FPFS wind turbine. Results show that the tip-hub loss and drag have apparent effects on both blade hub and tip region. Considering F (tip-hub loss factor) and drag effects, smaller blade chord and twist angle occur for Hub and tip region. This finding is particularly interesting for the blade tip and Hub design and power performance improvement. Three different linearisation strategies of blade chord and twist angle distributions were investigated. The un-linearised twist strategy (only chord is linearised) demonstrate higher power production compared with the linearised twist angle strategy (both twist angle and chord are linearised). Considering less materials and higher AEP, it is preferable to linearize chord according to the preliminary outer sections. A heuristic approach of blade design optimization through linearisation of radial profile of the chord and twist angle for FPFS small wind turbines was developed. This approach can be used in any practical FPFS wind turbine blade design and refurbishment.

The 2D CFD modelling and 3D CFD modelling were validated against measurements of the S809 airfoil and the NREL/NASA Phase VI wind turbine. Mesh dependency and turbulence dependency studies were conducted. In 2D CFD modelling, results show that the mesh node numbers around the airfoil affect the accuracy of the prediction. With a high mesh resolution, the accuracy can be improved but more computing time is needed. The SST transition model demonstrates better agreement in drag coefficient prediction than the fully turbulent SST k-ω model compared with measured results. The quasi-3D CFD modelling calculations produce very similar results in lift and drag coefficients prediction but consume more computing time compared with 2D CFD modelling. In 3D CFD modelling, a series of detailed flow characteristics were obtained including integrated forces and moments, blade surface pressure distributions and flow streamlines. Results show good qualitative and quantitative agreements with the measurements and other research works from literatures. The purposes of validation and deep insight view of detailed flows for stall phenomenon have been fully achieved. The comparative study of mesh and turbulence models is instructive for any kind of wind turbine CFD modelling and definitely represents a foundation for future work.

The 2D CFD analysis and wind tunnel tests of the DU93-W-210 airfoil were implemented at relatively low Reynolds numbers from 2×10^5 to 5×10^5. The wind tunnel tests were conducted at three wind speeds of 10m/s, 15m/s and 25m/s in the Aerodynamics Laboratory at Hertfordshire University. The lift, drag and moment coefficients of the airfoil DU93-W-210 were firstly measured at this range of Reynolds numbers without any published data available. All the measured coefficients show the same trend at the three Reynolds numbers. The lift coefficients increase with Reynolds number and the drag coefficients decrease with Reynolds number, which verifies that a higher lift to drag ratio is expected at a higher Reynolds number. The stall angle moves from 14° to 12° with Reynolds number changing from 2×10^5 to 5×10^5, while the stall angle of the same airfoil is around 10° at Reynolds number of 1×10^6 [93]. The wind tunnel test results and the 2D CFD results show reasonable agreements. It is noted that the measured drag coefficients are higher than the CFD calculated drag coefficients. The discrepancies in drag coefficients are mainly due to the complex flows at the ends of the airfoil section, which were caused by the gap between the two ends of the airfoil section model and the wind tunnel side walls.

3D CFD analysis was performed for the two BEM-designed wind turbines. In the 3D CFD modelling of the FPVS wind turbine rotor, a series of calculations were carried out by fixing the tip speed ratio. The power performance of the rotor is well-predicted compared with the BEM methods. In order to have a further insight of the flow details, more calculations were done with a fixed rotor speed. The 3D CFD predicted blade surface streamlines demonstrate that before stall the flow direction is parallel to the chord-wise direction for the mix airfoil blade. It is also notice that the span-wise flow exists at high wind speeds. For the FPFS wind turbine rotor, 3D CFD calculations were performed at four wind speeds before and after stall. The calculated results were then compared with the BEM results. Good coincidences occur at 7m/s, 8.4m/s and 10m/s. The 3D CFD predicts slightly higher power output at high wind speeds compared with the BEM method using coefficients obtained from TUDelft wind tunnel test and the standard flat plate method. And the 3D CFD under-predicts power output compared with the coefficients extrapolated from modified flat plate method. It is verified that the CFD approach is able to provide a more detailed qualitative and quantitative analysis for wind turbine airfoils and rotors. With more advanced turbulence model and more powerful computing capability, it is prospective to improve the BEM method

considering 3D flow effects.

7.2 Findings and Contributions

This research concerns the aerodynamic design and analysis of small wind turbine blades. From this research, it is possible to draw guidelines on small wind turbine blade design and analysis using the BEM and CFD approaches. The major findings are:

(1) A hybrid stall correction model is a viable option to improve the power prediction. Two aspects are suggested to improve the accuracy of the BEM method in power prediction: the input of the lift and drag coefficients, and the wake induction factors. The stall correction is highly dependent on wind turbine configuration and operation environments.

The original contribution by the author is: a hybrid stall correction model was proposed for power prediction. This hybrid model consists of multiple sections using different stall correction models. The results show improvement in power prediction.

(2) The effects of the rotor parameters along with the blade chord and twist angle distributions on power performance are distinctive for the two kinds of wind turbines studied, i.e. FPVS and FSFS wind turbines. The tip-hub loss and drag effects bring apparent differences in the blade root and tip regions. The blade hub region has a direct effect on low wind speed performance and the tip region plays an important role in power production at high wind speeds. A heuristic blade linearisation approach leads to reduced manufacturing cost and higher AEP, with minimised effects on low wind speed performance.

The original contributions by the author are: a blade design approach by searching optimal induction factors was developed. The tip-hub loss and drag effect can be included not only in the power performance analysis but also in the blade chord and twist design via this approach. This method can be used in the blade root and hub design. Different blade linearisation approaches were provided, which can be used in any wind turbine design and refurbishment.

(3) The detailed flow characteristics from CFD modelling are quantitatively comparable to measurements, such as blade surface pressure distribution and

integrated forces and moments. The CFD calculated results and BEM results are generally agreeable. The transient multiple reference frame modelling method is applicable for any kind of wind turbine rotor performance assessment. The CFD results are potentially improvable by applying hexahedral mesh with a finer boundary mesh and affordable total mesh.

The original contribution by the author is: the CFD modelling dependency study was thoroughly performed which is instructive for further research work in this field.

(4) The stall was observed more pronounced at the inner sections than the outer sections of the blade for all the wind turbines investigated. The flow moves in chord-wise direction at low wind speeds and the span-wise flow occurs at high wind speeds both for the mixed airfoil blade and the single airfoil blade.

The original contribution by the author is: the 3D CFD modelling was applied to the BEM-designed blades, which confirmed that the CFD approach is able to provide an analysis tool in 3D rotating frame for more complicated and innovative blade design.

7.3 Recommendations for Future Work

Further research work can be followed for the open questions regarding to improve the methods used in small wind turbine blade design and analysis:

(1) The BEM method can be further improved by applying 3D coefficients derived from fully 3D CFD simulations. Extensive CFD analysis of more measured wind turbines is needed to establish a 3D coefficients database. With the 3D coefficients extracted from 3D CFD analysis, it is possible to improve stall prediction considering rotational effects.

(2) Within the limited time and affordable computing capacity, the 3D CFD provides acceptable results in wind turbine power performance analysis. Using a total hexahedral mesh is an advantage to model boundary flows. Mesh refinement in boundary layers can be achieved using advanced multi-block mesh strategies. This could further improve the CFD results.

References

[1]   RenewableUK 2012, "Wind farms hit high of more than 12% of UK electricity demand",   http://www.bwea.com/media/news/articles/pr20120106.html.Accessed   on August 1, 2012.

[2]   Schreck.S.J & Robinson.M.C. 2007, "Horizontal axis wind turbine blade aerodynamics in experiments and modelling", IEEE transactions on energy conversion, vol. 22, no. 1.

[3]   RenewableUK   2011,   "State   of   the   industry   report", http://www.bwea.com/pdf/publications/SOI_2011.pdf.Accessed on August 1, 2012.

[4]   Deutsches windenergie-inst 2011, "Wind energy study 2006-market assessment of the wind energy industry up to the year 2014", (DEWI) Wilhelmshaven.

[5]   REpower 2012, "Successful technological transfer: the REpower 5M offshore wind   power   plant", http://www.repower.de/wind-power-solutions/wind-turbines/5m.Accessed on August 1, 2012.

[6]   RenewableUK   2011,   "Small   wind   systems   market   report   2011", http://www.bwea.com/pdf/small/Small_Wind_Systems_Market_Report_2011.pdf.Acces sed on August 1, 2012.

[7]   Thor.S.E. & Taylor.P.W. 2002, "Long-term research needs for wind energy for the time frame 2000-2020", Wind Energy, vol. 5, pp. 73-75.

[8]   Sanderse.B., van der Pij.S.P., & Koren.B. 2012, "Review of CFD for wind turbine wake aerodynamics", Netherlands.

[9]   Manwell, J. & McGowan, J. 2009, "Wind energy explained: theory, design and application, second eddition", John Wiley & Sons Inc pp. 83-138.

[10]   Lee, J. H., Park, S., Kim, A. H., Rhee, S. H., & Kim, M.-C. 2012, "Computational methods for performance analysis of horizontal axis tidal stream turbines", Applied Energy, vol. 98, pp. 512-523.

[11]   Glauert, H. 1935, "Airplane propellers", Durrand, W.F(Ed.) Aerodynamic Theory, Springer, vol. 4, pp. 169-269.

[12]   Whale, J., Anderson, C. G., Bareiss, R., & Wagner, S. 2000, "An experimental and numerical study of the vortex structure in the wake of a wind turbine", Journal of Wind Engineering and Industrial Aerodynamics no. 84, pp. 1-21.

[13]   Malki, R., Williams, A. J., Croft, T. N., Togneri, M., & Masters, I. 2012, "A coupled blade element momentum-computational fluid dynamics model for evaluating tidal stream turbine performance", Applied Mathematical Modelling(In Press)Avaiable online 16 August 2012.

[14]   Hansena, M. O. L. 2006, "State of the art in wind turbine aerodynamics and aeroelasticity". Progress in Aerospace Sciences, vol. 42, pp. 285-330.

[15] Ameku, K. 2008, "Design of a 3 kW wind turbine generator with thin airfoil blades". Progress in Energy and Combustion Science, no. 30, pp. 501-543.

[16] Benini, E. 2002, "Optimal design of horizontal-axis wind turbines using blade-element theory and evolutionary computation". Journal of Solar Energy Engineering-Transactions of the ASME, vol. 124, no. 4, pp. 357-363.

[17] Cenaelle, N. A. 2006, "Aerodynamic optimization of a small scale wind turbine, for low wind turbine blade for low speed conditions", University of Stellenbosch.

[18] Cheboxarov, V. V. 2004, "Aerodynamic efficiency prediction of large cross-flow turbine". Proceedings of the Fourteenth (2004) International Offshore and Polar Engineering Conference, vol. 1, pp. 150-157.

[19] Dai, J. C. 2011, "Aerodynamic loads calculation and analysis for large scale wind turbine based on combining BEM modified theory with dynamic stall model". Renewable Energy, vol. 36, no. 3, pp. 1095-1104.

[20] Erich, H. 2006, Wind Turbines: Fundamentals, Technologies, Application, Economics. Springer. Berlin, Germany.

[21] Giguère, P. & Selig, M. S. 1999, "Design of a tapered and twisted blade for the NREL combined experiment rotor", NREL/SR-500-26173.

[22] Grant Ingram 2005, Wind Turbine Blade Analysis using the Blade Element Momentum Method.

[23] Islam, M. 1994, "Aerodynamic performance of a horizontal-axis wind turbine calculated by strip theory and cascade theory". JSME International Journal, Series B, vol. 37, no. 4, pp. 871-877.

[24] Lanzafame, R. 2007, "Fluid dynamics wind turbine design: critical analysis, optimization and application of BEM theory". Renewable Energy, vol. 32, no. 14, pp. 2291-2305.

[25] Li, H. 2009, "Design optimization and site matching of direct-drive permanent magnet wind power generator systems". Renewable Energy, vol. 34, no. 4, pp. 1175-1184.

[26] Martíez, J., Bernabini, L., Probst, O., & Rodríuez, C. 2011, "An improved BEM model for the power curve prediction of stall-regulated wind turbines".

[27] Morcos, V. H. 1994, "Aerodynamic performance analysis of horizontal-axis wind turbines", Renewable Energy, vol. 4, no. 5, pp. 505-518.

[28] Singh, R. K., Ahmed, M. R., Zullah, M. A., & Lee, Y. H. 2012, "Design of a low Reynolds number airfoil for small horizontal axis wind turbines", Renewable Energy, vol. 42, pp. 66-76.

[29] Vaz, J. R. P. 2011, "An extension of BEM method applied to horizontal-axis wind turbine design". Renewable Energy, vol. 36, no. 6, pp. 1734-1740.

[30] Ye, Z. Q., Cheng, Z. X., Chen, J. Y., & Bai, S. B. 1992, "Aerodynamic optimum

design procedure and program for the rotor of a horizontal-axis wind turbine", Journal of Wind Engineering and Industrial Aerodynamics, vol. 39, no. 1-3, pp. 179-186.

[31]   Garrad Hassan 2009, "GH Bladed: wind turbine design software". http://www.gl-garradhassan.com/en/GHBladed.php. Accessed on August 1, 2012.

[32]   Moriarty.P.J & Hansen.A.C 2005, "AeroDyn theory manual", Technical report NREL/TP-500-36881.

[33] Marshall,   B.   2008,   "NWTC   design   codes", http://wind.nrel.gov/designcodes/simulators/wtperf/. Accessed on April 1st 2009.

[34]   Maalawi, K. Y. & Badawy, M. T. S. 2001, "A direct method for evaluating performance of horizontal axis wind turbines", Renewable and Sustainable Energy Reviews, vol. 5, no. 2, pp. 175-190.

[35]   Maalawi, K. Y. 2003, "A practical approach for selecting optimum wind rotors". Renewable Energy, vol. 28, no. 5, pp. 803-822.

[36]   Vitale, A. J. 2008, "Computational method for the design of wind turbine blades". International Journal of Hydrogen Energy, vol. 33, no. 13, pp. 3466-3470.

[37]   Somers, D. M. 1996, "Wind tunnel test of the S814 thick root airfoil". Journal of Solar Energy Engineering-Transactions of the Asme, vol. 118, no. 4, pp. 217-221.

[38]   XFOIL 2009, "XFOIL, subsonic airfoil development system", http://web.mit.edu/drela/Public/web/xfoil. Accessed on April 1, 2009.

[39]   Robinson, M. C., Hand, M. M., Simms, D. A., & Schreck, S. J. 1999, "Horizontal axis wind turbine aerodynamics: three-dimensional, unsteady, and separated flow influences", NREL/CP-500-26337.

[40]   Hu, D., Du, Z., & Zhu, C. 2006, "A study on the static stall for horizontal axis wind turbine", Taiyangneng Xuebao/Acta Energiae Solaris Sinica, vol. 27, no. 3, pp. 217-222.

[41]   Lindenburg.C.   2003,   "Investigation   into   rotor   blade   aerodynamics", ECN-C--03-025.

[42]   Wood.D.H.   1991,   "A   three-dimensional   analysis   of   stall-delay   on   a horizontal-axis   wind   turbine",   Journal   of   Wind   Engineering   and   Industrial Aerodynamics, vol. 37, pp. 1-14.

[43]   Søresen.N.N, Michelsen.J.A., & Schreck.S. 2002, "Navier-stokes predictions of the NREL Phase VI rotor in the NASA 80ft X 120ft wind tunnel", Wind Energy, vol. 5, pp. 151-169.

[44]   Madsen, H A. 2010, "Validation and modification of the blade element momentum theory based on comparisons with actuator disc simulations", Wind Energy, vol. 13, pp. 373-389.

[45]   Crawford, C. 2006, "Re-examining the precepts of the blade element momentum theory for coning rotors". Wind Energy, vol. 9, pp. 457- 478.

[46]   Marshall.L & Buhl.J 2005, "A new empirical relationship between thrust coefficient and induction factor for the turbulent windmill state", Technical report NREL/TP-500-36834.

[47]   Wang Jianli 2009, "A improved calculation method of induction factors". Journal of engineering thermophysics, vol. 30, no. 9, pp. 1489-1491.

[48]   Garrad Hassan & Partners Ltd 2010, Bladed 4.0 Theory Manual, Garrad Hassan & Partners Ltd.

[49]   Burton.T, Sharpe.D, Jenkins.N, & Bossanyi.E 2012, Wind Energy Handbook, John Wiley & Sons, Ltd pp. 66-68.

[50]   Vaz, J. R. P. 2011, "An extension of BEM method applied to horizontal-axis wind turbine design". Renewable Energy, vol. 36, no. 6, pp. 1734-1740.

[51]   Tangler, J. & David Kocurek, J. 2004, "Wind Turbine Post-Stall Airfoil Performance Characteristics Guidelines for Blade-Element Momentum Methods", NREL/CP-500-36900.

[52]   Breton.S.P., Coton.F.N, & Moe.G. 2008, "A study on rotational effects and different stall delay models using a prescribed wake vortex scheme and NREL Phase VI experiment data", Wind Energy, vol. 11, pp. 459-482.

[53]   Bak.C, Johansen.J, & Andersen.P.B 2006, "Three-dimensional corrections of aerofoil characteristics based on pressure distributions", Proceedings of the European Wind Energy Conference.

[54]   Chaviaropoulos.P.K & Hansen.M.O.L 2000, "Investigating three-dimensional and rotational effects on wind turbine blades by means of a quasi-3D navier stokes solver", Journal of Fluids Engineering, vol. 122, pp. 330-336.

[55]   Zhang, C. & Hu, J. 2010, "The UAE wind turbine performance prediction using wind tunnel airfoil data", IEEE 2010 978-1-4244-8921-3/10.

[56]   Myers, L. 2006, "Power output performance characteristics of a horizontal axis marine current turbine". Renewable Energy, vol. 31, no. 2, pp. 197-208.

[57]   Du.Z & Selig.M.A 1998, "A 3-D stall-delay model for horizontal axis wind turbine performance prediction", AIAA-98-0021.

[58]   van Rooij R.P.J.O.M, Bruining.A, & Schepers.J.G 2003, "Validation of some rotor stall models by analyses of the IEA Annex XVIII field data", Proceedings from the European Wind Energy Conference.

[59]   Schreck.S 2002, "The NREL full-scale wind tunnel experiment-introduction to the special issue", Wind Energy, vol. 5, pp. 77-84.

[60]   Anderson, J. D. 2011, Fundamentals of aerodynamics, Fifth edition, The McGraw-Hill Companies,Inc.Americas, New York.

[61]   Zikanov, O. 2010, Essential Computational Fluid Dynamics, John Wiley & Sons,Inc.Hoboken, New Jersey.

[62]   Sumner, J., Watters, C. S., & Masson, C. 2010, "CFD in wind energy: the virtual, multiscal wind tunnel", Energies no. 3, pp. 989-1013.

[63]   Jiménez, A. 2009, "Analysis of a wind turbine wake using a LES method. Application to wake meandering".Euromech Colloquim on Wind Turbine Wakes Madrid.

[64]   Chaviaropoulos, P. K., Nikolaou, I. G., Aggelis, K. A., Soerensen, N. N., Johansen, J., Hansen, M. O. L., Gaunaa, M., Hambraus, T., von Geyr, H. F., Hirsch, C., Shun, K., Voutsinas, S. G., Tzabiras, G., Perivolaris, Y., & Dyrmose, S. Z. 2003, "Viscous and aeroelastic effects on wind turbine blades.The VISCEL project. Part I: 3D Navier-Stokes rotor simulations", Wind Energy, vol. 6, no. 4, pp. 365-385.

[65]   Sezer-Uzol, N. "3-D time-accurate CFD simulations of wind turbine rotor flow fields". Collection of Technical Papers - 44th AIAA Aerospace Sciences Meeting, vol. 7, pp. 4620-4642.

[66]   Rajvanshi.D, Baig.R, Pandya.R, & Nikam.K 2011, "Wind turbine blade aerodynamics and performance analysis using numerical simulations", Proceeding of the 38th National Conference on Fluid Mechanics and Fluid Power.

[67]   ANSYS Inc 2009, "Turbulence models", ANSYS FLUENT 12.0 Theory Guide.

[68]   Villalpando.F 2011, "Assessment of turbulence models for flow simulation around a wind turbine airfoil". Modelling and simulation in engineering. Modelling and Simulation in Engineering, vol. 2011, Article ID 714146, 8 pagesdoi:10.1155/2011/714146.

[69]   Freudenreich.K 2004, "Reynolds number and roughness effects on thick airfoils for wind turbines". Wind Engineering, vol. 28, no. 5, pp. 529-546.

[70]   Menter.F.R, Esch.T, & Kubacki.S 2002, "Transition modelling based on local variables", the 5th International Symposium on Turbulence Modeling and Measurements.

[71]   Menter.F.R 2004, "A Correlation-Based Transition Model Using Local Variables, Part I - Model Formulation". Proceedings of ASME Turbo Expo 2004.

[72]   Catalano.P & Tognaccini.R 2011, "RANS analysis of the low Reynolds number flow around the SD7003 airfoil", Aerospace Science and Technology, vol. 15, pp. 615-626.

[73]   Langtry.R.B & Menter.F.R 2009, "Correlation based transition modelling for unstructured parallized computational fluid dynamics codes". AIAA Journal, vol. 47, no. 12, pp. 2894-2906.

[74]   Counsil.J.N.N & Boulama.K.G 2011, "Validating the URANS shear stress transport γ-Reθt model for low Reynolds number external aerodynamics", International Journal of Numerical Method in Fluids, vol 69, No. 8, pp 1411–1432.

[75]   Langtry.R.B, Gola.J, & Menter.F.R 2006, "Predicting 2D airfoil and 3D wind turbine rotor performance using a transition model for general CFD codes", AIAA Aerospace Sciences Meeting and Exihibition.

[76]   Lu.C & Li.Y 2009, "Effects of turbulence model and computational grid on the calculation accuracy of the aerodynamic performance of S814 airfoil based on RANS", International Conference on Energy and Environment Technology, IEEE Xplore.

[77]   Rafiuddin.A.M, Sumesh.N, & Asid.Z.M 2011, "Experimental and numerical studies on a low Reynolds number aerofoil for wind turbine blades", Journal of Fluid Science and Technology, vol. 6, no. 3.

[78]   Li, Y. 2012, "Dynamic overset CFD simulations of wind turbine aerodynamics". Renewable Energy, vol. 37, no. 1, pp. 285-298.

[79]   Snel, H. 2003, "Review of aerodynamics for wind turbines". Wind Energy, vol. 6, no. 3, pp. 203-211.

[80]   Hand.M.M, Simms.D.A, Fingersh.L.J, Jager.D.W, Cotrell.J.R, Schreck.S, & Larwood.S.M 2001, "Unsteady aerodynamics experiment phase VI: wind tunneltest configurations and available data campaigns", NREL/TP-500-29955.

[81]   Somers, D. M. 1997, "Design and experimental results for the S809 airfoil", NREL/SR-440-6918 UC Category: 1213 DE97000206.

[82]   Yu, G. 2011, "An insight into the separate flow and stall delay for HAWT". Renewable Energy, vol. 36, no. 1, pp. 69-76.

[83]   Lanzafame, R. 2012, "BEM theory: How to take into account the radial flow inside of a 1-D numerical code". Renewable Energy, vol. 32, no. 14, pp. 2291-2305.

[84]   Hampsey, M. 2002, "Multiobjective evolutionary optimisation of small wind turbine blades", PhD Thesis, University of Newcastle.

[85]   M'endez, J. & Greiner, D. 2009, "Wind blade chord and twist angle optimization by using genetic algorithms", Institute of Intelligent Systems and Numerical Applications in Engineering.Univ.Las Palmas de Gran Canaria.35011 Las Palmas,Spain.

[86]   Liu, X. 2006, "Application of genetic algorithms to HAWT rotor blades optimization", ACTA ENERGIAE SOLARIS SINICA, vol. 27, no. 2, pp. 180-184.

[87]   Vitale, A. J. 2008, "Computational method for the design of wind turbine blades". International Journal of Hydrogen Energy, vol. 33, no. 13, pp. 3466-3470.

[88]   Giguere, P., Selig, M. S., & Tangler, J. L. 1999, "Blade design trade-off using low lift airfoils for stall regulated HWATs", Journal of Solar Energy Engineerng, vol. 121, pp. 217-223.

[89]   Fuglsang, P. 2004, "Design and verification of the Riso-B1 airfoil family for wind turbines". Wind Energy, vol. 7, no. 2, pp. 145-162.

[90]   Fuglsang, P. 2004, "Development of the Riso wind turbine airfoils". Journal of Solar Energy Engineering-Transactions of the ASME, vol. 126, no. 4, pp. 1002-1010.

[91]   Selig, M. S. & Mcgranahan, B. D. 2004, "Wind tunnel aerodynamic tests of six airfoils for use on small wind turbines", NREL/SR-500-34515.

[92]   Bertagnolio.F 2006, "Profile catalogue for airfoil sections based on 3D computations". RisøR-1581(EN).

[93]   Timmer.W.A & van Rooij.R.P.J.O.M 2003, "Summary of the delft university wind turbine dedicated airfoils", AIAA 2003 0352.

[94]   D'Angelo.S 1995, "Two wind turbines dedicated airfoils tested in two different wind tunnels: comparison and results". Windpower'95 conference.

[95]   Yurduseva, M. A. 2006, "Assessment of optimum tip speed ratio in wind turbines using artificial neural networks". Energy, no. 31, pp. 2153-2161.

[96]   Wang, L., Tang, X., & Liu, X. 2012, "Optimized chord and twist angle distributions of wind turbine blade considering Reynolds number effects", Procedding of Indo-Danish International Conference on Wind Energy: Materials, Engineering and Policies 2012.

[97]   Tang, X., Liu, X., Sedaghat, A., & Shark, L. 2009, "Rotor design and analysis of stall-regulated horizontal axis wind turbine", Universities Power engineering Conference 2009-IEEE.

[98]   I.E.Commission 2006, "IEC 61400-2: wind turbines–Part 2:design requirements for small wind turbines", IEC.

[99]   Wood.D.H 2004, "Dual purpose design of small wind turbine blades", Wind Engineering, vol. 28, no. 5, pp. 511-528.

[100]   Azad, A. K. & kaysar, M. M. 2012, "Design of a horizontal axis wind turbine for electricity generation in low speed windy sites", International Journal of adavanced renewable energy research, vol. 1, no. 6, pp. 363-373.

[101]   Seki, K., Shimizu, Y., & Zhu, K. 1996, "A design strategy for the improvement of an existing 300kW WTGS motor blade", Renewable Energy, vol. 9, no. 1-4, pp. 858-861.

[102]   Tu, B. F. 2007, "3D numerical simulation and optimum design method of wind turbine". Proceedings of 2007 Non-Grid-Connected Wind Power Systems.

[103]   Wood, D. H. 1991, "A 3-Dimensional analysis of stall-delay on a horizontal-axis wind turbine", Journal of Wind Engineering and Industrial Aerodynamics, vol. 37, no. 1, pp. 1-14.

[104]   Phillips, D. G. 2002, "CFD modelling and the development of the diffuser augmented wind turbine". Wind and Structures, vol. 5, no. 2-4, pp. 267-276.

[105]   Suzuki, M. 2003, "Aerodynamic performance prediction for wind turbine blades with incompressible and compressible CFD codes". Nippon Kikai Gakkai Ronbunshu, B Hen/Transactions of the Japan Society of Mechanical Engineers, Part B, vol. 69, no. 681, pp. 1067-1072.

[106]   Gartmann, A. "CFD modelling and validation of measured wind field data in a portable wind tunnel". Aeolian Research, vol. 3, no. 3, pp. 315-325.

[107]   Dobrev, I. 2011, "CFD and PIV investigation of unsteady flow through Savonius wind turbine". Energy Procedia, vol. 6, pp. 711-720.

[108]   Wolfe, W. P. & Ochs, S. S. 1997, "CFD calculations of S809 aerodynamic characteristics", AIAA-97-0973.

[109]   Gómez-Iradi, S. 2009, "Development and validation of a CFD technique for the aerodynamic analysis of HAWT", Journal of Solar Energy Engineering, vol. 131, pp. 031009-1-13.

[110]   Hartwanger, D. & Horvat, A. 2008, "3D modelling of a wind turbine using CFD", NAFENS Conference.

[111]   Carcangiu, C. E. 2009, "CFD-RANS study of horizontal axis wind turbines", PhD Thesis, Università Degli Studi di Cagliari.

[112]   Ma.R & Liu.P 2009, "Numerical simulation of low-Reynolds-number and high-lift airfoil S1223", Proceedings of the World Congress on Engineering 2009.

[113]   Guerri, O., Bouhadef, K., & Harhad, A. 2006, "Turbulent flow simulation of the NREL S809 airfoil", Wind Engineering, vol. 30, no. 4, pp. 287-302.

[114]   Yang, R. & Li, R. 2009, "Research of the rotational effects on the aerodynamics characteristics of horizontal axis wind turbine", IEEE 978-1-4244-2487-0/09.

[115]   Gómez-Iradi, S. 2008, "Computational fluid dynamics investigation of some wind turbine rotor design parameters". Proceedings of the Institution of Mechanical Engineers Part A-Journal of Power and Energy, vol. 222, no. A5, pp. 455-470.

[116]   Razvan, M. & Popescu, F. 2010, "NREL Phase VI rotor modeling and simulation using ANSYS FLUENT 12.1", The First Conference of the Young Researchers from Technical University of Civil Engineering, Bucharest, Romania.

[117]   Barlow.J B, Rae.W H, & Alan Pope.J 1999, Low-speed wind tunnel testing, thrid edition John Wiley & Sons,Inc.

[118]   Selig.M S, Deters.R W, & Williamson.G A 2011, "Wind tunnel testing airfoils at low Reynolds numbers", 49th AIAA Aerospace science meeting, AIAA 2011-875 pp. 1-32.

Appendix A   Author Publications

[1] **Tang, X.**, Liu X., Sedaghat, A., Shark, L-K. Rotor Design and Analysis of Stall-regulated Horizontal Axis Wind Turbine. Proceedings of the 44th International Universities Power Engineering Conference.Glasgow,United kingdom, 1st–4th Sept, 2009.

[2] **Tang, X**.,Liu X. A Case Study of a 10kW Horizontal Axis Wind Turbine Blade Design. Proceedings of the 5th PhD Seminar on Wind Energy in Europe. Durham, United Kingdom, 30th Sept–2nd Oct, 2009.

[3] **Tang, X.**, Peng, R.T, Liu,X and Broad, I. A. Design and FE Analysis of Mixed Airfoil Wind Turbine Blades.Proceedings of the 7th PhD Seminar on Wind Energy in Europe. Delft, Netherlands, 27th Sept–28th Oct, 2011.

Rotor Design and Analysis of Stall-regulated Horizontal Axis Wind Turbine

Xinzi Tang
University of Central
Lancashire, Preston, UK
XTang4@uclan.ac.uk

Xiongwei Liu
University of Central
Lancashire, Preston, UK
XLiu9@uclan.ac.uk

Ahmad Sedaghat
University of Central
Lancashire, Preston, UK
ASedaghat@uclan.ac.uk

Lik-kwan Shark
University of Central
Lancashire, Preston, UK
LShark@uclan.ac.uk

Abstract — Wind energy provides energy security at a time when decreasing global reserves of fossil fuel threatens the long-term sustainability of energy supply. The power performance of a wind turbine depends on the site's wind speed distribution and the design characteristics of the wind turbine. Based on the relationship between the power performance and the rotor parameters, this paper addresses the design tip speed ratio, rated wind speed, rotor diameter, and blade geometry of a stall-regulated wind turbine. As a case study, a dedicated aerofoil is used for the design and analysis of a stall-regulated wind turbine blade based on a specific wind speed distribution.

Index Terms — Blade element momentum theory; Horizontal axis wind turbine; Power performance; Rotor design; Stall-regulated; Site-specific wind turbine

I. INTRODUCTION

Renewable energy is essential to the UK Government's objectives to reduce carbon dioxide emissions by 60% by 2050 and to generate 15% of the UK's electricity supply from renewable sources by 2020. As one of the main sources of renewable energy, wind energy is under development with an expectation of an additional 14GW energy capacity from onshore wind in the UK [1].

A wind turbine system extracts kinetic energy of the wind into mechanical power and converts it to electrical power. As power in the wind passes two different systems before it can be used, the output amount of power available is mainly affected by the efficiency of the turbine rotor and the efficiency of the mechanical and electrical systems. Rotor design is a complex problem and it is impossible to expect the maximum efficiency without an optimization process [2].

Based on the classical blade element momentum (BEM) theory, tremendous efforts have been put on wind turbine design and optimization, most of which take maximum annual energy production or minimum cost of energy as objectives [3]. The BEM theory has been widely applied as its comparable simplicity and verified having an acceptable accuracy before stall in many industrial cases. And the methods derived from the BEM theory have been converted into computational codes [4;5]. Providing a set of basic specifications and constrains, these methods are able to select a reasonable design over a range of options. As design parameters are given before the optimization procedure begins, the relationship between the power performance and the rotor parameters is not fully understood. Since the power performance of a wind turbine depends on the design characteristics but also the site specific wind resource, the rotor configuration should be carefully considered according to the site's wind speed distribution.

Fix-pitch variable-speed (FPVS) stall-regulated horizontal axis wind turbines (HAWT) are recognized as a viable approach of power controlling in lieu of expensive pitch-controlled wind turbines. The rotor speed can be controlled within a certain range according to the maximum power coefficient law below rated wind speed. At above rated wind speed, the turbine limits its peak power by well designed blade stall. The design procedure and power performance estimation of a three-blade, upwind, stall-regulated HAWT is discussed in the following sections. The relationship between power performance and rotor specific parameters is analyzed and presented with a case study.

II. ROTOR DESIGN METHODOLOGY

In the design procedure, the main parameters such as aerofoil type, design tip speed ratio, rated wind speed, rotor diameter, should be considered first before conducting blade geometry optimization.

A. Aerofoil selection

Aerofoil for HAWT is often designed to be used at low attack angle, where the drag coefficient is usually much lower than the lift coefficient. A general aviation aerofoil shape is NACA series, and dedicated aerofoil shapes used in modern wind turbines are: S8 series developed by National Renewable Energy Laboratory (NREL) in USA, FFA-W series developed by FOI in Sweden, RisØ-A1 series developed by RisØ in Denmark, DU series developed by Delft University of Technology in Netherlands. It has been found in some applications that more than one aerofoil shape can be used for the wind turbine blade design, but there will be bending between these aerofoils which may add to uncertainties in the design process.

For a stall-regulated wind turbine, it is better to choose an aerofoil shape to make sure that stall occurs gently after the maximum lift-to-drag point. Design a wind turbine for a specific site should not only include an optimum geometry with the maximum power coefficient but also the detailed power coefficient curve which is a function of wind speeds or the tip speed ratio. With more accurate aerodynamic coefficients at high attack angles, the more accurate design and performance prediction can be obtained. But the

aerodynamic coefficients of a rotating aerofoil are different from the ones of a linear moving aerofoil. The coefficients from wind tunnel testing are acceptably accurate in steady flow, but in stall conditions, these coefficients are always lack of accuracy or there is no coefficient measured at very high attack angles at all. The low maximum lift coefficient, 21% thickness-to-chord ratio NREL S809 aerofoil has been extensively used in HAWT, and the post-stall aerodynamic characteristics of S809 have been investigated and published. It is also used as a base case in this paper. The modified lift and drag coefficients for steady-state and post-stall performance prediction are shown in Fig.1. These coefficients were presented with consideration of 3-dimentional flow [6;7]. The lift coefficient for the S809 aerofoil increases to 1.32 at an attack angle of 15°, but then it decreases as attack angle increases. The drag coefficient increases after an attack angle of 9°, and the maximum lift-to-drag ratio occurs at 8°. As the wind speed increases to high wind speed, the blade comes into deep stall regime; therefore a constant power can be achieved with a well-designed blade aerofoil.
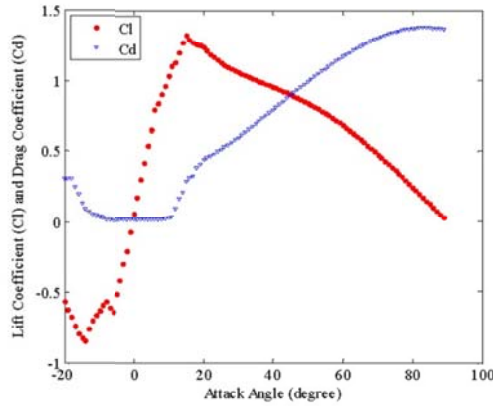
Fig.1. Modified lift and drag coefficients of S809 aerofoil

B. Design tip speed ratio

Given an aerofoil, the design tip speed ratio is the first parameter that used in a blade design procedure, which is generally taken as 6-8 in modern wind turbines. But the optimum value remains uncertain for different aerofoil shapes and blade numbers[8;9]. It was claimed that NACA 4415 has an optimum tip speed ratio of 8.5 while LS-1 has an optimum value of 10 in 3-blade turbines[8] .

As a higher lift coefficient means a larger lift force, a higher drag coefficient means a larger drag force, a turbine with the aerofoil of a higher lift coefficient and a lower drag coefficient is expected to produce more power with better load conditions. The maximum lift-to-drag ratio should be used in the optimal design, and the attack angle at which the maximum lift-to-drag ratio occurs should be considered to be the optimal attack angle. This optimal attack angle, which is equal to the angle of relative wind minus twist angle and

pitch angle at all sections when the blade geometry is optimal designed according to the BEM theory, should be used in the design to calculate ideal power coefficient.

The BEM theory divide a blade into several sections from root to tip and the total power coefficient is calculated by integrating the power coefficients at these sections, as described in [10]:

$$C_p = (8/\lambda^2) \int_{\lambda_h}^{\lambda} F \sin^2 \varphi (\cos \varphi - \lambda_r \sin \varphi)(\sin \varphi + \lambda_r \cos \varphi) \quad (1)$$

$$\lambda_r^2 [1 - (C_d/C_l) \cot \varphi] d\lambda_r$$

Here, C_p is the power coefficient, C_l is the lift coefficient, C_d is the drag coefficient, λ is the tip speed ratio, λ_h is the speed ratio at hub (root), λ_r is the local speed ratio at position r/R, φ is the angle of relative wind, and F is the tip loss factor. For a local loss calculation, it is described as Prandtl's loss factor [10], which is a function of the local relative angle and the local tip speed ratio. Here, for the overall power coefficient calculation of an ideal pre-designed blade, it can be referred as follows, where Z is the number of blades, Cpschmits is the theoretical coefficient including whirlpool losses[9]:

$$C_p = C_{pschmitz} \cdot (1 - \frac{\lambda}{\%_{Cd}}) \cdot (1 - \frac{1.84}{Z \cdot \lambda}) \quad (2)$$

From the above equations, it can be seen that there is a relationship between the ideal total power coefficient and different tip speed ratios. Given a maximum lift-to-drag ratio, the ideal total power coefficients versus different tip speed ratios can be obtained. From the modified lift and drag coefficients published, for S809 aerofoil, a maximum lift-to-drag ratio of 55.6 occurs at an attack angle of 8°, the ideal power coefficients versus different tip speed ratios are plotted in Fig. 2. It is shown that the optimum tip speed ratio for S809 is around 8.
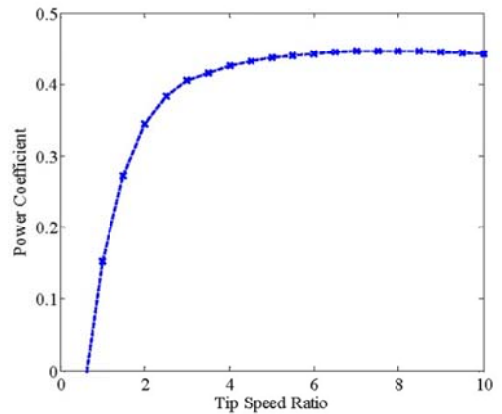
Fig.2. Ideal power coefficient curve of an S809 aerofoil

C. Rated wind speed

The rated wind speed is the wind speed at which the wind turbine is generating its rated power. And the wind power is proportional to the cube of the wind speed; high wind speed

means high power can be produced. However, a higher rated wind speed is not always a good choice as the annual power output is also a function of the local wind speed distribution, which is generally described as Weibull distribution with a shape parameter and a scale parameter. The annual power output can be calculated as:

$$P_{annual} = 10^{-6} \cdot 8760 \cdot \frac{1}{2} \cdot \rho A C_{me} \int_{cut\ in}^{cut\ out} v^3 Cp(v) f_{Weibull}(v) dv \quad (MWH)$$
(3)

Where, $\rho = 1.225\ kg/m^3$ is the air destiny at the sea level, A, is the wind turbine rotor area, in m^2, C_{me} is the mechanical and electrical system efficiency, and C_p is the aerodynamic power coefficient of the rotor, which is basically determined by the rotor design and is a dimensionless function of wind speed (or tip speed ratio).

For a stall-regulated wind turbine, there is not a simple way to express the real power output exactly in a mathematical expression at above rated speed. But for estimation, between the cut-in wind speed and the rated wind speed, the rotor should work at its maximum efficiency with an optimum control strategy, and between the rated wind speed and the cut-out wind speed, the rotor is expected to produce a constant rated power. And the Weibull parameters vary with local wind conditions, the shape parameter here is taken as 2 as an example here. With a shape parameter of 2 Weibull distribution is also known as Rayleigh distribution, then (3) is converted into:

$$P_{annual} = 10^{-6} \cdot 8760 \cdot \frac{1}{2} \cdot \rho A C_{me} \int_{cut\ in}^{rated\ speed} v^3 Cp(v) \cdot \frac{\pi}{2} \cdot \frac{v}{V_{mean}^2} \exp\left(-\frac{\pi}{4} \frac{v^2}{V_{mean}^2}\right) dv$$

$$+ 10^{-6} \cdot 8760 \cdot C_{me} \cdot P_{rated} \int_{rated\ speed}^{cut\ out} \frac{\pi}{2} \cdot \frac{v}{V_{mean}^2} \exp\left(-\frac{\pi}{4} \frac{v^2}{V_{mean}^2}\right) dv$$

$$(MWH)$$
(4)

Based on the above analysis, it is obviously that choosing an appropriate rated wind speed based on the local wind distribution is critical for the annual power output. An important parameter to describe wind resource used is annual mean wind speed. It seems that given a high mean wind speed Vmean, it is possible to produce more power with a high rated wind speed. With a low mean wind speed resource, it is likely to produce more power with a low rated wind speed. But it is shown in the following analysis that it is not the mean wind speed should be selected as rated wind speed.

As the wind power is proportional to the cube of the wind speed, let's define the annual mean cubic wind speed:

$$V_{meancubic} = \sqrt[3]{\int v^3 f_{Weibull}(v) dv} \quad (m/s)$$
(5)

and defining the annual mean wind speed as:

$$V_{mean} = \int v f_{Weibull}(v) dv \quad (m/s)$$
(6)

then we can establish the relationship between the annual mean cubic wind speed and the mean wind speed.

By defining a dimensionless factor c:

$$C = \frac{V_{meancubic}}{V_{mean}}$$
(7)

With a shape parameter of 2, the annual mean cubic wind speed is found about 1.24 times as mean wind speed:

$$C = \sqrt[3]{\int v^3 \frac{2}{\pi} \frac{v}{v_{mean}^2} \exp\left(\frac{-\pi}{4} \frac{v^2}{v_{mean}^2}\right) dv} \Big/ V_{mean} = 1.24$$
(8)

A Matlab program has been developed to find the relationship between the annual power output and the rated wind speed based on the ideal power output from (4). It is found that an optimum rated wind speed depends on the mean wind speed. With $C_p = 0.4$, $C_{me} = 0.82$, ss shown in Fig.3, for a 10kW wind turbine, with a mean wind speed higher than 3 m/s, the annual power output is lower with a higher factor k, where k is defined as k=Vrated / Vmean. But it is also worth emphasizing that a lower rated wind speed means a larger generator, which causes an increase in cost.
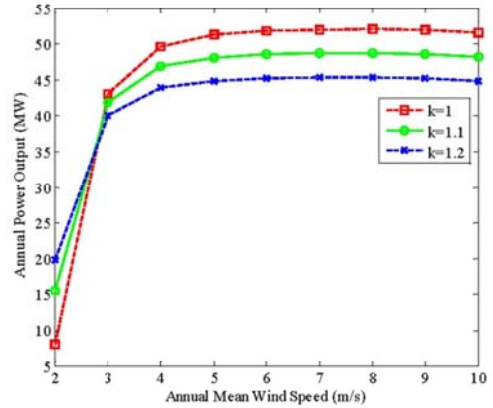
Fig.3. Annual power output versus average wind speed of a 10kW turbine, k=Vrated / Vmean

D. Rotor size

Given a rated wind speed, Vr, in m/s, the power extracted by the rotor from the wind, Pr, in W, is defined as:

$$P_r = C_p \frac{1}{2} \rho V_r^3 \pi R^2 \quad (W)$$
(9)

Here, R is the rotor radius, in meter, $\rho = 1.225 kg/m^3$ is the air destiny (assuming at the sea level), C_p is the power coefficient. Given the rated power Pr and the probable power coefficient C_p, the rotor radius can be estimated from the above equation.

Obviously, as the rotor radius increases, the power output increases. But it is not a good idea to expand the rotor radius to increase the power output as the expansion of the rotor radius will result in a higher cost. The power output can be only improved by a careful aerodynamic design of the blade shape.

E. Chord and twist distribution

Determination of the blade aerodynamic shape with the chord length distribution and twist distribution at a certain design tip speed ratio at which the blade has a maximum power coefficient is the main task of the design for blade with a known aerofoil. The geometry of the blade is an

aerodynamic shape with nonlinear chord and twist distribution, which can be obtained based on the BEM theory with respect to a certain aerofoil type.

It can be seen from (1) that, there is a relationship between these design parameters and the maximum power coefficient. If the main part of the equation is at its maximum, as shown in (10), the total power coefficient is maximized.

$$F\sin^2\varphi(\cos\varphi - \lambda_r\sin\varphi)(\sin\varphi + \lambda_r\cos\varphi) \quad (10)$$
$$\lambda_r^2[1 - (C_d/C_1)\cot\varphi] \rightarrow Max$$

Ignoring the drag-to-lift coefficient ratio and setting the partial derivative of the main part to zero, the optimum design equation for any kind of aerofoil can be obtained [10]:

$$\varphi_r = \left(\frac{2}{3}\right)\tan^{-1}\left(\frac{1}{\lambda_r}\right) \quad (11)$$

$$C_r = \frac{8\pi r}{ZC_1}(1-\cos\varphi_r) \quad (12)$$

The chord and twist distributions from the above equations are just an initial design values and iterations are followed normally. Some modifications of the twist angle and chord length distributions may be conducted to decrease the drag and thrust forces to the rotor at high winds. However they should be close to the theoretical distributions so as to make sure the maximum power coefficient and low start-up characteristics can be achieved.

III. Case study

A case study has been conducted with a 10kW fix-pitch variable-speed stall-regulated horizontal axis wind turbine, and with the specifications of the rotor listed in Table I. The local wind speed distribution is set to fit Rayleigh distribution with the UK mean wind speed of 5m/s at the rotor centre height, and a rated wind speed of 8m/s is selected. The blade has an aerofoil of S809 with a thickness of 21% chord length along the blade except for the transitional region from the root to the first section of S809 aerofoil, and the design tip speed ratio is set at 8.

IV. Results and discussion

The blade geometry is divided into 20 sections, and the initial distributions of the twist and the chord are shown in Fig.4 and Fig.5. The Power coefficients of all the sections are plotted in Fig.6. The power coefficients versus rotor rotational speed with different tip speed ratio are plotted in Fig.7.

TABLE I
ROTOR SPECIFICATIONS

Rated power	w	10000
Rated wind speed	m/s	8
Aerodynamic power coefficient		0.4
Number of blades		3
Design tip speed ratio		8
Mechanical and electrical efficiency		0.8
Radius of the rotor	m	5
Design attack angle	degree	8

Fig.4 and Fig.5 demonstrate that the chord length is larger at the inner sections of the blade (closer to the root) and

smaller at the outer sections of the blade. The twists of sections close to the root are larger than those close to the The root sections are set to high twist angles, w contribute to the lower start up performance as the large t angle makes the root sections to have an appropriate at angle at a low start-up wind but are more likely to sta high wind speed. And the twist angle at the tip sectic about –1.69 degree which also makes the tip sections n likely to stall at high wind speeds but will contribute at wind speed. Therefore modifications should be balan between the two aspects. Any modification should make real attack angle to approximate the optimum attack a and make sure the lift force is not decreased sharply.

Fig.6 reveals that the outer sections produce most of power at the rated wind speed. Therefore, any modifica for manufacturing considerations on the chord length twist distributions of these sections should be limited clo: the initial optimal design to ensure rated power.
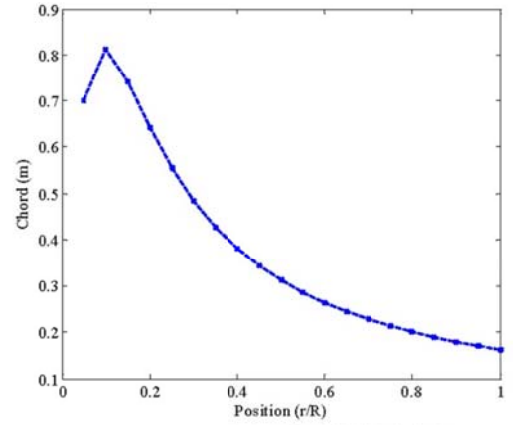
Fig.4. Chord distribution of an initial blade design
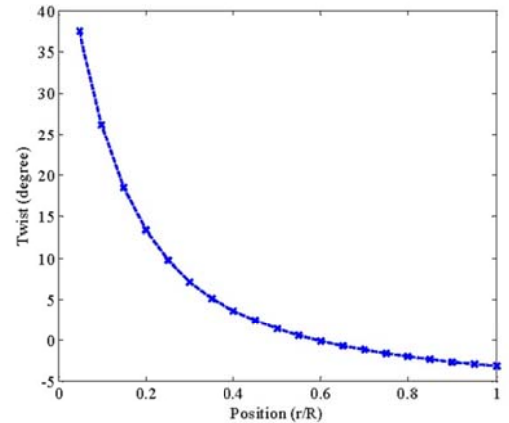
Fig.5. Twist distribution of an initial blade design

It is suggested in Fig.7 that, to obtain a maximum power coefficient before the rated wind speed, the rotor rotational speed should be variable according to the maximum power coefficient point. A detailed control strategy can be implied, which is out of the theme of in this paper.
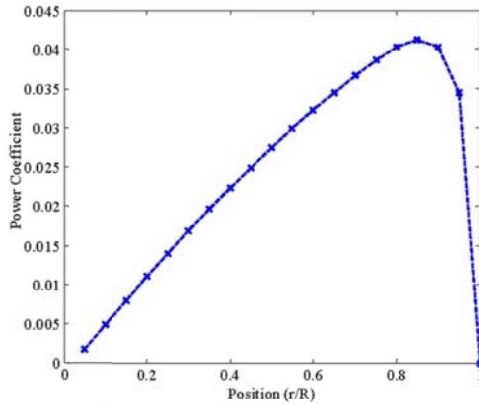
Fig.6. Power coefficient distribution of an initial blade design

V. CONCLUSION

Various rotor parameters were investigated in this paper, and the rotor design and analysis were conducted based on a case of S809 aerofoil. The outcome demonstrates that:

Fig.7. Power coefficient versus rotor rotational speed of an initial blade design

1) A set of optimum design parameters should be considered to achieve the maximum annual power output with a local wind speed distribution.
2) For a stall-regulated wind turbine, it is appropriate to choose an aerofoil shape to make sure gentle stall occurs after the maximum lift-to-drag point.
3) The design tip speed ratio should be selected according to the aerodynamic characteristics of the aerofoil.

4) The rated wind speed should be selected based on the local site's mean wind speed.
5) The chord and twist distribution of the blade can be obtained based on BEM theory, and any modifications on chord and twist distributions should approximate the optimum distribution.
6) A detailed power coefficient curve can be predicted based on lift and drag coefficients considering 3-dimentional flow for stall-regulated wind turbines. According to the power coefficient curve, the maximum power coefficient control strategy can be applied.

REFERENCES

[1] R. AMA, "Wind Power Construction Programme - UK 2008-2020," *Report*, 2008
[2] V. Ali and E. Bulent, "Principle of rotor design for horizontal axis wind turbines," *Journal of Applied Sciences*, vol. 6, no. 7, pp. 1527-1533, 2006
[3] E. Benini and A. Toffolo, "Optimal design of horizontal-axis wind turbines using blade-element theory and evolutionary computation," *Journal of Solar Energy Engineering-Transactions of the Asme*, vol. 124, no. 4, pp. 357-363, 2002
[4] K. Y. Maalawi and M. A. Badr, "A practical approach for selecting optimum wind rotors," *Renewable Energy*, vol. 28, no. 5, pp. 803-822, Apr.2003
[5] M. e. Juan and G. David, "Wind blade chord and twist angle optimization by using genetic algorithms," *Institute of Intelligent Systems and Numerical Applications in Engineering.Univ.Las Palmas de Gran Canaria.35011 Las Palmas,Spain.*, 2009
[6] J. Tangler and J. David Kocurek, "Wind Turbine Post-Stall Airfoil Performance Characteristics Guidelines for Blade-Element Momentum Methods," *NREL/CP-500-36900*, Oct.2004
[7] M. Kirk, "Site Specific optimization of Rotor/Generator Sizing of Wind Turbines," *Thesis,Georgia Institute of Technology*, Dec.2006
[8] N. S. Çetin, M. A. Yurdusev, R. Ata, and A. Özdemir, "Assessment of optimum tip speed ratio of wind turbines," *Mathematical and Computational Applications*, vol.10, no.1, pp. 147-154, 2005
[9] M. A. Yurduseva, R. Atab, and N. S. Çetin, "Assessment of optimum tip speed ratio in wind turbines using artificial neural networks," *Energy*, no. 31, pp. 2153-2161, 2006
[10] J. Manwell, "Wind energy explained: theory, design and application," *John Wiley & Sons Inc*, pp. 83-138, 2002

The European Academy of Wind Energy
Oral presentation only

A Case Study of a 10kW Horizontal Axis Wind Turbine Blade Design

Xinzi Tang[1], Xiongwei Liu[2]

[1] University of Central Lancashire, UK, [2] University of Central Lancashire, UK

ABSTRACT

Determination of the blade aerodynamic shape with a chord and twist distribution at a specified design tip speed ratio where the blade has a maximum power coefficient is the main task of the blade design. The aerofoil aerodynamic characteristics and the rotor specifications are highly important for the wind turbine power performance, which depends on the match between the site's wind resource, the rotor and the generator. This paper addresses a case study of a 10kW wind turbine rotor blade design considering an existing generator and a site-specific wind speed distribution. The design process and the power performance prediction are presented.

KEYWORDS

Blade design; Horizontal axis wind turbine, Power performance, Site-specific.

1 INTRODUCTION

Wind turbine technology has become a hot issue as renewable energy guarantees environment-friendly and sustainable energy supply. The power performance of a wind turbine depends on the match between the site's wind resource, the rotor and the generator. In order to maximum the annual power output, the aerofoil aerodynamic characteristics and rotor specifications should be carefully considered in the design process. In this paper, the key rotor specifications are discussed with regards to an existing generator and a site-specific wind speed distribution. The aerodynamic optimal blade shape design and power performance estimation are implemented based on the blade element momentum (BEM) theory [1, 2, 3]. Finally the blade geometry and the predicted power curve are presented for maximum power coefficient control purpose.

2 DESIGN CONSTRAINS

2.1 Wind speed distribution

The local wind speed distribution is the first consideration of erecting a wind turbine. Wind speed Weibull distribution is widely accepted for describing the wind resource, the probability density function of which is defined as:

XTang4@uclan.ac.uk

1

$$f(v) = \left(\frac{k}{c}\right) \cdot \left(\frac{v}{c}\right) \cdot \exp\left[-\left(\frac{v}{c}\right)^k\right] \qquad (1)$$

Here, v is the wind speed, k is the shape parameter, and c is the scale parameter. Considering some wind farm in northern part of Britain, a shape parameter of 2.1 and a scale parameter of 6.89 is used, and the annual wind speed distribution is shown in Figure 1. The mean wind speed is found to be 6.1m/s from Equation 2.

$$V_{mean} = \int v f_{weibull}(v) dv \qquad (2)$$
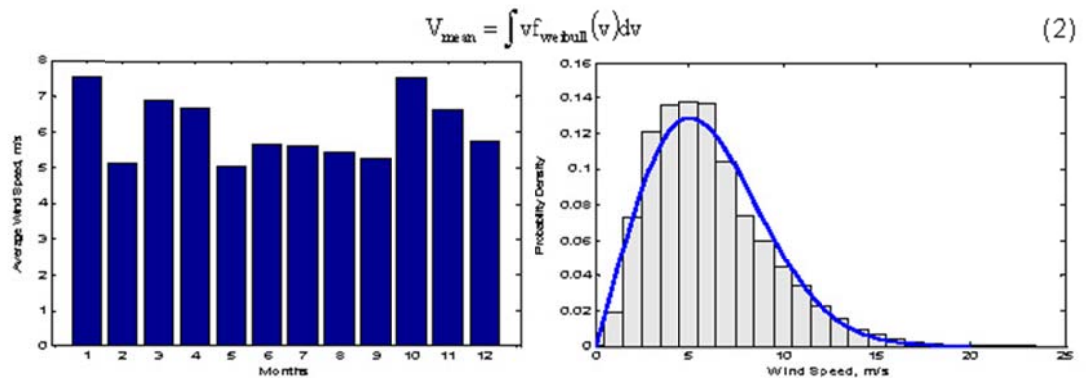
Figure 1: Annual Wind Speed Distribution

Considering maximum annual power output, it is better choose a rated wind speed which is close to the annual mean wind speed of 6.1m/s, but it is also worth emphasizing that a lower rated wind speed means a larger rotor, which causes an increase in cost. The rated wind speed is finally chosen according to the rated tip speed ratio in 3.2.

2.2 An existing generator

Due to economical reason, the turbine rotor is designed for an existing generator that is a permanent magnet synchronous alternator, rated power 10kW at the speed of 150 RPM.

3 ROTOR SPECIFICATIONS

3.1 Aerofoil type

Aerofoil for HAWT is often designed to be used at low attack angle, where the ratio of lift to drag coefficient is very high. A general aviation aerofoil shape is NACA series, and dedicated aerofoil shapes used in modern wind turbines are: S8, FFA-W, RisØ-A1, DU and etc. DU93-w-210 has been widely used in some European wind turbines, which has a max ratio of lift to drag coefficient of 118 and max lift coefficient of 1.39 at Reynolds of one million, and is chosen in our case. It has been found in some applications that more than one aerofoil shape can be used, but this may add to uncertainties in the design process, and in our design case only one aerofoil is used from root to tip except for the short root transition area.

The power extracted by the rotor from the wind is given as Equation (3), from which the rotor radius can be estimated.

$$P = 0.5C_p\rho V_r^3 \pi R^2 \qquad (3)$$

Note here, P is the mechanical power but not the electrical power, Cp is the aerodynamic power coefficient, Vr is the rated wind speed, ρ is the air density, r is the rotor radius. Assuming the alternator efficiency of 84%, the rated power of the rotor in our case is about 11620W rather than 10kW. Obviously, as the rotor radius increases, the power output increases. But it is not a good idea to expand the rotor radius so as to increase the power output as expansion of the rotor radius will result in higher cost. Due to structure reason with an existing tower, our rotor radius is not allowed to exceed 5m. The rotor diameter is selected to be 9m with a first estimated aerodynamic efficiency of 0.45 and a rated wind speed of 9 m/s.

The optimal design tip speed ratio for DU93-w-210 aerofoil locates around 10 according to Yurduseva method [3], and the maximum efficiency at the tip speed ratio of 5 to 8 does not vary sharply from a first estimation. Note the tip speed ratio at rated wind speed as λ_{rated}, the optimal design tip speed ratio λ_{design} should be equal to or larger than λ_{rated} to avoid sharp decrease of speed. Having a rotor radius of 4.5 m, a generator of 10 kW and 150 RPM, we can calculate λ_{rated}, Vr and Cp. And remember, Cp cannot be larger than 0.593(Betz limits). From a first estimation, tip speed ratio of 8 is selected to be the best match where Cp is about 0.45 for DU93-w-210. The rated wind speed is then calculated from Equation (4).

$$\lambda = \frac{\omega R}{V_r} \qquad (4)$$

Where ω is the rotor speed, R is the rotor radius and Vr is the rated wind speed.

The basic parameters of our wind turbine are listed in Table 1.

Table 1: Rotor Specifications

Parameters	Value
Power [W]	10000
Wind Velocity [m/s]	8.8
Number of Blades	3
Optimal Tip Speed Ratio	8
Air Density [kg/m3]	1.2
Rotor Radius [m]	4.5
Generator Rated Speed[RPM]	150
Aerofoil	DU93W210

4   BLADE GEOMETRY AND POWER PERFORMANCE

With the above specifications, the geometry of the blade is obtained based on the BEM theory, which has a maximum twist of 26.5° and a maximum chord of 0.489m. The blade geometry is shown in Figure 2. The Cp was predicted using the following equation and a computer program was coded to calculate:

XTang4@uclan.ac.uk   3

$$C_p = (8/\lambda^2)\int_{\lambda_h}^{\lambda} F\lambda_r^3 a'(1-a)\left[1-(C_d/C_l)\cot\varphi\right]d\lambda_r \tag{5}$$

Here C_l and C_d are the lift and drag coefficients, λ is the tip speed ratio, λ_h and λ_r are the local speed ratios at hub (root) and at position r/R, φ is the angle of relative wind, a is the axial induction factor, a' is the tangential induction factor and F is the tip loss factor. The maximum Cp is found at the tip speed ratio of 8, which is about 0.445. For maximum Cp control purpose, the corresponding rotor power output versus different wind speeds are shown in Figure 3.
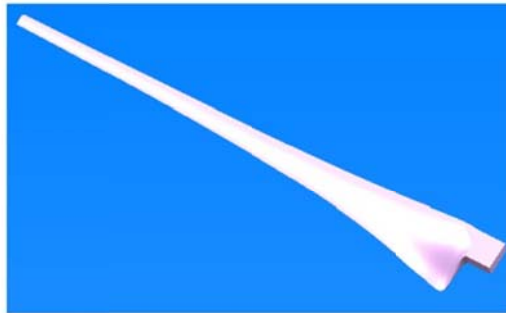
Figure 2: Blade Geometry
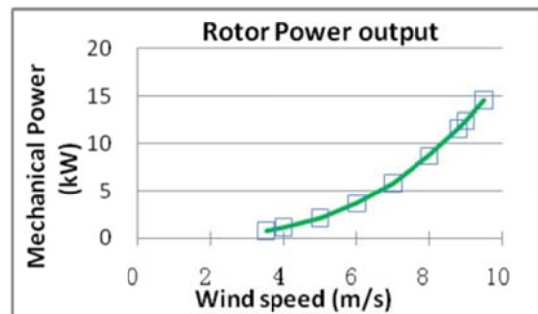
Figure3: Power Performance Prediction

5   CONCLUSIONS

A case study of a 10kW horizontal axis wind turbine blade design has been carried out with an existing generator and a site-specific wind speed resource. With a mean wind speed of 6.1m/s and a generator of 10kW and 150RPM, a rotor of 4.5m radius and the DU93-w-210 aerofoil has been applied. It has been predicted to be with a power coefficient of 0.445 at the tip speed ratio of 8 based on the BEM theory. A further structure analysis and testing will be developed in the future.

BIBLIOGRAPHY

[1]   Li, H. and Chen, Z., "Design optimization and site matching of direct-drive permanent magnet wind power generator systems," Renewable Energy, vol. 34, no. 4, pp. 1175-1184, 2009

[2]   Benini, E. and Toffolo, A., "Optimal design of horizontal-axis wind turbines using blade-element theory and evolutionary computation," Journal of Solar Energy Engineering-Transactions of the Asme, vol. 124, no. 4, pp. 357-363, 2002

[3]   Manwell, J., "Wind energy explained: theory, design and application," John Wiley & Sons Inc, pp. 83-138, 2002

[4]   Yurduseva, M. A., Atab, R., and Çetin, N. S., "Assessment of optimum tip speed ratio in wind turbines using artificial neural networks," Energy, no. 31, pp. 2153-2161, 2006

Design and Finite Element Analysis of Mixed Aerofoil Wind Turbine Blades

Xinzi Tang, Ruitao Peng, Xiongwei Liu, Anthony Ian Broad

School of Computing, Engineering and Physical Sciences, University of Central Lancashire

Fylde Road, Preston, UK

E-mail: {xtang4,rtpeng,xliu9}@uclan.ac.uk

1 INTRODUCTION

Wind turbine technology is one of the rapid growth sectors of renewable energy all over the world. As a core component of a wind turbine, it is a common view that the design and manufacturing of rotor blades represent about 20% of the total investment of the wind turbine [1]. Moreover, the performance of a wind turbine is highly dependent on the design of the rotor [2]. As well as rotor aerodynamic performance, the structure strength, stiffness and fatigue of the blade are also critical to the wind turbine system service life.

This paper presents the design and Finite Element Analysis (FEA) of a 10KW fixed-pitch variable-speed wind turbine blade with five different thickness of aerofoil shape along the span of the blade. The main parameters of the wind turbine rotor and the blade aerodynamic geometry shape are determined based on the principles of the blade element momentum (BEM) theory. Based on the FE method, deflections and strain distributions of the blade under extreme wind conditions are numerically predicted. The results indicate that the tip clearance is sufficient to prevent collision with the tower, and the blade material is linear and safe.

2 BLADE DESIGN

The wind turbine is a 10KW horizontal axis fixed-pitch variable-speed wind turbine. The design process of the three-bladed rotor initially comes with the determination of the rotor diameter and material.

2.1 Rotor Diameter and Material

The power extracted from the wind is proportional to the cube of wind speed as well as the area of the rotor. It is often preferable to have an effective rotor but not a too big one as the cost increases with the rotor size. In order to have an initialization of the efficiency of small wind turbines before any specific designs are conducted, it was suggested that the efficiency of modern wind turbine rotors is generally about 30%-40% [3]. Assuming a rotor efficiency of 40% and a total efficiency of 33.8%, a diameter of 5m is selected for the 10KW wind turbine. And the material of the blade is resin-reinforced fiber glass due to easy local availability.
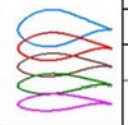
2.2 Blade Aerofoil Shape

For horizontal axis wind turbines, it is recommended to have a higher lift but lower drag aerofoil. There are many kinds of aerofoil including the general aviation aerofoil, such as NACA series, which are still used in some wind turbines. However, with the development of wind turbines, the dedicated aerofoil came about. The S series designed by NREL in USA, is mostly used in stall-regulated wind turbines for its gentle behavior in stall conditions; the FFA W series designed in Sweden and RIS series designed in Denmark, are preferable for lower Reynolds applications, and the DU series designed in Netherland, is popular in High Reynolds for large wind turbines. Each of these series has its own aerofoil shape with different thickness-to-chord ratio of 18%-40%. The thicker aerofoil shapes are often located at the inner part (close to rotor centre) of the blade while the thinner ones are set in the outer part of the blade due to ease of manufacturing and better strength and stiffness. The basic aerofoil (from 30% to 90% radius sections) selected in this wind turbine blade is DU93-W-210 which has a high lift-to-drag coefficient [4]. For similarity reason, the aerofoil shapes at other stations are also derived from the DU series by changing the thickness. The transition between sections is obtained by linear interpolation. The properties and distribution of these aerofoil shapes (named respectively DU93-W-210-40%, DU93-W-210-30%, DU93-W-210-25%, DU93-W-210, and DU93-W-210-18%) are listed in Table I. The aerodynamic coefficients derived from XFoil are shown in Figure 1. The rest coefficients at high attack angles are extended by the Viterna-Corrigan method [5].

Table 1: Blade configuration

Aerofoil Shapes	Thickness ratio	Aerofoil Shapes	Stations
DU93-W-210-40%	40%		0.05R

Aerofoil Shapes	Thickness ratio	Aerofoil Shapes	Stations
DU93-W-210-30%	30%		0.1R
DU93-W-210_25%	25%		0.15R-0.3R
DU93-W-210	21%		0.35R-0.9R
DU93-W-210-18%	18%		0.95R-1R
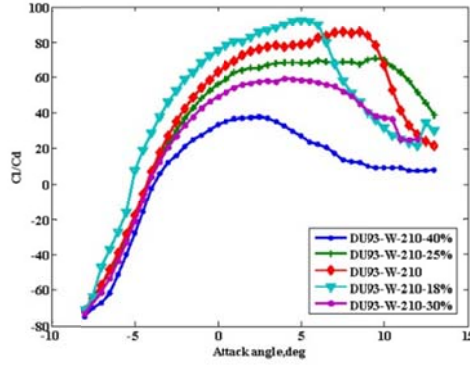
Figure 1: Aerodynamic coefficients Cl/Cd versus attack angles

2.3 Blade Chord and Twist

Given the rotor design parameters (e.g. rotor diameter, tip speed, aerofoil, rated wind speed and etc.), the main task of blade design is to determine the chord and twist distributions along the span of the blade. The optimal chords and twists are often calculated based on blade element momentum (BEM) theory. In this theory, complex flows are simplified into steady uniform conditions; and the total efficiency is integrated from several blade element sections which experience different flow velocity and different attack angle for the same hub wind speed. The integration equation is shown below [3]:

$$C_p = (8/\lambda^2) \int_{\lambda_h}^{\lambda} F_r \sin^2 \phi_r (\cos \phi_r - \lambda_r \sin \phi_r)(\sin \phi_r + \lambda_r \cos \phi_r) \quad (1)$$
$$\lambda_r^2 [1 - (C_d/C_l) \cot \phi] d\lambda_r$$

Ignoring the drag and setting the partial derivative of the main part to zero, the optimum design equation for any kind of aerofoil can be obtained:

$$\phi_r = \left(\frac{2}{3}\right) \tan^{-1} \left(\frac{1}{\lambda_r}\right) \quad (2)$$

$$C_r = \frac{8\pi r}{N C_l}(1 - \cos \phi_r) \quad (3)$$

Where the C_p is the power coefficient, C_l is the lift coefficient, C_d is the drag coefficient, λ is the tip speed ratio, ϕ is the angle of relative wind, N is the blade number and F is the tip loss factor. Subscript r represents position r/R, h is hub position and t is tip position.

The design tip speed of wind turbine is considered to be theoretically as high as possible since an aerofoil produces high lift at high Reynolds numbers; meanwhile, a lower tip speed is preferred to keep within noise limits. The design tip speed of this 10KW wind turbine is set to 68m/s. Aiming at an optimal power performance for an annual mean wind speed of 6m/s, the rated wind speed is set to 8.5m/s and the design tip speed ratio is 8. According to equation (2) and (3), as five different aerofoil shapes are employed, the initial chord and twist distribution showed non-continuous variations along the blade span and irregular chord length and twist angle appeared in the transition area between sections. This may cause bad effects both in aerodynamic and structure aspects: the aerodynamic flow over these blade sections is not two dimensional and may yield secondary loads and stress concentration. Furthermore, it looks rather poor when manufactured. Thus, the chords and twists of the main sections (0.35R-0.9R) are maintained, and the rest of the sections are obtained according to the basic aerofoil characteristics. Figure 2 shows the chord and twist distributions of the blade. Some small alternations have been made to the tip region which do not affect the power coefficients so much but would reduce thrusts at high winds. The twist angles of the tip region are set to be positive to have less thrust at high winds and better starting behaviours while the power coefficient is kept quite close to the theoretically optimum one.
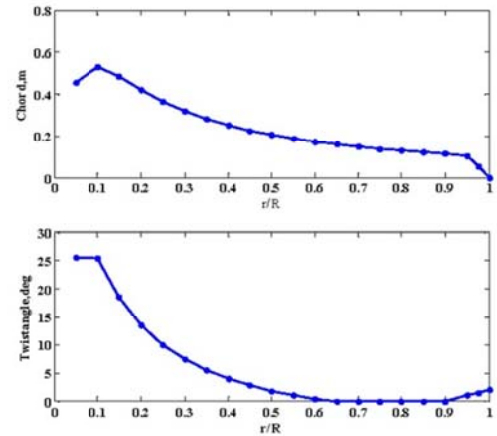
Figure 2: Blade chord and twist distributions

2.4 Power, torque and thrust coefficients

Following an optimal blade geometry design at an specific tip speed ratio, the power, torque, and thrust coefficients for the whole range of tip speed ratios are determined (as shown in Figure 3) from equation 4,5 and 6 [3]:

$$C_{Thrust} = \frac{8}{\lambda^2} \int_{\lambda_h}^{\lambda} F \lambda_r^3 a'(1-a)[1 - (C_d/C_l) \cot \phi_r] d\lambda_r \quad (4)$$

$$C_{Thrust} = \frac{\int_0^R \frac{1}{2} N \rho U_{rel}^2 (C_l \cos \phi_r + C_d \sin \phi_r) c dr}{0.5 \rho U_{rel}^2 \pi R^2} \quad (5)$$

$$C_{torque} = \frac{\int_0^R \frac{1}{2} N \rho U_{rel}{}^2 (C_l \sin\phi_r - C_d \cos\phi_r) c dr}{0.5 \rho U_{rel}{}^2 \pi R^2} \qquad (6)$$
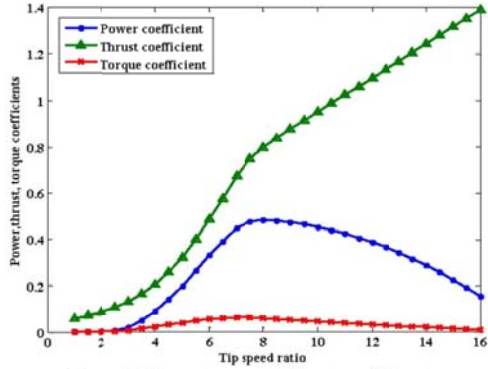
Figure 3: Power torque and thrust coefficients

4 FINITE ELEMENT MODELING

The ultimate strength of the blade was analyzed via finite element modelling techniques as follows.

4.1 Blade shell model

The blade geometry was modelled in CATIA, and the finite element model (FEM) was developed in ABAQUS, the structure of the blade was modelled with shell elements (S4R, capable of representing layer characteristics throughout the shell thickness).

The section view of components in layup schedule and the layup schedule were presented in Figure 4 and Table 2 respectively. According to section force characteristics, in order to improve the overall stiffness of the blade and increase the carrying capacity and prevent local buckling, spar cap and shear web structure were introduced. In the layup schedule, 0 degree plies were mainly used to withstand axial force, 45 degree plies mainly to withstand torque and shear forces.
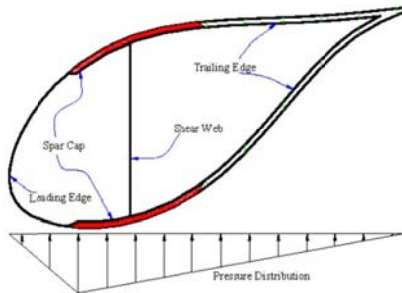
Figure 4: Display of components and pressure distribution

The material parameters were listed in Table 3[6], The A130, DB120 lamina were used for the 0 degree layups and ±45 degree layups respectively, balsa wood was introduced as a filler in sandwich-type layups to minimize the weight. The failure criteria applied for designing the blade were based on failure strains parameters [6, 7].

Table 2: Layup schedule for the blade

Component	Radius (%)	Z location (mm)	Layup schedule	Thickness
Root	2.8 to 5	140 to 250	$[\pm 45/0_6/\pm 45/0_6/+45]_s$	9.35
Spar cap	5 to 20	250 to 1000	$[\pm 45/0_6/\pm 45/0_6/+45]_s$	9.35
	20 to 40	1000 to	$[\pm 45/0_5/\pm 45/0_5/+45]_s$	7.5
	40 to 60	2000 to	$[\pm 45/0_4/\pm 45/0_4/+45]_s$	5.2
	60 to 80	3000 to	$[\pm 45/0_3/\pm 45/0_3/+45]_s$	3.85
	80 to	4000 to	$[\pm 45/0_2/\pm 45/0_2/+45]_s$	2.7
Leading edge	5 to 20	250 to 1000	$[\pm 45/0_3/\pm 45]_s$	3
	20 to	1000 to	$[\pm 45/0/\pm 45]_s$	1.85
Trailing edge	5 to 80	250 to 4000	$[\pm 45/0/balsa/0/\pm 45]_s$	7
	80 to	4000 to	$[\pm 45/0]_s$	1.3
Shear web	5 to 100	250 to 5000	$[\pm 45/0_2/\pm 45]_s$	3

Table 3: Material parameters in the layups [5]

	E_{11}/ GPa	E_{22}/ GPa	E_{33}/ GPa	v_{12}	v_{13}	v_{23}	G_{12}/ GPa	G_{13}/ GPa	
A130	31.7	7.58	7.58	0.32	0.32	0.32	3.45	3.10	
DB120	26.2	6.55	6.55	0.39	0.32	0.35	4.14	3.72	
Balsa	0.187	0.06	4.07	0.67	0.02	0.01	0.02	0.22	

4.2 Loads prediction and definition

The loadings affecting a wind turbine blade are important in two primary areas including ultimate strength and fatigue. Limit loads in gusts are used to design the ultimate strength of blade; correspondingly normal running loads are utilized to design the fatigue strength. The blade was designed to survive an extreme wind speed of 60 m/s [8] with the wind turbine was not in operation. To model the blade load for a stationary wind turbine in such an extreme wind condition, the dynamic pressure on the high pressure side of the blade was introduced for the FE model, which defined as [6]:

$$P = 0.5 \times \rho \times v^2 \qquad (7)$$

Where ρ is the air density (1.225 kg /m3), v is the wind velocity. A pressure distribution was applied to the blade model as shown in Figure 4.

In this study, for the layup schedule the static strength design of first layer was mainly taken into account. At the root end of the blade, all six degrees of freedom for the nodes in the root plane of the blade were fixed, and no other displacement constraints were imposed on the blade model.

4.3 Results and discussion

Simulations were performed in the solver of Abaqus/Standard, Figure 5 and Figure 6 present the contour plot and distribution of displacement under the wind speed of 60 m/s, it shows that the displacement of blade sections increase from the root to the tip, the maximum displacement in flap-wise direction is 454 mm, meanwhile the minimum displacement position locates at the blade root, which meets the characteristics of the cantilever, and indicates that the tip clearance is sufficient to avoid collision with the tower.

When looking at the maximum in-plane principal strains of the blade, as shown in Figure 7, it is apparent that the maximum strain occurs at the blade root section as the

oot experiences a larger load with a smaller area, however
he strain is still much less than the ultimate strains of the
naterial in layups. For weight consideration, thickness of
ayups rapidly declined in the direction from root to tip,
vhich results in local strain discontinuous areas.

Figure 8 shows a linear relationship between load and
p displacement, the deformation of the blade linearly
ncreases with rise in load, which again indicate the blade
naterial is still linear and safe.
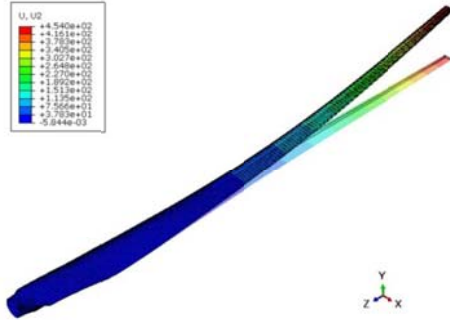
Figure 5: Distribution of displacement in flap-wise direction
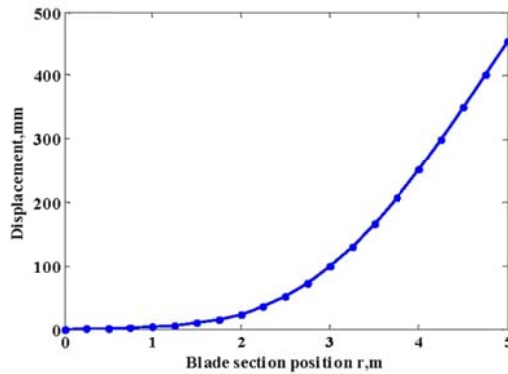
Figure 6: Displacements of sections
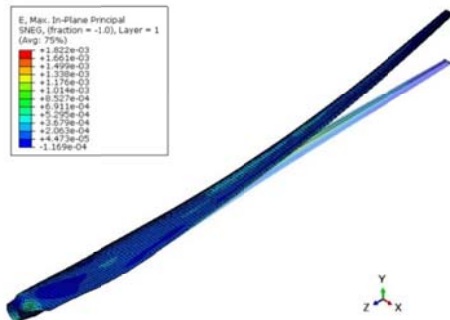
Figure 7: Distribution of maximum in-plane principal strain
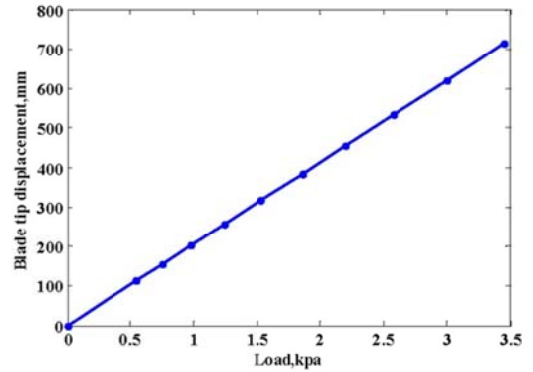
Figure 8: Relationship between load and tip displacement

5 CONCLUSIONS

A mixed airfoil composite blade for a 10KW
horizontal fixed-pitch variable-speed turbine was designed
based on BEM, it is concluded that the BEM theory is
efficient in predicting rotor aerodynamic characteristics.
The structural analysis was performed to evaluate the
proposed design configuration by using the FE modelling
method at the extreme wind conditions. The methodologies
presented here can be utilized and adopted for further aero-
elastic analysis.

REFERENCES

[1] H.Erich, Wind Turbines: Fundamentals, Technologies,
Application, Economics, 2nd edition edn. Springer,2006.

[2] B.Tony, S. David,J.Nick, B.Ervin, Wind Energy
Handbook.John Wiley & Sons Ltd,2001.

[3] J.Manwell,J.McGowan, J, Wind energy explained:
theory, design and application second eddition,John Wiley
& Sons Inc,2009.

[4] D'Angelo S, Timmer W.A.,"Two wind turbines
dedicated airfoils tested in two different wind
tunnels:comparison and results", Windpoer'95 Conference,
Washington D.C.USA,1995, March 26-30.

[5] J.Tangler, K.J. David, "Wind Turbine Post-Stall Airfoil
Performance Characteristics Guidelines for Blade-Element
Momentum Methods", NREL/CP-500-36900,2004.

[6] Ladean R. McKittrick, Douglas S. Cairns and John
Mandell, etc. "Analysis of a composite blade design for the
AOC1550 wind turbine using a finite element model[R]".
California: Sandia National Laboratories, 2001.

[7] Dassault Systèmes Simulia Corp. ABAQUS User's
Manual, Providence, RI, 2010.

[8] IEC 61400-1:2005(E). Wind turbines–Part 1:Design
requirements[S]. Switzerland: International
Electrotechnical Commission, 2005.

Appendix B   Blade Element Momentum Theory

This appendix describes the principles, definitions and fundamental equations of blade element moment (BEM) theory.

By introducing an axial induction factor and an angular induction factor (as defined below), the Momentum theory with wake rotation interprets how a wind turbine works with consideration of both axial and angular velocity changes, which can be found in many textbooks and works [9;22]. Considering the rotating annular stream tube, for the rotating annular element, the torque will be:

$$dT = \dot{m}(\omega r)r = \rho 2\pi r dr v \omega r^2 \tag{1}$$

Define angular induction factor $a^{'} = \omega / 2\Omega$, so the torque becomes:

$$dT = 4a^{'}(1-a)\rho v \Omega r^3 \pi dr \tag{2}$$

Introducing the variables $a = \dfrac{V_1 - V_2}{V_1}$, $a^{'}$ and $\lambda_r = \Omega r / U$, the power coefficient can be integrated:

$$C_p = (8/\lambda^2)\int_0^\lambda a^{'}(1-a)\lambda_r^3 d\lambda_r \tag{3}$$

The blade element theory considers that the blade is divided into N sections; each element experiences a slightly different flow, as they have different rotational speed, different chord and different twist angle. In many cases, the blade is divided into more than ten elements. The overall performance is determined by numerical integration of the elements along the blade, as shown in Figure 1. It relies on two assumptions: no interactions between blade elements; forces defined by lift and drag coefficients from wind tunnel test, which are defined as:

$$C_l = \frac{lift\ force}{dynamic\ force} = \frac{2F_L}{\rho U_{rel}^2 c dr} \tag{4}$$

$$C_d = \frac{drag\ force}{dynamic\ force} = \frac{2F_D}{\rho U_{rel}^2 c dr} \tag{5}$$
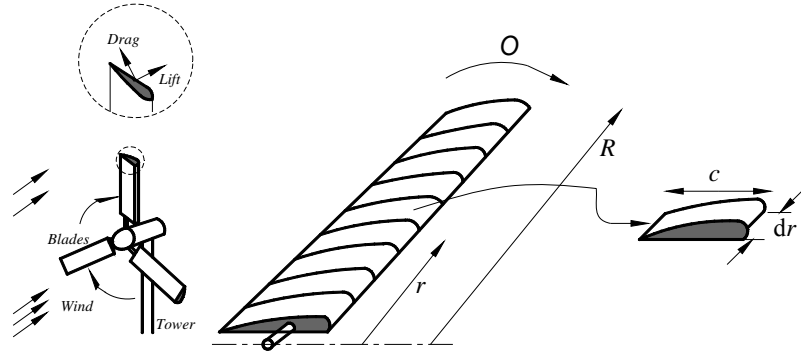
Figure 1 Blade element model described by Manwell and Grant

The definitions for a blade element (airfoil section) are shown in Figure 2.

The lift and drag force of a blade element, defined as:

$$dF_L = \frac{1}{2} C_l \rho U_{rel}^2 c dr \tag{6}$$

$$dF_D = \frac{1}{2} C_d \rho U_{rel}^2 c dr \tag{7}$$

Then we can obtain the forces in the flow direction F_N and perpendicular to the flow direction F_T:

$$dF_N = \frac{1}{2} Z \rho U_{rel}^2 (C_l \cos\varphi + C_d \sin\varphi) c dr \tag{8}$$

$$dF_T = \frac{1}{2} Z \rho U_{rel}^2 (C_l \sin\varphi - C_d \cos\varphi) c dr \tag{9}$$

Note that, the force in the flow direction F_N is the axial force and perpendicular to the flow direction F_T is the force of torque.

The lift to drag coefficient of an airfoil is nonlinearly dependent on angle of attack. When the lift to drag coefficient starts to decline after the maximum value at a threshold angle, the turbine becomes into "stall".
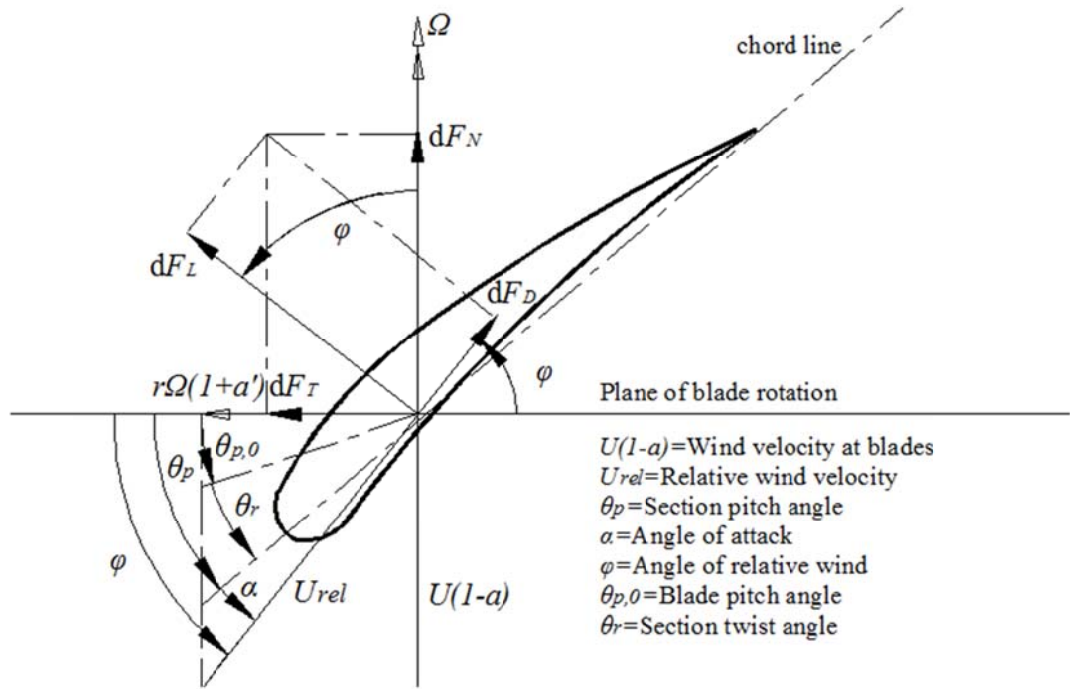
Figure 2 Definition of variables in a section described by Manwell

The total power produced by a rotor was integrated from the root sections to the tip sections:

$$C_p = (8/\lambda^2)\int_{\lambda_h}^{\lambda} F\sin^2\varphi(\cos\varphi - \lambda_r\sin\varphi)(\sin\varphi + \lambda_r\cos\varphi)\lambda_r^2\left[1-(\frac{C_l}{C_d})\cot\varphi\right]d\lambda_r \qquad (10)$$

Appendix C   S809 Airfoil Coordinates and Aerodynamic Data

The S809 airfoil coordinates (in Table 1) and published airfoil lift and drag coefficients (in Table 2) from wind tunnel tests are included in this appendix.

X/C	Y/C		X/C	Y/C
1	0		0.00021	-0.00177
0.9962	0.00049		0.00105	-0.00346
0.98519	0.00237		0.00121	-0.0037
0.96784	0.00596		0.0024	-0.00525
0.94507	0.01103		0.00931	-0.01148
0.91749	0.01703		0.02323	-0.02038
0.88529	0.02346		0.04232	-0.03025
0.84845	0.03028		0.06588	-0.0408
0.80747	0.03777		0.09343	-0.0519
0.76304	0.04598		0.12411	-0.06306
0.71595	0.05488		0.15765	-0.07371
0.66706	0.06436		0.19374	-0.08355
0.61733	0.07422		0.23191	-0.09243
0.56783	0.0841		0.27144	-0.09989
0.51983	0.09328		0.31197	-0.10527
0.47424	0.0994		0.35337	-0.10817
0.42846	0.10177		0.39533	-0.108
0.38261	0.10185		0.43827	-0.10454
0.33726	0.10008		0.48192	-0.09734
0.29297	0.09672		0.52793	-0.08656
0.25025	0.09192		0.57621	-0.07397
0.20958	0.08587		0.62609	-0.06064
0.17141	0.0787		0.67674	-0.04743
0.13617	0.0706		0.72721	-0.03509
0.10426	0.06171		0.77643	-0.0242
0.07603	0.05224		0.82328	-0.01516
0.05182	0.04237		0.86663	-0.0082
0.03191	0.03232		0.90536	-0.00336
0.01659	0.02231		0.93847	-0.00049
0.00603	0.01263		0.96509	0.00074
0.00066	0.00374		0.98448	0.00078
0.0002	0.00196		0.99614	0.00029
0	0		1	0

Table 1 S809 airfoil coordinates

The lift and drag coefficients of S809 at Re of 10^6 from TUDelft and OSU wind tunnel tests are listed below:

TUDelft			OSU		
α	Cl	Cd	α	Cl	Cd
-1.04	0.0190	0.0095	-6.2	-6.8	-0.61
-0.01	0.1390	0.0094	-4.1	-4.7	-0.4
1.02	0.2580	0.0096	-2.1	-2.7	-0.16
2.05	0.3780	0.0099	0	-0.6	0.07
3.07	0.4970	0.0100	2.1	1.5	0.3
4.10	0.6170	0.0100	4.1	3.5	0.55
5.13	0.7360	0.0097	6.1	5.5	0.79
6.16	0.8510	0.0095	8.2	7.6	0.9
7.18	0.9130	0.0127	10.1	9.5	0.94
8.20	0.9520	0.0169	11.2	10.6	0.93
9.21	0.9730	0.0247	12.2	11.6	0.97
10.20	0.9520	0.0375	13.3	12.7	1
11.21	0.9470	0.0725	14.2	13.6	1.02
12.23	1.0070	0.0636	15.2	14.6	1.03
13.22	1.0310	0.0703	16.2	15.6	1.01
14.23	1.0550	0.0828	17.2	16.6	0.95
15.23	1.0620	0.1081	18.1	17.5	0.9
16.22	1.0430	0.1425	19.2	18.6	0.78
17.21	0.9690	0.1853	20	19.4	0.67
18.19	0.9380	0.1853	22.1	21.5	0.7
19.18	0.9290	0.1853	24	23.4	0.77
20.16	0.9230	0.1853	26.1	25.5	0.91

Table 2 Lift and drag coefficients of S809 at Re of 10^6

Appendix D   DU93-W-210 Airfoil Coordinates and Aerodynamic Data

This appendix involves DU93-W-210 airfoil coordinates (in Table 3), lift and drag coefficients (in Table 4) from our wind tunnel tests in University of Hertfordshire (UH).

X/C	Y/C	X/C	Y/C	X/C	Y/C	X/C	Y/C	X/C	Y/C
1.0	0.0025	0.5004	0.1155	0.0532	0.0562	0.0794	-0.0555	0.5480	-0.0571
0.9945	0.0042	0.4882	0.1171	0.0456	0.0519	0.0891	-0.0586	0.5606	-0.0543
0.9877	0.0063	0.4760	0.1186	0.0387	0.0476	0.0993	-0.0615	0.5733	-0.0513
0.9789	0.0087	0.4640	0.1199	0.0324	0.0435	0.1097	-0.0644	0.5861	-0.0483
0.9683	0.0116	0.4519	0.1211	0.0269	0.0396	0.1202	-0.0670	0.5990	-0.0452
0.9565	0.0148	0.4399	0.1221	0.0221	0.0360	0.1310	-0.0695	0.6120	-0.0420
0.9440	0.0180	0.4280	0.1230	0.0181	0.0327	0.1420	-0.0718	0.6251	-0.0388
0.9311	0.0214	0.4161	0.1237	0.0146	0.0295	0.1530	-0.0739	0.6384	-0.0355
0.9180	0.0248	0.4042	0.1243	0.0117	0.0266	0.1642	-0.0759	0.6516	-0.0321
0.9048	0.0281	0.3924	0.1247	0.0092	0.0238	0.1755	-0.0777	0.6648	-0.0288
0.8916	0.0315	0.3807	0.1249	0.0071	0.0211	0.1869	-0.0793	0.6778	-0.0256
0.8783	0.0348	0.3690	0.1250	0.0053	0.0185	0.1984	-0.0808	0.6907	-0.0225
0.8650	0.0381	0.3573	0.1249	0.0039	0.0160	0.2100	-0.0821	0.7033	-0.0195
0.8516	0.0414	0.3456	0.1246	0.0026	0.0136	0.2216	-0.0832	0.7159	-0.0166
0.8383	0.0447	0.3339	0.1241	0.0017	0.0112	0.2333	-0.0842	0.7282	-0.0139
0.8251	0.0480	0.3222	0.1235	0.0010	0.0089	0.2451	-0.0850	0.7404	-0.0113
0.8118	0.0512	0.3105	0.1227	0.0006	0.0066	0.2569	-0.0856	0.7524	-0.0088
0.7986	0.0545	0.2988	0.1217	0.0002	0.0043	0.2687	-0.0861	0.7643	-0.0066
0.7853	0.0576	0.2871	0.1206	0.0000	0.0021	0.2806	-0.0865	0.7760	-0.0045
0.7721	0.0608	0.2754	0.1193	0.0000	0.0000	0.2925	-0.0866	0.7876	-0.0025
0.7589	0.0639	0.2637	0.1179	0.0001	-0.0021	0.3044	-0.0866	0.7992	-0.0008
0.7457	0.0670	0.2521	0.1163	0.0005	-0.0042	0.3163	-0.0865	0.8106	0.0007
0.7324	0.0701	0.2405	0.1145	0.0011	-0.0063	0.3283	-0.0862	0.8220	0.0021
0.7192	0.0731	0.2290	0.1125	0.0019	-0.0084	0.3404	-0.0858	0.8334	0.0032
0.7059	0.0761	0.2175	0.1104	0.0029	-0.0105	0.3525	-0.0852	0.8447	0.0042
0.6927	0.0791	0.2060	0.1082	0.0042	-0.0127	0.3646	-0.0844	0.8560	0.0049
0.6796	0.0820	0.1946	0.1057	0.0057	-0.0148	0.3767	-0.0836	0.8672	0.0055
0.6665	0.0849	0.1834	0.1032	0.0076	-0.0170	0.3889	-0.0825	0.8784	0.0059
0.6534	0.0877	0.1722	0.1004	0.0098	-0.0193	0.4010	-0.0814	0.8896	0.0060
0.6403	0.0905	0.1611	0.0975	0.0124	-0.0217	0.4131	-0.0801	0.9008	0.0060
0.6273	0.0932	0.1502	0.0944	0.0154	-0.0243	0.4252	-0.0787	0.9119	0.0058
0.6144	0.0958	0.1393	0.0912	0.0189	-0.0270	0.4373	-0.0771	0.9231	0.0053
0.6015	0.0984	0.1287	0.0879	0.0230	-0.0299	0.4494	-0.0754	0.9344	0.0047
0.5887	0.1009	0.1183	0.0843	0.0277	-0.0329	0.4616	-0.0736	0.9457	0.0038
0.5759	0.1033	0.1080	0.0807	0.0330	-0.0360	0.4737	-0.0716	0.9570	0.0028
0.5631	0.1056	0.0981	0.0769	0.0390	-0.0392	0.4860	-0.0695	0.9679	0.0017
0.5505	0.1078	0.0884	0.0729	0.0457	-0.0424	0.4982	-0.0673	0.9781	0.0005
0.5378	0.1099	0.0790	0.0689	0.0531	-0.0457	0.5106	-0.0649	0.9870	-0.0006

0.5253	0.1119		0.0700	0.0647		0.0613	-0.0490		0.5230	-0.0624		0.9943	-0.0017
0.5128	0.1138		0.0613	0.0604		0.0700	-0.0523		0.5354	-0.0598		1.0	-0.0025

Table 3 DU93-W-210 airfoil coordinates

Re=200,000				Re=300,000				Re=500,000		
α	Cl	Cd		α	Cl	Cd		α	Cl	Cd
-15.18	-0.6239	0.0967		-15.18	-0.6293	0.0912		-15.18	-0.6266	0.0875
-14.18	-0.5843	0.0863		-14.17	-0.5954	0.0825		-14.17	-0.5940	0.0764
-13.16	-0.5307	0.0740		-13.16	-0.5471	0.0705		-13.16	-0.5484	0.0668
-12.15	-0.4753	0.0650		-12.15	-0.4965	0.0629		-12.15	-0.4946	0.0583
-11.14	-0.4183	0.0576		-11.14	-0.4352	0.0537		-11.13	-0.4339	0.0507
-10.12	-0.3572	0.0501		-10.12	-0.3727	0.0457		-10.12	-0.3698	0.0435
-9.10	-0.2882	0.0454		-9.11	-0.3058	0.0412		-9.10	-0.3038	0.0380
-8.09	-0.2236	0.0415		-8.09	-0.2386	0.0372		-8.09	-0.2393	0.0340
-7.07	-0.1587	0.0396		-7.07	-0.1728	0.0345		-7.07	-0.1756	0.0312
-6.05	-0.0932	0.0379		-6.06	-0.1093	0.0328		-6.06	-0.1105	0.0289
-5.04	-0.0290	0.0377		-5.04	-0.0435	0.0314		-5.04	-0.0459	0.0275
-4.02	0.0342	0.0372		-4.03	0.0220	0.0310		-4.03	0.0181	0.0271
-3.01	0.0958	0.0381		-3.01	0.0868	0.0318		-3.01	0.0825	0.0273
-1.99	0.1625	0.0389		-1.99	0.1498	0.0326		-1.99	0.1470	0.0283
-0.97	0.2240	0.0406		-0.98	0.2155	0.0340		-0.98	0.2103	0.0301
0.04	0.2869	0.0436		0.04	0.2824	0.0372		0.04	0.2757	0.0326
1.06	0.3404	0.0456		1.05	0.3440	0.0404		1.05	0.3461	0.0365
2.07	0.4067	0.0499		2.07	0.4074	0.0446		2.07	0.4110	0.0406
3.09	0.4669	0.0549		3.09	0.4721	0.0497		3.09	0.4799	0.0460
4.11	0.5310	0.0595		4.10	0.5382	0.0552		4.11	0.5467	0.0521
5.12	0.5960	0.0667		5.12	0.6008	0.0621		5.12	0.6142	0.0590
6.14	0.6605	0.0738		6.14	0.6646	0.0691		6.14	0.6770	0.0666
7.16	0.7252	0.0812		7.15	0.7264	0.0771		7.15	0.7386	0.0745
8.17	0.7892	0.0893		8.17	0.7938	0.0854		8.17	0.7963	0.0831
9.19	0.8519	0.0994		9.19	0.8560	0.0949		9.18	0.8538	0.0921
10.21	0.9168	0.1091		10.20	0.9158	0.1047		10.20	0.9130	0.1016
11.23	0.9821	0.1199		11.22	0.9749	0.1155		11.21	0.9665	0.1110
12.24	1.0401	0.1299		12.23	1.0312	0.1255		12.23	1.0064	0.1198
13.26	1.0856	0.1409		13.25	1.0663	0.1351		13.23	1.0130	0.1299
14.27	1.1095	0.1494		14.25	1.0648	0.1454		14.23	1.0000	0.1408
15.26	1.0797	0.1633		15.24	1.0366	0.1575		15.23	0.9939	0.1506
16.26	1.0552	0.1733		16.24	1.0228	0.1682		16.23	0.9899	0.1602
17.26	1.0439	0.1822		17.24	1.0154	0.1778		17.23	0.9865	0.1694
18.26	1.0572	0.1840		18.25	1.0615	0.1927		18.23	1.0026	0.1564
19.26	1.0539	0.1925		19.25	1.0564	0.2003		19.23	0.9963	0.1636
20.26	1.0460	0.2017		20.25	1.0553	0.2104		20.23	0.9944	0.1716
21.27	1.0329	0.2127		21.25	1.0496	0.2212		21.23	0.9922	0.1802
22.27	1.0233	0.2273		22.25	1.0437	0.2314		22.23	0.9867	0.1893
23.22	0.9599	0.2380		23.25	1.0282	0.2464		23.23	0.9838	0.1973

Table 4 Lift and drag coefficients of DU93-W-210 from UH wind tunnel tests

Appendix E　NREL/NASA Phase VI Wind Turbine Blade Configuration

In this appendix, the blade chord and twist angle distributions of the NREL/NASA Phase VI wind turbine blade is listed

Radial Distance(m)	Chord(m)	Twist(°)	Thickness	Twist axis
0	Hub	Hub	Hub	Hub
0.508	0.218	0	0.218	50
0.6604	0.218	0	0.218	50
0.8835	0.183	0	0.183	50
1.0085	0.349	6.7	0.163	35.9
1.0675	0.441	9.9	0.154	33.5
1.1335	0.544	13.4	0.154	31.9
1.2575	0.737	20.04	0.154	30
1.343	0.728	18.074	21%	30
1.51	0.711	14.292	21%	30
1.648	0.697	11.909	21%	30
1.952	0.666	7.979	21%	30
2.257	0.636	5.308	21%	30
2.343	0.627	4.715	21%	30
2.562	0.605	3.425	21%	30
2.867	0.574	2.083	21%	30
3.172	0.543	1.15	21%	30
3.185	0.542	1.115	21%	30
3.476	0.512	0.494	21%	30
3.781	0.482	-0.015	21%	30
4.023	0.457	-0.381	21%	30
4.086	0.451	-0.475	21%	30
4.391	0.42	-0.92	21%	30
4.696	0.389	-1.352	21%	30
4.78	0.381	-1.469	21%	30
5.029	0.358	-1.775	21%	30

Table 5 The blade chord and twist angle distributions of the NREL/NASA Phase VI wind turbine blade

Appendix F BEM-Designed Wind Turbine Blade Configuration

The blade chord and twist angle distributions of two BEM-designed wind turbines (as discussed in Chapter 4 and Chapter 6) are listed in this appendix.

Section Position (r/R)	Radial Distance(m)	Airfoil	Twist(°)	Chord (m)
0.05	0.25	DU93-W-210-40%	38.47	0.471
0.1	0.5	DU93-W-30%	27.23	0.547
0.15	0.75	DU93-W-210-25%	19.54	0.499
0.2	1	DU93-W-210-25%	14.34	0.433
0.25	1.25	DU93-W-210-25%	10.71	0.374
0.3	1.5	DU93-W-210	8.08	0.326
0.35	1.75	DU93-W-210	6.1	0.288
0.4	2	DU93-W-210	4.57	0.257
0.45	2.25	DU93-W-210	3.35	0.231
0.5	2.5	DU93-W-210	2.36	0.21
0.55	2.75	DU93-W-210	1.54	0.192
0.6	3	DU93-W-210	0.85	0.177
0.65	3.25	DU93-W-210	0.26	0.164
0.7	3.5	DU93-W-210	-0.25	0.153
0.75	3.75	DU93-W-210	-0.69	0.143
0.8	4	DU93-W-210	-1.08	0.135
0.85	4.25	DU93-W-210	-1.42	0.127
0.9	4.5	DU93-W-210	-1.73	0.12
0.95	4.75	DU93-W-210-18%	-2	0.114
1	5	DU93-W-210-18%	-2.25	0.108

Table 6 The blade chord and twist angle distributions of the FPVS wind turbine blade

	Without F and drag				With F and drag		
r/R	Chord(m)	Twist(°)			r/R	Chord(m)	Twist(°)
0.05	0.708	40.98			0.05	0.632	22.03
0.1	0.877	30.51			0.1	0.88	28.61
0.15	0.837	22.91			0.15	0.833	22.24
0.2	0.747	17.53			0.2	0.745	17.15
0.25	0.657	13.67			0.25	0.656	13.43
0.3	0.579	10.82			0.3	0.579	10.65
0.35	0.515	8.64			0.35	0.514	8.54
0.4	0.461	6.94			0.4	0.462	6.85
0.45	0.417	5.58			0.45	0.417	5.51
0.5	0.38	4.47			0.5	0.38	4.4
0.55	0.349	3.55			0.55	0.349	3.48
0.6	0.322	2.77			0.6	0.322	2.7
0.65	0.299	2.1			0.65	0.299	2.03
0.7	0.279	1.53			0.7	0.279	1.44
0.75	0.261	1.03			0.75	0.261	0.91
0.8	0.246	0.59			0.8	0.245	0.43
0.85	0.232	0.2			0.85	0.231	-0.03
0.9	0.219	-0.15			0.9	0.216	-0.53
0.95	0.208	-0.46			0.95	0.197	-1.17
1	0.198	-0.74			1	0	-0.48

Table 7 The blade chord and twist angle distributions of the FPFS wind turbine blade

Appendix G   MATLAB Codes

This appendix includes some parts of MATLAB codes: (1) the code for searching optimal induction factors in BEM blade design with F and drag; (2) the code for XFOIL initialisation; (3) the code for blade coordinates transformation. The MATLAB codes are not fully presented considering space limitations.

(1)

```
%solve a,b inducing factors////////////////////////


factors=[0;0];%Innitialization


x0=[0;0];
ub=[];


options = optimset;
% Modify options setting
options = optimset(options,'Display', 'on');
options = optimset(options,'Algorithm', 'active-set');
[x,fval,exitflag,output,lambda,grad,hessian] = ...
fmincon(@objfun_max_cp,x0,[],[],[],[],[],ub,@nonlconstr_max_cp,options
,cl,cd,r,R,Rh,b,Laba0,n1,n4);


factors=[x(1);x(2)];
%///solving Q and theta////////////////////////////
a=factors(1);
bb=factors(2);
theta=atan((1/Laba)*(1-a)/(1+bb));%relative wind angle in rad


f=(b/2)*(R-r)/(R*sin(theta));
F=(2/pi)*acos(exp(-f));
Q=(8*pi*a*F*(1-a*F)*(sin(theta))^2)/((1-a)^2*(Cl*cos(theta)+Cd*sin(the
ta));% related to chord
%%////////////////////////////////////////////////


function y = objfun_max_cp (x,cl,cd,r,R,Rh,b,Laba0,n1,n4)
fai=atan((1-x(1))/((1+x(2))* Laba0*n1));
f=(b/2)*(R-r)/(R*sin(fai));
fh=(b/2)*(r-Rh)/(Rh*sin(fai));
F1=(2/pi())*acos(exp(-f));
```

```
F2=(2/pi())*acos(exp(-fh));
F=F1*F2;
y = -((8/(na0^2))*x(2)*(1-x(1))*F*((na0*n1)^3)*(na0/n4));
%%//////////////////////////////////////////////////

function [c,ceq] = nonlconstr_max_cp (x,cl,cd,r,R,Rh,b,Laba0,n1,n4)
fai=atan((1-x(1))/((1+x(2))*Laba0*n1));
f=(b/2)*(R-r)/(R*sin(fai));
fh=(b/2)*(r-Rh)/(Rh*sin(fai));
F1=(2/pi())*acos(exp(-f));
F2=(2/pi())*acos(exp(-fh));
F=F1*F2;
ceq =x(2)*(x(2)+1)*((Laba0*n1)^2)-x(1)*(1-x(1)*F);
c = [];


%%//////////////////////////////////////////////////////////////
(2)
%call XFOIL////////////////////////
    r=0;
    DataMinRows=0;
    Re1=get(handles.re_number,'String');
    Re=str2num(Re1);
    Mach1=get(handles.mach_number,'String');
    Mach=str2num(Mach1);

    Min_angle1=get(handles.min_angle,'String');
    Min_angle=str2num(Min_angle1);
    Max_angle1=get(handles.max_angle,'String');
    Max_angle=str2num(Max_angle1);
    Step_angle1=get(handles.step_angle,'String');
    Step_angle=str2num(Step_angle1);

    DataMinRows=(Max_angle-Min_angle)/Step_angle;

    [AirfoilFileName,AirfoilFilePathName] = uigetfile('*.dat','Select the
coordinates.dat-file');%%read airfoil coordinates file
 if(exist(AirfoilFileName,'file'))%this file should be in the matlab
directory
 %create XFOIL configuration file
    fidout=fopen('XFOILconfig.txt','w');
frewind(fidout);
```

```
fprintf(fidout,'LOAD %s\r\n',AirfoilFileName);            %write
date to XFOILconfig.txt
    fprintf(fidout,'PANE\r\n');
fprintf(fidout,'OPER\r\n');
fprintf(fidout,'VISC %d\r\n',Re);
fprintf(fidout,'MACH %d\r\n',Mach);
fprintf(fidout,'ITER 500\r\n');
fprintf(fidout,'PACC\r\n');
fprintf(fidout,'TempResults.plo\r\n');
fprintf(fidout,'TempResults.dum\r\n');
fprintf(fidout,'ASEQ %d %d %d\r\n',Min_angle,Max_angle,Step_angle);
fprintf(fidout,'PACC\r\n');
fprintf(fidout,'\r\n');
fprintf(fidout,'QUIT\r\n');
fprintf(fidout,'\r\n');
fclose(fidout);
 else
    msgbox('Can not find airfoil file!');
    return;
 end


%///////////////////////////////////////////////////////////////
(3)
%transfer blade chord and twist data to points////////////////////

tabledata_chordtwist=get(handles.sections_table,'Data');
[w,~]=size(tabledata_chordtwist);
QN=w;%section numbers
Ltheta=tabledata_chordtwist(:,6);%twist angle list
Lc=tabledata_chordtwist(:,8);%chord list
Lr=tabledata_chordtwist(:,2);%local radius list
 for i=1:w
%%///////////////////////////////////
    [coordinatesFileName,coordinatesFilePathName] =
uigetfile('*.dat','Select the section airfoil.dat-file');%%read blades
coordinates file
  if(exist(coordinatesFileName,'file'))%this file should be in the matlab
directory
  coordinates_file=load(coordinatesFileName);
  [m,n]=size(coordinates_file);
```

```matlab
    x0=coordinates_file(1:m,1);  % x coordinates
    y0=coordinates_file(1:m,2); % y coordinates
    z0=zeros(m,1);% z coordinates
    else
        msgbox('Can not find airfoil file!');
        return;
    end
    x=zeros(m,1);
    y=zeros(m,1);
    z=zeros(m,1);


    x1=zeros(m,1);
    y1=zeros(m,1);
    z1=zeros(m,1);


    x2=zeros(m,1);
    y2=zeros(m,1);
    z2=zeros(m,1);

 %%generate the dat file/////////
    str=sprintf('%d.dat',i);
    str2=sprintf('del /F /Q %d.dat',i);
    system(str2);%delete existing files
    fidout=fopen(str,'w');                         %create the new file,%this
file is in the matlab directory
    frewind(fidout);


    %%/////////////////////////
     for p=1:m
    x1(p)=x0(p)*Lc(i)*1000;%scale, position
    y1(p)=y0(p)*Lc(i)*1000;
    z1(p)=Lr(i)*1000;



    %%xc(p)=1/4*Lc(i)*1000;%1/4 chord, aerodynamic centre
    xc(p)=0.25*Lc(i)*1000;%25% chord, aerodynamic centre
    yc(p)=0;
    zc(p)=0;


    x2(p)=x1(p)-xc(p);%move
    y2(p)=y1(p)-yc(p);
```

194

```matlab
    z2(p)=z1(p)-zc(p);


    if(x2(p)==0)
    x(p)=-( (x2(p)^2+y2(p)^2)^(0.5)*cos( pi/2+Ltheta(i)*pi/180 ) );%rotate
    y(p)=-( (x2(p)^2+y2(p)^2)^(0.5)*sin( pi/2+Ltheta(i)*pi/180 ) );
    elseif( (x2(p)<0) &&( y2(p)>0 ))

x(p)=-( (x2(p)^2+y2(p)^2)^(0.5)*cos( atan( y2(p)/x2(p) )+Ltheta(i)*pi
/180 ) );%rotate

y(p)=-( (x2(p)^2+y2(p)^2)^(0.5)*sin( atan( y2(p)/x2(p) )+Ltheta(i)*pi/
180 ) );
    elseif( (x2(p)<0) &&( y2(p)<0 ))

x(p)=-( (x2(p)^2+y2(p)^2)^(0.5)*cos( atan( y2(p)/x2(p) )+Ltheta(i)*pi/
180 ) );%rotate

y(p)=-( (x2(p)^2+y2(p)^2)^(0.5)*sin( atan( y2(p)/x2(p) )+Ltheta(i)*pi/
180 ) );
    elseif( (y2(p)==0)&&(x2(p)<0) )
    x(p)=-( (x2(p)^2+y2(p)^2)^(0.5)*cos( Ltheta(i)*pi/180 ) );%rotate
    y(p)=-( (x2(p)^2+y2(p)^2)^(0.5)*sin( Ltheta(i)*pi/180 ) );
    else

x(p)=(x2(p)^2+y2(p)^2)^(0.5)*cos( atan( y2(p)/x2(p) )+Ltheta(i)*pi/180
);%rotate

y(p)=(x2(p)^2+y2(p)^2)^(0.5)*sin( atan( y2(p)/x2(p) )+Ltheta(i)*pi/180);
    end
    z(p)=z2(p);


    format long g;
    fprintf(fidout,'%.2f %.2f %.2f\r\n',x(p),y(p),z(p)); %write data
      end


    fclose(fidout);


 end


%%/////////////////////////////////////////////////////////////
```

Appendix H CFD Data Visualisation

This appendix shows more data visualisation from 3D CFD modelling for the NREL/NASA Phase VI wind turbine as discussed in Chapter 5.

These CFD post data visualization pictures are presented below: (1) Relative velocity and pressure contours at different span sections; (2) Streamlines at different span sections; (3) Velocity field of rotor plane at wind speed of 7m/s and 15m/s; (4) Pressure field of axis-cut plane at wind speed of 7m/s and 15m/s.
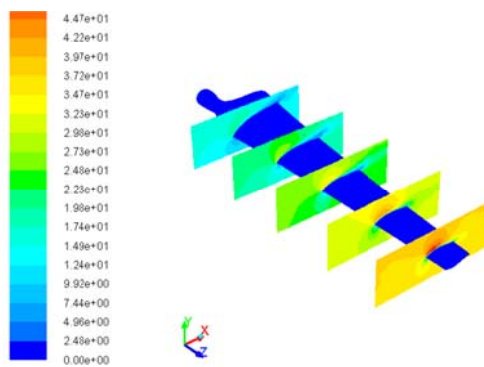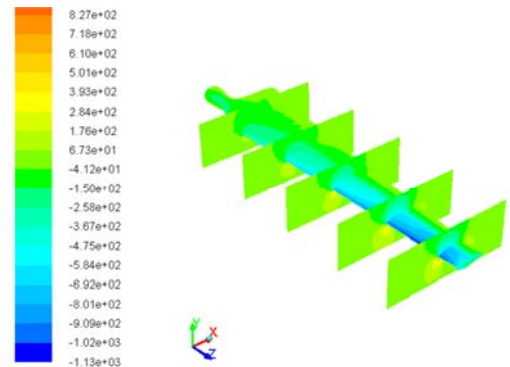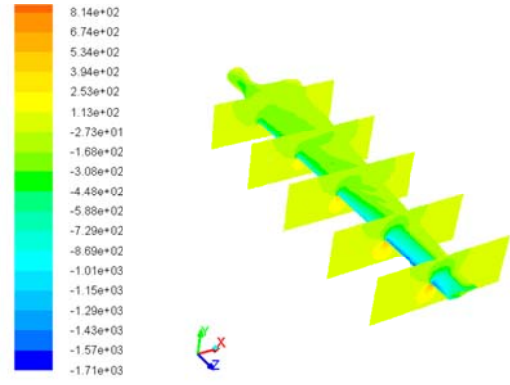

Velocity contour   Pressure contour

V= 7m/s
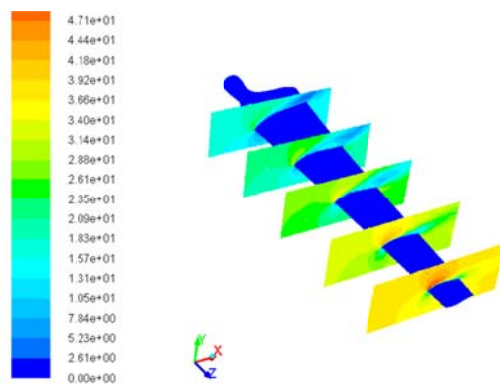
Velocity contour   Pressure contour

V= 10m/s
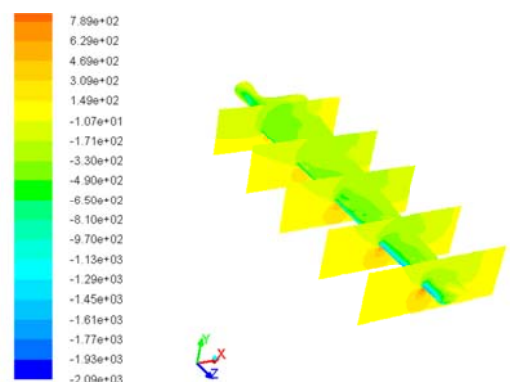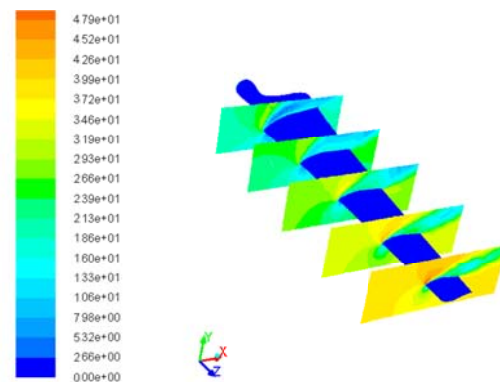
Velocity contour   Pressure contour

V= 15m/s
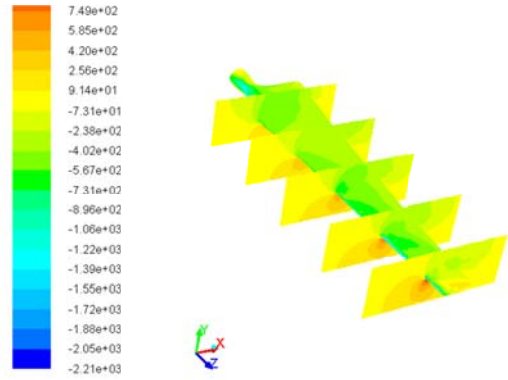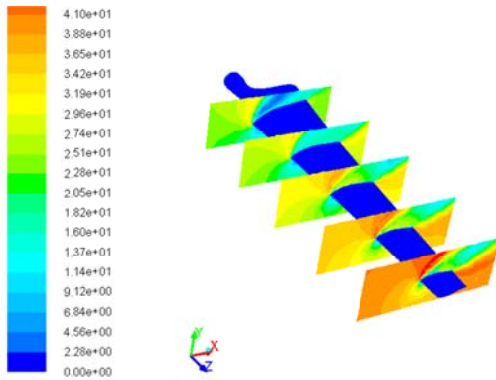
Velocity contour   Pressure contour

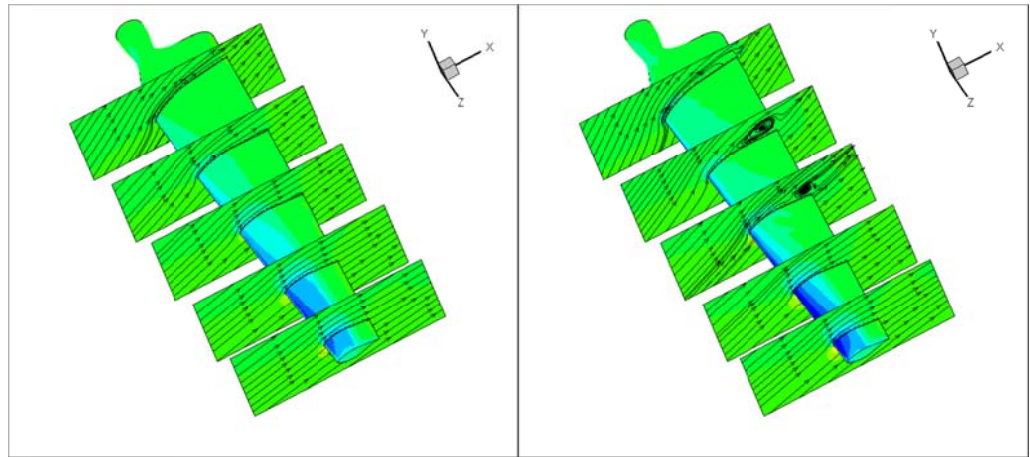V= 20m/s
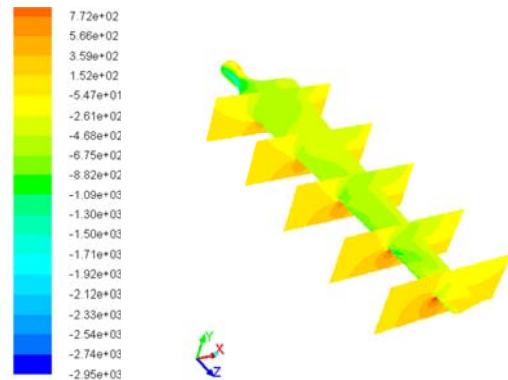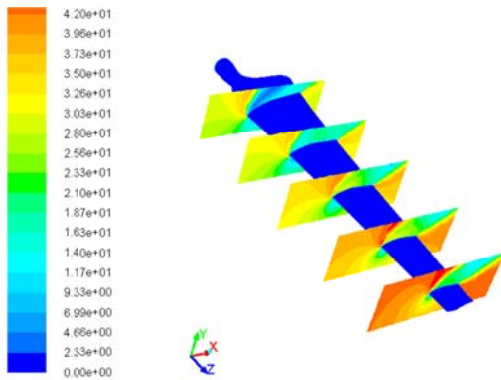
Velocity contour   Pressure contour
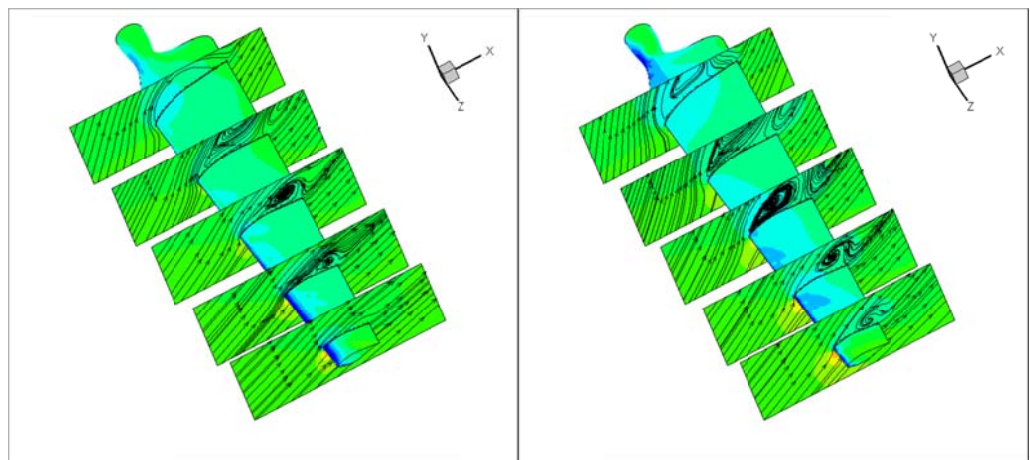
V= 25m/s

Figure 3 NREL/NASA Phase VI wind turbine section relative velocity and
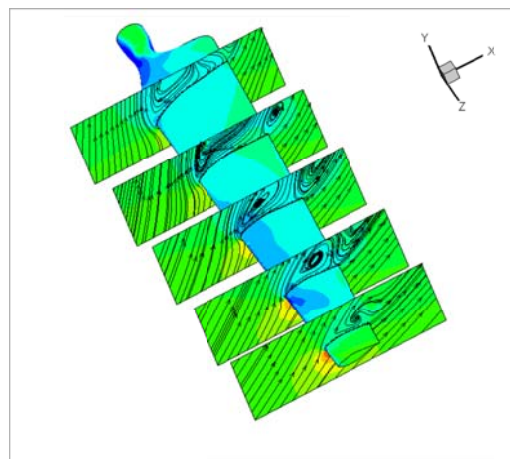
pressure contours

V=7m/s   V=10m/s

V=15m/s   V=20m/s

V=25m/s

Figure 4 NREL/NASA Phase VI wind turbine blade section streamlines
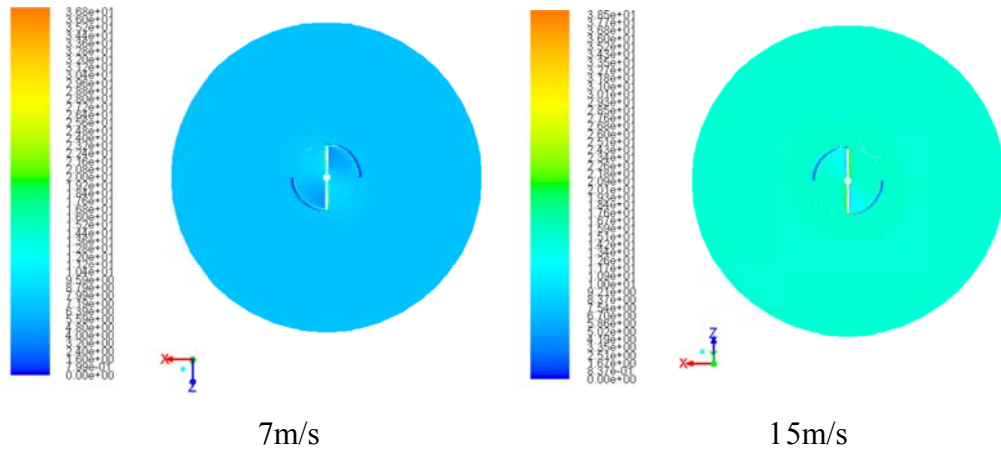
at different wind speeds

7m/s   15m/s

Figure 5 NREL/NASA Phase VI wind turbine velocity contours of rotor plane

at wind speeds of 7m/s and 15m/s

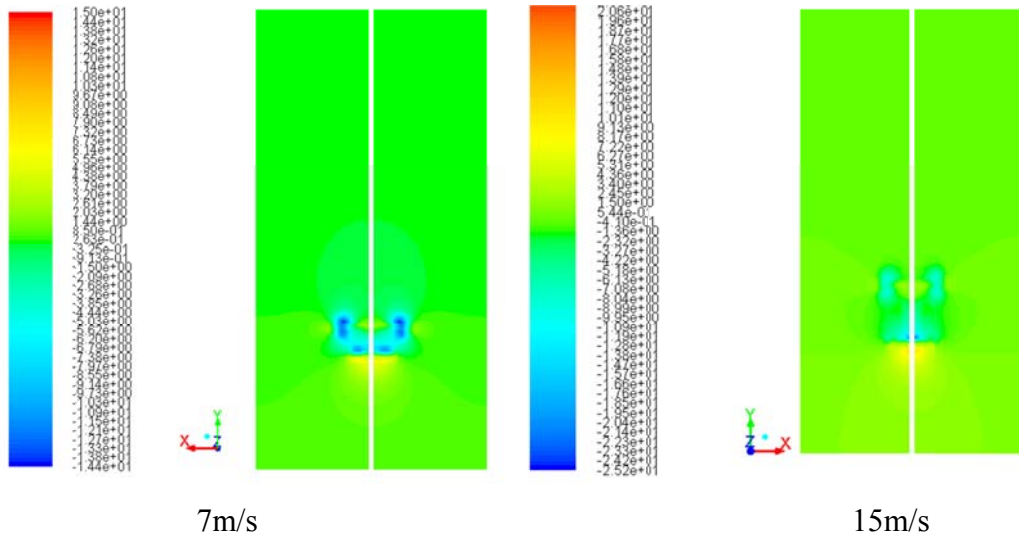7m/s   15m/s

Figure 6 NREL/NASA Phase VI wind turbine blade pressure contours of axis-cut plane

at wind speeds of 7m/s and 15m/s